

# Groundwater-induced geological disasters in underground engineering: Theoretical, experimental, and numerical approaches

**Edited by**

Shengli Yang, Liang Chen and Danqi Li

**Published in**

Frontiers in Earth Science

Frontiers in Ecology and Evolution



## FRONTIERS EBOOK COPYRIGHT STATEMENT

The copyright in the text of individual articles in this ebook is the property of their respective authors or their respective institutions or funders. The copyright in graphics and images within each article may be subject to copyright of other parties. In both cases this is subject to a license granted to Frontiers.

The compilation of articles constituting this ebook is the property of Frontiers.

Each article within this ebook, and the ebook itself, are published under the most recent version of the Creative Commons CC-BY licence. The version current at the date of publication of this ebook is CC-BY 4.0. If the CC-BY licence is updated, the licence granted by Frontiers is automatically updated to the new version.

When exercising any right under the CC-BY licence, Frontiers must be attributed as the original publisher of the article or ebook, as applicable.

Authors have the responsibility of ensuring that any graphics or other materials which are the property of others may be included in the CC-BY licence, but this should be checked before relying on the CC-BY licence to reproduce those materials. Any copyright notices relating to those materials must be complied with.

Copyright and source acknowledgement notices may not be removed and must be displayed in any copy, derivative work or partial copy which includes the elements in question.

All copyright, and all rights therein, are protected by national and international copyright laws. The above represents a summary only. For further information please read Frontiers' Conditions for Website Use and Copyright Statement, and the applicable CC-BY licence.

ISSN 1664-8714  
ISBN 978-2-8325-4125-8  
DOI 10.3389/978-2-8325-4125-8

## About Frontiers

Frontiers is more than just an open access publisher of scholarly articles: it is a pioneering approach to the world of academia, radically improving the way scholarly research is managed. The grand vision of Frontiers is a world where all people have an equal opportunity to seek, share and generate knowledge. Frontiers provides immediate and permanent online open access to all its publications, but this alone is not enough to realize our grand goals.

## Frontiers journal series

The Frontiers journal series is a multi-tier and interdisciplinary set of open-access, online journals, promising a paradigm shift from the current review, selection and dissemination processes in academic publishing. All Frontiers journals are driven by researchers for researchers; therefore, they constitute a service to the scholarly community. At the same time, the *Frontiers journal series* operates on a revolutionary invention, the tiered publishing system, initially addressing specific communities of scholars, and gradually climbing up to broader public understanding, thus serving the interests of the lay society, too.

## Dedication to quality

Each Frontiers article is a landmark of the highest quality, thanks to genuinely collaborative interactions between authors and review editors, who include some of the world's best academicians. Research must be certified by peers before entering a stream of knowledge that may eventually reach the public - and shape society; therefore, Frontiers only applies the most rigorous and unbiased reviews. Frontiers revolutionizes research publishing by freely delivering the most outstanding research, evaluated with no bias from both the academic and social point of view. By applying the most advanced information technologies, Frontiers is catapulting scholarly publishing into a new generation.

## What are Frontiers Research Topics?

Frontiers Research Topics are very popular trademarks of the *Frontiers journals series*: they are collections of at least ten articles, all centered on a particular subject. With their unique mix of varied contributions from Original Research to Review Articles, Frontiers Research Topics unify the most influential researchers, the latest key findings and historical advances in a hot research area.

Find out more on how to host your own Frontiers Research Topic or contribute to one as an author by contacting the Frontiers editorial office: [frontiersin.org/about/contact](https://frontiersin.org/about/contact)



# Groundwater-induced geological disasters in underground engineering: Theoretical, experimental, and numerical approaches

## Topic editors

Shengli Yang — China University of Mining and Technology, Beijing, China

Liang Chen — China University of Mining and Technology, China

Danqi Li — Curtin University, Australia

## Citation

Yang, S., Chen, L., Li, D., eds. (2023). *Groundwater-induced geological disasters in underground engineering: Theoretical, experimental, and numerical approaches*. Lausanne: Frontiers Media SA. doi: 10.3389/978-2-8325-4125-8

## Table of contents

- 04 **Fracturing criterion of rock hydrofracturing considering pore pressure effect**  
Bingxiang Huang, Heng Li, Xinglong Zhao and Yuekun Xing
- 17 **Experimental method and application of the slurry “diffusion-bleeding-seepage” of isolated overburden grout injection**  
Chaochao Wang, Jialin Xu, Dayang Xuan and Jian Li
- 28 **Permeation grouting mechanism of viscous time-varying fluid considering diffusion path**  
Hongbo Wang, Lianglin Dong, Qingsong Zhang, Zhipeng Li and Peiyuan Zhang
- 37 **Dynamic mechanical properties and energy dissipation analysis of frozen sandstone with initial damage**  
Qihang Xie, Yanlong Chen, Haoyan Lyu, Jun Gu, Yuanguang Chen, Huidong Cui and Peng Wu
- 47 **Study on prevention and control mechanism of runoff water hazard in thick coal seam mining in valley terrain**  
Yunfeng Zhang, Chenlong Qian, Xufeng Wang, Xuyang Chen, Zechao Chang, Jiyao Wang and Zhijun Niu
- 61 **Numerical study on heat storage efficiency of broken rock mass under different CO<sub>2</sub> injection conditions**  
Haozhe Geng, Yu Wu, Guan Hao, Yang Hao, Decheng Li and Haiyang Zhou
- 75 **Study on the clogging mechanism of upward inclined drainage holes in cut slopes**  
Jian Meng, An Chen, Kexin Yin and Caihui Zhou
- 88 **Theoretical and methodological approaches to identifying deep accumulations of oil and gas in oil and gas basins of the Russian Federation**  
O. M. Prischepa, S. B. Kireev, Yu. V. Nefedov, A. V. Martynov, D. S. Lutsky, T. N. Krykova, N. Sinitsa and Ruiming Xu
- 110 **Investigations into the failure mechanisms of coal bursts based on a real burst event in the Tangshan coal mine**  
Dongxu Jia, Zengzhu Zhi, Chen Cao and Ming Zhang
- 121 **An investigation on the thixotropic parameters and mechanical properties of loess**  
Le Wei, Faning Dang and Jiulong Ding
- 132 **An analysis of thixotropic micropore variation and its mechanism in loess**  
Le Wei, Faning Dang, Jiulong Ding, Xiaojuan Wu, Jiayang Li and Zhengzheng Cao
- 148 **Effect of weakening characteristics of mechanical properties of granite under the action of liquid nitrogen**  
Linchao Wang, Wan Zhang, Zhengzheng Cao, Yi Xue, Jianqiang Liu, Yang Zhou, Chenyang Duan and Tong Chen



## OPEN ACCESS

EDITED BY  
Shengli Yang,  
China University of Mining and  
Technology, Beijing, China

REVIEWED BY  
Jianhang Chen,  
China University of Mining and  
Technology, Beijing, China  
Sui Haitong,  
Yokohama National University, Japan

\*CORRESPONDENCE  
Bingxiang Huang,  
✉ huangbingxiang@cumt.edu.cn

SPECIALTY SECTION  
This article was submitted to  
Environmental Informatics and Remote  
Sensing,  
a section of the journal  
Frontiers in Earth Science

RECEIVED 29 November 2022

ACCEPTED 03 January 2023

PUBLISHED 13 January 2023

CITATION  
Huang B, Li H, Zhao X and Xing Y (2023),  
Fracturing criterion of rock  
hydrofracturing considering pore  
pressure effect.  
*Front. Earth Sci.* 11:1111206.  
doi: 10.3389/feart.2023.1111206

COPYRIGHT  
© 2023 Huang, Li, Zhao and Xing. This is an  
open-access article distributed under the  
terms of the [Creative Commons  
Attribution License \(CC BY\)](#). The use,  
distribution or reproduction in other  
forums is permitted, provided the original  
author(s) and the copyright owner(s) are  
credited and that the original publication in  
this journal is cited, in accordance with  
accepted academic practice. No use,  
distribution or reproduction is permitted  
which does not comply with these terms.

# Fracturing criterion of rock hydrofracturing considering pore pressure effect

Bingxiang Huang\*, Heng Li, Xinglong Zhao and Yuekun Xing

State Key Laboratory of Coal Resources and Safe Mining, China University of Mining and Technology, Xuzhou, China

Traditional hydraulic fracturing theory believes that as the initial pore pressure increases, the breakdown pressure of the rock will decrease. Previous experimental studies have shown that the breakdown pressure of rock hydraulic fracturing may increase with the increase of initial pore pressure (gradient), which cannot be explained by traditional theory. The current understanding of the effect of pore pressure and its gradient during hydraulic fracturing is still unclear. In this study, the pore pressure effect of rock hydraulic fracturing is analyzed based on a large number of macroscopic and microscopic phenomena of rock hydraulic fracturing in the previous study. Then, a new fracture criterion of rock fracturing is built considering the pressure-gradient effect. This new fracture criterion can reflect the main influence factors, including the rock particle size, porosity, pumping flow, inner diameter of open hole section, length of main fracture, height of main fracture (or length of open hole section), fluid viscosity, pore pressure, minimum initial *in situ* stress and rock tensile strength. The new fracture criterion is examined by the rock fracturing experiment which considering the pressure-gradient effect. The results show that the proposed fracture criterion considering the pore pressure effect can well predict the breakdown pressure of rock, and the prediction trend is consistent with the experimental results. The average error is less than 1% when adopting the present fracture criterion. The parameter sensitivity of the fracture criterion is analyzed. Results show that the fracture pressure increases with the rock porosity and this trend becomes more apparent with a larger initial pore pressure. It shows that the fracture pressure increases with the pumped flow rate. Besides, it shows that the fracture pressure decreases when increasing the particle size of the rock, but the decreasing trend gradually slows down. The research results can provide a theoretical basis for the mechanism of rock hydraulic fracturing and the structural modification effect of fluids in rock engineering.

## KEYWORDS

Rock, hydraulic fracturing, pore pressure, fracture criterion, porous medium

## 1 Introduction

Hydrofracturing refers to injecting high-pressure fluid (water, gas, etc.) into the formation through drilling, which induces the wellbore broken and fractures propagation under the action of hydro-mechanical coupling. Finally, artificial fractures are formed in the formation (Fjaer et al., 2008; King, 2012). Hydraulic fracturing is the most widely used and mature hydrofracturing technology. At present, it has been successfully applied to the development of shale oil and gas, tight oil and gas, coalbed methane and dry hot rock (Clarkson et al., 2016; Hou et al., 2018; Li et al., 2018; Zhang et al., 2018). Recently, hydraulic fracturing technology has been widely used in the coal industry. It is utilized for control of hard roofs, weakening of hard top coal, improvement of coal seam permeability, prevention of coal and gas outbursts, and rock

bursts, which have achieved remarkable results (Huang et al., 2016; Huang et al., 2017; Wu and Kang, 2017; Lv et al., 2020).

The hydraulic fracturing mechanism for coal and rock mass refers to the essential reason of borehole fracturing under the coupling effect of fluid pressure and solid stress field. It is to explain how coal and rock mass is cracked during hydraulic fracturing. It includes analysis of fracture mode and establishment of fracture criterion, prediction of breakdown pressure and determination of fracture direction. Fracture modes include tensile fracture and shear fracture, corresponding to tensile fracture criterion and shear fracture criterion.

Breakdown pressure refers to the pressure at which the high-pressure water injected into the wellbore (borehole) causes the wellbore (borehole) to rupture during the hydraulic fracturing. It is also known as the initiation pressure. The size of the breakdown pressure is mainly determined by the *in-situ* stress, the tensile strength of the stratum and the initial pore pressure. Breakdown pressure is a key technical parameter of fracturing design and construction process, which directly affects the effect of fracturing construction operations. The failure of hydraulic fracturing construction operations due to inaccurate prediction of breakdown pressure often occurs during engineering construction (Cuisiat and Haimson, 1992; Enever et al., 1992; Guo et al., 1993). Therefore, it is significant to study the fracture mechanism of coal and rock mass and give the corresponding breakdown pressure prediction formula for coal and rock mass hydraulic fracturing construction.

The early classical hydraulic fracturing theory believes that under the borehole water pressure and stress field, the borehole wall would undergo tensile fracture, resulting in a single hydraulic fracture. At the same time, the effective stress principle is introduced to consider the initial pore pressure of the stratum. The fracture process of rock hydraulic fracturing is analyzed, and many theoretical calculation formulas of the breakdown pressure are derived (Ito and Hayashi, 1991; Hossain et al., 2000; Huang et al., 2012; Zhang et al., 2011; Detournay and Carbonell, 1997; Jeffrey, 1989; Hubbert and Willis, 1957). Among them, the most widely used model is the classic H-W formula proposed by Hubbert M.K. and Willis D G in 1957 (Hubbert and Willis, 1957).

$$P_b = 3\sigma_h - \sigma_H + T - P_0 \quad (1)$$

Where  $\sigma_h$  is the minimum horizontal principal stress, MPa;  $\sigma_H$  is the maximum horizontal principal stress, MPa;  $T$  is the rock tensile strength, MPa;  $P_0$  is the rock pore pressure, MPa. This formula uses elastic theory to analyze the stress distribution around the borehole before fracturing. It is derived based on the maximum tensile stress strength criterion. Besides, it is aimed at the fracturing process of impermeable rock masses without considering the seepage effect of rock pore fluids. Therefore, the calculation results are larger than the actual value.

In 1967, under the assumptions of isotropy, homogeneity and small deformation, Bezael Haimson and Charles Fairhurst (Haimson and Fairhurst, 1967; Haimson and Fairhurst, 1969) introduced Darcy's law and Biot's effective stress principle based on the H-W formula. Then, they proposed the H-F formula for calculating the breakdown pressure of permeable rock.

$$P_b = \frac{3\sigma_h - \sigma_H + T - 2\eta P_i}{2(1 - \eta)} \quad (2)$$

When the rock is not structurally deformed, there are:

$$\eta = \frac{\phi(1 - 2\nu)}{2(1 - \nu)} \quad (3)$$

In the formula,  $\eta$  is the parameter of rock permeability, ranging from 0 to  $\sim 0.5$ .  $\phi$  is the porosity of the stratum, and  $\nu$  is the Poisson's ratio of the rock. This formula takes into account the influence of filtration of fracturing fluid on the breakdown pressure. For rocks with high permeability, the calculated breakdown pressure is higher than the actual value.

Anderson et al., 1973 proposed the calculation formula of the breakdown pressure under uniform horizontal *in-situ* stress, which considered the stress concentration of the borehole wall and the influence of pore pressure on the stress and strain of the rock.

$$P_b = \frac{2\nu}{1 - \nu} (P_v - \beta P_p) + \alpha P_p \quad (4)$$

Where  $P_v$  is the overburden pressure,  $P_p$  is the stratum pore pressure, and  $\beta$  is the Biot coefficient. This formula is modified on the basis of the H-W formula, but does not consider the influence of tectonic stress on the breakdown pressure.

Huang 1981 revised the H-W formula, and proposed the following formula for calculating breakdown pressure, which comprehensively considered the influence of borehole wall stress concentration, pore pressure, tectonic stress and tensile strength on breakdown pressure.

$$P_b = \left( \frac{2\nu}{1 - \nu} + 3c_1 - c_2 \right) (P_v - P_p) + P_p + \sigma_t \quad (5)$$

Where  $c_1$  and  $c_2$  are the two geological structural stress coefficients in the horizontal principal stress direction.  $\sigma_t$  is the rock tensile strength. The Terzaghi effective stress principle used in H-W is still used to calculate the effective stress in this formula, but the considerations are more comprehensive.

Li and Kong 2000 re-derived the effective stress principle of porous media, and deduced the breakdown pressure formula that can be applied to any permeable rock.

$$P_b = \frac{3\sigma_h - \sigma_H + \sigma_t - \varphi \frac{1-2\nu}{1-\nu} P_p}{1 + \varphi_c - \varphi \frac{1-2\nu}{1-\nu}} \quad (6)$$

Where  $\varphi$  is the rock porosity,  $\varphi_c$  is the rock contact porosity, and  $\nu$  is the Poisson's ratio. This formula effectively unifies the H-W formula and the H-F formula. The basic principle is the same as the H-W formula, and a modified effective stress principle is introduced at the same time.

Compared with the research on tensile failure mechanism in traditional hydraulic fracturing theory, the shear failure mechanism in hydraulic fracturing is rarely involved. In recent years, with the large-scale development of unconventional natural gas resources such as shale gas and coalbed methane, it has been discovered that not a single hydraulic fracture but a complex fracture network system is produced during hydraulic fracturing (Yao et al., 2016). The traditional single fracture theory based on tension fracture can no longer explain the fracture process of unconventional natural gas reservoir hydraulic fracture. Therefore, based on tension fracture and shear fracture, it has become a theoretical problem that studying the fracture mechanism of the fracture network system, which needs to be solved urgently. This problem has gradually become one of the current research hotspots in the field of hydraulic fracturing.

Some studies are conducted on whether the borehole wall undergo shear failure during fracturing. The results show that when the three-

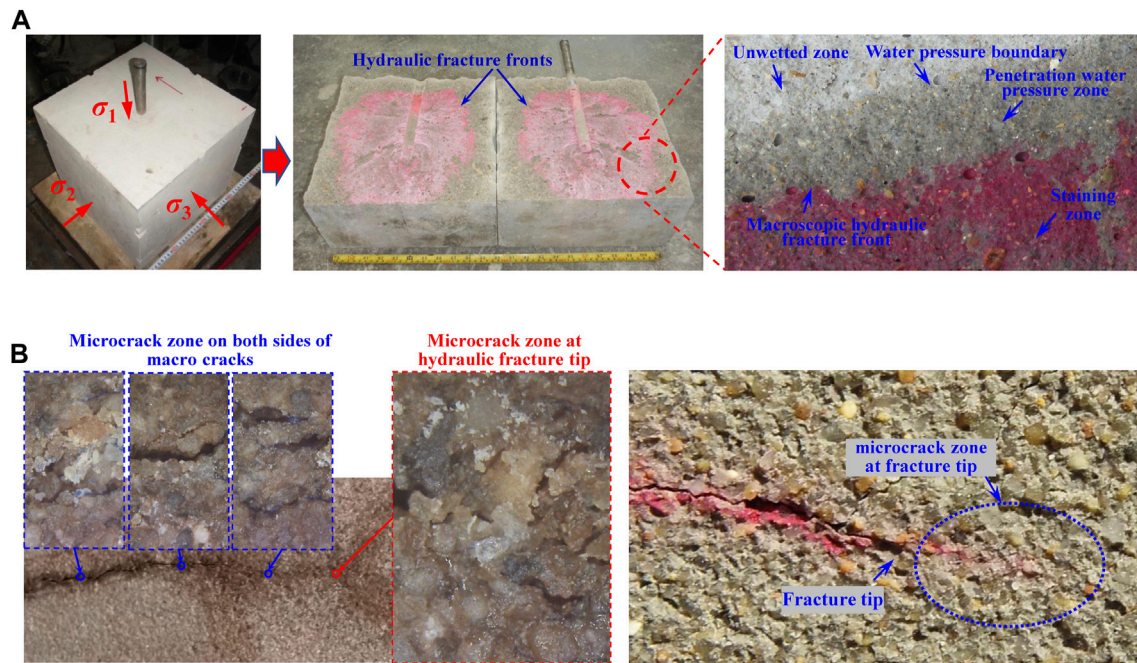


**FIGURE 1**  
Rock hydraulic fracturing. (A) Hydraulic fracturing in borehole under true triaxial stress and permeability water pressure zone morphology at hydraulic fracture tip; (B) Microcrack zone at hydraulic fracture tip.

dimensional principal stresses are all compressive stresses, shear failure may also occur at the borehole wall (Lockner and Byerlee, 1977). The shear failure condition of the borehole wall is analyzed by the Mohr-Coulomb failure criterion, and the identification method of hole wall failure mode is given (Yang et al., 1993). However, the analysis process is still using the elastic theory. The possibility of shear fracture of borehole wall under compressive principal stress is analyzed. But the effect of fluid pressure in the borehole is ignored during the hydraulic fracturing, and the permeability of the rock is not considered. The source of shear stress that causes shear fracture of borehole wall during the hydraulic fracturing is also not analyzed.

Traditional hydraulic fracturing theory does not consider the permeability of the rock (Hubbert and Willis, 1957; Haimson and Fairhurst, 1967), and uses the tensile fracture criterion to describe its fracture and propagation behavior (Olovyanyn, 2005). Pressurized water penetrates into the rock along the fractures, forms pore pressure, and generates pore pressure gradient (Lenoach, 1995; Tang et al., 2002). The influence on pore pressure is mainly based on the effective stress principle of saturated soil mechanics. But the understanding of the influence of pore pressure and its gradient during hydraulic fracturing is still unclear (Takatoshi, 2008). The practice of hydraulic fracturing of gas-bearing coal seams and the previous theoretical experimental research show that the breakdown pressure of hydraulic fracturing may increase with the increase of pore pressure (gradient) (Huang et al., 2018). This is unexplainable by traditional theory. Therefore, it is necessary to deeply understand the effect mechanism of the pore pressure gradient on hydraulic fracturing from the root.

In this study, aiming at the effect of pore pressure and its gradient during hydraulic fracturing, the mesoscopic structure of the rock is taken as the entry point of this study. The mesoscopic effect of fluid pressure on matrix particles during rock hydraulic fracturing is

analyzed by constructing a mesoscopic structure model of rock. A rock mesoscopic fracture model considering the effect of pore pressure and its gradient is established. The effect mechanism of pore pressure and its gradient on rock hydraulic fracturing is revealed. The research results can provide a theoretical basis for the mechanism of rock hydraulic fracturing and the structural modification effect of fluids in rock engineering.

## 2 Pore pressure gradient effect of rock hydraulic fracturing

When the rock hydraulic fracturing experiment is performed, the rose-red dye used in the poster is added to the fracturing fluid. Then stir it evenly, so that the sample is opened to observe the shape of the hydraulic fracture after the experiment (Figure 1). It is found that there is an osmotic water pressure zone at the front of the hydraulic fracture tip. It indicates that the particle bonding plane is permeable before it is fractured in the hydraulic fracturing process. The pressure water is osmotically filtered along the particle bonding plane, forming pore pressure and producing pore pressure gradient. When the borehole walls fracture, the hydraulic fracture tip and the front of the seepage zone expand forward simultaneously. Besides, the front of seepage pressure zone is ahead of the hydraulic fracture tip.

Through the above analysis, it is clear that the following factors must be considered when analyzing the fracture of the matrix particle bonding during hydraulic fracturing: 1) The rock is a permeable pore medium composed of mineral particles and has a certain initial pore pressure; 2) hydraulic fracturing leads to an increase in pore pressure in front of the fracture tip, which in turn generates a pore pressure gradient; 3) seepage caused dynamic water pressure (drop).



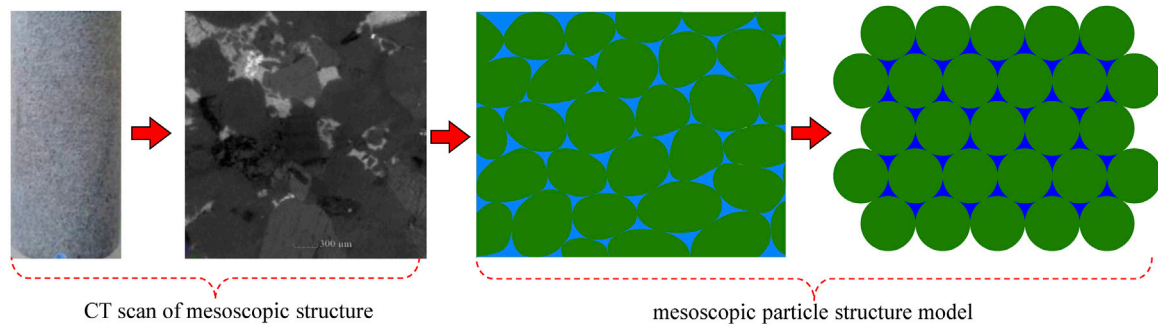


**FIGURE 2**  
Mesoscopic structure of sandstone (Zhao, 2019).

### 3 Construction of rock fracture model considering pore pressure effect

#### 3.1 Typical rock mesoscopic structure

Traditional hydraulic fracturing theory uses the effective stress principle of saturated soil mechanics to deal with the pore pressure when analysing the fracture process of rock. It is believed that the pore pressure and the particle framework share the external load, and the rock is assumed to be an impermeable medium. Therefore, the greater the initial pore pressure, the lower the breakdown pressure of the rock. The theory of hydraulic fracturing has been continuously updated in recent years, especially with the development of numerical calculations. There are many hydraulic fracturing theoretical models considering rock permeability and fluid-solid coupling, but the effect of pore pressure is still analyzed based on the effective stress principle.

When dealing with the problem of rock fracture induced by fluid pressure, pore pressure will affect the seepage process of fluid. Therefore, whether the effective stress principle of saturated soil mechanics is still applicable? This requires deep thinking.

To bypass the principle of effective stress and analyze the mechanism of pore pressure and its gradient on rock hydraulic fracturing, it is necessary to start from the mesoscopic structure of the rock. The effect of pore pressure on the mesoscopic framework of the rock during the hydraulic fracturing can be analyzed by constructing a rock mesoscopic structure model.

Hydraulic fracturing technology is mainly used in sedimentary rock series such as oil and gas reservoirs and coal strata, the typical lithology is sandstone. The mesoscopic structure of the sandstone sample is scanned, and the mesoscopic structure including the matrix structure and pore structure is observed. On this basis, the mesoscopic conceptual model can be abstracted to perform the mesoscopic mechanical analysis and establish the mesoscopic fracture model of rock hydraulic fracturing.

It can be seen from the scan results of the rock mesoscopic structure that the rock is formed by the bonding of mineral particles with pores between the particles. The pores contain fluid and have a certain pore pressure. The particles squeeze each other to form matrix stress under the action of external force. The matrix stress interacts with the pore pressure to form the stable mesoscopic structure of the sandstone. Based on the above analysis, a two-

dimensional mesoscopic bond particle model of the rock is constructed, including particles, pores, and bonding plane between particles (Figure 2).

The actual shape of the rock matrix particles is irregular spherical, and the size is different. Their shape and size distribution have certain randomness. This paper focuses on the failure process of the bonding plane between mineral particles under the action of matrix stress and pore pressure. Therefore, the influence of particle shape and size is ignored, and it is simplified into circular equal-diameter particles.

#### 3.2 Basic assumptions

- (1) Because real rocks are composed of rock matrix and pores, it is assumed that rocks are composed of basic units that include: i) Rock particles A, and ii) inter-rock binders B.
- (2) Assuming that rock particles A are dense non-permeable elastomers.
- (3) Assuming that the binder B is a permeable porous medium.
- (4) Rock fracture occurs only between the rock particles A and the binder B, including tension and shear.
- (5) Seepage exists within the binder under the action of pore pressure gradient, and the flow obeys Darcy's law.

#### 3.3 Relationship between tensile failure and pore pressure gradient

In the process of water injection and pressurization, the water pressure inside the main fracture is significantly higher than the pore pressure inside the rock. So, there is seepage from the fracture into the rock. The nature of seepage is pressure-driven flow. The direction of seepage flow is the same as the direction of fluid pressure gradient. The fracture in  $y$ -direction is used as an example for illustration. The pressure gradient direction is approximately along the  $x$ -direction, as shown in Figure 3. The following discussion is based on the case of zero water pressure gradient and the case with water pressure gradient respectively.

- (1) At zero water pressure gradient, the bond stress is

$$\sigma'_b = p'_w - p'_w \varphi_b - p_0 \varphi_0 \quad (7)$$

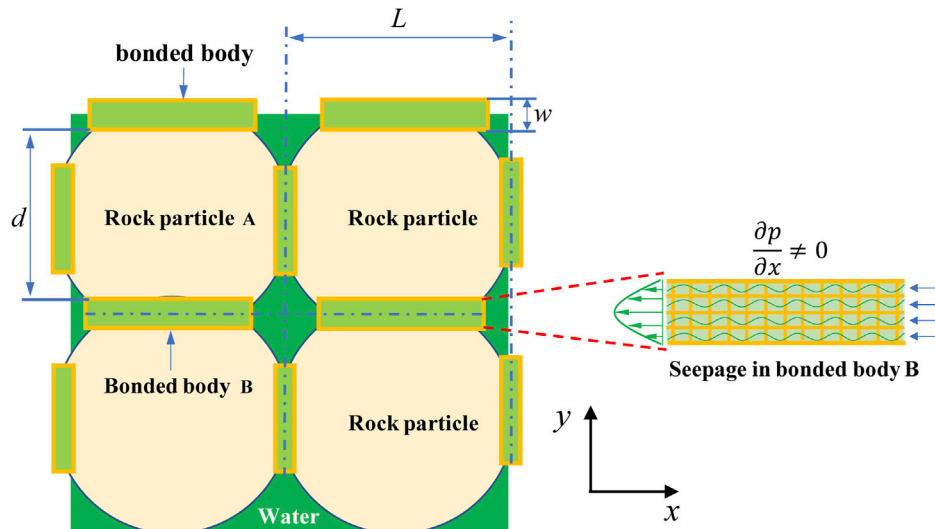


**FIGURE 3**  
Size of the basic particle unit.

Where,  $p'_w$  is the water pressure in fracture,  $\varphi_b$  is the binder porosity,  $\varphi_0$  is the blind pore porosity,  $p_0$  is the pore pressure in the blind pore.

- (2) When there is a water pressure gradient (Figure 4), the bond stress is

$$\sigma_b = p_w - \left( p_w - \frac{\partial p}{\partial x} L \right) \varphi_b - p_0 \varphi_0 \quad (8)$$

Where,  $p_w$  is the water pressure in fracture,  $\frac{\partial p}{\partial x} L$  indicates the pressure difference between the left and right sides of the particle. When the water pressure in fracture is the same  $p'_w = p_w$ , take  $\Delta\sigma_b = \sigma_b - \sigma'_b$ , then

$$\Delta\sigma_b = \sigma_b - \sigma'_b = \frac{\partial p}{\partial x} L \varphi_b \quad (9)$$

Where  $\Delta\sigma_b$  indicates the bond bear the additional compressive stress due to the existence of the water pressure gradient effect. That is, if the rock particles and the bond undergo tensile failure in the  $x$  direction, the additional stress increment which need to be overcome. At this point, the tensile failure condition is

$$p_b \geq (\sigma_3 + \sigma_t) + \frac{\partial p}{\partial x} L \varphi_b \quad (10)$$

Where,  $\sigma_3$  is the minimum *in situ* stress,  $\sigma_t$  is the rock tensile strength. A similar idea is used to analyze the effect of water pressure gradient at the crack tip on the rock rupture, as shown in Figure 5. According to the basic theory of seepage and seepage phenomenon, the water pressure gradient at the crack tip approximately shows a semicircular distribution around the tip. The unit body composed of rock particles and binder is selected. Under the action of the water pressure gradient, the additional stress to be borne by the binder along the direction of the water pressure gradient is  $\Delta\sigma_b$ , as shown in Figure 5. Then, the additional stress increment that needs to be overcome for the binder to break at the crack tip is  $\Delta\sigma_{bx}$ . The following relationship exists with  $\Delta\sigma_b$  and  $\Delta\sigma_{bx}$

$$\Delta\sigma_{bx} = \Delta\sigma_b \cos \beta \quad (11)$$

Based on the approximate semicircular distribution of the water pressure gradient at the tip of the seam, it is known that  $\beta = 45^\circ$ . Therefore, the tensile failure condition of crack tip at this time is

$$p_b \geq (\sigma_3 + \sigma_t) + \frac{\sqrt{2}}{2} \frac{\partial p}{\partial x} L \varphi_b \quad (12)$$

### 3.4 Relationship between shear failure and pore pressure gradient

Considering the general situation, the schematic diagram of the water pressure on the rock particles is shown in Figure 6. Shear failure occurs when the shear force in  $x$ -directional is greater than the shear strength between the particle and the binder. Therefore, the shear failure condition in  $x$ -direction is

$$\frac{\partial^2 p}{\partial x \partial y} L^2 \geq \tau_x \quad (13)$$

For hydraulic fracturing in round borehole,  $\frac{\partial^2 p}{\partial x \partial y}$  usually tends to 0. So, shear failure generally does not occur. The failure form is mainly tensile failure. Based on the above analysis, this study mainly considers the rock fracture criterion under the tensile failure condition.

## 4 Fracturing criterion of rock hydraulic fracturing considering pore pressure effect

### 4.1 Relationship between rock porosity $\varphi$ and particle size $d$ and binder size $w$

The rock is composed of rock matrix particles and pores, which is confirmed by experimental electron microscopy scans. The rock

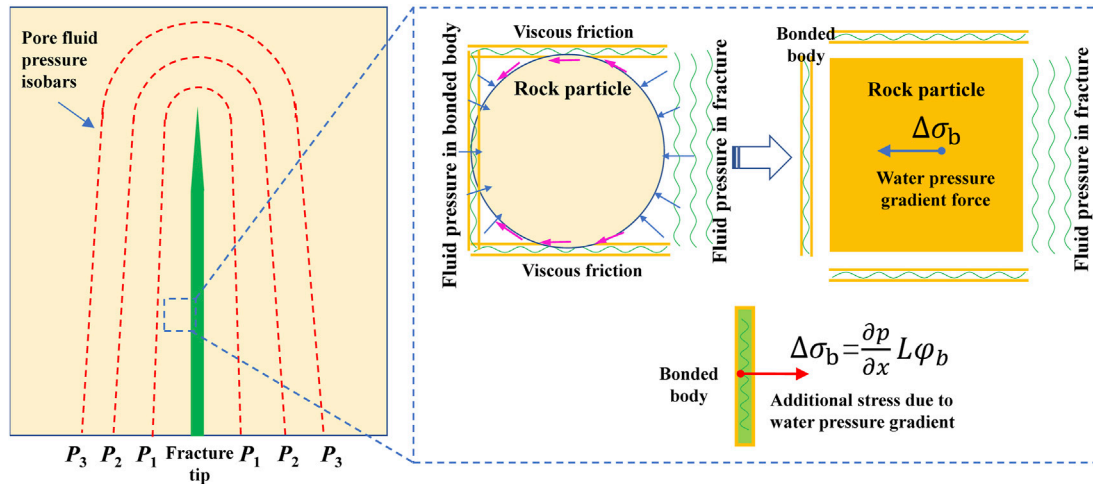


FIGURE 4

Stress diagram of rock unit on the left wall of the crack: additional stress due to water pressure gradient.

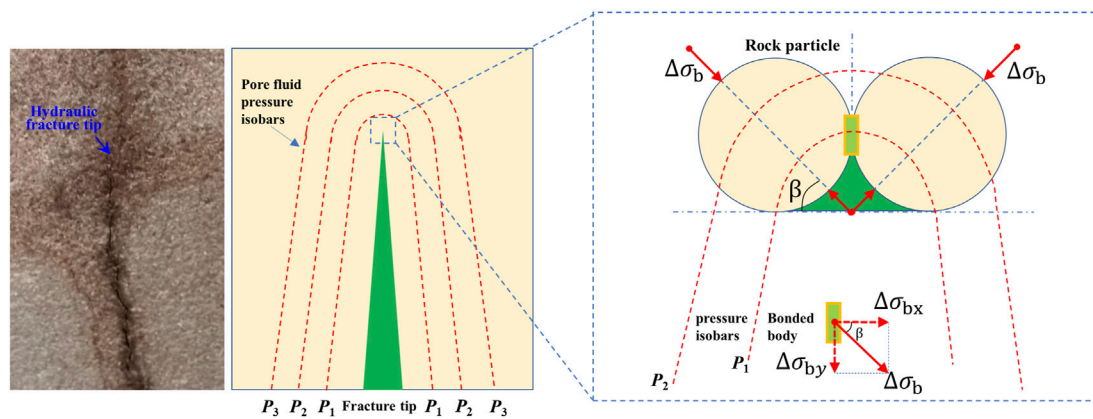


FIGURE 5

Schematic diagram of the stress on the rock unit at the crack tip: the additional stress increment required on the crack tip binder due to the water pressure gradient effect.

matrix structure is formed by rock particles under the action of *in situ* stress through bonding. Objectively speaking, rock particles have various shapes, including ellipsoidal, spherical, tetrahedral, hexahedral, and irregular particles. In order to describe rock porosity quantitatively more conveniently, spherical particles are temporarily equated to square particles here, and it is assumed that the rock is composed of square particles and a cemented body. The porosity of rock is mainly related to the size and stacking form of rock particles. Therefore, under the above assumptions, the characteristic length of the rock particles and the width of the binder are the keys to describe the rock porosity. Based on the above assumptions, the definition of rock porosity is given as

$$\varphi = \varphi_b \left( 1 - \frac{d^3}{(d+w)^3} \right) = \varphi_b \left( 1 - \frac{1}{(1+w/d)^3} \right) \quad (14)$$

Where  $d$  is the rock particle length (size after equivalence for spherical particles),  $w$  is the equivalent width of the binder, usually  $.5 \leq \varphi_b \leq 1$ . In the above porosity definition process, although the assumption of square particle structure is used, the particle characteristic size is based on the approximation of the real rock particle size, and the real porosity is only related to the particle equivalent size. Therefore, the above porosity formula is feasible. For rocks with different porosity characteristics, it is only necessary to adjust the particle size  $d$ , binder size  $w$  and binder porosity  $\varphi_b$  in the formula to obtain rock materials with the same porosity as the real rock. Denote  $a = w/d$ , then

$$\varphi = \varphi_b \left( 1 - \frac{1}{(1+a)^3} \right) \quad (15)$$

Rectifying the formula gives

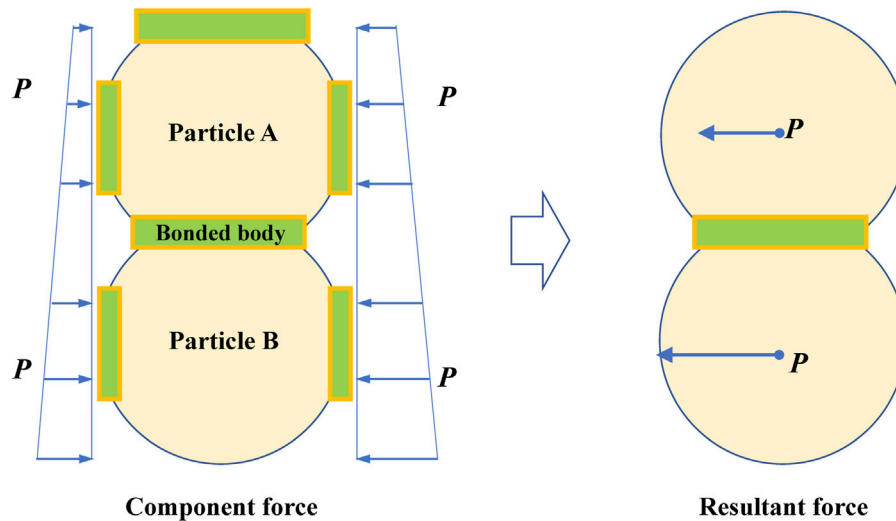


**FIGURE 6**  
Schematic diagram of pore water pressure distribution and resultant force when x-direction shear failure is considered.

$$a = \left( \frac{1}{1 - \varphi/\varphi_b} \right)^{\frac{1}{3}} - 1 \quad (16)$$

## 4.2 Relationship of pump injection flow rate and pore pressure gradient

The basic particle unit is composed of particle A, its lower side binder Bx, right side binder By, and rear side binder Bz. According to Darcy's law, the flow rate within the binder is.

$$Q_{Bx} = -\frac{\nabla p}{12\mu} L \cdot h^3 = -\frac{\partial p}{\partial x} \frac{1}{12\mu} L \cdot \varphi_b w^3 \quad (17)$$

Where  $h$  denotes the seepage channel width, which is equal to the binder width  $w$ ,  $\mu$  is the fluid viscosity,  $L$  is the characteristic length of the rock unit, then the flow rate along the  $x$ -direction within the particle unit is

$$Q_{cx} = Q_{Bx} + Q_{Bz} = -\frac{\partial p}{\partial x} \frac{1}{12\mu} (L + d) \cdot \varphi_b w^3 \quad (18)$$

Neglecting the flow direction (negative sign), then the relationship between the pore pressure gradient and the flow rate in the  $x$ -direction is

$$\frac{\partial p}{\partial x} = \frac{12\mu}{(L + d) \cdot \varphi_b w^3} Q_{cx} \quad (19)$$

The relationship between the flow rate  $Q_{cx}$  in the particle cell along the  $x$ -direction and the pumping flow rate  $Q_i$  is

$$Q_{cx} = \frac{L^2}{(2\pi R + 2L_f)L_z} Q_i \quad (20)$$

Where  $R$  is the radius of the injection hole,  $L_f$  is the length of the main fracture, and  $L_z$  is the length of the naked hole section (or refers to the main fracture height). The final pressure gradient is

$$\frac{\partial p}{\partial x} = \frac{6\mu}{(L + d) \cdot \varphi_b w^3} \frac{L^2}{(\pi R + L_f)L_z} Q_i \quad (21)$$

Then the differential pressure is

$$\begin{aligned} \frac{\partial p}{\partial x} L &= \frac{12\mu}{(L + d) \cdot \varphi_b w^3} L Q_{cx} = \frac{12\mu}{(L + d) \cdot \varphi_b w^3} L \frac{L^2}{2\pi R L_z} Q_i \\ &= \frac{12\mu}{(2d + ad) \cdot \varphi_b a^3 d^3} \frac{(1 + a)^3 d^3}{(2\pi R + 2L_f)L_z} Q_i \\ &= \frac{6\mu}{(\pi R + L_f)L_z d} \frac{(1 + a)^3}{\varphi_b (2 + a)a^3} Q_i \end{aligned} \quad (22)$$

That is

$$\frac{\partial p}{\partial x} L = \frac{6\mu}{(\pi R + L_f)L_z d} \frac{(1 + a)^3}{\varphi_b (2 + a)a^3} Q_i \quad (23)$$

Considering the porosity factor, then

$$\frac{\partial p}{\partial x} L \varphi_b = \frac{6\mu}{(\pi R + L_f)L_z d} \frac{(1 + a)^3}{(2 + a)a^3} Q_i \quad (24)$$

## 4.3 Tensile failure criterion of rock hydraulic fracturing considering pore pressure effect

The tensile failure criterion of rock hydraulic fracturing considering pore pressure effect has been given in the previous section, which takes the following form:

$$p_b \geq (\sigma_3 + \sigma_t) + \frac{\sqrt{2}}{2} \frac{\partial p}{\partial x} L \varphi_b \quad (25)$$

Then considering the influence of pore pressure  $p\varphi^{2/3}$  and combined with the definition of pore pressure gradient effect given in Eq. 24, the following tensile failure criterion of rock hydraulic fracturing is obtained.

$$p_b \geq (\sigma_3 + p\varphi^{2/3} + \sigma_t) + \frac{3\sqrt{2}\mu}{(\pi R + L_f)L_z d} \frac{(1+a)^3}{(2+a)a^3} Q_i \quad (26)$$

Consider the effect of instanton deformation on rock particle size  $d$  in fluid-solid coupling:

$$d = \frac{d_0}{e^{\xi p}} \quad (27)$$

Where  $d_0$  is the rock particle diameter at zero pore pressure,  $\xi$  is a small amount and determined by experiment.

According to the compressive experiments of rock materials, it is known that the strain per unit length of rock materials before compressive damage is negligible relative to the unit length 1. Analogously, it is known that the compression of the finite pore pressure on the rock particle size is also very limited. Therefore, (27) can be approximated as  $d \approx d_0$ . Eq. 26 is still applicable to the problem of rock breakdown pressure prediction under the action of fluid-solid coupling.

The above tensile failure criterion takes into account the effects of rock particle size  $d$ , porosity  $\varphi$ , pumping flow  $Q_i$ , inner diameter of naked hole section  $R$ , main fracture length  $L_f$ , main fracture height (or length of naked hole section)  $L_z$ , fluid viscosity  $\mu$ , pore pressure, initial minimum *in situ* stress  $\sigma_3$ , and tensile strength  $\sigma_t$ .

Note: The effect of porosity  $\varphi$  is reflected in parameter  $a$ , as detailed in the previous equation;  $\sigma_3$  denotes the initial minimum *in situ* stress.

#### 4.4 Shear failure of rock hydraulic fracturing considering pore pressure effect

Shear failure condition in  $x$ -direction

$$\frac{\partial^2 p}{\partial x \partial y} L^2 \geq \tau_x \quad (28)$$

Pore pressure gradient in  $x$ -direction

$$\frac{\partial p}{\partial x} = \frac{6\mu}{(L+d) \cdot \varphi_b w^3} \frac{L^2}{(\pi R + L_f)L_z} Q_i \quad (29)$$

The physical quantities to the right of the equal sign are all independent of the parameter  $y$ , so

$$\frac{\partial^2 p}{\partial x \partial y} = \frac{6\mu}{(L+d) \cdot \varphi_b w^3} \frac{L^4}{(\pi R + L_f)L_z} \frac{\partial Q_i}{\partial y} = 0 \quad (30)$$

Therefore, there is no shear failure.

## 5 Experimental verification of fracture criterion

To examine the new fracturing criterion proposed in this paper, we choose the recent experimental data based on hydraulic fracturing to validate the present model.

The experiment was carried out using standard cylindrical coarse sandstone samples, as shown in Figure 7, with a diameter of 50 mm and a height of 100 mm. Drill a cylindrical water injection hole on the end face of the cylindrical rock sample, where the hole length is 65 mm and its diameter is 6 mm. An open hole section with a length of 30 mm is reserved at the bottom of the borehole as the fracture zone. The experiment was carried out on the pseudo triaxial fluid-solid coupling hydraulic fracturing experimental system. For detailed physical experiment parameter settings and experimental steps, please refer to the previous research of our research group (Huang et al., 2018; Zhao, 2019).

The mechanical property parameters of rock samples are obtained by averaging the values obtained through multiple tests in indoor experiments. See Table 1 for detailed mechanical property parameters of rock samples.

During triaxial pressurization experiments, the axial pressure is 12 MPa, and the confining pressure is 8 MPa. Then the experiments were carried out under six different pore pressure conditions, including 0 MPa, 1.5 MPa, 3 MPa, 4.5 MPa, 6 MPa, and 7.5 MPa, respectively (Table 2). The rock fracture pressure obtained from the experiment is summarized in Table 3. From experimental results shown in Table 3, it is found that the fracture pressure of rock samples increases gradually with pore pressure, and there is an approximate linear relationship between the fracture pressure and pore pressure  $P_b = 4.586P_f + 12.762$  where the linear correlation coefficient reaches  $R^2 = 0.9973$ .

First, under the condition of zero pore pressure, we compare the fracture pressure obtained from the experiment with that given by the traditional H-W and H-F criterion models. As shown in Table 3, the experimental results are between the traditional H-W and H-F criteria, and are the closest to the L-K model results, which indicates that the experimental results given by us are qualitatively reasonable. This is because when the pore pressure is equal to zero ( $P_f = 0$ ), the traditional H-W criterion usually overestimates the rock fracture pressure, while the H-F criterion usually underestimates the rock fracture pressure, which can also be judged from the two definitions (refer to the previous Formulas shown in introduction). For zero pore pressure, compared with several existing fracture criteria, it is found that the predicted value of fracture pressure given by our fracture criteria is more consistent with the experimental test results, and the relative error of predicted fracture pressure is only  $-0.47\%$ , which is significantly less than the relative error of traditional fracture criteria as shown in Table 4.

In addition, by comparing with the experimental data, it is found that the relative error of the predicted fracture pressure in this paper is  $-0.35\%$  when the pore pressure is 1.5 MPa. When the pore pressure is 3.0 MPa, the relative error of the predicted fracture pressure is  $-0.32\%$ . When the pore pressure increases to 4.5 MPa, the relative error of the predicted fracture pressure in this paper is  $0.64\%$ . Under the condition that the pore pressure is 6.0 MPa, the relative error of the predicted fracture pressure in this paper is  $0.67\%$ . When the pore pressure further increases to 7.5 MPa, the relative error of the predicted fracture pressure in this paper is only  $0.13\%$ . The overall prediction error is within 1%. It is worth noting that the contact porosity of  $0.58$  (twice the porosity) is selected in the calculation process of L-K criterion in this paper. In fact, according to Li's rock fracture theory [25], the contact porosity is between the porosity and 1, and the selection of contact porosity will affect the final prediction results. How to accurately measure the contact porosity is also noteworthy, which is crucial for the L-K criterion model.



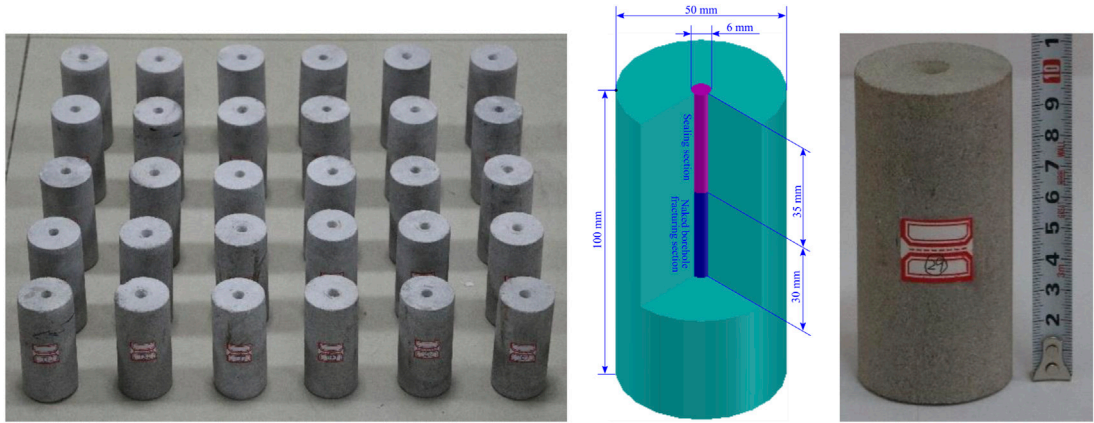


**FIGURE 7**  
The size of sample (Zhao, 2019).

**TABLE 1** Structural and mechanical characteristic parameters of sample materials (Huang et al., 2018; Zhao, 2019).

Material name	Porosity $\varphi$	Elastic modulus $E/\text{GPa}$	Tensile strength $\sigma_t/\text{MPa}$	Uniaxial compressive strength $\sigma_c/\text{MPa}$	Poisson's ratio $\nu$
Coarse sandstone	0.221~0.290	21.25	3.735	41.03	.15

**TABLE 2** Pressure environment and corresponding fracture pressure of rock samples in the experiment.

Test number	Initial pore pressure $P_f/\text{MPa}$	Confining pressure $\sigma_{\min}/\text{MPa}$	Axial pressure $\sigma_{\max}/\text{MPa}$	Fracture pressure $P_b/\text{MPa}$	Increase of fracture pressure
0	0	8	12	12.762 <sup>#</sup>	0
1	1.5	8	12	13.465	5.51%
2	3.0	8	12	14.179	11.1%
3	4.5	8	12	14.757	15.6%
4	6.0	8	12	15.464	21.2%
5	7.5	8	12	16.262	27.4%

Note: # in experiment No. 0 represents the estimated experimental value obtained by linear fitting of experimental results, and the linear regression function is  $P_b=0.4586P_f+12.762$ , where the linear correlation coefficient  $R^2=0.9973$ .

**TABLE 3** Comparison of fracture pressure when the pore pressure is zero.

Type	Fracture pressure $P_b/\text{MPa}$	Relative error
Experimental result	12.76	—
H-W criterion	15.73	23.3%
H-F criterion	8.934	−30.0%
Present criterion	12.70	−0.47%

To compare the predicted accuracy of different models, we draw the fracture pressure lines in the same Figure, as shown in Figure 8. It is seen that fracture pressure predicted by the traditional H-W criterion, H-F criterion and L-K criterion is quite different from the experimental results, especially the predicted trend is contrary to the experimental results. The present experimental results indicate that the fracture pressure of rock

increases with the pore pressure, which is also verified by the previous theoretical analysis. However, the prediction results of the traditional fracture criteria show that the fracture pressure of rock decreases with the increase of pore pressure. It is obvious that the traditional fracture criterion is insufficient in accurately predicting the rock fracture pressure under the influence of variable pore pressure. By contrast, the new fracture criterion (HLZX criterion) proposed in this paper can well predict the rock fracture pressure, the prediction trend is consistent with the experimental results, and the predicted values are also very consistent with the experimental results.

## 6 Sensitive parameter analysis

In the calculation process, the parameters set include: minimum geo-stress, rock tensile strength, length of water-injected hole (open

TABLE 4 Basic parameters of rock fracturing.

Parameter	Value	Parameter	Value
Minimum geo-stress $\sigma_3$ /MPa	8	Rock particle diameter $d$ /m	0.0006
Tensile strength of rock $\sigma_t$ /MPa	3.735	Porosity of bonded body $\varphi_b$	$2\varphi$
Length of water-injected hole $L_2$ /m	0.03	Fluid viscosity $\mu$ /(Pa s)	0.001
Inner diameter of water-injected hole $D$ /m	0.006	Pumped rate $Q_i$ /ml/min ( $\text{m}^3/\text{s}$ )	30 ( $5\times 10^{-7}$ )
Length of main fracture $L_f$ /m	0	Rock porosity $\varphi$	0.22

Note: The initial crack pressure of rock is analyzed here, so the length of main crack is 0.

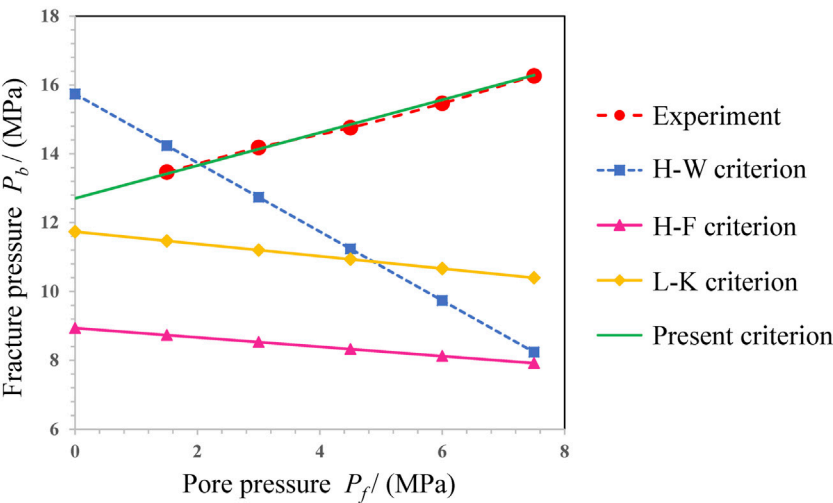


FIGURE 8 Comparison of rock fracture pressures predicted by different fracture criteria under variable pore water pressure.

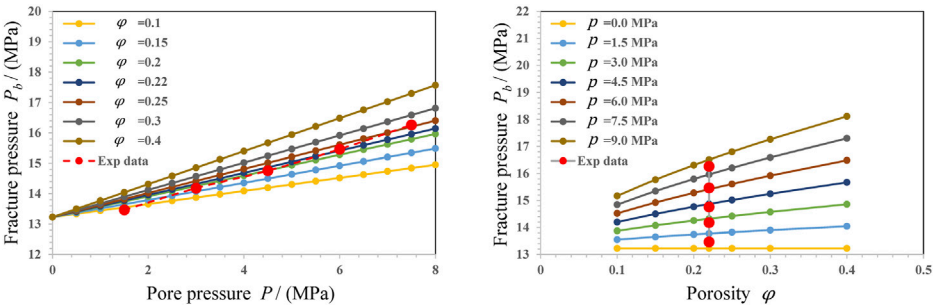


FIGURE 9 Influence regularity of the rock porosity  $\varphi$  on the fracture pressure  $P_b$ .

hole), inner diameter of water-injected hole, length of main fracture, porosity of bonded body, and fluid viscosity. See Table 4 for specific parameters. In the following part, we discuss the effects of rock porosity, pumping capacity and particle size on rock fracture pressure.

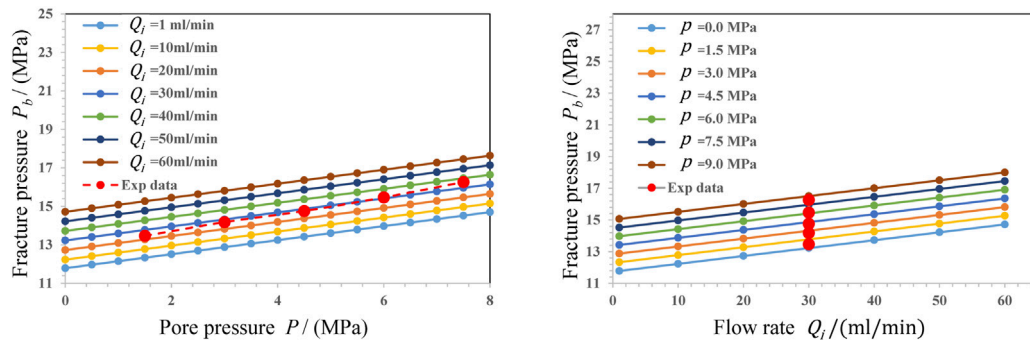


FIGURE 10

Influence regularity of the pumped flow rate  $Q_i$  on the fracture pressure  $P_b$ .

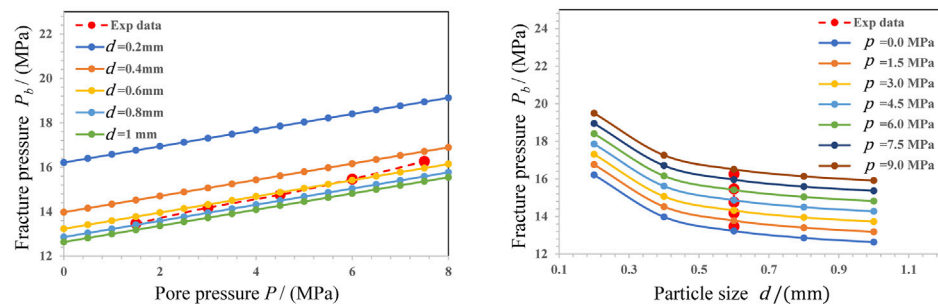


FIGURE 11

Influence regularity of the particle size  $d$  on the fracture pressure  $P_b$ .

## 6.1 Influence of rock porosity on fracture pressure

In this part, we discuss the influence of rock porosity on fracture pressure. Results are shown in Figure 9. It shows that the fracturing pressure of the rock increases with the rock porosity during the hydraulic fracturing process. When the porosity of the rock is larger, its permeability is better. The larger the permeability range of the same water injection pressure in the rock, the smaller the pore pressure gradient formed. Therefore, when the initial pore pressure is constant, the greater the rock porosity, the greater the fracture pressure of rock hydraulic fracturing. The essential reason is that, with the increase of rock porosity, the additional compressive stress  $\Delta\sigma_b$  increases, which is borne by the bounded body, causing the increase of fracturing pressure. It is also found that the increasing trend of the fracturing pressure is more significant if giving a larger initial pore pressure.

## 6.2 Influence of pump injection rate on fracture pressure

In this part, we discuss the influence of pump injection rate on the fracture pressure. Results are shown in Figure 10. With the increase of pump flow rate, the fracturing pressure of rock hydraulic fracturing increases

correspondingly. It can be seen from Eqs. 3, 8 that the larger the pump injection flow is, the greater the pore pressure gradient on both sides of the particle is the greater the additional pressure stress that the particle binder needs to bear due to the effect of water pressure gradient, therefore, the greater the fracturing pressure of rock hydraulic fracturing is.

## 6.3 Influence of rock particle size on fracture pressure

In this part, we analyze the influence regularity of the particle size on the rock fracturing pressure. Results are shown in Figure 11. With the increase of the rock particle size, the fracturing pressure of rock hydraulic fracturing decreases, and the decreasing trend gradually slows down. From the formula of rock fracture criterion (3.9), it is found that there is a negative correlation between the fracture pressure  $P_b$  and particle size  $d$ . Therefore, as the particle size decreases, the fracture pressure increases.

## 7 Conclusion

- (1) This study analyzes the pressure-gradient effect of the pore fluid during the rock fracturing process. Based on the observation of the

morphology of microcrack zone near the fracture tip, the key factors are identified and clarified when analyzing the fracture of the bonding surface of the skeleton particles in the process of hydraulic fracturing. It shows that the rock is a porous medium composed of mineral particles and has a certain initial pore pressure. It is the fracturing that leading to the change of pore pressure in the front area of the fracture tip, thus producing pore pressure gradient. Besides, there is a hydrodynamic pressure (drop) caused by the seepage.

- (2) Based on the mesoscopic structure of rock, this paper analyzes the rock fracturing process when considering the pressure-gradient effect of the pore fluid. Then, a new fracture criterion of rock fracturing is built considering the pressure-gradient effect. This new fracture criterion can reflect the main influence factors, including the rock particle size, porosity, pumping flow, inner diameter of open hole section, length of main fracture, height of main fracture (or length of open hole section), fluid viscosity, pore pressure, minimum initial geo-stress and rock tensile strength.
- (3) The new fracture criterion is examined by the rock fracturing experiments which consider the pressure-gradient effect. Results show that the fracture pressure predicted by the traditional criterion is quite different from the experimental results, especially the predicted trend. The traditional theory gives an inversed trend line, which is inconsistent with the experiments. In contrast, the present fracture criterion provides a satisfied prediction, including the variation trend and magnitude of the fracture pressure, which agrees well with the experiments. The average error is less than 1% when adopting the present fracture criterion.
- (4) The parameter sensitivity of the fracture criterion is analyzed. Results show that the fracture pressure increases with the rock porosity and this trend becomes more apparent with a larger initial pore pressure. It shows that the fracture pressure increases with the pumped flow rate. Besides, it shows that the fracture pressure decreases when increasing the particle size of the rock, but the decreasing trend gradually slows down.

## References

- Anderson, R. A., Ingram, D. S., and Zanier, A. M. (1973). Determining fracture pressure gradients from well logs. *J. Pet. Technol.* 25 (11), 1259–1268. doi:10.2118/4135-pa
- Clarkson, C. R., Ghaderi, S. M., Kanfar, M. S., Iwuoha, C., Pedersen, P., Nightingale, M., et al. (2016). Estimation of fracture height growth in layered tight/shale gas reservoirs using flowback gas rates and compositions—Part II: Field application in a liquid-rich tight reservoir. *J. Nat. Gas. Sci. Eng.* 36, 1031–1049. doi:10.1016/j.jngse.2016.11.014
- Cuisiat, F. D., and Haimson, B. C. (1992). Scale effects in rock mass stress measurements. *Int. J. Rock Mech. Min. Sci. Geomech. Abstr.* 29 (2), 99–117. doi:10.1016/0148-9062(92)92121-r
- Detournay, E., and Carbonell, R. (1997). Fracture-mechanics analysis of the breakdown process in minifracture or leakoff test. *SPE. Prod. Fac.* 12 (03), 195–199. doi:10.2118/28076-pa
- Enever, J. R., Cornet, F., and Roegiers, J. C. (1992). ISRM commission on interpretation of hydraulic fracture records. *Int. J. Rock Mech. Min. Sci. Geomech. Abstr.* 29, 69–72.
- Fjaer, E., Holt, R. M., Horsrud, P., Raaen, A. M., and Risnes, R. (2008). *Mechanics of hydraulic fracturing in developments in petroleum science*. Amsterdam: Elsevier, 369–390.
- Guo, F., Morgenstern, N. R., and Scott, J. D. (1993). Interpretation of hydraulic fracturing breakdown pressure. *Int. J. Rock Mech. Min. Sci. Geomech. Abstr.* 30 (6), 617–626. doi:10.1016/0148-9062(93)91221-4
- Haimson, B., and Fairhurst, C. (1969). Hydraulic fracturing in porous-permeable materials. *J. Pet. Technol.* 21 (07), 811–817. doi:10.2118/2354-pa
- Haimson, B., and Fairhurst, C. (1967). Initiation and extension of hydraulic fractures in rocks. *Spe. J.* 7 (03), 310–318. doi:10.2118/1710-pa
- Hossain, M. M., Rahman, M. K., and Rahman, S. S. (2000). Hydraulic fracture initiation and propagation: Roles of wellbore trajectory, perforation and stress regimes. *J. Pet. Sci. Eng.* 27 (3–4), 129–149. doi:10.1016/s0920-4105(00)00056-5
- Hou, B., Zhang, R. X., Zeng, Y. J., Fu, W. N., Muhadasi, Y., and Chen, M. (2018). Analysis of hydraulic fracture initiation and propagation in deep shale formation with high horizontal stress difference. *J. Pet. Sci. Eng.* 170, 231–243. doi:10.1016/j.petrol.2018.06.060
- Huang, B. X., Chen, S. L., and Cheng, Q. Y. (2016). Basic problems of hydraulic fracturing for mining and control zone gas in coal seams. *J. China Coal Soc.* 41 (01), 128–137.
- Huang, B. X., Zhao, X. L., Chen, S. L., and Liu, J. W. (2017). Theory and technology of controlling hard roof with hydraulic fracturing in underground mining. *Chin. J. Rock Mech. Eng.* 36 (12), 2954–2970.
- Huang, B. X., Zhao, X. L., Xue, W. C., and Sun, T. Y. (2018). Experimental investigation on the impact of initial pore pressure on breakdown pressure of borehole radial fracture for unsaturated mortar hydraulic fracturing under true triaxial stress. *J. Porous. Media* 21 (11), 1041–1057. doi:10.1615/jpormedia.2018021402
- Huang, J. S., Griffiths, D. V., and Wong, S. W. (2012). Initiation pressure, location and orientation of hydraulic fracture. *Int. J. Rock Mech. Min.* 49, 59–67. doi:10.1016/j.ijrmms.2011.11.014
- Huang, Z. R. (1981). Crack initiation and expansion of hydraulic fracturing. *Petroleum Explor. Dev.* 7 (5), 44–74.

## Data availability statement

The original contributions presented in the study are included in the article/supplementary material, further inquiries can be directed to the corresponding author.

## Author contributions

BH presented the idea and write the original manuscript, HL built the new fracture model, XZ performed the experiment, YX analysis the datas, all authors reviewed the manuscript.

## Funding

Financial support for this work, provided by the National Key Research and Development Program of China (No. 2021YFC2902102), the National Natural Science Foundation of China (No. 52004269), is gratefully acknowledged.

## Conflict of interest

The authors declare that the research was conducted in the absence of any commercial or financial relationships that could be construed as a potential conflict of interest.

## Publisher's note

All claims expressed in this article are solely those of the authors and do not necessarily represent those of their affiliated organizations, or those of the publisher, the editors and the reviewers. Any product that may be evaluated in this article, or claim that may be made by its manufacturer, is not guaranteed or endorsed by the publisher.

- Hubbert, M. K., and Willis, D. G. (1957). Mechanics of hydraulic fracturing. *Trans* 210 (01), 153–168. doi:10.2118/686-g
- Ito, T., and Hayashi, K. (1991). Physical background to the breakdown pressure in hydraulic fracturing tectonic stress measurements. *Int. J. Rock Mech. Min. Sci. Geomech. Abstr.* 28 (4), 285–293. doi:10.1016/0148-9062(91)90595-d
- Jeffrey, R. G. (1989). “The combined effect of fluid lags and fracture toughness on hydraulic fracture propagation,” in Low Permeability Reservoirs Symposium, March 68, 1989, Denver, Colorado, USA. SPE-18957-MS.
- King, G. E. (2012). “Hydraulic fracturing 101: What every representative, environmentalist, regulator, reporter, investor, university researcher, neighbor and engineer should know about estimating frac risk and improving frac performance in unconventional gas and oil wells,” in SPE Hydraulic Fracturing Technology Conference, February 68, 2012, The Woodlands, Texas, USA. SPE-152596-MS. doi:10.2118/152596-MS
- Lenoach, B. (1995). The crack tip solution for hydraulic fracturing in a permeable solid. *J. Mech. Phys. Solids*. 43 (7), 1025–1043. doi:10.1016/0022-5096(95)00026-f
- Li, C. L., and Kong, X. Y. (2000). A theoretical study on rock breakdown pressure calculation equations of fracturing process. *Oil Drill. Prod. Technol.* 22 (2), 54–56.
- Li, Y. W., Yang, S., Zhao, W. C., Li, W., and Zhang, J. (2018). Experimental of hydraulic fracture propagation using fixed-point multistage fracturing in a vertical well in tight sandstone reservoir. *J. Pet. Sci. Eng.* 171, 704–713. doi:10.1016/j.petrol.2018.07.080
- Lockner, D., and Byerlee, J. D. (1977). Hydrofracture in Weber Sandstone at high confining pressure and differential stress. *J. Geophys. Res.* 82 (14), 2018–2026. doi:10.1029/jb082i014p02018
- Lv, S. F., Wang, S. W., Liu, H. T., Li, R., and Dong, Q. X. (2020). Analysis of the influence of natural fracture system on hydraulic fracture propagation morphology in coal reservoir. *J. China Coal Soc.* 45 (07), 2590–2601.
- Olovyanyn, A. G. (2005). Mathematical modeling of hydraulic fracturing in coal seams. *J. Min. Sci.* 41 (1), 61–67. doi:10.1007/s10913-005-0064-6
- Takatoshi, I. (2008). Effect of pore pressure gradient on fracture initiation in fluid saturated porous media: *Rock. Eng. Fract. Mech.* 75, 1753–1762. doi:10.1016/j.engfracmech.2007.03.028
- Tang, C. A., Tham, L. G., Lee, P. K. K., Yang, T., and Li, L. (2002). Coupled analysis of flow, stress and damage (FSD) in rock failure. *Int. J. Rock Mech. Min.* 39 (4), 477–489. doi:10.1016/s1365-1609(02)00023-0
- Wu, Y. Z., and Kang, H. P. (2017). Pressure relief mechanism and experiment of directional hydraulic fracturing in reused coal pillar roadway. *J. China Coal Soc.* 42 (05), 1130–1137.
- Yang, Y. K., Xiao, C. F., Wu, G., and Qiu, X. D. (1993). Hydrofracturing breakdown modes under different *in-situ* stress states. *J. Chongqing Univ.* 16 (03), 30–35.
- Yao, J., Sun, Z. U., Zhang, K., Zeng, Q. D., and Yan, X. (2016). Scientific engineering problems and development trends in unconventional oil and gas reservoirs. *Petroleum Sci. Bull.* 1 (01), 128–142.
- Zhang, X., Jeffrey, R. G., Bungler, A. P., and Thiercelin, M. (2011). Initiation and growth of a hydraulic fracture from a circular wellbore. *Int. J. Rock Mech. Min.* 48 (6), 984–995. doi:10.1016/j.ijrmms.2011.06.005
- Zhang, Z. X., Wang, H. T., Deng, B. Z., Li, M. H., and Zhang, D. M. (2018). Field investigation of hydraulic fracturing in coal seams and its enhancement for methane extraction in the Southeast Sichuan Basin, China. *Energies* 11 (12), 3451. doi:10.3390/en11123451
- Zhao, X. L. (2019). The Mechanism of pore pressure gradient effect and the fracturing effect induced by disturbing stress during hydrofracturing. [PhD thesis]. Xuzhou: China University of Mining and Technology.





## OPEN ACCESS

## EDITED BY

Danqi Li,  
Curtin University, Australia

## REVIEWED BY

Jianhang Chen,  
China University of Mining and  
Technology, Beijing, China  
Saisai Wu,  
Xi'an University of Architecture and  
Technology, China

## \*CORRESPONDENCE

Jialin Xu,  
cumtxjl@cumt.edu.cn  
Dayang Xuan,  
dayang.xuan@cumt.edu.cn

## SPECIALTY SECTION

This article was submitted to  
Environmental Informatics  
and Remote Sensing,  
a section of the journal  
Frontiers in Earth Science

RECEIVED 17 November 2022

ACCEPTED 24 November 2022

PUBLISHED 19 January 2023

## CITATION

Wang C, Xu J, Xuan D and Li J (2023),  
Experimental method and application of  
the slurry “diffusion-bleeding-seepage”  
of isolated overburden grout injection.  
*Front. Earth Sci.* 10:1101371.  
doi: 10.3389/feart.2022.1101371

## COPYRIGHT

© 2023 Wang, Xu, Xuan and Li. This is an  
open-access article distributed under  
the terms of the [Creative Commons  
Attribution License \(CC BY\)](https://creativecommons.org/licenses/by/4.0/). The use,  
distribution or reproduction in other  
forums is permitted, provided the  
original author(s) and the copyright  
owner(s) are credited and that the  
original publication in this journal is  
cited, in accordance with accepted  
academic practice. No use, distribution  
or reproduction is permitted which does  
not comply with these terms.

# Experimental method and application of the slurry “diffusion-bleeding-seepage” of isolated overburden grout injection

Chaochao Wang<sup>1</sup>, Jialin Xu<sup>1,2\*</sup>, Dayang Xuan<sup>1\*</sup> and Jian Li<sup>1</sup>

<sup>1</sup>School of Mines, China University of Mining and Technology, Xuzhou, Jiangsu, China, <sup>2</sup>State Key Laboratory of Coal Resources and Safe Mining, China University of Mining and Technology, Xuzhou, Jiangsu, China

Isolated overburden grout injection (IOGI) is a green mining method to control surface subsidence. Slurry water significantly influences grouting effectiveness and mining safety. This study establishes a three-dimensional visualization experimental system for slurry “diffusion-bleeding-seepage” to investigate the seepage law of slurry water. The system is composed primarily of a transparent box (1.2 m × 0.5 m × 0.25 m) and support, with the solid–liquid coupling seepage similar material and modules for mining, grouting injection, slurry pressure and displacement monitoring, overburden saturation monitoring, and water leakage monitoring of the working face. A similar material with good permeability and non-disintegration is obtained by hydrophilic, water absorption, and permeability tests. Grouting and mining are simulated by pulling acrylic sheets and pumping slurry. With the fly ash slurry entering the injection layer, the slurry undergoes water–cement separation, and the water bleeding is formed to seep into the similar material. The volumetric water content of the similar material is obtained by arranging multiple groups of volumetric water content sensors into the similar material. The corresponding saturation is obtained by theoretical calculation. The experimental system is used to simulate the seepage of slurry water in a high initial saturation overburden, and the characteristics of injection slurry diffusion and water bleeding are obtained. The profile distribution of seepage of slurry water is found to possess a semi-elliptical shape. Under the condition of high initial saturation, slurry water appears in the working face. The system provides a convenient method for further research of IOGI slurry water seepage.

## KEYWORDS

isolated overburden grout injection, water bleeding, seepage, physical simulation experiment, saturation

# 1 Introduction

The isolated overburden grout injection (IOGI) is a key technology for surface subsidence control (Xuan et al., 2014; Xuan and Xu, 2014; Xu et al., 2015a; Xu et al., 2015b). Under the action of pumping pressure, slurry mixed with fly ash (Horiuchi et al., 2000) and water is transported to the mining-induced fracture below the key stratum (Xu et al., 2019; Wang et al., 2022) along the grouting borehole connecting the surface and fracture. Subsequently, the slurry diffuses along the mining-induced space, and water-cement separation occurs. Portions of the slurry water is bleeding, whereas some consolidate to form a wet compacted injection body (Xuan et al., 2016) which supports the overlying strata to reduce its subsidence and control the surface subsidence.

The amount of water contained in the slurry is large; the specific amount of water is closely related to the mining length of the working face, typically at 100,000 m<sup>3</sup> or more. The amount of bleed water accounts for approximately half of the total volume (Zhang et al., 2017). This is because the injection layer is close to the working face, and collapse and hydraulic fracture zones exist between them. After a large amount of water bleeds from the slurry, it goes through the pore space of the underlying rock. The seepage of bleed water in the underlying rock and its leakage into the working face are key issues that gained substantial attention. However, studies have focused primarily on the effectiveness of grout injection (Xuan et al., 2015), injection ratio control (Xuan et al., 2016) and rock reinforcement in mining engineering (Chen et al., 2022; Chen et al., 2023).

IOGI is affected by different geological and mining conditions. Therefore, studying seepage through mathematical and mechanical methods is challenging. Owing to the “dark box” characteristic of the stratum, field test research also has limitations. Therefore, numerical simulation is a more suitable method to study seepage problem presently, the literature contains numerous seepage simulation studies. For example, COMSOL software was used to study water inrush in fault zones (Yu et al., 2020; Yu et al., 2021; Wu et al., 2022), and the seepage and stability of embankment dams (Tulus and Marpaung, 2018; Wang and Yu, 2021; Zhang et al., 2021). The SEEP/W software was used to study seepage in the landfill leachate layers (Gang et al., 2020), and the smoothed particle hydrodynamics method is efficient and capable of seepage analysis, particularly for the problems with complex geometries (Fadaei-Kermani et al., 2019). Moreover, the UDEC software was used to simulate mining stress of coal seams (Xuan et al., 2014; Fadaei-Kermani et al., 2019), and the FLAC3D was widely used in the study of seepage problems, such as saturated and unsaturated seepage (Li et al., 2012), mined rock seepage (Ma et al., 2006), and slope seepage (Zhang et al., 2020; Zhang et al., 2022). Research on the slurry water bleeding and seepage problem of IOGI involves mining, grouting, slurry flow, and other factors, which renders complexity to analysis. The above numerical methods have limitations in simulating the slurry

water seepage problem of IOGI. Physical simulation experiments have high reliability, strong intuitiveness, and good repeatability (Yang et al., 2018). Thus, physical simulation is expected to be an effective way of solving the slurry bleed water seepage of IOGI.

Similar simulation materials are necessary for the physical simulation of seepage (Sun et al., 2019). Traditional similar simulation materials are used in physical similarity experiments. However, these materials disintegrate easily when they come in contact with water (Wen et al., 2021). The new fluid-solid coupling similar simulation materials can meet solid deformation and penetration at low strength, with sand as aggregate; additionally, it can be adjusted by paraffin and talcum (Li et al., 2010). High water resistance materials with sand, paraffin, calcium carbonate, petroleum jelly, and gypsum as raw materials have been used to simulate the waterproof layer (Lian et al., 2015). They are used as water-proof materials with low water permeability to simulate the slurry diffusion law at the non-pressure stage (Li J et al., 2020) and the longwall overburden isolated grout injection (Xuan et al., 2020). Polyvinyl alcohol (PVA) is added with river sand, paraffin wax, talcum powder, hydraulic oil, and straw to adjust the permeability. Which does not disintegrate with water and has a specific water storage and

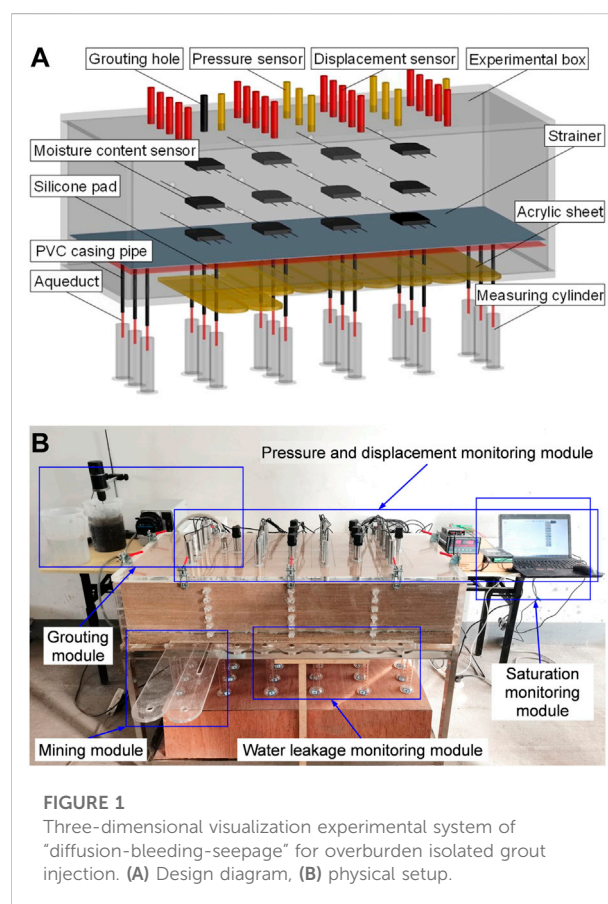


**FIGURE 1**  
Three-dimensional visualization experimental system of “diffusion-bleeding-seepage” for overburden isolated grout injection. (A) Design diagram, (B) physical setup.

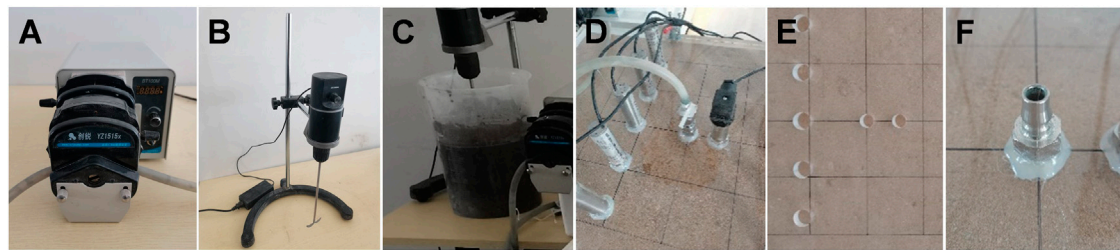


FIGURE 2

Grouting module. (A) Slurry pump, (B) slurry mixer, (C) slurry storage tank, (D) grouting pipe, (E) grouting hole, and (F) pipe hole connector.

TABLE 1 Hydraulic properties of specimens with different ratios of similar materials.

Proportion	Sand	Talcum powder	Paraffin (%)	Water absorption/%	Permeability coefficient/cm·s <sup>-1</sup>	Hydrophobicity
1	7	1	1.5	5.60	1.05E-04	Good
2	7	1	1.2	5.82	1.66E-04	Good
3	7	1	1.0	6.00	3.24E-04	Good
4	7	1	0.8	6.50	7.18E-04	Poor

permeability capacity (Zheng et al., 2022). Mountain sand, laterite, cement, and water are used as raw materials for different low- and medium-strength fractured rock masses (Guo et al., 2022). Sand and barite powder are used as aggregates; polyurethane and white silicate cement as binders; and water and silicone oil as conditioners to simulate similar materials for rocks of different permeabilities and strengths (Li Z et al., 2020). The material with river sand and clay as aggregate and engine oil and low temperature grease as binder is suitable for coal excavation and seepage (Yang and Zhang, 2020).

In recent years, numerous studies on 3D physical simulation, including simulation of asymmetric destabilization of mine-void rock masses (Lai et al., 2016), large-scale physical simulation experimental system of coal and gas co-mining (Li et al., 2019), and large-scale 3D physical simulation experimental platform of rock strata movement (Zhu et al., 2020; Yang et al., 2021) have been conducted. However, none of these studies involved grouting. For the physical simulation of IOGI, the subsidence problem of grouting injection was studied by injecting water into water bags arranged in similar materials in the early stage (Xuan et al., 2016; Xuan and Xu, 2017). Although grouting could be realized, the slurry water bleeding and seepage of grouting injection could not be realized. With technological improvements, a visual experimental system that can simulate the flow of IOGI was established (Li J et al., 2020; Xuan et al., 2020). Although this system can more adequately respond to the actual slurry diffusion, slurry diffusion studies were performed

under the condition of predefined regular injection space. Moreover, none of these studies involved seepage. Locating water in the overburden for visualization and to determine the relationship between the mining layer and water is essential to the experimental system for the seepage of slurry bled water. Fan et al., 2016 applied a fluorescent leak detection agent and experimental ultraviolet lamp to the physical simulation system and developed a new visualized simulation system for solid-liquid two-phase migration in mining-induced overburden. However, it is a two-dimensional system, and thus, the method is unsuitable for three-dimensional models. Based on the current research status, the experimental system cannot fully meet the requirements of monitoring the seepage of slurry bled water and water leakage to the working face.

In this study, a three-dimensional visual and physical simulation experiment system of “diffusion-bleeding-seepage” of IOGI was developed to study the seepage problem of IOGI slurry bled water. The system can simulate coal mining, grouting, slurry diffusion, the slurry bleeding and seepage, the water leakage to working face, and other problems.

## 2 Experimental system and method

IOGI involves working face mining, grouting injection, slurry diffusion, slurry water bleeding, bled water seepage, and rock strata movement. The experimental system used in this study

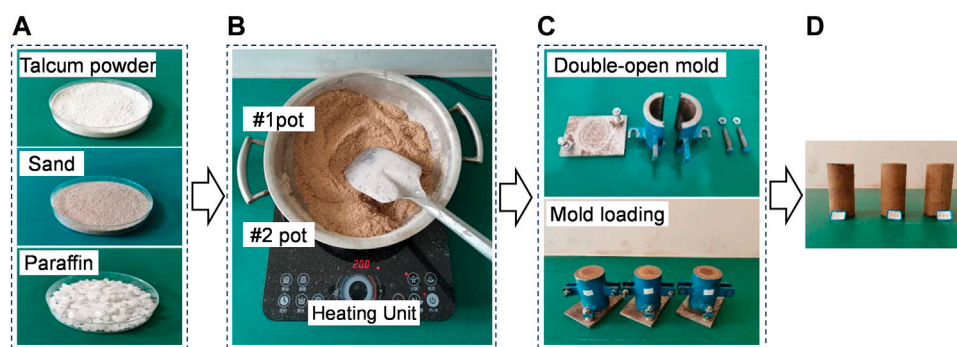


**FIGURE 3**  
Schematic of the production process of similar material specimens. (A) Raw materials, (B) thermostatic heating, (C) test piece forming, and (D) test piece.

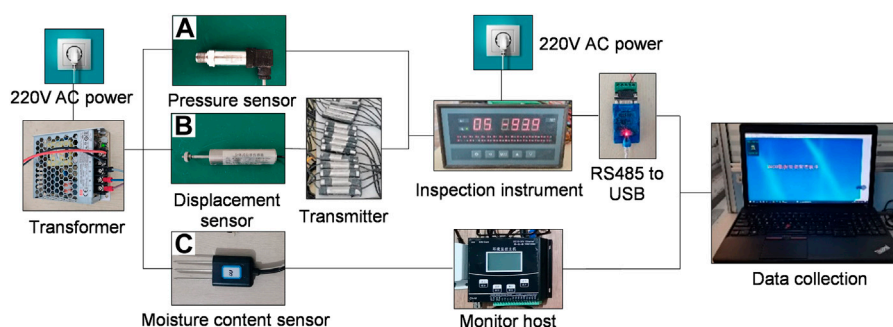


**FIGURE 4**  
System diagram of monitoring data transmission. (A) Pressure, (B) displacement, and (C) saturation.

(Figure 1A) adopted a modular design. The similarity ratio between (Figure 1B) and actual slurry injection working conditions was 1:400. The system was composed primarily of a transparent box and support, with the solid-liquid coupling seepage similar material and modules for mining, grouting injection, slurry pressure monitoring, the injection body thickness monitoring, overburden saturation monitoring, and water leakage monitoring of the working face. The box is made of high-strength acrylic plates with a thickness of 2 cm, which are spliced together by means of high-strength special glue.

## 2.1 Mining module

The coal seam mining process and the characteristics of its mining space were considered to effectively realize the mining function of the experimental system. Coal seam mining is a process of mining fixed-size rectangular coal blocks along the inclination direction and along the strike direction cyclically and

accumulatively. The three-dimensional mining space presents small rectangular spaces formed per unit time and a large rectangular space composed of small rectangular spaces formed cyclically and accumulatively. Therefore, based on this characteristic, several equal volume acrylic sheets were selected as the mining layer. The sheets were placed inside the system, and the bottom end of the front side plate of the experimental box was slotted to meet the requirements of acrylic sheets pulling. The coal seam mining conditions were simulated by pulling the acrylic sheets.

Acrylic sheets with thickness of 1 cm and width of 10 cm were used for mining unit of the mining module. Each piece of acrylic sheet was pulled out to simulate 40 m of coal seam mining along the strike direction. The length of coal seam mining along the inclination and strike directions can be controlled by the number and length of acrylic sheets pulled, respectively. The strike boundary pillar of the model was 15 cm, the inclination boundary pillar was 7.5 cm, acrylic sheet pulling spaces in the system is 90 cm × 35 cm × 1 cm (length × width × height,



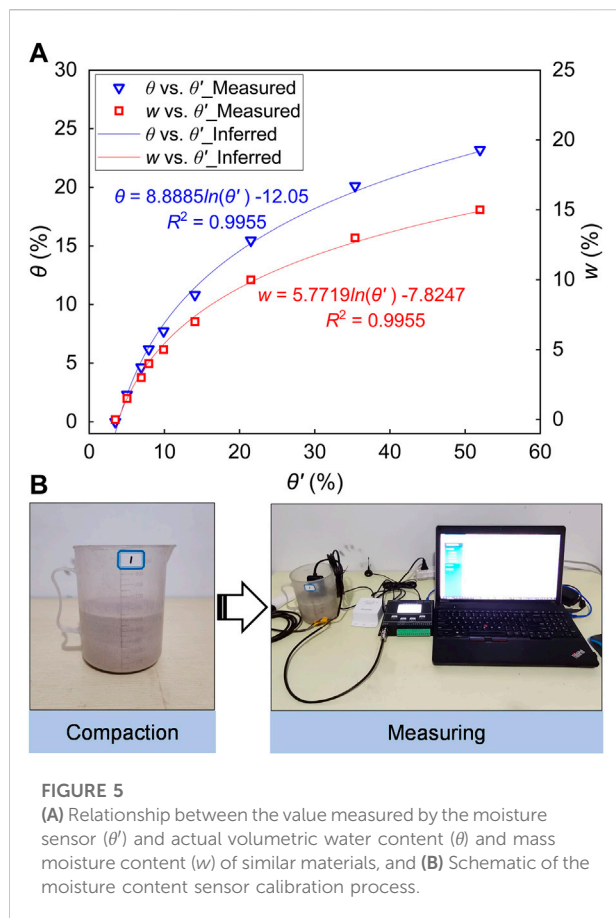


FIGURE 5

(A) Relationship between the value measured by the moisture sensor ( $\theta'$ ) and actual volumetric water content ( $\theta$ ) and mass moisture content ( $w$ ) of similar materials, and (B) Schematic of the moisture content sensor calibration process.

respectively), and the actual mining range of the simulated coal seam was 360 m  $\times$  140 m  $\times$  4 m (length  $\times$  width  $\times$  height, respectively).

## 2.2 Grouting module

The grouting module consists of a slurry pump, a slurry mixer, slurry storage tank, grouting pipe, grouting hole, and pipe hole connector (Figures 2A–F). The experimental system did not consider the overlying rock of the injection layer considering the visualization of slurry diffusion and the ease of sensor placement. The injection layer was located at the interface between the top plate of the system and the top of the simulated similar material.

During the construction of the simulation system, the grouting pipe connector was inserted into the prefabricated grouting hole location of the top plate and the interface was sealed with hot melt adhesive. Subsequently, one end of the grouting pipe was inserted into the prepared slurry in the slurry storage tank. The other end was drawn out from the slurry in the slurry storage tank and is connected with the slurry pump and

pipe hole connector on the top plate of the model. The slurry pump was a constant rate peristaltic metering pump with a pump volume range of 0–380 ml/min.

## 2.3 Similar simulation material

The similar simulation material should meet the requirements of slurry water seepage while possessing good permeability and not disintegrate water. Therefore, river sand, talcum powder, and solid paraffin were selected as raw materials. The river sand and talcum powder were used as aggregate, and paraffin was used as the cementing material. Different similar material proportioning schemes were tested. Considering the length of the article, this study considered only four similar material proportioning schemes (Table 1), focusing on the non-hydrophilic property, water absorption, and permeability of the similar materials in different proportions.

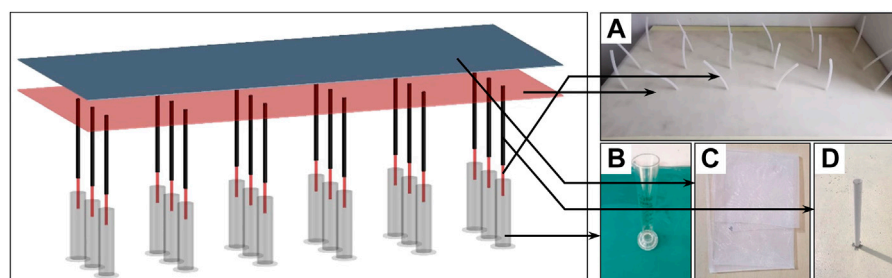
The material specimens were obtained, as shown in Figure 3, and tested for hydrology. The specimens were soaked for 2 days. The integrity of the specimens after soaking was observed to determine their non-hydrophilicity. The molds were opened and the specimens were taken out and put into the drying oven to be weighed and marked as the drying mass  $m_1$ . The specimens with different ratios were put into different hydrostatic pressure barrels according to the program, and the specimens were put into the barrels and taken out after every certain time interval to weigh the specimen mass  $m_2$ , at which time the water absorption rate of the specimens was  $(m_2 - m_1)/m_1$ . The measurement results of the variable head permeability coefficient of specimens were calculated based on the expression of the variable head permeability coefficient  $K$ , expressed as follows: (Tao et al., 2018):

$$K = 2.3 \frac{aL}{A(t_2 - t_1)} \log \frac{H_1}{H_2} \quad (1)$$

where  $a$  is the sectional area of the variable head pipe ( $\text{cm}^2$ ), 2.3 is the change factor of  $\ln$  and  $\log$ ,  $L$  is the height of the sample (cm),  $t_1$  and  $t_2$  are the start and end times of measuring the height of the water column of the pressure measuring tube (s), respectively.  $H_1$  and  $H_2$  are the start and end head (cm), respectively.

Table 1 presents the hydrologic results of different proportions of similar materials. Proportion 3 did not disintegrate with water and had good permeability. Therefore, proportion 3 was used as the solution for this experiment to permeate similar simulated materials. Because the experiment was performed in a pressurized state for approximately 90 min, the water absorption rate of similar materials should be considered for both time and pressure. The results of different hydrostatic pressures for 90 min of the selected proportions of similar materials were tested before the experiment performed to better show the real conditions of the experiment.



**FIGURE 6**

Water leakage monitoring module of the working face. (A) Silicone pad and silicone aqueducts, (B) measuring cylinders, (C) strainer, and (D) PVC casing pipes.

According to the test results, the water absorption rate of similar materials at normal temperature conditions under different hydrostatic pressure for 90 min could be expressed as:

$$w_{sa} = 9 \exp(-5h) + 0.0209 \quad (2)$$

## 2.4 Pressure and displacement monitoring module

The slurry pressures at different locations of the injection layer could be monitored in real time. Pressure sensors were installed on the holes of the top plate of the system. The interface was sealed with hot melt adhesive to monitor the slurry pressure at different locations in the injection layer in real time during the grouting process; the range of the pressure sensor was 0–100 kPa. To study the thickness distribution of the injection body during the grouting process, holes were punched in the top plate of the system and displacement sensors were installed on the hole locations. The displacement sensors were used to monitor the displacement of the bottom interface of the injection body to obtain its thickness. Figure 4 shows the pressure and displacement monitoring data transmission and data acquisition systems.

## 2.5 Saturation monitoring module

To study the porosity saturation of overburden during the grouting process, sensors (Figure 4C) were arranged at different locations along the strike direction in the central location of the internal inclination of similar materials. This was performed to realize the dynamic monitoring of the moisture content of the underlying overburden in the horizontal and vertical directions. Not that the output data of the sensor is volumetric water content. The relationship between the actual volumetric water content of the similar materials and that of the sensor were

established through experiments to ensure the accuracy of the sensors. The materials used in the sensor calibration experiment were consistent with the similar seepage materials in this study. According to the production process of similar materials, similar cylindrical material specimens with mass moisture contents of 0%, 1.5%, 3%, 4%, 5%, 7%, 10%, 13%, and 15% were made. The dry density of similar materials selected in the calibration experiment was consistent with that of similar materials laid in practice. Figure 5B shows the specific calibration process.

First, river sand was sieved into particle size of less than 1.7 mm. The sieved river sand was dried using a drying baker such that the initial moisture content of the material was zero. Subsequently, the river sand and talcum powder were weighed according to the material proportion (Table 1, proportion 3), added into the water bath thermostatic heating device to mix, and stirred thoroughly. The required water was added according to the predetermined mass moisture content to ensure that the moisture uniformly distributed.

Second, the material was heated by the water bath thermostatic heating device. When the heating device reached the water bath state, the weighed paraffin was added to the material and stirred repeatedly. The water bath temperature was controlled between 50 and 120°C for the paraffin to melt into the material evenly. Subsequently, the similar material was poured into the prepared measuring cup and compacted. The compaction was performed according to the calculated volume. Finally, the measuring cup was sealed with plastic wrap to prevent moisture evaporation. The experimental material was left to cool for approximately 1 h. Sensor measurement was performed only after the material had cooled down and the paraffin and material were completely mixed and solidified. During the experimental measurement, the sensor probe was inserted into the similar material in the measuring cup to read the measured volumetric water content. Three specimens of each mass moisture content were used for the sensor calibration. Each specimen was measured with #1–12 moisture content sensors.

TABLE 2 Distribution of experimental lithology.

Lithology	Material	Ratio	Thickness/cm	Layers	Strength/kPa
Permeable layer	Paraffin: river sand: talcum powder	0.08: 7: 1	20	17	71
Filter layer	Strainer	—	—	1	—
Seepage layer	Silicone pad	—	—	1	—
Non-seepage layer	Sand: calcium carbonate: gypsum: water	6: 7: 3: 2	4	4	78
Coal seam	Acrylic sheets	—	1	1	—

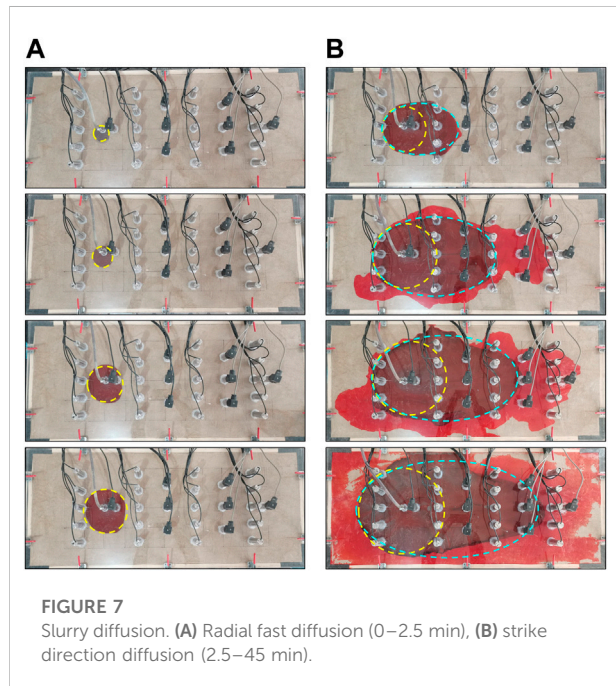


FIGURE 7  
Slurry diffusion. (A) Radial fast diffusion (0–2.5 min), (B) strike direction diffusion (2.5–45 min).

As shown in Figure 5A, the scatter relationship between the actual volumetric water content ( $\theta$ ) and the volumetric water content ( $\theta'$ ) measured by the sensors could be obtained. The relationship between the actual and measured volumetric water content determined through fitting can be expressed as follows:

$$\theta = 8.8887 \ln(\theta') - 12.05 \quad (3)$$

According to the relationship between mass moisture content and volume moisture content, The relationship between the actual mass moisture content ( $w$ ) of similar materials and volumetric water content ( $\theta'$ ) measured by the sensors could be expressed as:

$$w = 5.7719 \ln(\theta') - 7.8247 \quad (4)$$

According to the definition of saturation, the relationship between the saturation ( $S$ ) of the overburden and the volumetric water content ( $\theta'$ ) measured by the sensors is as follows:

$$S = 0.7353 \ln(\theta') - 0.9967 \quad (5)$$

where  $\theta$  is the volumetric water content of similar materials (%),  $\theta'$  is the volumetric water content measured by the sensors (%),  $w$  is the mass moisture content (%), and  $S$  is the saturation (%).

## 2.6 Water leakage monitoring module of working face

The working face water leakage monitoring module comprised four parts: silicone pad and aqueducts, measuring cylinder, strainer, and PVC casing pipes (Figures 6A–D). To monitor the leakage of slurry bled water in the working face in real time, the rock layer was simplified, and the water flowing fractured and collapse zones (non-seepage layer) were not considered. Bled water was expected to enter the working face through the non-seepage layer. Therefore, the bled water at the upper interface of the non-seepage layer was regarded as the water leakage at the working face.

Silicone pad were arranged at the interface of the water flowing fractured zone. Subsequently, the silicone aqueducts were connected to the outside of the experimental box by drilling holes in the silicone pad to pass into the measuring cylinders to monitor water leakage to the working surface. Eighteen holes with a diameter of 6 mm were made on the silicone pad, representing 18 measuring points. The aqueducts were connected to the silicone pad using quick-setting adhesive. Since the aqueducts are soft silicone pipes, PVC casing pipes were inserted on the outside of the aqueducts as protective pipes to prevent similar materials moving during mining from compressing the aqueducts so that the water did not flow through the aqueducts. Therefore, PVC casing pipes that are not easily deformed were placed on the outside of the silicone aqueducts. Sealing material was used to prevent bled water from flowing out from the inner wall of the experimental box. A strainer was laid on the upper part of the silicone pad to prevent the similar material on the upper part of the silicone pad from blocking the silicone aqueducts.

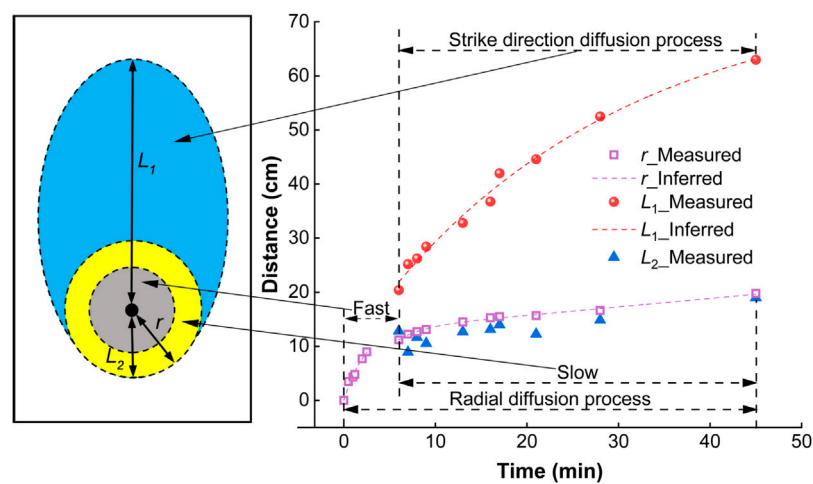


FIGURE 8

Slurry diffusion distance (from the grouting hole to slurry diffusion boundary) vs. time. Here,  $r$  indicates the radial diffusion radius,  $L_1$  indicates the distance from the front end of the strike diffusion boundary to the grouting hole, and  $L_2$  indicates the distance from the front back of the strike diffusion boundary to the grouting hole.

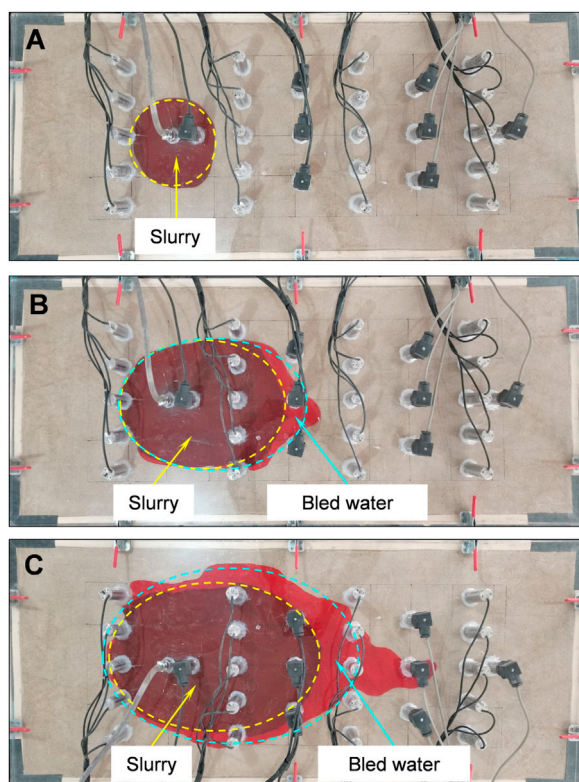


FIGURE 9

Distribution of slurry water bleeding. (A) Radial fast diffusion, (B) strike direction diffusion (early stage), and (C) Strike direction diffusion (later stage).

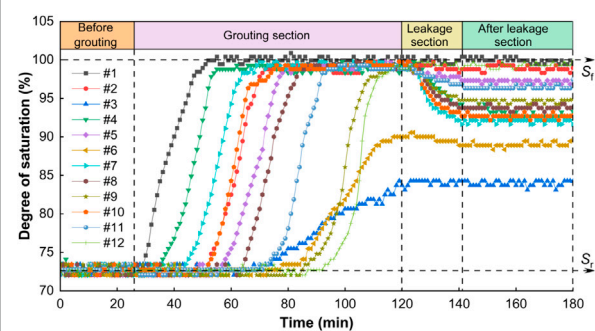


FIGURE 10

Degree of saturation for #1–12 vs. time. Here,  $S_i$  indicates initial saturation and  $S_f$  indicates complete saturation.

### 3 Application of experimental system

Before the experiment, the experimental similar material was made according to the predetermined initial saturation. After the production was completed, the traditional similar material was partially placed to meet the experimental requirements. The monitored saturation was stable, and the initial saturation was obtained as 73%. The layering of similar materials is shown as Table 2. The other modules were assembled to complete the experimental system and ensure good confinement of the experiment. The injection layer was located 25 cm above the coal seam. During the experiment, the acrylic sheet was pumped out

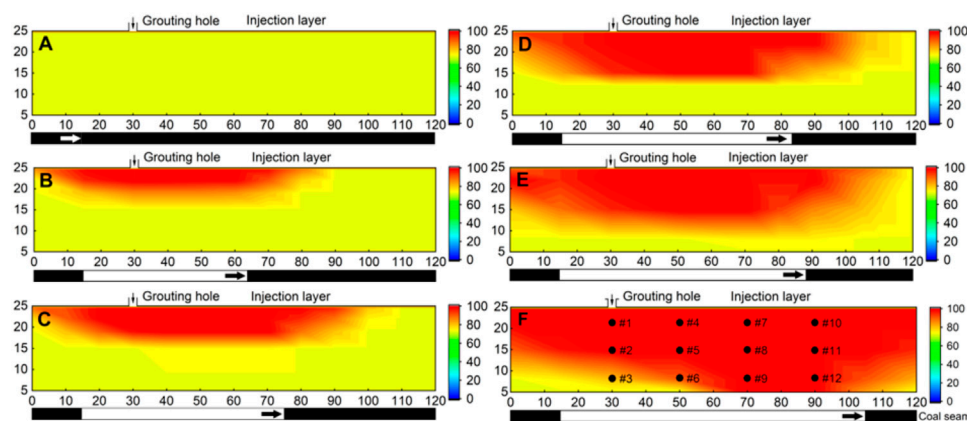


FIGURE 11

Strike profile contour of saturation for  $\alpha = 0\%$ – $55\%$  along the central location of the inclination during grouting. (A)  $0\%$ , (B)  $15.6\%$ , (C)  $25\%$ , (D)  $30\%$ , (E)  $38\%$ , and (F)  $55\%$ . Here,  $\alpha$  is the injection ratio.

35 cm at an interval of 11 min with a volume of  $350 \text{ cm}^3$  each time. The total number of acrylic sheets was nine, with a total volume of  $3,150 \text{ cm}^3$ . The sequential relationship between mining and grouting in the modelling is completely based on the field grouting injection condition. Grouting began after the third acrylic sheet was pumped out. The fly ash slurry was made in accordance with the 2:1 water-cement ratio. The grouting flow rate was 75 ml/min. The slurry diffusion was monitored during the grouting process. The grouting was stopped when the working face was mined completely.

### 3.1 Slurry diffusion

Under the condition of predefined regular injection space, slurry diffusion with and without pressure were studied. In the non-pressure stage, the slurry exhibited radial and bidirectional diffusion. By contrast, the slurry diffused along the main dominant channel in the pressure stage (Li Z et al., 2020; Li, 2021). The test effectively revealed the basic law of IOGI slurry diffusion. However, no reserved fracture was observed in the actual grouting condition. Figure 10 shows the slurry diffusion at different times under no reserved mining-induced fracture condition (consistent with the actual mining and grouting).

In combination with the grid reference line on the top plate of the experimental system, the distance was measured at different times from the grouting hole to the slurry diffusion boundary (Figure 7). The figure shows that the slurry diffusion was divided into the following two stages. The first stage was the radial fast diffusion stage (Figure 7A), characterized by circular diffusion centered on the grouting hole. Herein, the diffusion radius increased with time and exhibited a power function distribution. The second stage was strike direction diffusion accompanied by radial slow diffusion (Figure 7B) and characterized by elliptical

diffusion. As shown in Figure 8, the distance ( $L_1$ ) from the front end of the strike diffusion boundary to the grouting hole increased with time and was distributed as a power function. Moreover, the radial diffusion was accompanied by the radial diffusion during the radial diffusion process. The radial diffusion speed in the second stage was slower than that in the first stage. The distance ( $L_2$ ) from the back end of the strike diffusion boundary to the grouting hole coincided with the radius ( $r$ ) of the radial diffusion, thus indicating that radial diffusion exists during the strike diffusion process.

### 3.2 Slurry bleeding

When fly ash slurry diffuses, water-cement separation occurs; the process is known as slurry water bleeding. When the slurry diffused rapidly in the radial direction, the diffusion speed of the slurry was high, and the amount of bled water was small (Figure 9A). When the slurry diffused in the strike direction, the diffusion speed of the slurry was reduced, and the amount of bled water increased. The bled water is distributed primarily in the front end of the slurry in the early stage (Figure 9B) and in the front and both sides of the slurry in the late stage (Figure 9C).

### 3.3 Bled water seepage

The saturation curves (Figure 10) of different measurement points in the overburden were obtained, according to the method in Section 2.4. The saturation of the overburden was shown at four stages: before grouting, during grouting, during leakage, and after leakage. Before grouting, the initial saturation ( $S_r$ ) of the overburden was 73%. This value did not change with time and was uniform in different locations. During grouting, the saturation of the



overburden increased from 73% to 100%; this value remained unchanged, thus indicating that the slurry bled water seeped into the overburden from the injection layer, and the saturation finally reached complete saturation ( $S_p$ ). After grouting, the locations of measuring points #3 and #6 (Figure 11F) did not reach complete saturation, whereas the rest of the points reached full saturation state ( $S_p$ ). When the water leakage monitoring for 120 min, grouting was stopped immediately. When the bled water entered the working face, the saturation of measuring point locations #1–#3 and #12 did not change significantly, whereas that of other measuring point locations decreased significantly. The saturation decreased faster, and the amount of reduction was larger at the location closer to the water leakage point of the working face. By contrast, the decrease was slow, and the amount of reduction was small at the location farther from the water leakage point of the working face. After water leakage, the saturation of all measuring point locations in the overburden remained unchanged.

Based on the saturation monitoring method in Section 2.5, the strike profile contour (Figures 11A–F) of the overburden saturation with different injection ratios ( $\alpha = 0\%–55\%$ ) in the grouting process was obtained according to Eq. 5. The profile revealed that the overburden full saturation range increased with an increase in the injection ratio. This indicates that the amount of the bled water increased with an increase in the amount of grouting slurry in the injection layer. Moreover, the bled water continued to seep into the overburden and to a more distant location, thereby increasing the overburden full saturation range. The distribution pattern of the slurry bled water seepage in the overburden was semi-elliptical. Its dynamic distribution pattern was not always centered on the grouting hole instead, but the center of its pattern continued to move in the mining direction as the grouting fracture expanded to the mining direction.

## 4 Conclusion

A physical simulation experimental method was used to study the slurry bled water seepage problem of IOGI. Considering the actual IOGI technical conditions and their interrelationship, an experimental simulation method for the slurry bled water seepage of IOGI was established to realize the visualization study of slurry diffusion and water secretion, and locating water in the overburden for visualization and to determine the relationship between the mining layer and water is essential to the experimental system for the seepage of slurry bled water. The experimental method can be used to further develop the water leakage in working face and other related problems.

Based on this experimental system, physical simulation experiments of IOGI under the initial saturation of 73% were performed. The slurry diffusion was divided into two stages: radial fast diffusion and strike direction diffusion accompanied by radial slow diffusion. When the slurry diffused radially and rapidly, the slurry diffused faster, and the amount of bled water was very small. When the slurry diffused in the strike direction, the diffusion speed

of the slurry was reduced, and the amount of bled water increased. The bled water was distributed primarily in the front end of the slurry in the early stage and in the front end and both sides of the slurry in the late stage. The relationship between the dynamic change in saturation and grouting condition was obtained. The seepage process of slurry bled water in the overburden and the strike profile contour saturation distribution was obtained; its distribution pattern was semi-elliptical.

The influence of factors, such as grouting volume, grouting pressure, initial saturation, and permeability coefficient, on the seepage law of bled water was not studied. Therefore, the following research focuses on these factors and establishes the seepage boundary model under different mining and geological conditions to build the seepage prediction method of working face to evaluate the risk of slurry water.

## Data availability statement

The original contributions presented in the study are included in the article/Supplementary Material, further inquiries can be directed to the corresponding authors.

## Author contributions

CW contributed to the conception of the study; CW and JL performed the experiment; CW contributed significantly to analysis and manuscript preparation; CW performed the data analyses and wrote the manuscript; JX and DX helped perform the analysis with constructive discussions.

## Funding

This research was supported by Fundamental Research Funds for Central Universities [2020ZDPYMS15].

## Conflict of interest

The authors declare that the research was conducted in the absence of any commercial or financial relationships that could be construed as a potential conflict of interest.

## Publisher's note

All claims expressed in this article are solely those of the authors and do not necessarily represent those of their affiliated organizations, or those of the publisher, the editors and the reviewers. Any product that may be evaluated in this article, or claim that may be made by its manufacturer, is not guaranteed or endorsed by the publisher.



## References

- Chen, J., Liu, L., Zeng, B., Tao, K., Zhang, C., Zhao, H., et al. (2023). A constitutive model to reveal the anchorage mechanism of fully bonded bolts. *Rock Mech. Rock Eng.* 56, 3.
- Chen, J., Zeng, B., Liu, L., Tao, K., Zhao, H., Zhang, C., et al. (2022). Investigating the anchorage performance of full-grouted anchor bolts with a modified numerical simulation method. *Eng. Fail. Anal.* 141, 106640–106714. doi:10.1016/j.engfailanal.2022.106640
- Fadaei-Kermani, E., Shojae, S., Memarzadeh, R., and Barani, G. (2019). Numerical simulation of seepage problem in porous media. *Appl. Water Sci.* 9 (4), 79–88. doi:10.1007/s13201-019-0965-1
- Fan, G., Zhang, S., Zhang, D., and Chen, M. (2016). Development and application of a solid-liquid coupling physical experiment system for modeling mining-induced overburden movement. *J. Min. Saf. Eng.* 33 (5), 898–903. doi:10.13545/j.cnki.jmse.2016.05.021
- Gang, L., Li, G., Zhang, J., and Liu, J. (2020). Numerical simulation of seepage in the landfill leachate layers. *IOP Conf. Ser. Earth Environ. Sci.* 545, 012038. doi:10.1088/1755-1315/545/1/012038
- Guo, Y., Yang, Y., Kong, Z., and He, J. (2022). Development of similar materials for liquid-solid coupling and its application in water outburst and mud outburst model test of deep tunnel. *Geofluids* 2022, 1–12. doi:10.1155/2022/8784398
- Horiuchi, S., Kawaguchi, M., and Yasuhara, K. (2000). Effective use of fly ash slurry as fill material. *J. Hazard Mater* 76 (2), 301–337. doi:10.1016/S0304-3894(00)00205-3
- Lai, X., Shan, P., Cao, J., Cui, F., and Sun, H. (2016). Simulation of asymmetric destabilization of mine-void rock masses using a large 3D physical model. *Rock Mech. Rock Eng.* 49 (2), 487–502. doi:10.1007/s00603-015-0740-z
- Li, J. (2021). *Experimental study on the flow law of slurry of isolated grouting in mining-induced overburden*. China: China University of Mining and Technology.
- Li, J., Zheng, K., Xuan, D., and Xu, J. (2020). Experimental study on slurry diffusion law during the non-pressure stage in overburden isolated grouting. *J. China Coal Soc.* 45, 78–86. doi:10.13225/j.cnki.jccs.2019.1669
- Li, S., Feng, X., Li, S., Li, L., and Li, G. (2010). Research and development of a new similar material for solid-fluid coupling and its application. *Chin. J. Rock Mech. Eng.* 29 (2), 281–288.
- Li, S., Wei, Z., Lin, H., Zhao, P., Xiao, P., and Hao, Y. (2019). Research and development of 3D large-scale physical simulation experimental system for coal and gas co-extraction and its application. *J. China Coal Soc.* 44 (1), 236–245. doi:10.13225/j.cnki.jccs.2018.1635
- Li, Y., Wu, J., and Li, K. (2012). Saturated-unsaturated seepage analysis based on FLAC3D. *Rock Soil Mech* 33 (2), 617–622. doi:10.16285/j.rsm.2012.02.001
- Li, Z., Ma, M., and Bao, Y. (2020). Development and application of fluid-solid coupling similar materials in discharge test of old goaf water. *Geofluids* 2020, 1–12. doi:10.1155/2020/8834885
- Lian, H., Xia, X., Ran, W., and Zhao, Q. (2015). Experimental research on water-resistance property of new-style fluid-solid coupling material for analogue simulation. *Coal Min. Technol.* 20 (1), 12–16. doi:10.13532/j.cnki.cn11-3677/td.2015.01.004
- Lu, H., Zhang, K., Yi, J., and Wei, A. (2022). A study on the optimal selection of similar materials for the physical simulation experiment based on rock mineral components. *Eng. Fail. Anal.* 140, 106607. doi:10.1016/j.engfailanal.2022.106607
- Ma, L., Zhang, D., Miao, X., Wang, H., and Feng, J. (2006). Numerical simulation of seepage regularities with FLAC3D in the overlying strata in mining rockmass. *J. Hunan Univ. Sci. Technol(Nat Sci. Ed.* 21 (3), 1–5.
- Sun, W., Zhou, F., Shao, J., Du, H., and Xue, Y. (2019). Development status and prospects of mine physical similar material simulation experiments. *Geotech. Geol. Eng.* 37 (4), 3025–3036. doi:10.1007/s10706-019-00821-4
- Tao, G., Wu, X., Yang, X., Liu, W., He, J., and Chen, Y. (2018). Pore distribution of cement-soil and its effect on permeability. *J. Eng. Geol.* 26 (5), 1243–1249. doi:10.13544/j.cnki.jeg.2018011
- Tulus, S., and Marpaung, T. (2018). Sedimentation optimization on river dam flow by using COMSOL multiphysics. *IOP Conf. Ser. Mat. Sci. Eng.* 300, 012051. doi:10.1088/1757-899X/300/1/012051
- Wang, F., Chen, T., Ma, B., and Chen, D. (2022). Formation mechanism of stress arch during longwall mining based on key strata theory. *Energy Explor. Exploitation* 40 (2), 816–833. doi:10.1177/01445987211042701
- Wang, R., and Yu, K. (2021). Stress and deformation analysis of high concrete face rockfill dam based on COMSOL multiphysics. *IOP Conf. Ser. Earth Environ. Sci.* 643, 012013. doi:10.1088/1755-1315/643/1/012013
- Wen, Z., Jiang, P., Jing, S., Cao, Z., and Guan, Y. (2021). Development and verification of simulation testing system for floor seepage in coal mine underground reservoir. *J. China Coal Soc.* 46 (5), 1487–1497. doi:10.13225/j.cnki.jccs.2020.1601
- Wu, J., Wang, X., Wu, L., Lu, Y., and Han, Y. (2022). Parametric study of water inrush in a tunnel crossing a fault based on the “three zones” fault structure. *KSCSE J. Civ. Eng.* 26 (8), 3600–3619. doi:10.1007/s12205-022-1310-z
- Xu, J., Ni, J., Xuan, D., and Wang, X. (2015a). Coal mining technology without village relocation by isolated grout injection into overburden. *Coal Sci. Technol.* 43 (12), 8–11. doi:10.13199/j.cnki.cst.2015.12.002
- Xu, J., Xuan, D., Zhu, W., and Wang, X. (2019). Partial backfilling coal mining technology based on key strata control. *J. Min. Strata Contr Eng.* 1 (1), 69–76. doi:10.13532/j.jmsce.cn10-1638/td.2019.02.006
- Xu, J., Xuan, D., Zhu, W., Wang, X., Wang, B., and Teng, H. (2015b). Study and application of coal mining with partial backfilling. *J. China Coal Soc.* 40 (6), 1303–1312. doi:10.13225/j.cnki.jccs.2015.3055
- Xuan, D., Li, J., Zheng, K., and Xu, J. (2020). Experimental study of slurry flow in mining-induced fractures during longwall overburden grout injection. *Geofluids* 2020, 1–10. doi:10.1155/2020/8877616
- Xuan, D., and Xu, J. (2014). Grout injection into bed separation to control surface subsidence during longwall mining under villages: Case study of liudian coal mine, China. *Nat. Hazards* 73 (2), 883–906. doi:10.1007/s11069-014-1113-8
- Xuan, D., and Xu, J. (2017). Longwall surface subsidence control by technology of isolated overburden grout injection. *Int. J. Min. Sci. Technol.* 27 (5), 813–818. doi:10.1016/j.ijmst.2017.07.014
- Xuan, D., Xu, J., Wang, B., and Teng, H. (2015). Borehole Investigation of the effectiveness of grout injection technology on coal mine subsidence control. *Rock Mech. Rock Eng.* 48 (6), 2435–2445. doi:10.1007/s00603-015-0710-5
- Xuan, D., Xu, J., Wang, B., and Teng, H. (2016). Investigation of fill distribution in post-injected longwall overburden with implications for grout take estimation. *Eng. Geol.* 206, 71–82. doi:10.1016/j.enggeo.2016.04.007
- Xuan, D., Xu, J., and Zhu, W. (2014). Dynamic disaster control under a massive igneous sill by grouting from surface boreholes. *Int. J. Rock Mech. Min. Sci.* 71, 176–187. doi:10.1016/j.ijrmms.2014.06.019
- Yang, K., Liu, W., Jiao, B., Zhang, Q., Liu, S., and Zhang, Z. (2021). Three-dimensional physical simulation of overburden migration in deep thick hard roof fully-mechanized caving mining. *Chin J Geotechn Eng* 43 (1), 85–93. doi:10.11779/CJGE202101010
- Yang, R., Zhang, Y., Wang, Z., Wang, Y., Lv, C., Wang, C., et al. (2018). A newly-built geomaterial model test system and its application. *J. China Coal Soc.* 43 (2), 398–404. doi:10.13225/j.cnki.jccs.2017.1476
- Yang, T., and Zhang, J. (2020). Experimental research on simulation material for water-resisting soil layer in mining physical simulation. *Adv. Mater. Sci. Eng.* 2020, 1–8. doi:10.1155/2020/3456913
- Yu, H., Zhu, S., and Wang, X. (2021). Research on groundwater seepage through fault zones in coal mines. *Hydrogeol. J.* 29, 1647–1656. doi:10.1007/S10040-021-02336-W
- Yu, H., Zhu, S., Xie, H., and Hou, J. (2020). Numerical simulation of water inrush in fault zone considering seepage paths. *Nat. Hazards* 104, 1763–1779. doi:10.1007/s11069-020-04246-8
- Zhang, L., Xu, J., and Xuan, D. (2017). Experimental research on slurry bleeding properties grouting filling for overburden. *China coal.* 43 (9), 121–124. doi:10.19880/j.cnki.ccm.2017.09.025
- Zhang, Q., Wang, L., Zhang, H., and Gao, H. (2022). Parameter sensitivity and unsaturatedstochastic seepage field of bench slope. *J. Saf. Environ.* 22, 665–672. doi:10.13637/j.issn.1009-6094.2020.1625
- Zhang, W., Shen, Z., Ren, J., Bian, J., Xu, L., and Chen, G. (2021). Multifield coupling numerical simulation of the seepage and stability of embankment dams on deep overburden layers. *Arab. J. Sci. Eng.* 47 (6), 7293–7308. doi:10.1007/s13369-021-06112-6
- Zhang, Y., Zhang, X., Wang, Z., and Zhu, W. (2020). Study on the reservoir dam slope stability considering the effect of seepage. *IOP Conf. Ser. Earth Environ. Sci.* 560, 012049. doi:10.1088/1755-1315/560/1/012049
- Zheng, K., Xuan, D., and Li, J. (2022). Study on fluid-solid characteristics of grouting filling similar-simulation materials. *Minerals* 12 (5), 502. doi:10.3390/min12050502
- Zhu, W., Yu, B., Ju, J., Liu, W., and Qi, X. (2020). Experimental study on “horizontal U-Y” periodical breakage characteristics of key strata in stope roof. *Coal Sci. Technol.* 48 (2), 36–43. doi:10.13199/j.cnki.cst.2020.02.004



## OPEN ACCESS

## EDITED BY

Shengli Yang,  
China University of Mining and  
Technology, Beijing, China

## REVIEWED BY

Qin Yan,  
Taiyuan University of Technology, China  
Tianqi Jiang,  
Kyushu University, Japan

## \*CORRESPONDENCE

Zhipeng Li,  
✉ lizhipengsdu@163.com

## SPECIALTY SECTION

This article was submitted to  
Environmental Informatics and Remote  
Sensing, a section of  
the journal Frontiers in Earth Science

RECEIVED 16 November 2022

ACCEPTED 12 December 2022

PUBLISHED 30 January 2023

## CITATION

Wang H, Dong L, Zhang Q, Li Z and  
Zhang P (2023), Permeation grouting  
mechanism of viscous time-varying  
fluid considering diffusion path.  
*Front. Earth Sci.* 10:1100196.  
doi: 10.3389/feart.2022.1100196

## COPYRIGHT

© 2023 Wang, Dong, Zhang, Li and  
Zhang. This is an open-access article  
distributed under the terms of the  
[Creative Commons Attribution License  
\(CC BY\)](https://creativecommons.org/licenses/by/4.0/). The use, distribution or  
reproduction in other forums is  
permitted, provided the original  
author(s) and the copyright owner(s) are  
credited and that the original  
publication in this journal is cited, in  
accordance with accepted academic  
practice. No use, distribution or  
reproduction is permitted which does  
not comply with these terms.

# Permeation grouting mechanism of viscous time-varying fluid considering diffusion path

Hongbo Wang<sup>1</sup>, Lianglin Dong<sup>1</sup>, Qingsong Zhang<sup>2</sup>, Zhipeng Li<sup>3\*</sup> and Peiyuan Zhang<sup>4</sup>

<sup>1</sup>College of Civil Engineering and Architecture, Shandong University of Science and Technology, Qingdao, China, <sup>2</sup>Geotechnical and Structural Engineering Research Center, Shandong University, Jinan, China, <sup>3</sup>School of Transportation and Civil Engineering, Shandong Jiaotong University, Jinan, China, <sup>4</sup>Qingdao West Coast Rail Transit Co., Ltd., Qingdao, China

Due to the hidden nature of the grouting project, it has not been possible to get a clear picture of the slurry transport law, and most of the existing permeation grouting theories have ignored the tortuous characteristics of the pore channels of porous media. Based on the fractal theory of porous media and the equation of seepage motion of viscous time-varying Bingham fluid, a theoretical model of permeation grouting with viscous time-varying Bingham fluid is established, and viscosity tests are carried out for C-S slurry to obtain the time-varying equation of viscosity of C-S slurry. A set of permeation grouting simulation experiment device was designed, and the permeation grouting simulation experiment of C-S slurry was carried out to obtain the variation curve of grouting pressure with time under different injection media and different grouting rates. The results show that the grouting pressure considering the diffusion path of the slurry is 0.9–1.1 times of the experimental results, the grouting pressure obtained from the experimental is 0.7–1.2 times of the theoretical value considering the diffusion path, and the calculated value considering the diffusion path agrees well with the experimental value. The theoretical model can provide scientific guidance for field grouting construction.

## KEYWORDS

permeation grouting, fractal theory, porous medium, diffusion path, viscous time-varying Bingham fluid, C-S slurry

## 1 Introduction

Grouting is to inject some solidified slurry into the cracks or pores of rock and soil mass through grouting equipment, and to achieve the purpose of seepage prevention and leakage stoppage of rock and soil mass through permeation, filling, compaction and splitting. Among them, permeation grouting is widely used in porous medium strata, such as medium, coarse sand layers and gravel layers, etc. These strata have large pore sizes, and slurry mostly diffuses in the form of permeation (Kuang et al., 2000). Because the gel time of quick-setting slurry is controllable, it ranges from tens of seconds to several minutes (Li et al., 2013a), the gel time can be effectively controlled, and the quick-setting slurry can be

used to quickly and effectively block and reinforce the sand layer in view of the water inrush and other disasters in the construction process. At present, there is a lack of scientific guidance for the application of penetration grouting of quick-setting slurry, and the relevant grouting parameters are still determined by engineering experience.

At present, in the theoretical research of permeation grouting in sand layer, Maag (Kuang et al., 2000) derives the theoretical formula of permeation grouting with Newtonian fluid based on Darcy's law and the initial viscosity of slurry; Ma (Ma et al., 2000) gave the theoretical formula of spherical diffusion of Newtonian fluid; Yang (Yang et al., 2006) considered four factors: grouting pressure, grouting time, permeability coefficient and water-cement ratio, and studied the permeation diffusion mechanism of slurry in sand layer through grouting simulation test. Yang (Yang et al., 2015) derived the calculation formulas of cylindrical and spherical diffusion radius based on the rheological equation of Bingham fluid; Yang (Yang et al., 2004; Yang et al., 2005) established theoretical models of Bingham fluid and power-law fluid permeation grouting respectively; Yang (Yang et al., 2016) established a theoretical model of cylindrical diffusion of power-law fluid based on the rheological equation of power-law fluid. With the development of permeation grouting theory, the viscosity parameters of viscous time-varying fluid were gradually introduced, and Li (Li et al., 2013a) established the diffusion model of C-S slurry in a single slab crack; Yang (Yang et al., 2011) derived the formula for calculating the permeation diffusion radius of Bingham fluid based on the equation of time-dependent viscosity of slurry; Zhou (Zhou et al., 2019) obtained the calculation formula of diffusion radius of viscous time-varying fluid through theoretical derivation; Based on the rheological equation of Bingham fluid, Zhang (Zhang et al., 2017) established the theoretical model of permeation grouting diffusion of quick-setting slurry; Ye (Ye et al., 2012; Ye et al., 2013) and Liu (Liu et al., 2015) studied the permeation diffusion mechanism of viscous time-varying slurry behind the shield wall. In addition, some scholars have studied the theory of permeation grouting diffusion from the aspect of percolation filtration effect, such as Axelsson M (Axelsson et al., 2009), Jong-Sun Kim (Kim et al., 2009) and so on. Feng (Feng et al., 2016) and Li (Li et al., 2015) have studied the influence of percolation filtration effect on slurry diffusion process.

To sum up, at present, some progress has been made in the research of permeation grouting theory, but most of the above theoretical studies have not considered the tortuous effect of the pore channel of the injected sand body. Because of the pore structure characteristics of the injected sand body itself, the diffusion path of the slurry is not a simple straight line, and it often migrates and spreads along the channels connected with the pores of the sand layer. Therefore, the above theory has low applicability to the permeation grouting engineering of the sand layer. Zhou (Zhou et al., 2016), Chen (Chen and Yuan, 2021), Yang (Yang et al., 2021) and Zhang (Zhang et al., 2018) discussed the theoretical models of the diffusion path of Newton, Bingham and power-law slurries in porous medium respectively, but the research on the migration and diffusion

law of viscous time-varying slurries in porous medium was not deep enough. In this paper, based on fractal theory of porous medium, a theoretical model of permeation grouting with viscous time-varying fluid is established.

## 2 Theoretical model of Bingham fluid permeation grouting considering diffusion path of porous medium

### 2.1 Basic assumptions of grouting theory

To study the permeation diffusion mechanism of Bingham fluid in injected porous medium, the following assumptions were made:

1. The slurry is isotropic, homogeneous and incompressible Bingham fluid.
2. The injected porous medium is homogeneous and isotropic, which meets the conditions of injectability.
3. The grouting rate is constant, the seepage of slurry is laminar flow, and the flow pattern of slurry remains unchanged during the seepage process.
4. The influence of gravity is not considered in the grouting process.

### 2.2 Fractal theory of porous medium

Due to the fractal characteristics of porous medium, the seepage path of slurry in porous medium often presents a "tortuosity" effect. Figure 1 shows a schematic diagram of the seepage diffusion path of slurry in porous medium,  $l$  denotes the actual route length of the seepage channel and  $l_0$  denotes the straight line length of the seepage channel. It can be seen from Figure 1 that the seepage path of slurry in porous medium is not all straight lines, but flows along the curved channels connected by pores, showing a typical "tortuosity" effect.

The seepage channel in porous medium conforms to the fractal scale law, and the fractal form of seepage channel (Pitchumani and Ramakrishnan, 1999) can be specifically expressed as follows

$$l = l_0^{D_t} (2b)^{1-D_t} \quad (1)$$

Derivation of Eq. 1 gives:

$$dl = l_0^{D_t-1} (2b)^{1-D_t} D_t dl_0 \quad (2)$$

Where:  $D_t$  is the fractal dimension of tortuosity of pore channel;  $b$  is the radius of the pore channel. Tortuosity is usually defined as (Yu and Li, 2004)

$$\tau = \frac{l}{l_0} \quad (3)$$

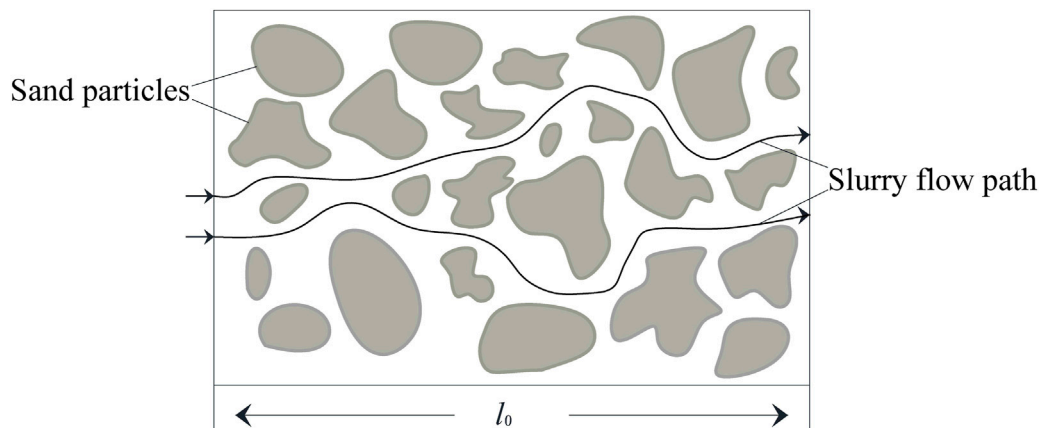


**FIGURE 1**  
Schematic diagram of porous medium seepage channel.

The relationship between average tortuosity  $\tau_{av}$  and porosity  $\varphi$  can be expressed as (Yu and Li, 2004)

$$\tau_{av} = \frac{1}{2} \left[ 1 + \frac{1}{2} \sqrt{1-\varphi} + \sqrt{1-\varphi} \frac{\sqrt{\left(\frac{1}{\sqrt{1-\varphi}} - 1\right)^2 + \frac{1}{4}}}{1 - \sqrt{1-\varphi}} \right] \quad (4)$$

The tortuosity fractal dimension of pore channels in porous medium (Yu and Li, 2001) can be expressed as

$$D_t = 1 + \frac{\ln \tau_{av}}{\ln \frac{l_0}{2b_{av}}} \quad (5)$$

Where:  $\tau_{av}$  is the average tortuosity of pore channels of porous medium;  $b_{av}$  is the average radius of pore channels in porous medium.

According to references (Yu, 2005), the average radius of pore channels in porous medium can be expressed as

$$b_{av} = \frac{1}{2} \frac{D_f}{D_f - 1} b_{\min} \left[ 1 - \left( \frac{b_{\min}}{b_{\max}} \right)^{D_f - 1} \right] \quad (6)$$

The relationship between  $b_{\min}/b_{\max}$  and porosity  $\varphi$  of porous medium can be expressed by the following formula:

$$\frac{b_{\min}}{b_{\max}} = \frac{\sqrt{2}}{d^+} \sqrt{\frac{1-\varphi}{1-0.342\varphi}} \quad (7)$$

The maximum radius of porous medium can be expressed by the following formula:

$$b_{\max} = \frac{\bar{r}}{4} \left( \sqrt{2 \left( \frac{1-0.342\varphi}{1-\varphi} - 1 \right)} + \sqrt{\frac{2\pi}{\sqrt{3}} \frac{1-0.342\varphi}{1-\varphi}} - 2 \right) \quad (8)$$

Where:  $D_f$  is the fractal dimension of pore channels;  $b_{\min}$  and  $b_{\max}$  represent the minimum radius and maximum radius of

porous medium pore channels, respectively;  $d^+$  is generally taken as 24;  $r$  is the average radius of particles in porous medium.

According to fractal theory, the fractal dimension of pores can be expressed as (Yun et al., 2008)

$$D_f = 2 - \frac{\ln \varphi}{\ln (b_{\min}/b_{\max})} \quad (9)$$

Reference (Yu and Cheng, 2002) gives the structural parameters of porous medium:

$$l_0 = \bar{r} \sqrt{\frac{2\pi}{\sqrt{3}}} \frac{1-0.342\varphi}{1-\varphi} \quad (10)$$

The expressions for the fractal dimension of the tortuosity of the pore channels in porous media can be obtained by combining (Eqs 4–10).

$$D_t = 1 + \frac{\ln \left[ 1 + \frac{1}{2} \sqrt{1-\varphi} + \sqrt{1-\varphi} \frac{\sqrt{\left(\frac{1}{\sqrt{1-\varphi}} - 1\right)^2 + \frac{1}{4}}}{1 - \sqrt{1-\varphi}} \right]}{\ln \frac{l_0}{2b_{av}}} \quad (11)$$

## 2.3 Temporal and spatial distribution equation of grouting pressure

According to advance mech mechanics of fluids in porous medium (Kong, 2010), the average velocity of Bingham fluid in a single seepage channel is

$$\bar{v} = \frac{b^2}{8\mu(t)} \left( -\frac{dp}{dl} \right) \left[ 1 - \frac{4}{3} \left( \frac{2\tau_0/b}{-dp/dl} \right) \right] \quad (12)$$

Where:  $\bar{v}$  is the average velocity in the seepage channel;  $b$  is the radius of seepage channel;  $dp/dl$  is the pressure gradient in the direction of slurry seepage;  $\tau_0$  is the initial yield stress of the slurry.

The seepage velocity  $v$  at any point in the injected porous medium, the average velocity of seepage channel at that point and the porosity of the porous medium satisfy (Li et al., 2013b):

$$v = \varphi \bar{v} \quad (13)$$

Radius  $b$  of seepage channel of injected porous medium and permeability  $k$  satisfy (Kong, 2010):

$$k = \varphi b^2 / 8 \quad (14)$$

Under the condition of constant grouting rate, the grouting flow rate meets

$$q = Sv \quad (15)$$

The pressure gradient along the diffusion direction of the Bingham fluid is obtained by combining (Eqs 12–15)

$$\frac{dp}{dl} = -\frac{q\mu(t)}{Sk} - \frac{2\tau_0}{3} \sqrt{\frac{2\varphi}{k}} \quad (16)$$

Substituting Eqs 2, 14 into Eq. 16 to obtain

$$\frac{dp}{dl_0} = \left( -\frac{q\mu(t)}{Sk} - \frac{2\tau_0}{3} \sqrt{\frac{2\varphi}{k}} \right) l_0^{D_t-1} \left( 4\sqrt{\frac{2k}{\varphi}} \right)^{1-D_t} D_t \quad (17)$$

When there is boundary condition  $l_0 = l_m$ ,  $p = p_0$ ,  $p_0$  are groundwater pressure.

$$p = \int_{l_0}^{l_m} \left( -\frac{q\mu(t)}{Sk} - \frac{2\tau_0}{3} \sqrt{\frac{2\varphi}{k}} \right) l_0^{D_t-1} \left( 4\sqrt{\frac{2k}{\varphi}} \right)^{1-D_t} D_t dl_0 + p_0 \quad (18)$$

Grouting pressure at grouting port position  $l_0 = 0$  can be expressed as

$$p_c = \int_0^{l_m} \left( -\frac{q\mu(t)}{Sk} - \frac{2\tau_0}{3} \sqrt{\frac{2\varphi}{k}} \right) l_0^{D_t-1} \left( 4\sqrt{\frac{2k}{\varphi}} \right)^{1-D_t} D_t dl_0 + p_0 \quad (19)$$

Where:  $q$  is the slurry flow rate;  $\mu$  is the viscosity of slurry;  $S$  is the cross-sectional area of slurry diffusion;  $k$  is the permeability of the injected medium;  $\tau_0$  is the initial yield stress of slurry;  $\varphi$  is the porosity of the injected medium;  $D_t$  is the tortuosity fractal dimension of seepage channel;  $p_0$  is the groundwater pressure;  $p_c$  is the pressure at the grouting mouth.

## 3 Permeation grouting simulation experiment of sand body

### 3.1 Experiment device

In order to study the penetration diffusion mechanism of C-S slurry in sand body, a set of visual penetration grouting

simulation experiment device has been designed, as shown in Figure 2. The experiment device consists of transparent plexiglass tube, pressure sensor, flow sensor, double-liquid mixer and manual grouting pump.

#### 3.1.1 Permeation grouting tube

In order to obtain the dynamic process of slurry diffusion clearly and intuitively, the permeation grouting tube is made of PMMA (plexiglass), which can withstand the grouting pressure of 10 MPa. The permeation grouting tube is arranged vertically with an inner diameter of 10 cm and a length of 2 m. The inner part of the transparent plexiglas tube is filled with river sand as the injected medium with fixing device at both ends. The fixing device only allows the slurry to pass through and does not allow the injected medium to pass through, so as to prevent the whole movement of river sand during grouting.

#### 3.1.2 Data recorder

In order to monitor the grouting rate and grouting pressure in the process of grouting in real-time, flow sensor and pressure sensor are set on the grouting tubeline. The pressure sensor has a measuring range of 0–10 MPa and a measuring accuracy of 0.02 MPa. The flow sensor has a measuring range of 0–30 L/min and a measuring accuracy of 0.3 L/min.

#### 3.1.3 Manual grouting pump

The cement slurry and silicate slurry used in the experiment are pumped by manual grouting pump. The manual grouting pump can control the grouting pressure at 0–10 MPa and the pumping flow range is 0–10 L/min.

## 3.2 Viscosity time-dependent test of C-S slurry

The C-S slurry is a two-liquid slurry material made of a mixture of cement slurry and silicate slurry, the gel time of the slurry can be controlled within a few tens of seconds to a few minutes. The cement used for the test was 32.5R ordinary portland cement, the quality of the cement complied with the standard “Common Portland Cement” GB175-2007, the silicate modulus  $M=3.0$ , the concentration  $Be'=38$ , the water/cement ratio  $W/C$  is 1:1 and the mixing volume ratio is 1:1.

SV-10/SV-100 sine wave vibration viscometer (see Figure 3) is selected as the test instrument with a measuring range of 0.3–10,000 mPa s/1–100 Pa s. The viscosity and temperature curve of C-S slurry can be measured directly with time.

The curves of the viscosity and temperature of the C-S slurry with time are shown in Figure 4.

It can be seen from Figure 4 that although the temperature of slurry increases after mixing, the change range is within 1°C, so the slurry temperature can be considered to be basically



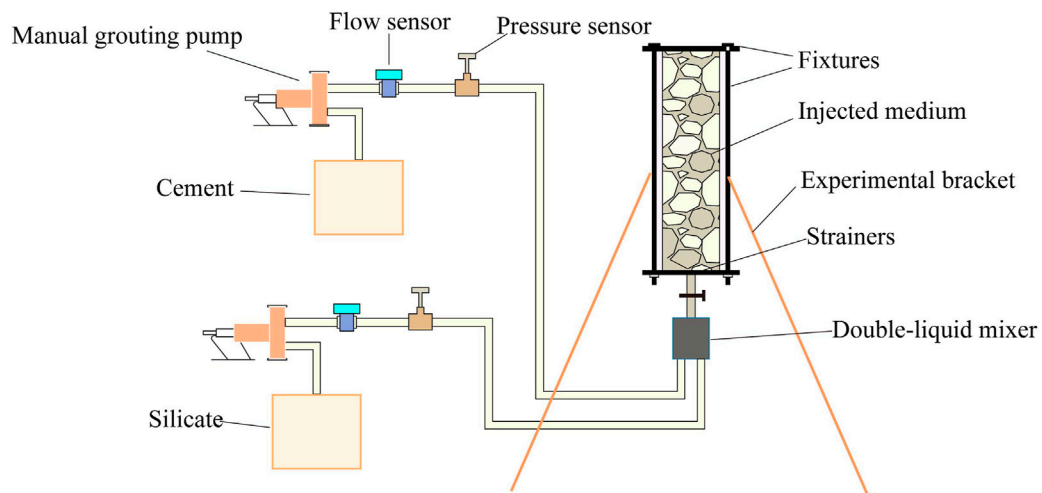


**FIGURE 2**  
Schematic diagram of experiment device.

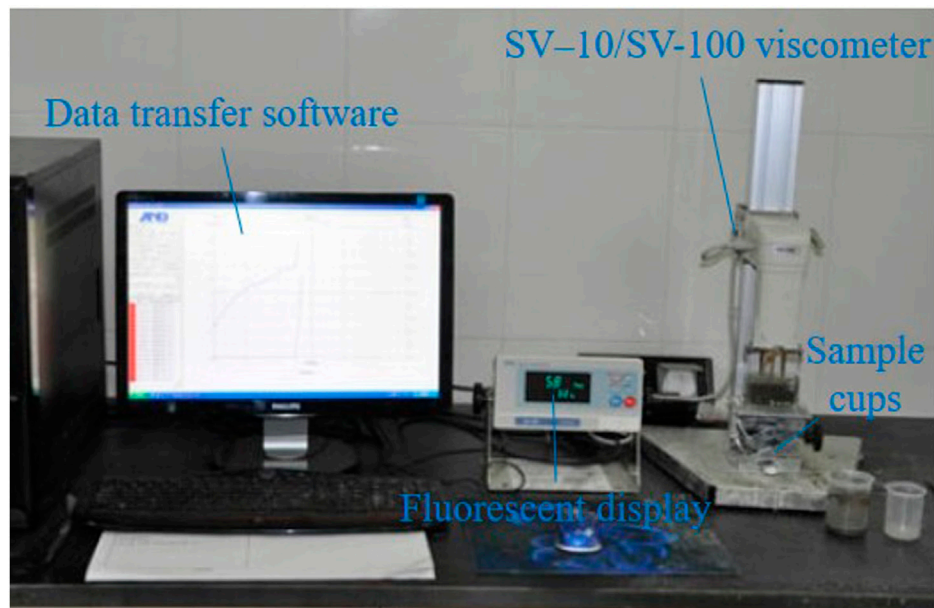


**FIGURE 3**  
SV-10/SV-100 sine wave vibrating viscometer.

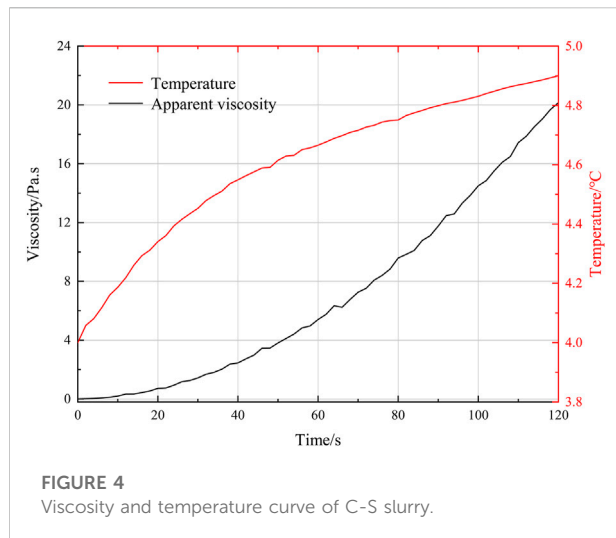
unchanged. The initial viscosity growth of C-S slurry is small. With the reaction time, the slurry viscosity increases rapidly. The slurry viscosity curve can be fitted by power function form  $At^B + C$ :

$$\mu(t) = 0.00208t^{1.93} + 0.01 \quad (20)$$

Where:  $\mu(t)$  is the apparent viscosity of C-S slurry;  $t$  is the time after mixing the C-S slurry.

### 3.3 Experiment plan

Three kinds of river sand with different particle size gradations are selected as the injected medium and the grouting experiment environment is anhydrous. The permeability coefficient and porosity of the injected medium are determined according to the constant head permeability test and “Standard for geotechnical testing method” (GB/T50123-1999, 1999).



The physical and mechanical parameters of the three types of river sands injected are shown in Table 1.

During this experiment the grouting rate was kept constant and designed at 1, 2 and 3 L/min. 5 sets of experiment conditions were designed according to the porosity of the injected media and the grouting rate, as shown in Table 2.

It is inevitable that there will be certain fluctuation of grouting rate when using manual grouting pump in the experiment. Therefore, it is considered that the fluctuation of grouting rate is constant within 10%.

## 4 Analysis of experimental results

With the growth of time, the slurry pressure is increasing, and the growth rate of slurry pressure also has a significant

increase. The analysis suggests that the C-S slurry is at a low viscosity stage due to the low viscosity of the slurry mix at the beginning, the slurry viscosity grows slowly and the slurry flow diffusion resistance is at a low range; as time grows, the C-S slurry viscosity increases rapidly and the slurry flow diffusion resistance rises rapidly, making the grouting pressure increase as well. The variation curve of grouting pressure is shown in Figure 5.

The grouting pressure is positively related to the grouting rate, while the grouting pressure is negatively related to the porosity of the injected medium.

## 5 Comparison and analysis of theoretical model and experimental results

During the experiment the diffusion front on the wall of the Plexiglas tube and the diffusion front in the river sand are basically consistent, the slurry is diffused in a one-dimensional form, the slurry diffusion distance can be directly obtained by measuring the position of the slurry front on the wall of the tube.

For one-dimensional diffusion penetration grouting, the diffusion distance and grouting time of grout meet:

$$Q = qt = \varphi S l_0 \quad (21)$$

The relationship between grouting pressure and diffusion distance in one-dimensional permeation diffusion process can be obtained by the simultaneous Eqs 19, 21.

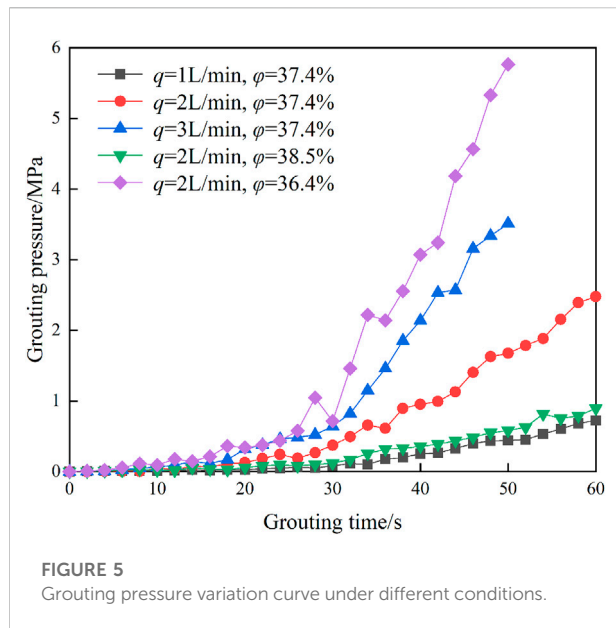
$$p_c = \int_0^{l_m} \left[ -\frac{q}{Sk} \mu \left( \frac{\varphi S l_0}{q} \right) - \frac{2\tau_0}{3} \sqrt{\frac{2\varphi}{k}} \right] l_0^{D_t-1} \left( 4 \sqrt{\frac{2k}{\varphi}} \right)^{1-D_t} D_t dl_0 + p_0 \quad (22)$$

**TABLE 1** The physical and mechanical parameters of injected medium.

Number of injected media	Particle size range/mm	Porosity $\varphi$ (%)	Permeability $k/m^2$
1	0.5–1	36.4	$2.218 \times 10^{-9}$
2	1–2	37.4	$5.857 \times 10^{-9}$
3	2–5	38.5	$1.512 \times 10^{-8}$

**TABLE 2** Experiment conditions.

Condition number	Grouting rate/(L/min)	Porosity of injected medium $\varphi$ (%)	Grouting time/s
1	1	37.4	60
2	2	37.4	60
3	3	37.4	50
4	2	38.5	60
5	2	36.4	50



Simultaneous (Eqs 16, 21) obtainable:

$$p_c = \int_0^{l_m} \left[ \frac{q}{Sk} \mu \left( \frac{\phi S l_0}{q} \right) - \frac{2\tau_0}{3} \sqrt{\frac{2\phi}{k}} \right] dl_0 + p_0 \quad (23)$$

Whereas Eq. 22 is the temporal and spatial distribution equation of grouting pressure considering diffusion path and Eq. 23 is the temporal and spatial distribution equation of grouting pressure without considering seepage path.

Again, by substituting  $l_m = qt_m/\phi S$  into Eqs 22, 23 the equation for grouting pressure versus time can be obtained, without going into too much detail here. The relevant calculation parameters for the theoretical model are shown in Table 3.

## 5.1 Analysis of the variation of grouting pressure with time

By substituting the relevant parameters into the variation of grouting pressure versus time equation, the variation of grouting pressure versus time curve can be obtained, and the specific

calculation results are compared with the experimental data as shown in Figure 6.

As can be seen from Figure 6, at the beginning of the grouting period, the grouting pressure is small and the growth rate is also small; as the grouting proceeds, there is a significant increase in the growth rate of the grouting pressure. There is a certain difference between the calculated results considering the slurry diffusion path compared to the model without considering the slurry diffusion path, and the theoretical difference increases with time. When the final design grouting time is reached, the calculated results considering the slurry diffusion path are 2.9–3.6 times higher than those without considering the slurry diffusion path, and the grouting pressure considering the slurry diffusion path is 0.9–1.1 times higher than the experimental results, and the experimental values are in good agreement with the theoretical.

## 5.2 Analysis of relationship between grouting pressure and diffusion distance

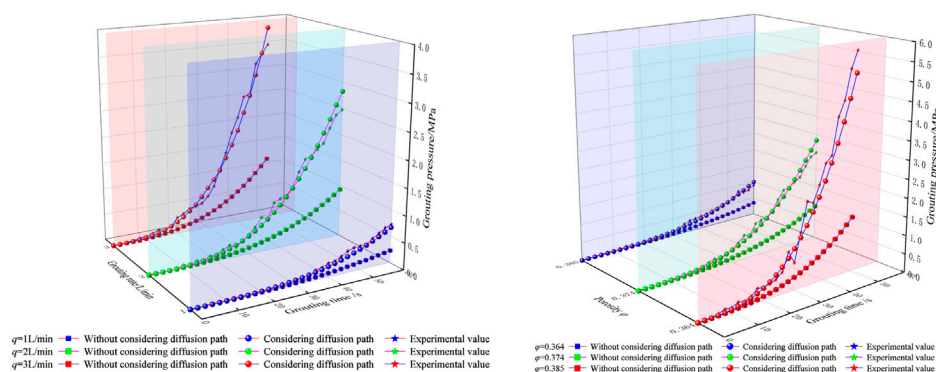
The calculated parameters are substituted into Eqs 22, 23 to obtain the variation curve of grouting pressure versus diffusion distance, and the specific calculated results are compared with the test data as shown in Figure 7.

As can be seen from Figure 7, the grouting pressure has a significant effect on the slurry diffusion distance when the grouting pressure is at a low level; when the grouting pressure is at a high level, the slurry diffusion distance is significantly reduced by the grouting pressure. The theoretical model considering the diffusion path of slurry has a faster growth rate, while the theoretical model without the diffusion path has a slower growth rate, and the difference in slurry pressure increases as the diffusion distance increases. When the same diffusion distance as the test value is reached, the grouting pressure value obtained from the experimental is 2.4–4.1 times the value without considering the diffusion path, and the grouting pressure value obtained from the experimental is 0.7–1.2 times the theoretical value with considering the diffusion path, which is within the acceptable error range.

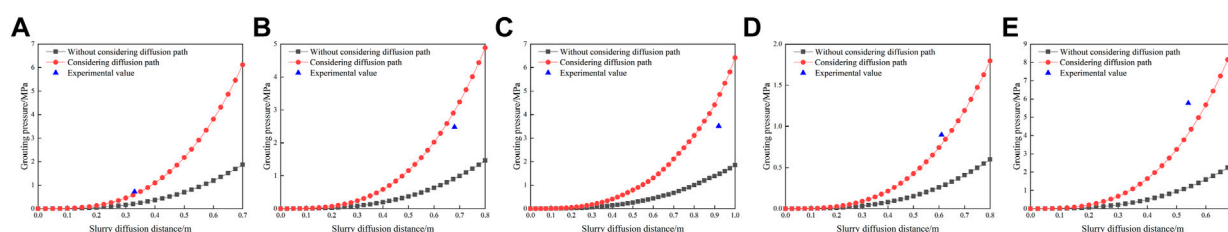
In summary, during penetration grouting, the grouting pressure values obtained from the experiment differed

TABLE 3 Calculation parameters of theoretical model.

Condition number	$q$ (L/min)	$k$ ( $10^{-9}\text{m}^2$ )	$\phi$	$t$ (s)	$S$ ( $\text{m}^2$ )	$P_0$ (MPa)
1	1	5.857	0.374	60	0.00785	0
2	2	5.857	0.374	60		
3	3	5.857	0.374	50		
4	2	15.12	0.385	60		
5	2	2.218	0.374	50		



**FIGURE 6**  
Variation curve of grouting pressure with time.



**FIGURE 7**  
Relationship curve between grouting pressure and diffusion distance. (A) Condition 1; (B) Condition 2; (C) Condition 3; (D) Condition 4; (E) Condition 5.

significantly from the calculated values without considering the diffusion path, while the calculated values considering the diffusion path agreed better with the experimental values, so it was necessary to consider the slurry diffusion path.

## 6 Conclusion

- (1) Based on the fractal theory of porous media and the equation of seepage motion of viscous time-varying Bingham fluid, a theoretical model of permeation grouting with viscous time-varying Bingham fluid is established.
- (2) The viscosity of the C-S slurry was tested and the variation curve of the viscosity of the C-S slurry with time was obtained. A set of permeation grouting simulation experiment device was designed, and the permeation grouting simulation experiment of C-S slurry was carried out to obtain the variation curve of grouting pressure with time under different injection media and different grouting rates.
- (3) When the designed grouting time is reached, the calculation results considering the diffusion path are 2.9–3.6 times the results without the diffusion path, and the grouting pressure

considering the slurry diffusion path is 0.9–1.1 times the experimental results.

- (4) For the same diffusion distance conditions as the experimental, the grouting pressure values obtained from the experimental are 2.4–4.1 times the values obtained without considering the diffusion path, and the grouting pressure obtained from the experimental is 0.7–1.2 times the theoretical value considering the diffusion path.

## Data availability statement

The raw data supporting the conclusion of this article will be made available by the authors, without undue reservation.

## Author contributions

HW is mainly responsible for the overall writing of the full text. LD and QZ are responsible for data processing and analysis. ZL is responsible for the innovative ideas of the article. PZ are responsible for the test operation. All authors have read and agreed to the published version of the manuscript.

## Funding

This work was supported by the National Natural Science Foundation of China (Grant No. 52109131); the Natural Science Foundation of Shandong Province (Grant No. ZR2020QE290); and the National Natural Science Foundation of China (Grant No. 52179120 and 52171267).

## Conflict of interest

Author PZ was employed by Qingdao West Coast Rail Transit Co., Ltd.

## References

- Axelsson, M., Gustafson, G., and Fransson, Å. (2009). Stop mechanism for cementitious grouts at different water-to-cement ratios. *Tunn. Und. Space Technol.* 24, 390–397. doi:10.1016/j.tust.2008.11.001
- Chen, X., and Yuan, C. (2021). Law of columnar penetration of Bingham type slurry in porous medium. *J. Min. Safe. Eng.* 38 (04), 800–809+856.
- Feng, X., Liu, R., Li, S., Han, W., Zhao, S., and Wang, H. (2016). Characteristics of moving interface of grout considering deep bed filtration. *Chin. J. Rock Mech. Eng.* 35 (05), 1000–1008.
- GB/T50123-1999 (1999). *Standard for soil test method*. Beijing, China: Ministry of Water Resources. (In Chinese).
- Kim, J. S., Lee, I. M., Jang, J. H., and Choi, H. (2009). Groutability of cement-based grout with consideration of viscosity and filtration phenomenon. *Int. J. Numer. Anal. Mater. Geomech.* 33, 1771–1797. doi:10.1002/nag.785
- Kong, X. (2010). *Advance mech mechanics of fluids in porous medium*. 2nd. Hefei: University of Science and Technology of China Press, 409.
- Kuang, J., Zan, Y., and Wang, J. (2000). *Theory and example of grouting in geotechnical engineering*. 1rd ed. Beijing, China: Science press, 39–42.
- Li, G., Zhang, B., and Yu, Y. (2013). *Soil mechanics*. 2nd. Beijing: Tsinghua University Press, 51.
- Li, S., Liu, R., Zhang, Q., Sun, Z., Zhang, X., and Zhu, M. (2013). Research on C-S slurry diffusion mechanism with time-dependent behavior of viscosity. *Chin. J. Rock Mech. Eng.* 32 (12), 2415–2421.
- Li, S., Zheng, Z., Liu, R., Feng, X., Sun, Z., and Zhang, L. (2015). Analysis of diffusion of grout in porous medium considering permeation effects. *Chin. J. Rock Mech. Eng.* 34 (12), 2401–2409.
- Liu, J., Zhang, Z., Han, Y., and Wu, X. (2015). Backfilled grouting diffusion law and model of pressure on segments of shield tunnel considering viscosity variation of cement grout. *Rock Soil Mech.* 36 (02), 361–368.
- Ma, H., Yang, M., and Xia, Q. (2000). Research on formula based on the theory of permeable grouting. *Ind. Con.*, 02, 47–50+61.
- Pitchumani, R., and Ramakrishnan, B. (1999). A fractal geometry model for evaluating permeabilities of porous preforms used in liquid composite molding. *Int. J. Heat. Mass Transf.* 42 (2), 2219–2232. doi:10.1016/s0017-9310(98)00261-0
- Yang, P., Tang, Y., Peng, Z., and Chen, A. (2006). Study on grouting simulating experiment in sandy gravels. *Chin. J. Geotech. Eng.*, 28, (12), 2134–2138.
- Yang, X., Lei, J., Xia, L., and Wang, X. (2005). Study on grouting diffusion radius of exponential fluids. *Rock Soil Mech.*, 26, (11), 112–115.
- Yang, X., Wang, X., and Lei, J. (2004). Study and application of Bingham slurry diffusion radius. *J. Hydraul. Eng.*, 06, 75–79.
- Yang, Z., Hou, K., Guo, T., and Ma, Q. (2011). Study of column-hemispherical penetration grouting mechanism based on Bingham fluid of viscous time-varying. *Rock Soil Mech.* 32 (09), 2697–2703.
- Yang, Z., Lu, J., Wang, Y., Zhang, Z., Yang, Y., Zhu, Y., et al. (2021). Column penetration grouting mechanism for power-law fluids considering tortuosity effect of porous medium. *Chin. J. Rock Mech. Eng.* 40 (02), 410–418.
- Yang, Z., Niu, X., Hou, K., Guo, Y., Liang, W., and Zhou, Z. (2016). Column penetration grouting mechanism researches based on Power-law fluid. *J. Harbin Inst. Technol.* 48 (03), 178–183.
- Yang, Z., Niu, X., Hou, K., Guo, Y., Zhou, Z., Chen, F., et al. (2015). Study on diffusion parameters of Bingham fluid based on column-hemispherical penetration grouting. *J. Sichuan Univ. Eng. Sci. Ed.*, 47 (S2), 47–53.
- Ye, F., Gou, C., Chen, Z., Liu, Y., and Zhang, J. (2013). Back-filled grouts diffusion model of shield tunnel considering its viscosity degeneration. *China J. Highw. Transp.* 26 (01), 127–134.
- Ye, F., Gou, C., Liu, Y., and Sun, H. (2012). Half-spherical surface diffusion model of shield tunnel back-filled grouts. *J. Tongji Univ. Nat. Sci.*, 40 (12), 1789–1794.
- Yu, B. (2005). Character for tortuous streamtubes in porous medium. *Chin. Phys. Lett.* 22 (1), 158–160.
- Yu, B., and Cheng, P. (2002). A fractal permeability model for bi-dispersed porous media. *Int. J. Heat. Mass Transf.* 45 (14), 2983–2993. doi:10.1016/s0017-9310(02)00014-5
- Yu, B., and Li, J. (2004). A geometry model for tortuosity of flow path in porous medium. *Chin. Phys. Lett.* 21 (8), 1569–1571.
- Yu, B., and Li, J. (2001). Some fractal characters of porous medium. *Fractals* 09 (03), 365–372. doi:10.1142/s0218348x01000804
- Yun, M., Yu, B., and Cai, J. (2008). A fractal model for the starting pressure gradient for Bingham fluids in porous media. *Int. J. Heat. Mass Transf.* 51 (5-6), 1402–1408. doi:10.1016/j.jheatmasstransfer.2007.11.016
- Zhang, L., Zhang, Q., Liu, R., Li, S., Wang, H., Li, W., et al. (2017). A study of the application of Brain Atlas with and without +Gz acceleration conditions. *Rock Soil Mech.* 38 (02), 443–448. doi:10.3233/THC-171347
- Zhang, Q., Wang, H., Liu, R., Li, S., Zhang, L., Zhu, G., et al. (2018). Permeation grouting mechanism of porous medium considering diffusion paths of grout. *Chin. J. Geotech. Eng.* 40 (05), 918–924.
- Zhou, J., Lu, J., Zhang, Y., and Wang, Z. (2019). Calculation formula of permeation grouting considering slurry viscosity variation. *J. Mat. Sci. Eng.* 37 (05), 758–762.
- Zhou, Z., Du, X., Chen, Z., Zhao, Y., and Chen, L. (2016). Slurry diffusion pressure considering pore tortuosity effect. *Chin. J. Nonferrous Mater.* 26 (08), 1721–1727.

The remaining authors declare that the research was conducted in the absence of any commercial or financial relationships that could be construed as a potential conflict of interest.

## Publisher's note

All claims expressed in this article are solely those of the authors and do not necessarily represent those of their affiliated organizations, or those of the publisher, the editors and the reviewers. Any product that may be evaluated in this article, or claim that may be made by its manufacturer, is not guaranteed or endorsed by the publisher.





## OPEN ACCESS

EDITED BY  
Danqi Li,  
Curtin University, Australia

REVIEWED BY  
Li Ma,  
Xi'an University of Science and  
Technology, China  
Wenshui Li,  
Shandong University of Science and  
Technology, China

\*CORRESPONDENCE  
Yanlong Chen,  
✉ chenyanlong@cumt.edu.cn

SPECIALTY SECTION  
This article was submitted to  
Environmental Informatics and Remote  
Sensing,  
a section of the journal  
Frontiers in Earth Science

RECEIVED 21 December 2022

ACCEPTED 23 January 2023

PUBLISHED 02 February 2023

CITATION  
Xie Q, Chen Y, Lyu H, Gu J, Chen Y, Cui H  
and Wu P (2023), Dynamic mechanical  
properties and energy dissipation analysis  
of frozen sandstone with initial damage.  
*Front. Earth Sci.* 11:1128634.  
doi: 10.3389/feart.2023.1128634

COPYRIGHT  
© 2023 Xie, Chen, Lyu, Gu, Chen, Cui and  
Wu. This is an open-access article  
distributed under the terms of the [Creative  
Commons Attribution License \(CC BY\)](#).  
The use, distribution or reproduction in  
other forums is permitted, provided the  
original author(s) and the copyright  
owner(s) are credited and that the original  
publication in this journal is cited, in  
accordance with accepted academic  
practice. No use, distribution or  
reproduction is permitted which does not  
comply with these terms.

# Dynamic mechanical properties and energy dissipation analysis of frozen sandstone with initial damage

Qihang Xie<sup>1</sup>, Yanlong Chen<sup>2\*</sup>, Haoyan Lyu<sup>1</sup>, Jun Gu<sup>1</sup>,  
Yuanguang Chen<sup>1</sup>, Huidong Cui<sup>1</sup> and Peng Wu<sup>2</sup>

<sup>1</sup>School of Mechanics and Civil Engineering, China University of Mining and Technology, Xuzhou, China,  
<sup>2</sup>State Key Laboratory for Geomechanics and Deep Underground Engineering, China University of Mining and  
Technology, Xuzhou, China

Damaged rock masses on the slopes of open pit coal mines are prone to geological disasters such as landslides under low temperatures and dynamic loads such as blasting impacts. Based on the Low Temperature Split Hopkinson Pressure Bar (LT-SHPB) system, dynamic compressive tests were done on sandstone specimens, which were damaged by uniaxial loading and unloading test. Dynamic stress–strain curves and dynamic mechanical properties of frozen sandstone with initial damage were analyzed as well as the energy dissipation characteristics. The results indicate that both compressive state and plastic deformation state of the dynamic stress–strain curves increase with the increase of the damage value. Dynamic peak stress and dynamic elastic modulus exhibit an evident damage weakening effect while the dynamic peak strain, in contrast, exhibits a damage enhancement effect. In addition, all three dynamic mechanical properties of the damaged frozen sandstone exhibit an impact effect. The dissipation energy ratio and reflection energy ratio of frozen sandstone increase with the increase of initial damage value while the transmission energy ratio decreases. With the increase of initial damage value and strain rate, the energy utilization rate during the sandstone failure process increases, resulting in more small fragments and powders.

## KEYWORDS

open pit coal mine, initial damage, LT-SHPB, frozen sandstone, energy dissipation

## 1 Introduction

Many large open-pit coal mines in China are distributed in the Western cold regions such as Xinjiang (Zhao et al., 2020; Lu et al., 2021). Under the action of low temperature, a special frozen rock slope is formed. Depending on the temperature and moisture content, the freezing expansion of free water in the rock mass brings two effects (Weng et al., 2021): On the one hand, it accelerates the development of damage cracks and weakens the mechanical properties of the rock mass (Ghobadi and Babazadeh, 2015); On the other hand, freezing water fills part of the rock cracks and enhances rock mass strength to some extent (Wang et al., 2019). At present, scholars have made abundant achievements in the study of static mechanical properties of rock at low temperature, mainly in terms of failure strength, elastic modulus, and failure characteristics (Ulrich and Darling, 2001; Feuer and Ince, 2015; Liu X. Y. et al., 2021). In addition, some scholars have studied the triaxial creep properties of frozen rock and obtained the creep equation which can better describe the creep process of the frozen rock (Zhu W. C. et al., 2019; Zhu Z. Y. et al., 2019; Shan et al., 2021).

Open-pit coal mine rocks are generally subjected to loose blasting before stripping, and the external loading mode of the rock by the stress waves generated by blasting is in the form of dynamic impact at a high strain rate (Ding et al., 2019; Shen et al., 2021). Rock mechanical properties under impact load are significantly different from those under static loading (Wang et al., 2016; Zhou et al., 2020). With the increase of geotechnical engineering in cold regions, the research on dynamic mechanical properties of rock under low temperature environments is increasing. Mardoukhi et al. (2021) and Liu C. J. et al. (2021) studied the dynamic tensile properties of granite at low temperature. Weng et al. (2020) compared the dynamic mechanical of dry and saturated Siltstones under sub-zero temperatures, and investigated the mechanism of weakening and strengthening the dynamic mechanical properties of saturated rock samples at sub-zero temperatures by using NMR technology. Yang et al. (2021a; 2021b) found that the dynamic mechanical strength of red sandstone gradually increased from  $-5^{\circ}\text{C}$  to  $-30^{\circ}\text{C}$ , but decreased sharply when the temperature was below  $-30^{\circ}\text{C}$ ; Li et al. (2018) investigated the freeze-thaw effect on the pore structure and dynamic mechanical properties of sandstone, and the result shows that sandstone porosity increased with the adding-up of freeze-thaws cycles, which leads to the attenuation of the dynamic mechanical properties of sandstone. Nikolenko et al. (2021) studied the effect of freeze-thaw cycle on the propagation of cracks in coal and found that a large number of cracks formed after a single freeze-thaw cycle. In addition, it has been found by literature review that since the deformation and failure process of rocks is essentially an energy-driven destabilization phenomenon (Xie et al., 2009; Song et al., 2015), the energy analysis method is a convenient and critical perspective to respond to the extent of fracture development within the rock impact damage process (Yang et al., 2020; Wang et al., 2021). For example, Wang et al. (2017) analyzed the energy evolution characteristics of red sandstone during dynamic impact after freeze-thaw cycles and defined Freeze-Thaw-Mechanical coupling damage based on energy dissipation ratio; Weng et al. (2019b) have found that the dynamic fragmentation of dry and saturated siltstones decreased first and then increased from  $18^{\circ}\text{C}$  to  $-50^{\circ}\text{C}$ , reaching a minimum value at  $-30^{\circ}\text{C}$  while the energy dissipation density of saturated siltstones reached a maximum value at  $-30^{\circ}\text{C}$ . Wang et al. (2020) studied the variation law of energy dissipation rate during the impact of frozen sandstone to reflect the strain rate effect and temperature effect of sandstone.

However, previous studies on the dynamic mechanical properties of rock at low temperature mainly focused on intact rock samples, ignoring the influence of initial damage of rock. Defects such as cracks and holes can exist within the rock mass of open pit coal mines. There are two main reasons for the existence of these defects: 1) Geological effects (internal forces such as crustal movement and external forces such as weathering) during the formation of the rock body in nature makes defects of various shapes and sizes appear inside the rock (Cao et al., 2016; Ahmed et al., 2020); 2) The disturbing effect of mining, such as rolling of slope rock mass by large mining trucks and impact of blasting (Hou et al., 2019; Li et al., 2021; Wu et al., 2022). These damages aggravate the deterioration of the mechanical properties of slope rocks and bring about major potential hazards such as landslides. Therefore, it is necessary to analyze the influence of rock damage on the dynamic mechanical properties of rocks.

In this paper, sandstone is chosen as the test object because it is widely present in open-pit coal mine slopes as the main rock layer and

its characteristic is representative and applicable (Li et al., 2022). Sandstones with different initial damage were prepared by uniaxial loading and unloading test, and the initial damage value was defined based on the porosity. The real-time low-temperature dynamic compression test was carried out on the damaged sandstone to obtain the variation law of dynamic mechanical parameters of frozen sandstone under different damage conditions. The dynamic damage process of frozen sandstone is analyzed from the perspective of energy, and the energy dissipation characteristics of freeze-damaged sandstone are obtained. The research results can provide a reference for the prevention and control of slope instability during open-pit coal mining in cold regions.

## 2 Materials and experimental methods

### 2.1 Preparation of specimen

The sample rock was taken from the area near an open-pit coal mine (Xinjiang, China), which had not been damaged by disturbances such as blasting operations and large mining trucks in the open-pit mine. Judging from the cutting surfaces, the sandstone is in dark red with fine particles and hard texture. The main mineral components of the sandstone are as follows: quartz (61%), muscovite (28%), kaolinite (5%), montmorillonite (3%) as well as small amounts of illite and hematite.

According to the ISRM suggested methods, sandstone was made into  $\Phi 50 \times 100$  mm cylindrical specimens for initial damage treatment. In order to avoid the experimental error caused by the dispersion of sandstone, the longitudinal wave velocity of standard samples was detected. The specimens with similar wave velocities were selected as the test objects, and the basic physical and mechanical parameters of the natural air-dried sandstone specimens are shown in Table 1.

### 2.2 Initial damage treatment

The initial damage condition of the sandstone specimens was obtained through loading and unloading test using MTS816 electro-hydraulic servo system. According to the uniaxial compressive strength (UCS)  $\sigma_c = 27.50$  MPa of sandstone specimens, four loading stress levels were determined as 0%  $\sigma_c$ , 50%  $\sigma_c$ , 60%  $\sigma_c$ , and 70%  $\sigma_c$ , respectively. When the specimen reached the set stress level during the loading process, the specimen was held for 30 min to ensure that the cracks inside the specimen were fully developed. In this regard, 9 specimens were prepared for each group of damage levels. Finally, three specimens of each group after initial damage treatment were taken for mercury intrusion test to determine the change of porosity, and the remaining six specimens of each group will be used to prepare disk specimens for real-time low temperature SHPB test.

Characterization of damage is the key to defining rock damage and establishing the damage evolution law. In this paper, the initial damage value is defined by the porosity of sandstone specimens. Weng et al. (2019a) proves the validity and feasibility of porosity to evaluate the degree of rock damage. An equation for describing the damage using the porosity is proposed as follows:

TABLE 1 Basic physical and mechanical parameters of sandstone specimens.

Specimen	Density (g·cm <sup>-3</sup> )	Uniaxial compressive strength (MPa)	Elasticity modulus (GPa)	Poisson's ratio	Longitudinal wave velocity (m·s <sup>-1</sup> )
1	2.19	26.17	2.25	0.17	2,624
2	2.34	28.06	2.34	0.18	2,634
3	2.31	28.26	2.38	0.17	2,657
Average	2.28	27.50	2.32	0.17	2,638

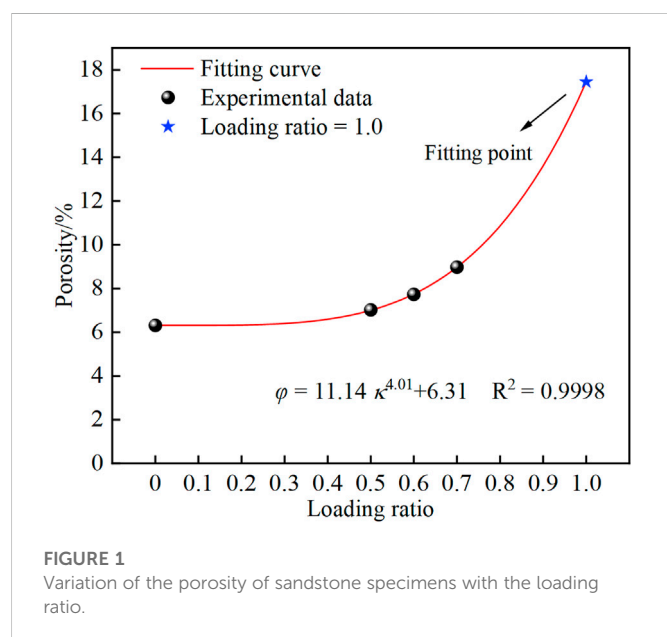


TABLE 2 Initial damage value of sandstone specimen under different loading stress.

Loading stress (MPa)	Loading ratio	φ (%)	D (%)
0	0	6.31	0
13.75	0.50	7.02	6.37
16.50	0.60	7.73	12.75
19.25	0.70	8.98	23.97

$$D = 1 - \frac{\varphi_1 - \varphi}{\varphi_1 - \varphi_0} \quad (1)$$

where,  $D$  is the damage value of the rock;  $\varphi_0$  is the porosity of the undamaged rock;  $\varphi_1$  is the porosity of the rock at failure;  $\varphi$  is the porosity of the damaged rock. Eq. 1 reflects the overall weakening degree of rock specimen without considering the anisotropy of damage.

Figure 1 shows the variation of the porosity of sandstone specimens with the loading ratio (loading stress over UCS). In fact, the porosity of rock failure is difficult to obtain by experiment. However, the approximation of  $\varphi_1$  can be obtained by the porosity fitting curve. The fitting equation is as follows:

$$\varphi = 11.14\kappa^{4.01} + 6.31 \quad R^2 = 0.9998 \quad (2)$$

where,  $\kappa$  is the loading ratio. When the loading ratio  $\kappa = 1$ , we may obtain the approximate porosity of sandstone at failure  $\varphi_1 = 17.45\%$ . Substituting  $\varphi_1$  to Eq. 1, the initial damage value under different loading stress can be obtained. Table 2 shows the loading ratio, porosity and initial damage value of sandstone under different loading stresses.

## 2.3 Real-time low temperature SHPB test

First, four sets of sandstone specimens with different initial damage were processed into disc specimens with 50 mm diameter and 25 mm height. Then, the disc specimens were subjected to natural air-drying treatment in order to eliminate the effects of changes in moisture content during specimen processing and initial damage treatment. Finally, real-time low temperature SHPB test was performed. The test setup and procedure are shown in Figure 2.

Natural air-drying treatment scheme is as follows: first, the sandstone specimens were baked in the oven at 105°C for 24 h; Then, the disk specimens were saturated in a vacuum saturation device for 6 h; Finally, the sandstone specimens were left to dry naturally in an indoor environment for 48 h and then wrapped with plastic wrap and stored in sealed bags. The average moisture content of the natural air-dried sandstone disc specimens is 2.02%.

The LT-SHPB system is used for the real-time low temperature impact test. The test system includes: low-temperature system, launching system, pressure bar system, data collection and processing system, and energy absorption system. Except for the low-temperature system, the composition and functions of the other four systems are the same as those of the conventional SHPB system. The diameter of the compression bar is 50 mm, the density is 7.82 g/cm<sup>3</sup>, the longitudinal wave speed is 5,123 m/s, and the modulus of elasticity is 210 GPa. During the test, the low-temperature system provides a real-time low-temperature environment for the sandstone specimen. The temperature control range of low-temperature system is -60°C to room temperature. Cryogenic nitrogen gas is vaporized from liquid nitrogen under the action of electric thermocouple and flows into the cryostat through the hose. When the low-temperature sensor detects that the temperature of the cryostat reaches the preset value, the thermocouple stops working, which is automatically controlled by the low temperature controller. The test shows that the temperature in the cryostat can be stably maintained at the preset temperature with the temperature difference of ±0.2°C.

The temperature of the real-time low-temperature impact test is set at -20°C which is selected based on the average temperature of the sampling mine in winter. It has been found that the sandstone interior needs to be kept freezing for at least 30 min in order to reach the temperature set in the test. In this paper, the temperature holding time

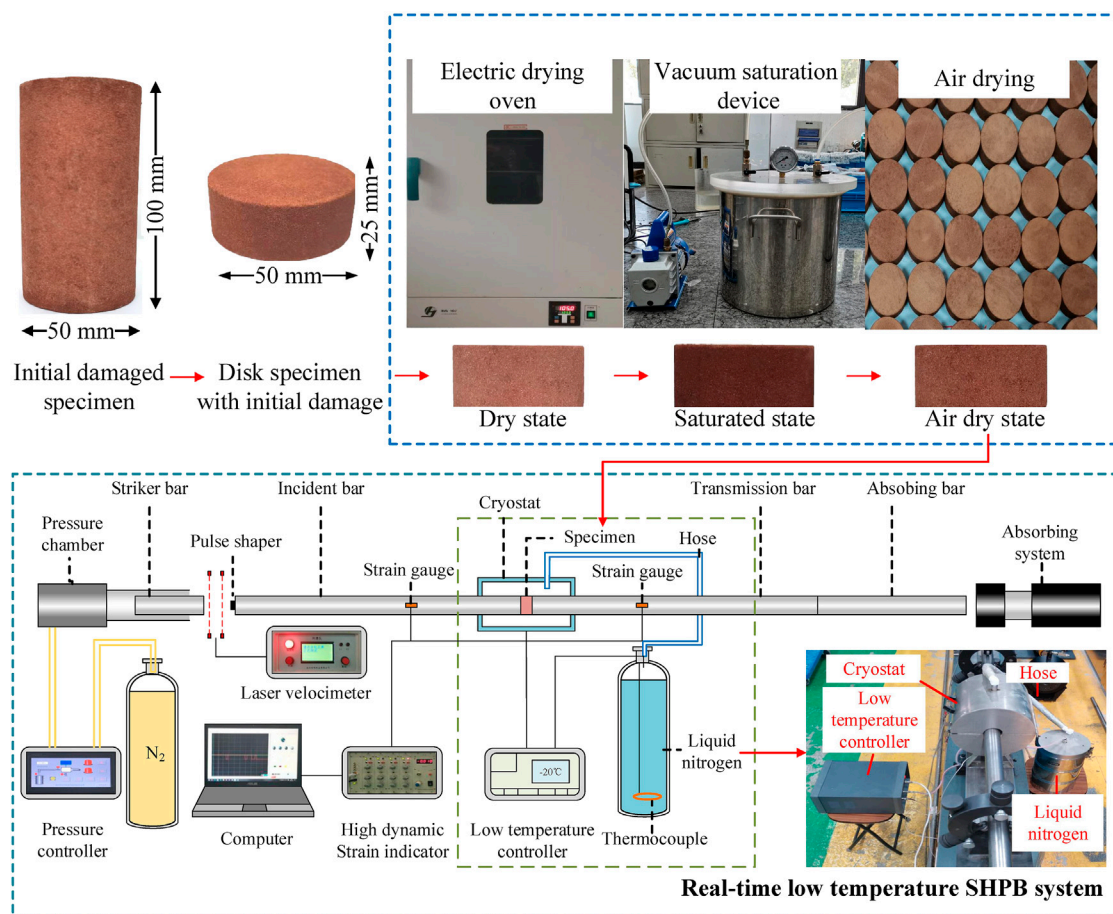


**FIGURE 2**  
Process of real-time low temperature SHPB test.

is set to 1 h for the accuracy of the test data. According to the actual working conditions of blasting in the open pit mine and laboratory equipment conditions, four groups of impact velocity are designed as 3.5, 4.0, 4.5, and 5.0 m/s. The test covered four kinds of initial damage level and four kinds of impact velocity, a total of 16 groups, each group of tests repeated 3 times. And the average strain rates at different impact velocities are 42.1, 76.7, 105.2, and 129.5  $s^{-1}$ , respectively.

## 3 Results and discussion

### 3.1 Dynamic stress-strain curve

The dynamic stress-strain curves of frozen sandstone with different initial damage are given in Figures 3A–D. It also shows the dynamic stress-strain curves of damaged sandstone at the strain rate of 76.7  $s^{-1}$  (Figure 3E). Meanwhile, according to the change characteristics of the curve, a typical stress-strain curve for this test is given (Figure 3F), and the typical stress-strain curve is divided into the following four stages:

(I) **Compaction stage:** This stage is characterized by an upwardly concave curve in appearance. This phenomenon is due to the

damage fractures produced in the initial damage treatment process. During the initial loading phase of the sandstone specimen, the fractures are gradually compacted and closed, and plastic deformation is produced.

- (II) **Elastic deformation stage:** This stage manifests itself in appearance as a nearly straight line. The cracks inside the sandstone specimen tend to a stable state after the compaction stage, and no new cracks are generated. As the load continues to increase, the specimen begins to store a large amount of strain energy and will only release a small amount of energy. Since the slope of the curve at this stage is approximately constant, the slope of the curve at this stage is taken as the dynamic elastic modulus in this paper.
- (III) **Plastic deformation stage:** The form of this stage shows a downward concave curve. After the elastic phase, the sandstone specimen develops new cracks as the load continues to increase. The old and new cracks will enter a non-stable extension phase and will gradually penetrate releasing a large amount of energy which will cause increased deformation and even local failure.
- (IV) **Failure stage:** In this stage, the stress of sandstone decreases rapidly in a nearly linear form with the increase of strain. As the sandstone specimen is in the unloading stage, the specimen has been detached from the incident and transmission bar.



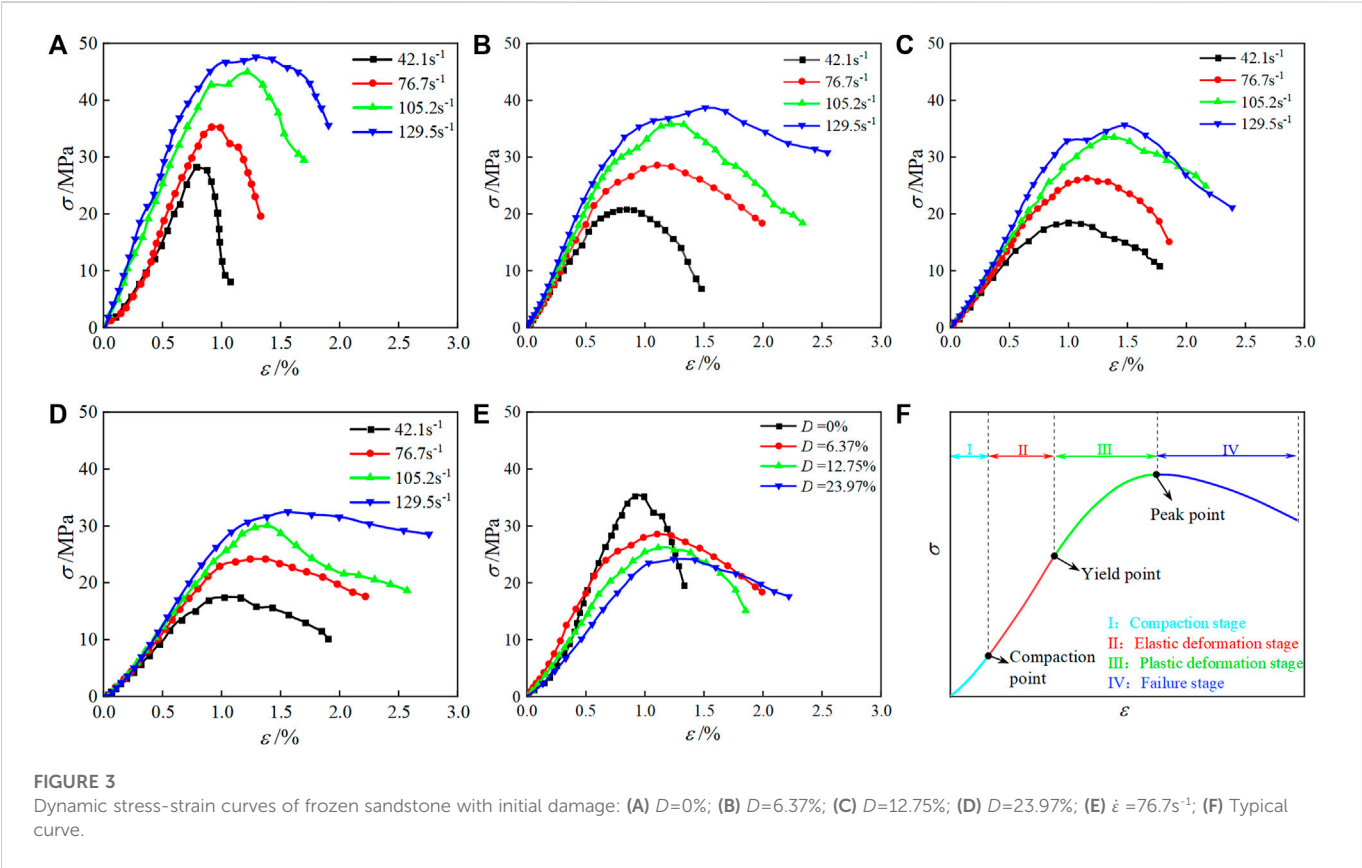


**TABLE 3** Dynamic mechanical parameters of frozen sandstone under different conditions.

$D$ (%)	$\dot{\epsilon}$ ( $\text{s}^{-1}$ )	$\sigma_c$ (MPa)	$\epsilon_c$ (%)	$E_c$ (GPa)
0	42.1	28.63	0.82	4.43
	76.7	35.42	0.95	4.68
	105.2	44.82	1.18	5.80
	129.5	47.64	1.36	6.12
6.37	42.1	20.88	0.84	3.38
	76.7	28.58	1.10	4.14
	105.2	35.80	1.28	4.32
	129.5	38.70	1.51	4.81
12.75	42.1	19.50	0.95	2.57
	76.7	26.28	1.20	3.02
	105.2	33.54	1.35	3.12
	129.5	35.21	1.54	3.86
23.97	42.1	17.52	1.07	2.51
	76.7	24.20	1.28	2.82
	105.2	30.27	1.40	2.85
	129.5	32.50	1.60	3.34

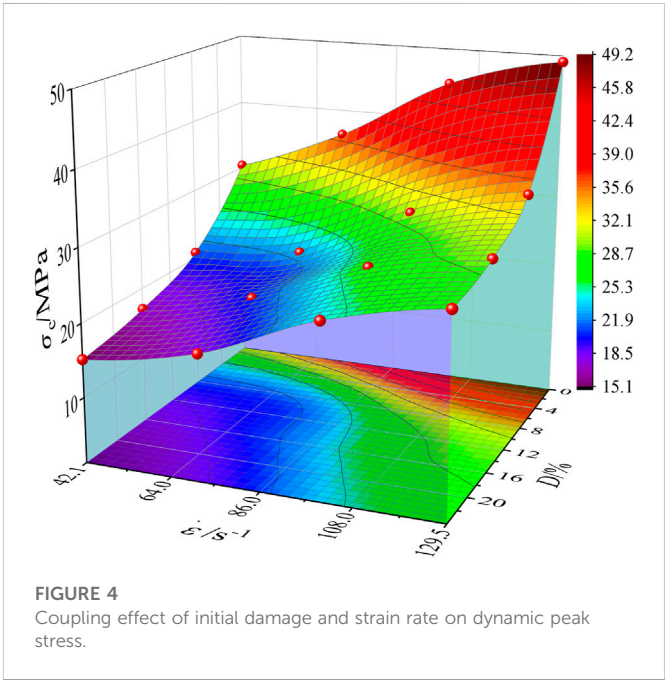
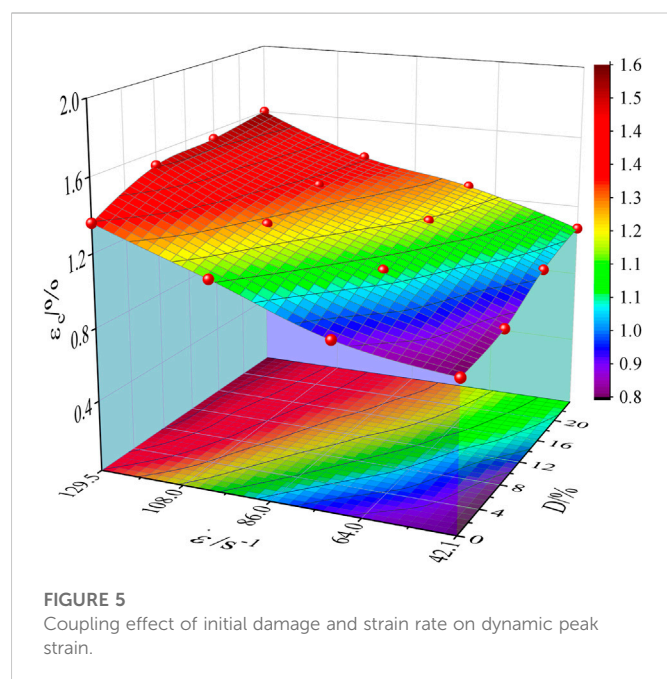


**FIGURE 4**  
Coupling effect of initial damage and strain rate on dynamic peak stress.

As can be seen from Figures 3A–E, the shapes of the curves are basically the same, but there are differences in their trends. Under a certain strain rate, the compaction stage increases with the increase of





damage value. This is because with the increase of damage value, there will be more micro defects in the sandstone sample. In the initial stage of impact loading, defects will gradually close with the increase of load, resulting in a longer compaction stage of the curve. At the same time, with the increase of initial damage, the plastic deformation stage also shows an obvious increasing feature.

## 3.2 Dynamic compressive mechanical parameters of sandstone

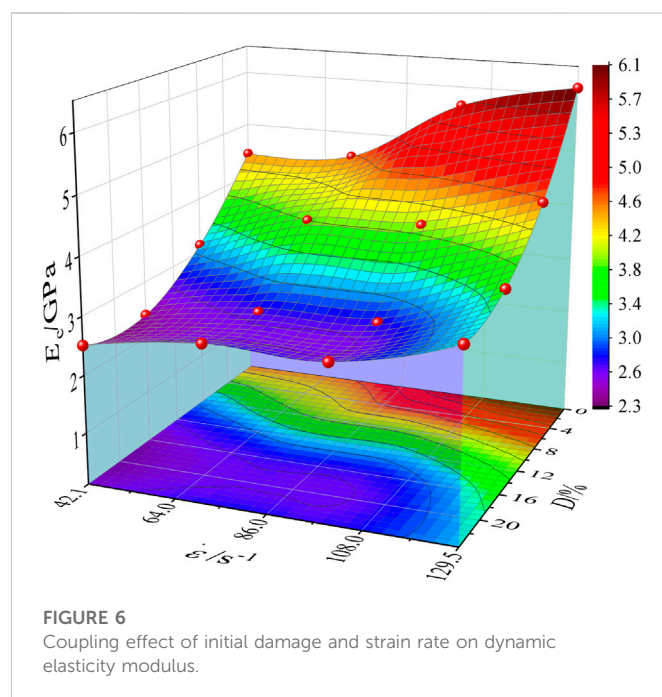
Dynamic mechanical parameters of frozen sandstone at different strain rates and different initial damage values, including dynamic peak stress, dynamic peak strain and dynamic elastic modulus, were obtained from the dynamic stress-strain curves (Table 3).

### 3.2.1 Dynamic peak stress

Figure 4 shows the variation surface of dynamic peak stress of frozen sandstone under the coupling effect of initial damage and strain rate. As can be seen from the figure, the initial damage value and strain rate significantly affect the dynamic peak stress of the frozen sandstone.

The dynamic peak stress in the frozen sandstone decreases as the initial damage value increases, showing a significant damage weakening effect. Specifically, as the initial damage increased from 0 to 23.97% under four sets of strain rate, the dynamic peak stress of the frozen sandstone decreased from 28.63, 35.42, 44.82, and 47.64 MPa to 17.52, 24.20, 30.27, and 32.50 MPa with a reduction of 38.81%, 31.68%, 32.46%, and 31.78%, respectively. This is due to the increase of damage value, more crack defects appear in the frozen sandstone, which reducing the bearing capacity of frozen sandstone.

For the same condition of initial damage value, the dynamic peak stress of frozen sandstone increases with increasing strain rate, showing a significant strain rate strengthening effect. Under the four sets of damage values, with the increase of strain rate, the



dynamic peak stress of frozen sandstone increased from 28.63, 20.88, 19.50, and 17.52 MPa to 47.64, 38.70, 35.21, and 32.50 MPa, which increased by 66.40%, 85.34%, 80.56%, and 85.50%, respectively.

### 3.2.2 Dynamic peak strain

Figure 5 shows the variation surface of dynamic peak strain of frozen sandstone under the coupling effect of initial damage and strain rate. Contrary to the dynamic peak stress, the dynamic peak strain of frozen sandstone increases with the increase of damage value, showing a damage strengthening effect. As the initial damage increased from 0 to 23.97% under four sets of strain rate, the dynamic peak strain decreased from 0.82%, 0.95%, 1.18%, and 1.36% to 1.07%, 1.28%, 1.40%, and 1.60% with an increase of 30.49%, 34.74%, 18.64%, and 17.65%, respectively. Due to the presence of initial damage, cracks and defects within the sandstone increase, causing a tendency of plasticity enhancement.

With the increase of strain rate, the peak strain increases linearly and rapidly, showing a strain rate strengthening effect. The dynamic peak strain of the frozen sandstone increases from 0.82%, 0.84%, 0.95%, and 1.07% to 1.36%, 1.51%, 1.54%, and 1.60% with an increase of 65.85%, 79.76%, 62.11%, and 49.53% respectively when the strain rate increases from 42.1 s<sup>-1</sup> to 129.5 s<sup>-1</sup> for the four sets of initial damage conditions.

### 3.2.3 Dynamic elastic modulus

As can be seen from the Figure 6, the variation characteristics of dynamic elastic modulus of the frozen sandstone are basically consistent with the dynamic peak stress. When the initial damage increases from 0 to 23.97% under the conditions of four groups of strain rates, the dynamic elastic modulus decreases from 4.43, 4.68, 5.80, and 6.12 GPa to 2.51, 2.82, 2.85, and 3.34 GPa, respectively, which decreases by 43.34%, 39.74%, 50.86%, and 45.42%, showing obvious damage weakening characteristics. In addition, under the four

groups of initial damage, with the increase of strain rate, the dynamic elastic modulus increases from 4.43, 3.38, 2.57, and 2.51 GPa to 6.12, 4.81, 3.86, and 3.34 GPa, respectively, which increased by 38.15%, 42.31%, 50.19%, and 33.07%, showing a strain rate strengthening effect.

### 3.3 Energy dissipation characteristics

The failure of sandstone samples under external load will experience the propagation and growth of defects such as internal cracks and holes until these defects penetrate the whole sample and make it completely destroyed. All these processes involve the absorption, transformation and dissipation of energy. It can be seen that the analysis of the dynamic damage process of frozen sandstone from an energy perspective can effectively reveal the damage effect and impact effect of frozen sandstone in the process of dynamic failure.

#### 3.3.1 Energy calculation

The failure process of sandstone specimens under dynamic loading is accompanied by the variation in energy. The incident energy  $W_I$  input to the sandstone specimen from the impact bar is converted into three components, namely the transmitted energy  $W_T$  entering the transmission bar, the reflected energy  $W_R$  reflected back into the incident bar and the dissipated energy  $W_D$  used to destroy the sandstone specimen. The relationship between these four components of energy can be expressed in Eq. 3:

$$W_D = W_I - W_R - W_T \quad (3)$$

According to classical elastic pressure bar theory, the incident energy  $W_I$ , reflected energy  $W_R$ , transmitted energy  $W_T$ , and dissipated energy  $W_D$  in the above equation can all be calculated by the equation, which is expressed as:

$$\begin{cases} W_I(t) = E_s C_s A_s \int_0^t \epsilon_I^2(t) dt \\ W_R(t) = E_s C_s A_s \int_0^t \epsilon_R^2(t) dt \\ W_T(t) = E_s C_s A_s \int_0^t \epsilon_T^2(t) dt \end{cases} \quad (4)$$

where  $E_s$ ,  $C_s$  and  $A_s$  are the elastic modulus, stress wave propagation velocity and cross-sectional area of the pressure bar in the SHPB system.

$R_R$ ,  $R_T$  and  $R_D$  represent the ratios of reflected energy  $W_R$ , transmitted energy  $W_T$  and dissipated energy  $W_D$  to their incident energy  $W_I$ , respectively, as calculated in Eq. 5:

$$\begin{cases} R_R = W_R/W_I \\ R_T = W_T/W_I \\ R_D = W_D/W_I \end{cases} \quad (5)$$

The dissipated energy in the SHPB dynamic compression test is mainly used for the expansion and penetration of defects such as cracks and holes within the sandstone specimen, but is also accompanied by kinetic energy and other forms of energy carried by the broken rock mass during the destruction of the specimen, such as heat energy and acoustic energy. However, 95% of the dissipated energy is mainly used for the expansion and penetration of defects, with a small proportion of the remaining 5% being

used for other forms of energy (Zhang et al., 2000). Therefore, this 5% of other forms of energy will be ignored in this study and the dissipated energy will be considered directly as the fracture energy of the sandstone specimen during dynamic compression failure.

Through Eqs 3–5, the calculation results of  $W_I$ ,  $W_R$ ,  $W_T$ , and  $W_D$  of damaged sandstone under different initial damage values and strain rates in the real-time low-temperature dynamic compression failure process and the ratio of each energy to the incident energy  $W_I$  are obtained. The specific results are shown in Table 4.

#### 3.3.2 Effect of initial damage value and strain rate on the energy dissipation characteristic

Figure 7 shows the histogram of the variation of incident energy, reflected energy, transmitted energy, and dissipated energy with damage values and the impact failure morphology of the damaged sandstone, which helps to analyze the change of sandstone failure characteristics in the process of dynamic compression from the aspect of energy change.

As can be seen from Figure 7, the incident, reflected, transmitted and dissipated energies all increase with increasing strain rate. For the same strain rate, the incident energy of the damaged frozen sandstone remains in a relatively constant state, and basically does not change with the change of damage value. This is due to the fact that the incident energy is related to the impact velocity. And the strain rate is almost corresponding to the impact velocity. When the impact velocity is relatively constant, the incident energy of the rod is also relatively constant, which reflects the stability of the LT-SHPB system. In addition, with the increase of damage value, the reflected energy and dissipated energy increase, while the transmitted energy decreases. In terms of sandstone failure morphology, the frozen sandstone will failure in a higher degree of fragmentation with more powder particles. The increased damage value also increases the degree of impact damage to the frozen sandstone, resulting in more and smaller fragments. This is due to the fact that as the damage value increases, the cracks and fissures within the frozen sandstone increase significantly, its structural integrity decreases obviously. Based on the basic morphology of fragments, it can be judged that the failure of frozen sandstone is mainly transformed from tensile failure mode to composite failure mode with the increase of strain rate and initial damage.

Figure 8 shows the variation curves of the reflected energy ratio  $R_R$ , transmitted energy ratio  $R_T$  and dissipated energy ratio  $R_D$  with damage values for different strain rates. The reflected energy ratio increases gradually with increasing damage values, which corresponds to the increase in dynamic peak strain in frozen sandstone with increasing damage values. Moreover, the transmitted energy ratio and dissipated energy ratio of the damaged frozen sandstone at the four sets of strain rates show a clear damage effect. The transmitted energy ratio decreases as the damage value increases while the dissipated energy ratio increases. In other words, the energy utilization rate during sandstone failure process increases with the increase of damage value. It shows that with the increase of damage value in dynamic failure of damaged frozen sandstone, more energy is consumed for the propagation of internal cracks and holes. This is consistent with the phenomenon that more block debris and granular

TABLE 4 The energy value during dynamic failure of damaged frozen sandstone.

$\dot{\epsilon}$ ( $s^{-1}$ )	$D$ (%)	$W_I$ (J)	$W_R$ (J)	$R_R$ (%)	$W_T$ (J)	$R_T$ (%)	$W_D$ (J)	$R_D$ (%)
42.1	0	44.56	21.68	48.65	16.91	37.95	5.97	13.40
	6.37	48.17	23.00	47.75	17.46	36.25	7.71	16.01
	12.75	45.14	23.78	52.68	13.13	29.09	8.23	18.23
	23.97	46.65	25.26	54.15	12.02	25.77	9.37	20.09
76.7	0	74.99	38.73	51.65	23.85	31.80	12.41	16.55
	6.37	76.99	40.35	52.41	20.08	26.08	16.56	21.51
	12.75	76.86	42.02	54.67	16.36	21.29	18.48	24.04
	23.97	78.90	42.54	53.92	17.05	21.61	19.31	24.47
105.2	0	110.83	59.91	54.06	26.67	24.06	24.25	21.88
	6.37	113.10	62.50	55.26	21.09	18.65	29.51	26.09
	12.75	114.05	61.17	53.63	22.12	19.40	30.76	26.97
	23.97	111.40	63.74	57.22	16.91	15.18	30.75	27.60
129.5	0	140.12	80.40	57.38	30.08	21.47	29.64	21.15
	6.37	143.31	82.89	57.84	26.46	18.46	33.96	23.70
	12.75	141.55	84.58	59.75	21.78	15.39	35.19	24.86
	23.97	138.76	85.44	61.57	15.67	11.29	37.65	27.13

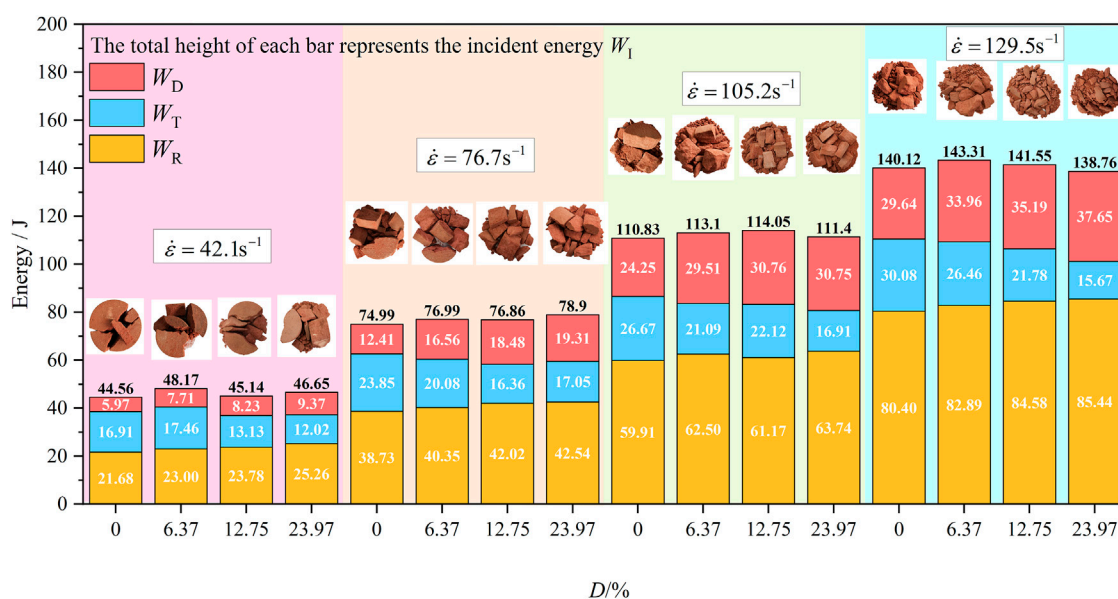


FIGURE 7

Energy variation and failure morphology of frozen sandstone with different initial damage values and strain rates.

powder will appear with the increase of damage value in the dynamic failure process of sandstone. In addition, as the strain rate increases, the dissipated energy ratio gradually increases, and the energy utilization rate in the process of sandstone failure increases, which

is similar to the influence of the initial damage value on the dissipated energy ratio. The strain rate can effectively improve the energy utilization rate during sandstone failure process and reduce the proportion of energy lost due to transmission.

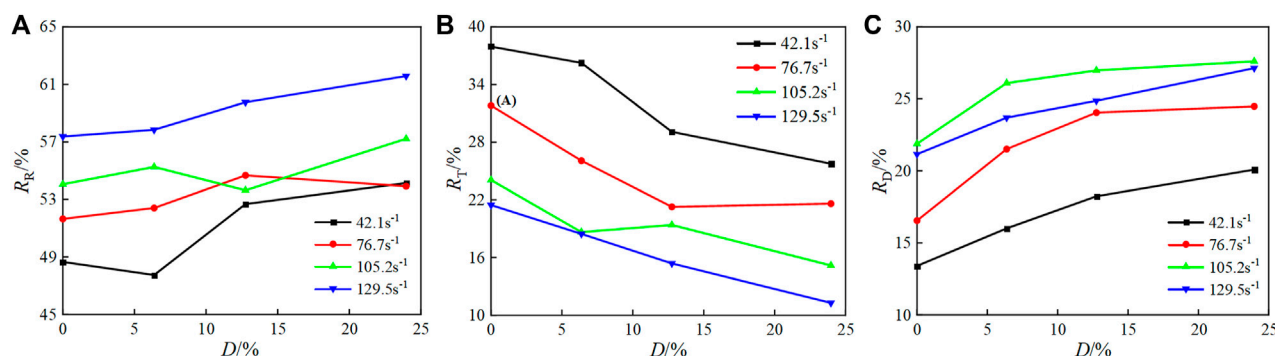


FIGURE 8

Energy ratio variation curves of frozen sandstone with different initial damage values (A) Reflected energy ratio; (B) Transmitted energy ratio; (C) Dissipated energy ratio.

## 4 Conclusion

This paper aims to investigate the effect of initial damage on dynamic mechanical response of the frozen sandstone. The dynamic compression test of frozen sandstone under different initial damage was carried out by LT-SHPB test system. Based on the theory of energy dissipation, the dynamic mechanical properties and the energy dissipation law were studied. The main conclusions are as follows:

- (1) The stress-strain curve of the damaged frozen sandstone can be divided into four stages: compaction stage, elastic deformation stage, plastic deformation stage, and failure stage. The compression stage and plastic deformation stage of the frozen sandstone increase with the increasing initial damage value at the same strain rate.
- (2) Initial damage has a significant effect on the dynamic mechanical response of frozen sandstone. The dynamic peak stress and dynamic elastic modulus of frozen sandstone decrease with the increase of the initial damage value, showing an obvious damage weakening effect. Dynamic peak strains, in contrast, increase with the increasing damage value. In addition, the dynamic peak stress, dynamic elastic modulus and dynamic peak strain all exhibit a strain rate effect that increase with the increase of strain rate.
- (3) As the strain rate and initial damage value increase, the frozen sandstone will failure in a higher degree of fragmentation with more powder particles. The failure of frozen sandstone is mainly transformed from tensile failure to composite failure with the increase of strain rate and initial damage value.
- (4) Under the same strain rate, the incident energy of damaged frozen sandstone can remain in a relatively stable state. The reflected energy ratio and dissipated energy ratio increase with the increasing initial damage value, while the transmitted energy ratio reduces. As initial damage value and strain rate increase, the energy utilization rate increases, which is consistent with the phenomenon that more small fragments and granular powders appear during the dynamic failure process of the frozen sandstone.

## Data availability statement

The original contributions presented in the study are included in the article/Supplementary Material, further inquiries can be directed to the corresponding author.

## Author contributions

QX and YaC designed the study and wrote the manuscript. QX, HL, JG, YuC, and HC obtained and analyzed data for the research. QX, HC, and PW prepared the figures. All authors contributed to the discussion of research results and manuscript revision.

## Funding

This work was financially supported by the National Key R&D Program of China (2022YFC2903902) and the National Natural Science Foundation of China (51974295).

## Acknowledgments

The authors thank State Key Laboratory for Geomechanics and Deep Underground Engineering for providing experimental equipment. It is also grateful for the financial support provided by the National Key R&D Program of China and the National Natural Science Foundation of China.

## Conflict of interest

The authors declare that the research was conducted in the absence of any commercial or financial relationships that could be construed as a potential conflict of interest.



## Publisher's note

All claims expressed in this article are solely those of the authors and do not necessarily represent those of their affiliated

organizations, or those of the publisher, the editors and the reviewers. Any product that may be evaluated in this article, or claim that may be made by its manufacturer, is not guaranteed or endorsed by the publisher.

## References

- Ahmed, Z., Wang, S. H., Hashmi, M. Z., Zhang, Z. S., and Zhu, C. J. (2020). Causes, characterization, damage models, and constitutive modes for rock damage analysis: A review. *Arabian J. Geosciences* 13 (16), 806. doi:10.1007/s12517-020-05755-3
- Cao, R. H., Cao, P., Lin, H., Pu, C. Z., and Ou, K. (2016). Mechanical behavior of brittle rock-like specimens with pre-existing fissures under uniaxial loading: Experimental studies and particle mechanics approach. *Rock Mech. Rock Eng.* 49 (3), 763–783. doi:10.1007/s00603-015-0779-x
- Ding, X. H., Zhou, W., Lu, X., Li, M., Manda, E., Shi, X. Y., et al. (2019). Distribution characteristics of fragments size and optimization of blasting parameters under blasting impact load in open-pit mine. *IEEE Access* 7, 137501–137516. doi:10.1109/Access.2019.2942968
- Feuer, M., and Ince, I. (2015). Effects of the freeze-thaw (F-T) cycle on the andesitic rocks (Sille-Konya/Turkey) used in construction building. *J. Afr. Earth Sci.* 109, 96–106. doi:10.1016/j.jafrearsci.2015.05.006
- Ghobadi, M. H., and Babazadeh, R. (2015). Experimental studies on the effects of cyclic freezing-thawing, salt crystallization, and thermal shock on the physical and mechanical characteristics of selected sandstones. *Rock Mech. Rock Eng.* 48 (3), 1001–1016. doi:10.1007/s00603-014-0609-6
- Hou, R. B., Zhang, K., Tao, J., Xue, X. R., and Chen, Y. L. (2019). A nonlinear creep damage coupled model for rock considering the effect of initial damage. *Rock Mech. Rock Eng.* 52 (5), 1275–1285. doi:10.1007/s00603-018-1626-7
- Li, J. L., Kaunda, R. B., and Zhou, K. P. (2018). Experimental investigations on the effects of ambient freeze-thaw cycling on dynamic properties and rock pore structure deterioration of sandstone. *Cold Regions Sci. Technol.* 154, 133–141. doi:10.1016/j.coldregions.2018.06.015
- Li, X., Li, Q., Hu, Y., Teng, L., and Yang, S. (2021). Evolution characteristics of mining fissures in overlying strata of stope after converting from open-pit to underground. *Arabian J. Geosciences* 14 (24), 2795. doi:10.1007/s12517-021-08978-0
- Li, X., Peng, J., Xie, Y., Li, Q., Zhou, T., Wang, J., et al. (2022). Influence of high-temperature treatment on strength and failure behaviors of a quartz-rich sandstone under true triaxial condition. *Lithosphere* 2022 (10). doi:10.2113/2022/3086647
- Liu, C. J., Wang, D. G., Wang, Z. X., Ke, B., Li, P., and Yu, S. T. (2021a). Dynamic splitting tensile test of granite under freeze-thaw weathering. *Soil Dyn. Earthq. Eng.* 140, 106411. doi:10.1016/j.soildyn.2020.106411
- Liu, X. Y., Liu, L. L., Li, Z., and Yao, Z. M. (2021b). Experimental analysis on creep properties of frozen silty mudstone considering conservation of energy. *J. Test. Eval.* 49 (1), 417–434. doi:10.1520/JTE20180707
- Lu, X., Zhou, W., Cai, Q., Li, M., Luan, B., and Liu, F. (2021). Mechanical properties and meso fracture mechanism of mudstone under freeze-thaw cycle. *J. Min. Saf. Eng.* 38 (04), 819–829. doi:10.13545/j.cnki.jmse.2020.0633
- Mardoukhi, A., Mardoukhi, Y., Hokka, M., and Kuokkala, V. T. (2021). Effects of test temperature and low temperature thermal cycling on the dynamic tensile strength of granitic rocks. *Rock Mech. Rock Eng.* 54 (1), 443–454. doi:10.1007/s00603-020-02253-6
- Nikolenko, P. V., Epshtein, S. A., Shkuratnik, V. L., and Anufrenkova, P. S. (2021). Experimental study of coal fracture dynamics under the influence of cyclic freezing-thawing using shear elastic waves. *Int. J. Coal Sci. Technol.* 8 (4), 562–574. doi:10.1007/s40789-020-00352-x
- Shan, R. L., Bai, Y., Ju, Y., Han, T. Y., Dou, H. Y., and Li, Z. L. (2021). Study on the triaxial unloading creep mechanical properties and damage constitutive model of red sandstone containing a single ice-filled flaw. *Rock Mech. Rock Eng.* 54 (2), 833–855. doi:10.1007/s00603-020-02274-1
- Shen, W. L., Shi, G. C., Wang, Y. G., Bai, J. B. A., Zhang, R. F., and Wang, X. Y. (2021). Tomography of the dynamic stress coefficient for stress wave prediction in sedimentary rock layer under the mining additional stress. *Int. J. Min. Sci. Technol.* 31 (4), 653–663. doi:10.1016/j.ijmst.2021.04.003
- Song, D., Wang, E., Li, Z., Liu, J., and Xu, W. (2015). Energy dissipation of coal and rock during damage and failure process based on EMR. *Int. J. Min. Sci. Technol.* 25 (05), 787–795. doi:10.1016/j.ijmst.2015.07.014
- Ulrich, T. J., and Darling, T. W. (2001). Observation of anomalous elastic behavior in rock at low temperatures. *Geophys. Res. Lett.* 28(11), 2293–2296. doi:10.1029/2000gl012480
- Wang, C., Li, S., Zhang, T., and You, Z. (2019). Experimental study on mechanical characteristics and fracture patterns of unfrozen/freezing saturated coal and sandstone. *Materials* 12 (6), 992. doi:10.3390/ma12060992
- Wang, F., Wang, H. B., Xu, Y., Cheng, B., and Wang, Q. Q. (2021). Analysis of energy dissipation characteristics of damaged sandstone under impact load. *Shock Vib.* 2021, 1–10. doi:10.1155/2021/4200452
- Wang, L., Qin, Y., Jia, H. B., Su, H. M., and Chen, S. G. (2020). Study on mechanical properties and energy dissipation of frozen sandstone under shock loading. *Shock Vib.* 2020, 1–12. doi:10.1155/2020/8893128
- Wang, P., Xu, J. Y., Fang, X. Y., and Wang, P. X. (2017). Energy dissipation and damage evolution analyses for the dynamic compression failure process of red-sandstone after freeze-thaw cycles. *Eng. Geol.* 221, 104–113. doi:10.1016/j.enggeo.2017.02.025
- Wang, P., Xu, J. Y., Liu, S., Wang, H. Y., and Liu, S. H. (2016). Static and dynamic mechanical properties of sedimentary rock after freeze-thaw or thermal shock weathering. *Eng. Geol.* 210, 148–157. doi:10.1016/j.enggeo.2016.06.017
- Wang, L., Wu, Z. J., Liu, Q. S., Chu, Z. F., and Zhang, S. L. (2021). Evolutions of the unfrozen water content of saturated sandstones during freezing process and the freeze-induced damage characteristics. *Int. J. Rock Mech. Min. Sci.* 142, 104757. doi:10.1016/j.ijrmms.2021.104757
- Wang, L., Wu, Z. J., and Liu, Q. S. (2020). Dynamic mechanical properties of dry and water-saturated siltstones under sub-zero temperatures. *Rock Mech. Rock Eng.* 53 (10), 4381–4401. doi:10.1007/s00603-019-02039-5
- Wang, L., Wu, Z. J., and Liu, Q. S. (2019a). Evaluating damage and microcracking behavior of granite using NMR testing under different levels of unconfined compression. *Int. J. Geomechanics* 19 (1). doi:10.1061/(ASCE)GM.1943-5622.0001335
- Wang, L., Wu, Z. J., Liu, Q. S., and Wang, Z. Y. (2019b). Energy dissipation and dynamic fragmentation of dry and water-saturated siltstones under sub-zero temperatures. *Eng. Fract. Mech.* 220, 106659. doi:10.1016/j.engfracmech.2019.106659
- Wu, H., Chen, Y., Lv, H., Xie, Q., Chen, Y., and Gu, J. (2022). Stability analysis of rib pillars in highwall mining under dynamic and static loads in open-pit coal mine. *Int. J. Coal Sci. Technol.* 9 (1), 38. doi:10.1007/s40789-022-00504-1
- Xie, H., Li, L., Peng, R., and Ju, Y. (2009). Energy analysis and criteria for structural failure of rocks. *J. Rock Mech. Geotechnical Eng.* 1 (01), 11–20. doi:10.3724/sp.j.1235.2009.00011
- Yang, R. S., Li, W. Y., and Yue, Z. W. (2020). Comparative study on dynamic mechanical properties and energy dissipation of rocks under impact loads. *Shock Vib.* 2020, 1–15. doi:10.1155/2020/8865099
- Yang, Y., Zhang, N. N., and Wang, J. G. (2021b). A study on the dynamic strength deterioration mechanism of frozen red sandstone at low temperatures. *Minerals* 11 (12), 1300. doi:10.3390/min11121300
- Yang, Y., Zhang, N. N., and Wang, J. G. (2021a). Fracture morphology analysis of frozen red sandstone under impact. *Shock Vib.* 2021, 1–12. doi:10.1155/2021/4388132
- Zhang, Z. X., Kou, S. Q., Jiang, L. G., and Lindqvist, P. A. (2000). Effects of loading rate on rock fracture: Fracture characteristics and energy partitioning. *Int. J. Rock Mech. Min. Sci.* 37(5), 745–762. doi:10.1016/S1365-1609(00)00008-3
- Zhao, H., Tian, Y., Guo, Q., Li, M., and Wu, J. (2020). The slope creep law for a soft rock in an open-pit mine in the Gobi region of Xinjiang, China. *Int. J. Coal Sci. Technol.* 7 (2), 371–379. doi:10.1007/s40789-020-00305-4
- Zhou, L., Niu, C. Y., Zhu, Z. M., Ying, P., Dong, Y. Q., and Deng, S. (2020). Fracture properties and tensile strength of three typical sandstone materials under static and impact loads. *Geomechanics Eng.* 23 (5), 467–480. doi:10.12989/gae.2020.23.5.467
- Zhu, W. C., Li, S. H., Li, S., and Niu, L. L. (2019a). Influence of dynamic disturbance on the creep of sandstone: An experimental study. *Rock Mech. Rock Eng.* 52 (4), 1023–1039. doi:10.1007/s00603-018-1642-7
- Zhu, Z. Y., Luo, F., Zhang, Y. Z., Zhang, D. J., and He, J. L. (2019b). A creep model for frozen sand of Qinghai-Tibet based on Nishihara model. *Cold Regions Sci. Technol.* 167, 102843. doi:10.1016/j.coldregions.2019.102843





## OPEN ACCESS

## EDITED BY

Danqi Li,  
Curtin University, Australia

## REVIEWED BY

Jianhang Chen,  
China University of Mining and  
Technology, Beijing, China  
Saisai Wu,  
Xi'an University of Architecture and  
Technology, China

## \*CORRESPONDENCE

Chenlong Qian,  
✉ [chenlong\\_qian@163.com](mailto:chenlong_qian@163.com)

## SPECIALTY SECTION

This article was submitted to  
Environmental Informatics  
and Remote Sensing,  
a section of the journal  
Frontiers in Earth Science

RECEIVED 09 January 2023

ACCEPTED 10 February 2023

PUBLISHED 21 February 2023

## CITATION

Zhang Y, Qian C, Wang X, Chen X,  
Chang Z, Wang J and Niu Z (2023), Study  
on prevention and control mechanism of  
runoff water hazard in thick coal seam  
mining in valley terrain.  
*Front. Earth Sci.* 11:1140491.  
doi: 10.3389/feart.2023.1140491

## COPYRIGHT

© 2023 Zhang, Qian, Wang, Chen, Chang,  
Wang and Niu. This is an open-access  
article distributed under the terms of the  
[Creative Commons Attribution License  
\(CC BY\)](https://creativecommons.org/licenses/by/4.0/). The use, distribution or  
reproduction in other forums is  
permitted, provided the original author(s)  
and the copyright owner(s) are credited  
and that the original publication in this  
journal is cited, in accordance with  
accepted academic practice. No use,  
distribution or reproduction is permitted  
which does not comply with these terms.

# Study on prevention and control mechanism of runoff water hazard in thick coal seam mining in valley terrain

Yunfeng Zhang<sup>1,2</sup>, Chenlong Qian<sup>1\*</sup>, Xufeng Wang<sup>1,3,4</sup>,  
Xuyang Chen<sup>1</sup>, Zechao Chang<sup>1</sup>, Jiyao Wang<sup>1</sup> and Zhijun Niu<sup>1</sup>

<sup>1</sup>School of Mines, China University of Mining and Technology, Xuzhou, China, <sup>2</sup>Shangyuquan Coal Mine of Shanxi Luneng Hequ Electric Coal Development Co., Ltd., Xuzhou, China, <sup>3</sup>State Key Laboratory of Coal Resources and Safe Mining, China University of Mining and Technology, Xuzhou, Jiangsu, China, <sup>4</sup>Jiangsu Engineering Laboratory of Mine Earthquake Monitoring and Prevention, Xuzhou, Jiangsu, China

During the mining of thick coal seams under the gully slope, the mining-induced fractures are prone to connect with the gully runoff, which may induce potential water hazards and affect underground production. Based on the occurrence characteristics of coal seams and the landform in the gully-developed mining area, the coal seam mining under the slope of Na'er Coal Mine and Baoshan Coal Mine was taken as the engineering background, the seasonal runoff of gullies was considered as the influencing factors of the safe mining, and the spatial relationship between the working face and the gully slope was analyzed when the mining-induced fractures were connected with the gully surface and caused the gully runoff water disaster. The research results show that the occurrence structure of the gully slope has a greater impact on the strata movement of the slope. When the key layer is incomplete, the horizontal sliding and local block overturning of the slope rock strata are strong; when the key layer is complete, the horizontal sliding and local block overturning of the slope rock strata are weakened. According to the safety distance of the working face and the generalized model of safety coal pillar setting, the method of setting the safety coal pillar was used to prevent the connection of slipping cracks of the rock strata at the slope bottom and the gully surface during the slope mining, thus preventing the occurrence of runoff hazards during the thick coal seams mining in the valley terrain. The results can provide a theoretical basis and technical support for the prevention and control of seasonal runoff hazards, as well as a reference for the prevention and control of mining-induced landslides, water conservation mining, and ecological environment protection.

## KEYWORDS

valley terrain, rock strata evolution, mining-induced fractures, runoff water, water-conducting fracture zone

## 1 Introduction

Research on the overburden movement and fracture development characteristics caused by coal seam mining is the theoretical basis for safe and efficient mining in gully-developed mining areas. To ensure the normal shallow coal seam mining under the gully, researchers have revealed the impact of slope under the gully on the mining pressure of the stope (Liu et al., 2021). At the same time, some researchers have summarized the disaster-causing

mechanism of water disasters on the surface of coal mines (Gui et al., 2020). It is pointed out that seasonal rainfall and natural watercourses formed by valleys are the main factors of water inrush disasters in the mining process of shallow coal seams. To solve the problem of roadway water inrush and water conservation mining caused by the development of fracture zones (Zhang and López, 2019; Xie et al., 2021; Chen et al., 2022), Xie obtained five development stages of the water-conducting fracture zones. Besides, previous studies have shown that different mining methods (Du and Gao, 2017; Zhou and Yu, 2022), mining parameters (Wang et al., 2020; Qi et al., 2022) and repeated mining of coal seams (Tian et al., 2019; Cheng et al., 2020) also affect the development height of water-conducting fracture zones. Based on a large number of engineering practices, different numerical analysis models (Zhang et al., 2017; Zeng et al., 2022), mechanical theoretical models (Ning et al., 2020; Zhu et al., 2020; Yang et al., 2021; Tan et al., 2022) and monitoring methods (Wang et al., 2016; Mondal et al., 2020) have been successively introduced into the prediction and exploration of the height of water-conducting fracture zones. In addition, some researchers have effectively observed the development of water-conducting fracture zones from the perspective of strain energy (Swift, 2013; Qi et al., 2019; Sainoki et al., 2019).

In the existing studies, remarkable achievements have been made in the following aspects of the overburden movement and mining-induced fractures development characteristics, safe mining in gully-developed mining areas, and water protection (preservation) of gully water sources. However, there are still some limitations: 1) the influence of the geometry variability of the gully slope and the complexity of coal (rock) bed occurrence conditions on the overburden movement of the gully slope and the development of the mining-induced fracture is ignored; 2) the possible connection between advance fractures caused by mining-induced overburden movement and gully runoff is not fully considered. To this end, the mining of coal seams under the gully slope was taken as the engineering background, and the impact of seasonal runoff of the valley on safe mining was fully considered in this study. Based on the characteristics of overburden movement and fracture development of mining slopes with different occurrence structures, the main modes of strata movement of the slope rock, the basic manifestations and the main distribution areas of mining-induced fractures connecting the gully surface were analyzed, the basic modes, conditions and prediction methods that cause gully runoff water disasters were obtained, and the technical measures for prevention and control of runoff hazards caused by mining under gully slope were proposed.

## 2 Characteristics of engineering geology and hydrological environment

### 2.1 Characteristics of the occurrence structure of gully slope

In the mining area with valley terrain, the integrity of the overburden (soil layer) of the coal seam is damaged due to the cutting of the gully. For a typical shallow coal seam, there is only one main key layer in the overburden. With the increase of burial depth of coal seams and the change of overburden occurrence structure,

the number of key layers also increases in varying degrees. Since the contact layer between the gully slope and surface runoff on both sides of the gully is mainly located at the slope bottom, there are two types of gully slope with key layers at the slope bottom: ① rock strata with an incomplete key layer at the slope bottom; ② rock strata with a complete key layer at the slope bottom, as shown in Figure 1.

### 2.2 Hydrological environment characteristics

The coalfield in border areas of Shanxi, Northern Shaanxi Provinces and Inner Mongolia Autonomous Region was taken as the study area. The ecological environment of the study area is sensitive and fragile, and the hydrological environment also shows regional characteristics. In general, the study area has an arid semi-arid climate, with relatively scarce water resources, sparse vegetation, and low precipitation. The annual precipitation of this area is unevenly distributed, mainly from July to September. The precipitation in the rainy season (July–September) accounts for more than 50%–60% of the annual precipitation, as shown in Table 1.

In the gully-developed mining area, the atmospheric precipitation is mainly discharged along the valley in the form of surface runoff at the bottom of the gully. During the seasonal rainfall period, especially the concentrated rainfall, the precipitation is collected at the bottom of the gully under the conditions of valley terrain, forming seasonal rivers and even gully floods. When mining activities are conducted under the gully slope, the gully runoff will enter the slope along the crack pathway if the mining-induced fracture connects with the surface or bottom of the gully slope, as shown in Figure 2.

## 3 Fracture development characteristics of the slope during the mining under the gully

Based on the landform and geological conditions of two gully slopes encountered in the mining process of Na'er Coal Mine and Baoshan Coal Mine, the physical experimental models of similar materials for two types of gully slope structures were established, including geological models of gully slope with an incomplete key layer and that with a complete key layer (as shown in Figures 3, 4). Besides, the characteristics of overburden movement caused by mining activities under the gully slope were studied and analyzed, and the main types and manifestations of the slope under the mining were focused on.

### 3.1 Mining under the gully slope with an incomplete key layer

In terms of the overall development height of mining-induced fractures, under the geological condition of Na'er Coal Mine, mining-induced fractures develop to the surface, that is, there are only a caving zone and fracture zone on the vertical section of overburden. The heights of the caving zone and the fracture zone are about 23.4 m and 61.1 m, which are similar to those in the mining of typical shallow buried coal seams.

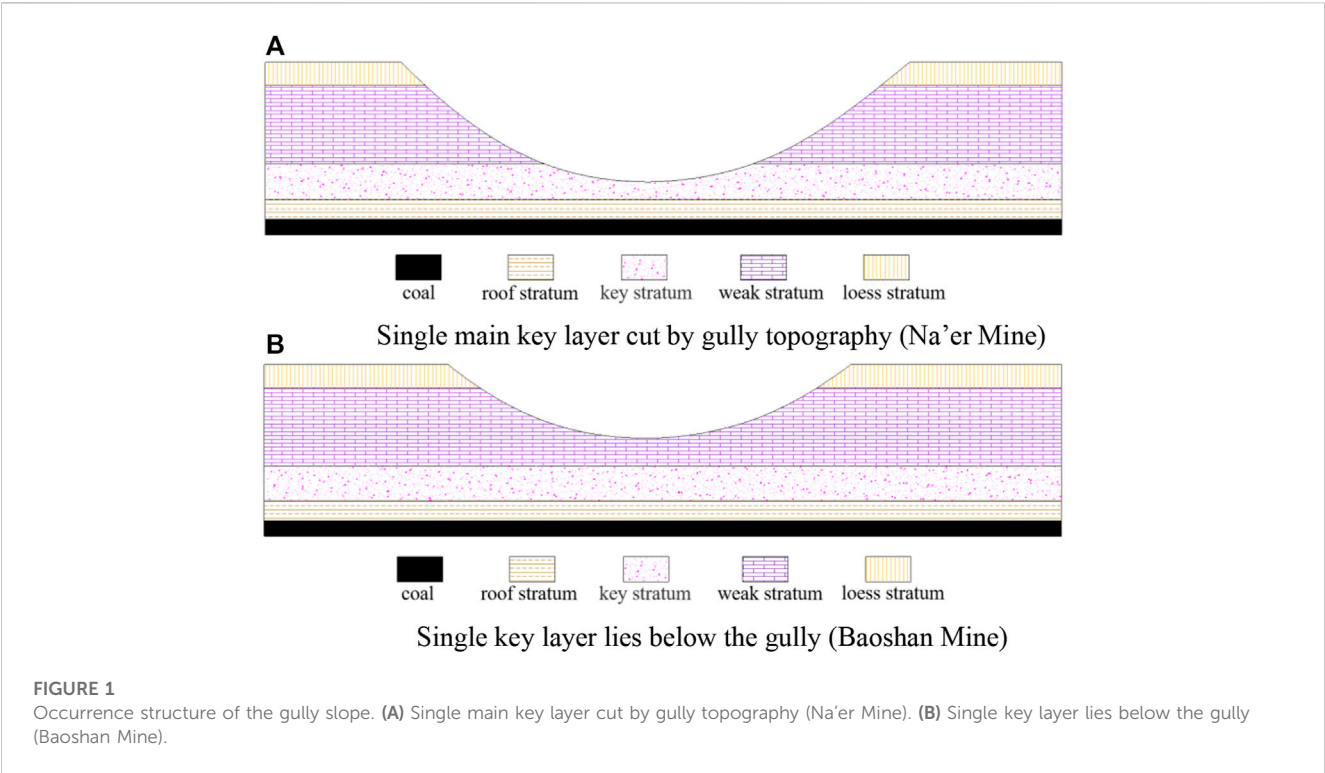


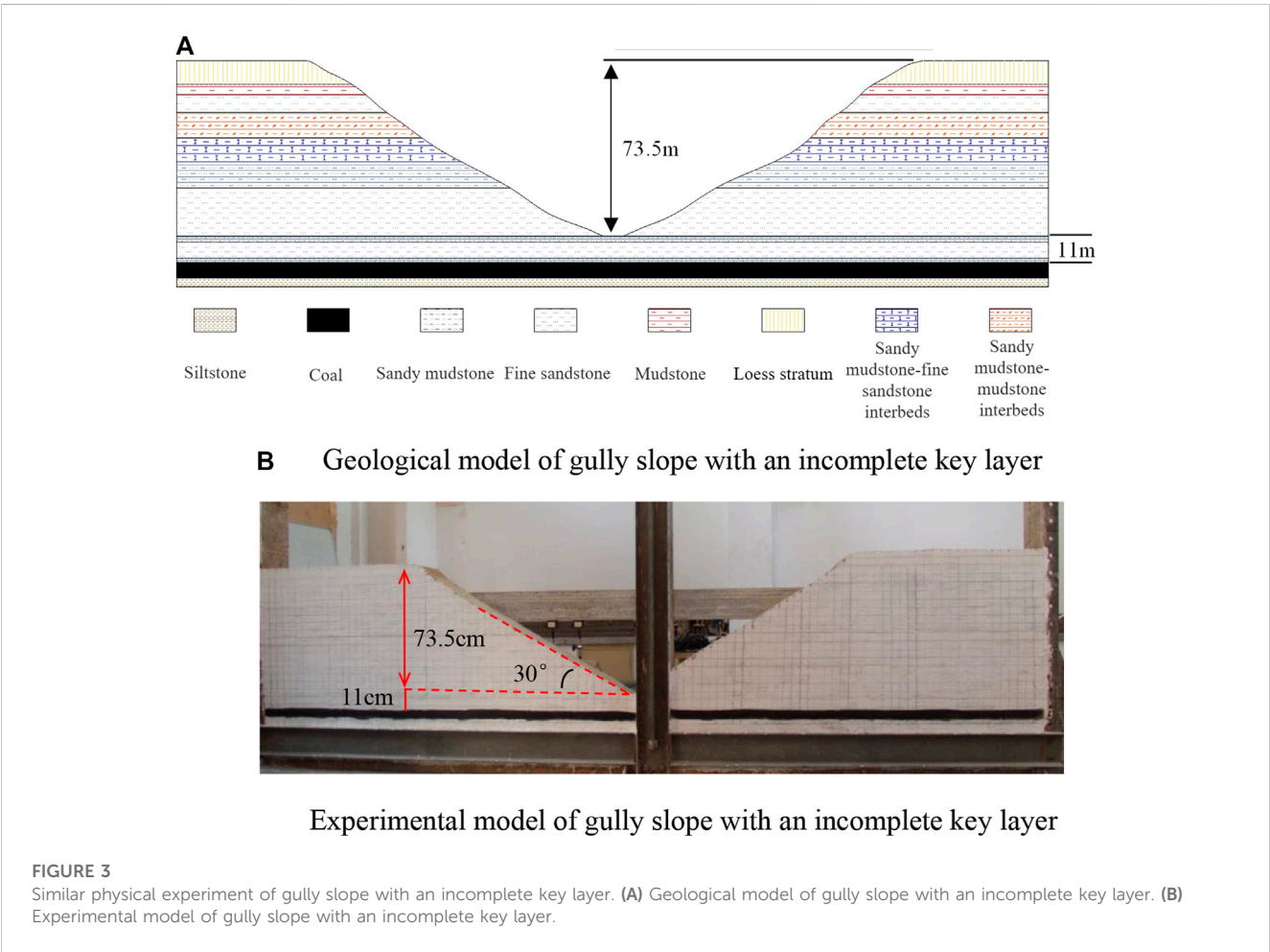
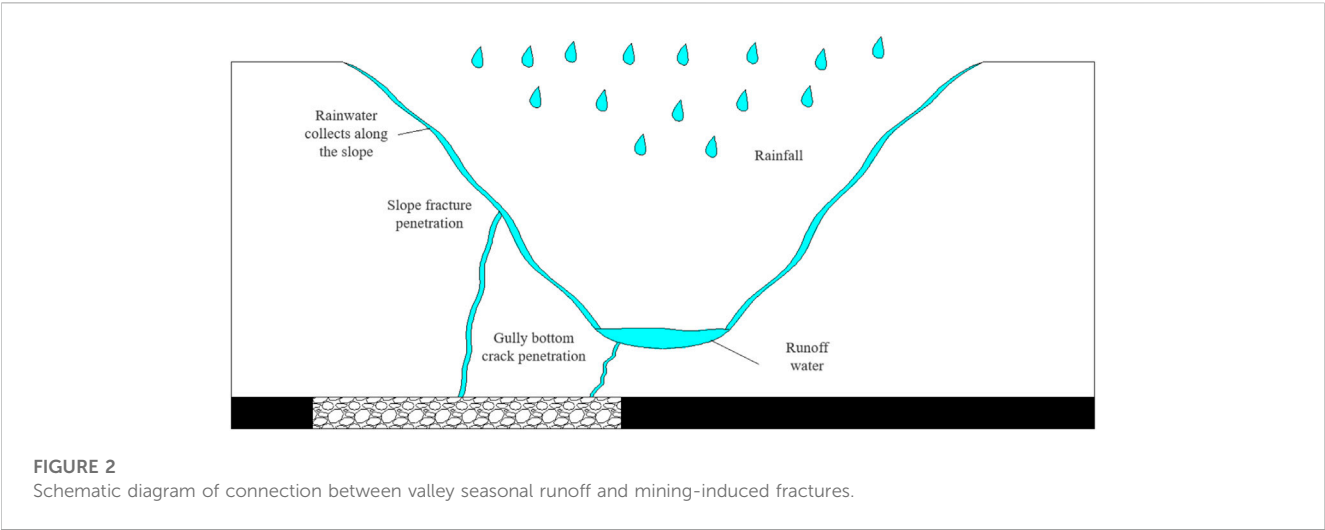
**TABLE 1** Precipitation statistics of some cities in the study area.

Region	January	February	March	April	May	June	July	August	September	October	November	December
Hejin	17.2	25.2	64.3	83.6	162	127.6	177.1	272.7	170.9	123.4	45.5	17.5
Shuozhou	6.2	10.3	52	72.2	101	117.4	210.6	195.3	152.8	57.6	39.5	11.4
Baode	10.5	11	47.3	85.8	89.2	127.6	280.1	231.4	138.6	83.4	23.2	16.9
Hequ	9.5	9.7	58.2	53.4	74.4	103.7	257.3	200.4	108.7	83.2	20.7	11
Yijinhuluo	6.5	10.3	44.6	51.7	88.3	106.7	240.4	284.2	113.1	63.9	17.3	9.5
Jungar	8	11.9	51.4	67	91.9	91.6	286	214.1	76	66.2	17.1	11.6
Qingshuihe	8.2	11.2	46.4	56.8	82.2	129.7	194.6	208.4	126	71	22.3	10.2
Shenmu	11.4	16.6	59.4	58.2	82	162.4	262.3	207.4	160.4	79.7	28.3	12.4
Yulin	12.3	10.8	62.7	58.7	99.9	156.1	169.2	276.4	140.5	103.9	32.6	10.4
Fugu	11.0	13.6	51.8	84.5	85.6	121.7	313.3	217.8	128.4	79.1	25.6	14.8

As shown in Figure 5, most of the adjacent areas collapse in layered form. The development height of mining-induced fractures in the adjacent area of the slope rises slowly, while it develops rapidly in the area below the slope. When the working face is advanced to 30 m, the roof begins to cave, and a small amount of longitudinal cracks is produced. When the working face is advanced to 60 m, there is a massive collapse of rock beneath the main roof, and cracks with different development degrees are generated. As the working face advances forward and enters the mining area below the gully, the collapsed strata continue to develop upward, and the cracks near the slope develop rapidly. When the working face is advanced to 160 m,

a large tensile crack appears at the upper part of the slope section because one side of the overburden of the working face is a free surface, and it continues to develop downward with the increase of mining space. When the working face is advanced to 190 m, the surface crack is connected with the longitudinal crack of overburden. During the whole mining process, the surface subsidence gradually deviates to the gully direction, and mining-induced fractures develop to the surface.

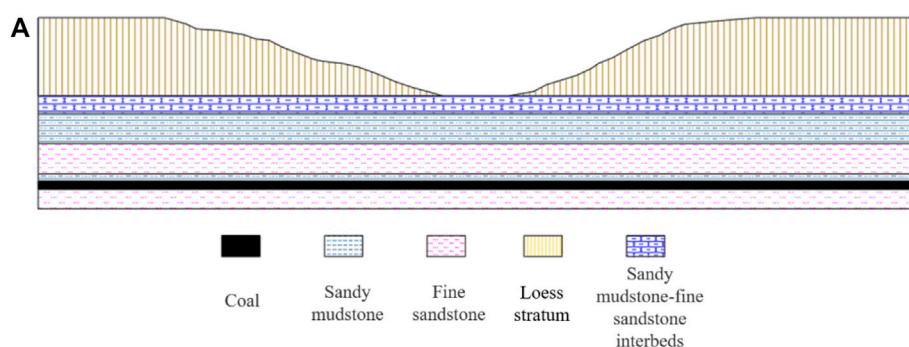
After coal seam mining, the development of mining-induced fractures and overburden movement are related and promote each other. The development and distribution characteristics of mining-induced fractures in overburden after mining are treated with digital



binarization, as shown in Figure 6. Besides, the shape and distribution of the mining-induced fractures in overburden are highly consistent with the overburden movement, which is mainly reflected in the following two aspects:

① During the mining toward the gully, separated layers or horizontally staggered cracks are the main mining-induced fractures in overburden, and there are some vertical cracks connecting separated layers or horizontally staggered cracks





Geological model of gully slope with a complete key layer (Baoshan Coal Mine)



Experimental model of gully slope with a complete key layer (Baoshan Coal Mine)

FIGURE 4

Similar physical experiment of gully slope with an incomplete key layer. (A) Geological model of gully slope with a complete key layer (Baoshan Coal Mine). (B) Experimental model of gully slope with a complete key layer (Baoshan Coal Mine).

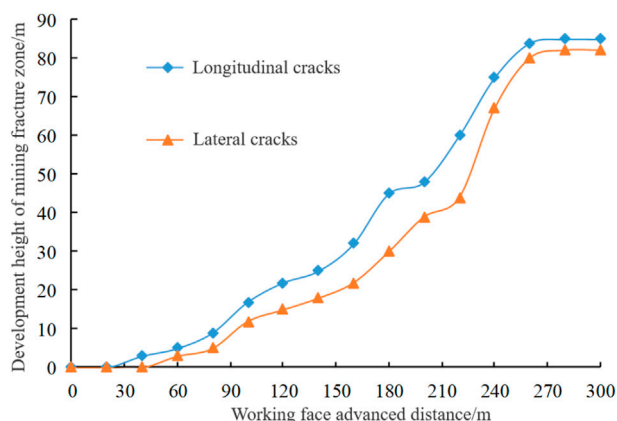


FIGURE 5

Development characteristics of Mining-induced Fractures in Na'er Coal Mine.

in different layers. The mining-induced fractures in the overburden of the Xianggou mining area are closely related and promote the overburden movement. This phenomenon is particularly obvious at the bottom of the slope. Consequently, the goaf below the slope bottom is directly connected with the gully bottom, with a large

degree of connectivity. The maximum width of the cracks is about 1.9 m. If there is perennial or seasonal surface runoff at the bottom of the gully, there will be a large risk of water inrush.

- ② During the mining backward the gully, tensile cracks are the main mining-induced fractures in overburden, which directly connect the goaf and the slope surface. The experimental results show that there are three large tensile cracks in the overburden of the slope area. The maximum width of the tensile cracks can reach 3.6 m and these cracks hardly close. As a result of the crack cutting, the overburden presents a massive structure, and the goaf is connected with the slope surface. If the surface runoff level at the bottom of the gully is large, it can also lead to a greater risk of water inrush.

### 3.2 Mining under the gully slope with a complete key layer

Figure 7 shows the development characteristics of mining-induced fractures under the conditions of the Baoshan Coal Mine. The overburden in the adjacent area is dominated by layered collapse. When the working face is advanced to 20 m, the strata directly under the immediate roof generate separation, and longitudinal cracks appear at both ends of the strata directly under the immediate roof simultaneously. When the working face is advanced to 30 m, the stratification phenomenon is intensified,



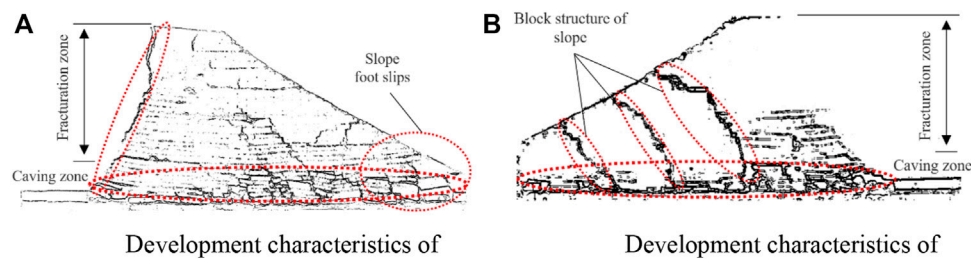


FIGURE 6

Final state of overburden fracture development in the slope model of Na'er Coal Mine during the mining under the gully. (A) Development characteristics of fractures during the mining toward the gully. (B) Development characteristics of fractures during the mining backward the gully.

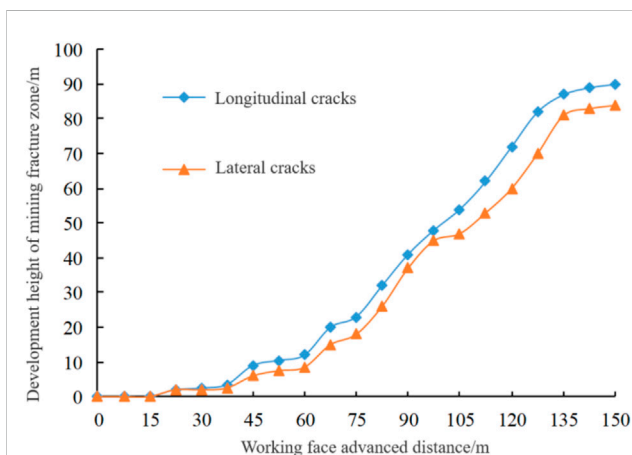


FIGURE 7

Development characteristics of mining-induced fractures in Baoshan coal mine.

and the crack in the immediate roof further increases and gradually extends to the coal wall. When the working face is advanced to 60 m, the rock strata under the main roof collapse in a large area, the separation layer between the direct roof and the basic roof increases, and the longitudinal cracks gradually become connected around. As the working face advances to the gully mining area, the crack development characteristics are similar to those of Na'er Coal Mine, and the cracks are gradually developed. When the working face is advanced to 110 m, the advanced tensile cracks are developed on the surface. When the working face is advanced to 140 m, the tensile crack is connected with the crack in the caving zone. When the working face advances to 160 m, new cracks are generated on the surface. As the working face advances, the longitudinal cracks gradually close and generate new tensile cracks. After the excavation of the working face, the cracks develop to the surface, and the development law of surface cracks is consistent with the activity law of periodic roof breaking.

As Baoshan Coal Mine is a typical shallow coal seam, there is only a single key layer in the bedrock, and the mining thickness of the coal seam is about 6 m. The development height of mining-induced fracture in the Baoshan Coal Mine is the same as that of the mining slope test in Na'er Coal mine. As shown in Figure 8, there are only two zones (the caving zone and fracture zone) on the vertical profile. The experimental

results show that the height of the caving zone is about 21.2 m, and the fracture zone is developed to the surface, with a height of about 68.8 m. The experimental results show that Baoshan Coal Mine has the following development and distribution characteristics of mining-induced fractures during the mining under the slope.

- ① During the mining toward the gully, overburden separation and staggered cracks are developed, and are penetrated by vertical cracks layer by layer. During the mining backward the gully, the vertical cracks are developed, and the separation and staggered cracks are only developed in the bedrock. Besides, the overburden mining-induced fractures during the mining of the Xianggou and Beigou are similar to those of Na'er Coal Mine. At the same time, it also shows that the overburden movement and the crack development characteristics during the coal seam mining toward and backward the gully slope have certain particularity and homogeneity.
- ② The mining-induced fractures of the slope are not directly connected with the goaf. After the coal seam is mined, the mining-induced fracture in overburden also develops to the surface (or gully surface). Different from the mining in the Na'er coal mine, after the mining under the slope of Baoshan coal mine, the slope cannot be directly involved in the roof movement of coal seam because the main key layer is still a certain distance (45 m) from the bottom of the gully. Combined with the buffering effect of the soft rock between the main key layer and the slope, the mining-induced fractures in the slope area do not directly connect with the goaf, but indirectly connect with the goaf through the mining-induced fractures in the rock layer under the slope.

### 3.3 Prediction of mining-induced fracture development height in overburden

The physical simulation experiment shows that when the development height of mining-induced fractures develops to the slope, the slope rock strata directly or indirectly participate in the roof activities of the coal seam, resulting in the unique strata movement of the slope rock and the characteristics of crack development. When applying the key layer theory to analyze the development height of the water-conducting fractures in overburden, it is generally believed that if the key layer is broken, the rock strata

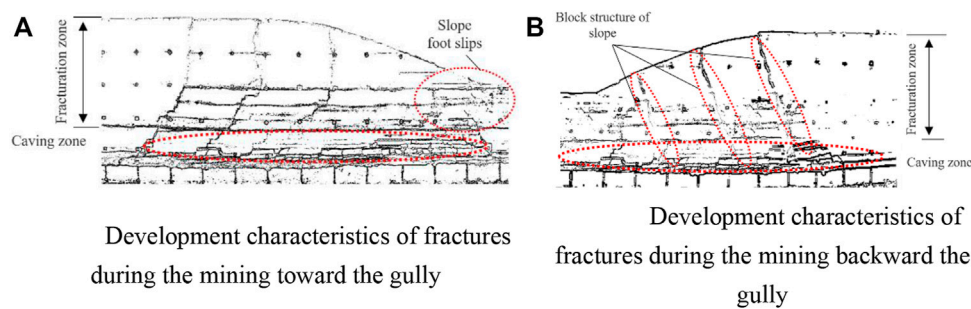


FIGURE 8

Final state of overburden fracture development in the slope model of Baoshan Coal Mine during the mining under the gully. (A) Development characteristics of fractures during the mining toward the gully. (B) Development characteristics of fractures during the mining backward the gully.

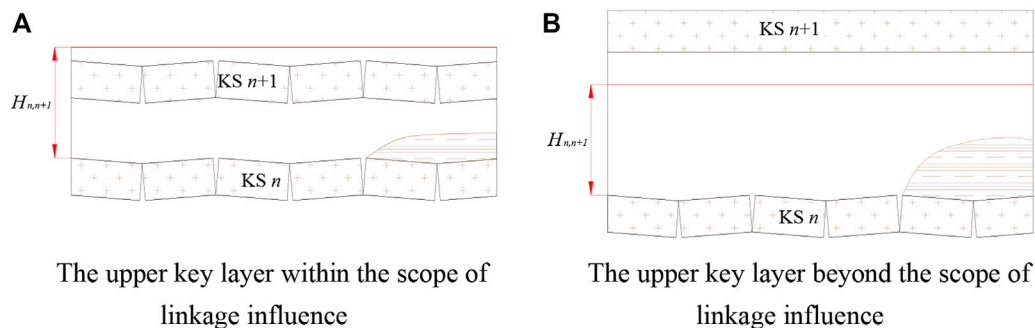


FIGURE 9

Linkage influence height of key layers. (A) The upper key layer within the scope of linkage influence. (B) The upper key layer beyond the scope of linkage influence.

controlled by the key layer will be broken successively, and the mining-induced fractures will penetrate the strata under their control. The coal seam produces relatively large space after mining, and the roof strata have a certain dilatancy after caving and can reduce the free space under the key layer. Nevertheless, if the lower key layer is broken and the higher key layer still reaches the breaking condition, the cracks will pass through the higher key layer and continue to develop upward, leading to the increase in the height of mining-induced fractures, as shown in Figure 9.

According to whether there is free space below the key layer, the spatial position of the key layer to be broken can be analyzed. It is assumed that  $H'_{i-1,i}$  is the actual thickness of the rock stratum between the key layers  $i-1$  and key layer  $i$ ;  $k_{i-1,i}$  is the crushing expansion coefficient of the rock stratum between the key layers  $i-1$  and key layer  $i$ ;  $h_i$  is the thickness of the key layer  $i$ ;  $H'_{0,1}$  and  $k_{0,1}$  are the actual thickness and the crushing expansion coefficient of the rock stratum between the coal seam and key layer 1. Therefore, Eq. 1 can be obtained as follows:

$$H_{n,n+1} = \begin{cases} \frac{m - H'_{0,1}(k_{0,1} - 1)}{(k_{1,2} - 1)} - h_1, & (n = 1) \\ \frac{m - H'_{0,1}(k_{0,1} - 1) - \sum_{i=1}^{n-1} (h_i + H'_{i,i+1})(k_{i,i+1} - 1)}{(k_{n,n+1} - 1)} - h_n, & (n > 1) \end{cases} \quad (1)$$

Besides,  $H_{n,n+1}$  is defined as the spatial linkage influence height of the key layer breaking (referred to as the linkage height of the key layer). The linkage height is explained as follows: after key layer  $n$  is broken, if its upper adjacent key layer (key layer  $n+1$ ) is within the linkage height range, it can cause the breakage of key layer  $n+1$ , as shown in Figure 9A. Otherwise, as there are enough thick rock layers with strong deformation resistance between the two key layers, the breakage of key layer  $n$  cannot cause the breakage of key layer  $n+1$ , as shown in Figure 9B. Due to the linkage height of the key layer, when the relative spatial position of the key layer in overburden meets the conditions, the breakage of the lower key layer can induce the breakage of the adjacent key strata, thus resulting in the breakage of the upper key layer. When mining-induced fractures pass through the upper key layer, the mining-induced fractures continue to develop upward in overburden.

#### 4 The influence of slope occurrence and mining conditions on the development of mining-induced fractures in overburden

The change of slope occurrence and mining conditions of coal seams will greatly affect the movement of the gully slope and the crack development. In this section, the discrete element program

TABLE 2 Basic slope models.

Slop models	Number of key layers	Integrity of key layers	Buried depth seams H/m	Slope angle $\alpha/^\circ$	Slope height h0/m	Mining height M/m
I	1	Complete	90	30	60	6
II	1	Incomplete	105			

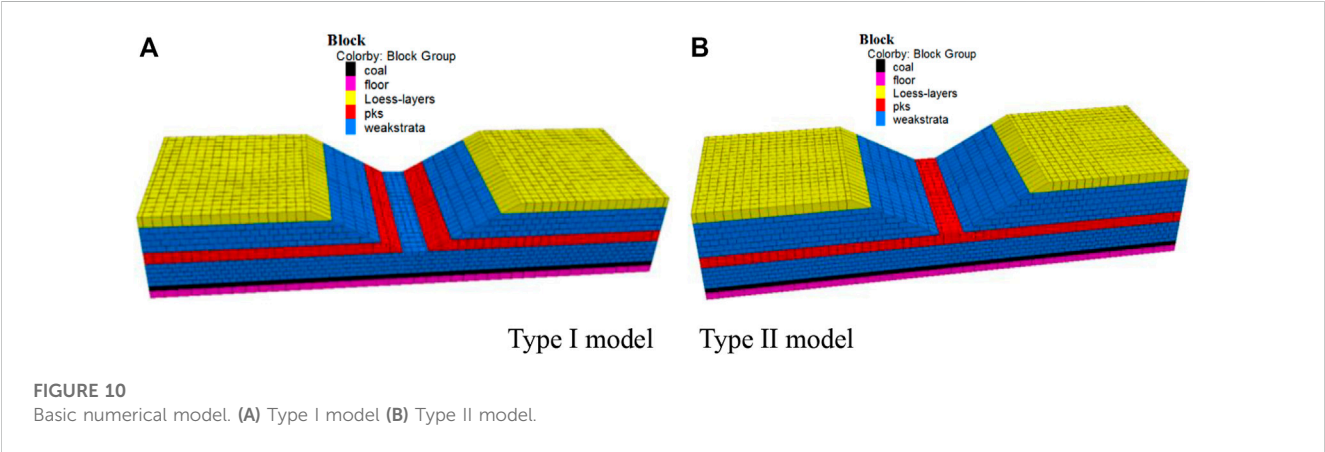


TABLE 3 Experimental model scheme for Class I slope.

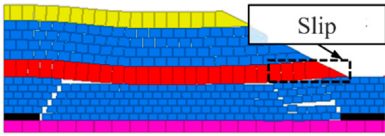
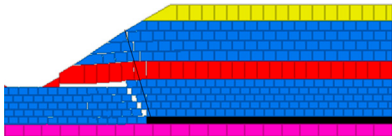
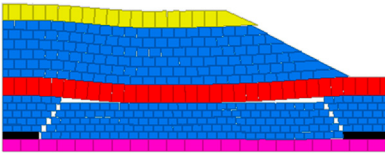
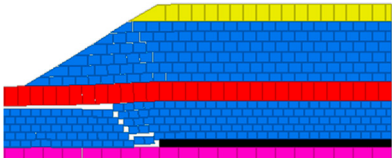
Factor variable	Scheme No.	Slope angle $\alpha/^\circ$	Maximum burial depth of coal seam H/m	Slope height $h_0/m$	Mining height M/m
Slope angle	I-SA20	20	90	60	6
	I-SA30	30			
	I-SA40	40			
	I-SA50	50			
Slope height	I-SH40	30	70	40	6
	I-SH60		90	60	
	I-SH80		110	80	
	I-SH100		130	100	
Mining height	I-MH4	30	90	60	4
	I-MH6				6
	I-MH8				8
	I-MH10				10
Buried depth of coal seam (F7)	I-BH90	30	150	60	6
	I-BH60		120		
	I-BH30		90		

3DEC was used to conduct numerical simulation experiments, and the influencing factors (slope angle, slope height, coal seam mining thickness, burial depth of gully bottom) on the movement and destruction of the overburden of the gully slope with two structural types, namely, the absence of key layers and the integrity of the sequence, It lays a foundation for the prevention and control of gully

TABLE 4 Experimental model scheme for Class II slope.

Factor variable	Scheme No.	Slope angle $\alpha/^{\circ}$	Maximum burial depth of coal seam H/m	Slope height $h_0$ /m	Mining height M/m
Slope angle	II-SA20	20	105	60	6
	II-SA30	30			
	II-SA40	40			
	II-SA50	50			
Slope height	II-SH40	30	85	40	6
	II-SH60		105	60	
	II-SH80		125	80	
	II-SH100		145	100	
Mining height	II-MH4	30	105	60	4
	II-MH6				6
	II-MH8				8
	II-MH10				10
Buried depth of coal seam (F7)	II-BH105	30	165	60	6
	II-BH75		135		
	II-BH45		105		

TABLE 5 Characteristics of overburden movement and failure in the basic model.

	Advancing 190 m	Advancing 370 m
Class I slope		
Class II slope		

runoff. Based on the two models and the analysis results of slope occurrence characteristics in Section 3, the actual typical slope of Na’er Coal Mine was taken as a reference. In the above two slope models, the slope angle was set as 30°, the slope height as 60 m, and the coal seam mining thickness as 6 m. Table 2 shows test schemes of the basic slope model, and Figure 10 shows the numerical model. Based on the test schemes of the two slope models, the simulation schemes for the influence characteristics of main factors are formulated as shown in Tables 3, 4.

In this section, according to the main influencing factors of mining under the slope, the slope terrain and the occurrence conditions of coal and rock, based on the 3DEC discrete element program, a total of 26 slope numerical models of nine groups of two types have been established, simulation experiments have been carried out, Table 5 and

the fitting formulas between the horizontal safety distance from the working face of Class I and Class II mining slope to the slope bottom and the slope angle, slope height, and the minimum buried mining ratio at the gully bottom have been obtained, as shown in Figure 11.

The analysis results show that: 1) the changes of slope angle, slope height, coal seam mining height and buried depth of gully bottom coal seam have different degrees of influence on the Class I slope model (with an incomplete key layer) and Class II slope model (with a complete key layer). The experimental results show that the damage degree of slope rock with an incomplete key layer is more significant. 2) Under the same slope structure type, the response degree of slope rock strata movement and failure to the four influencing factors (slope angle, slope height, coal seam mining height, and coal seam burial depth of gully bottom) is different. The

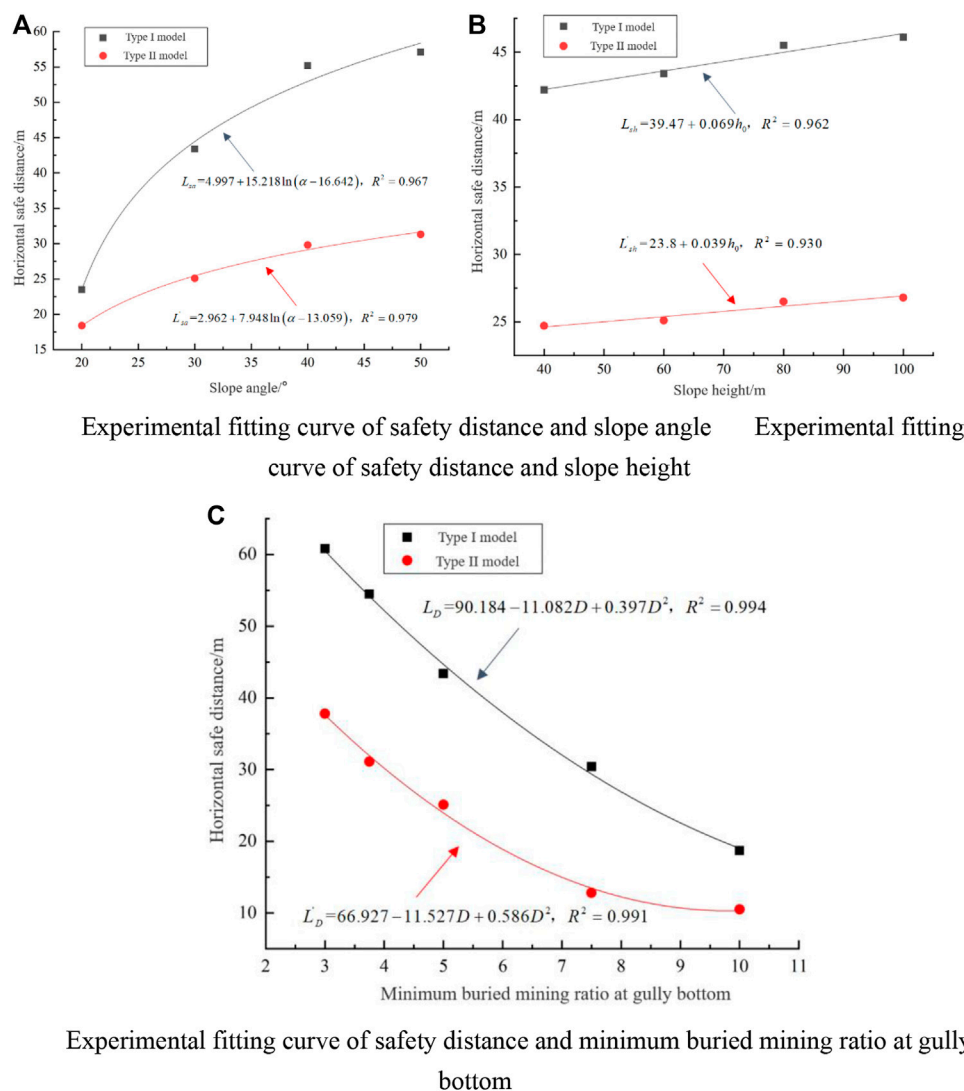


FIGURE 11

Safe distance of working face under different slope parameters. (A) Experimental fitting curve of safety distance and slope angle (B) Experimental fitting curve of safety distance and slope height. (C) Experimental fitting curve of safety distance and minimum buried mining ratio at gully bottom.

larger the slope angle, coal seam mining height, and slope height, the more significant the influence on strata movement and failure of the slope rock, while the influence degree of slope height is relatively weaker than that of slope angle and mining height. The larger the coal seam buried at the bottom of the gully, the smaller the strata movement and damage degree of the slope rock.

## 5 Prevention and control measures for water hazard of valley runoff during coal seam mining under the slope

### 5.1 Conditions of gully runoff water hazard caused by mining under slope

Due to the different engineering geology and technical conditions of coal seam mining, the mining-induced damage

degree and scope of rock strata in the slope are different. Based on the previous research on the mining of coal seams under the gully slope, the conditions that cause the water inrush hazard of gully runoff during the slope mining can be summarized as follows: 1) water source conditions 2) catchment channel conditions 3) water inrush pathway conditions (as shown in Figure 12). When the conditions of water source, catchment channel and water inrush pathway are reached together, the gully runoff will pose a threat to safe mining when the working face is advanced under the gully slope. In addition, due to the fragile ecological environment in the gully development area and the scarcity of surface runoff, the gully runoff is the main water source for surface vegetation and animal husbandry activities. Therefore, mining under the slope not only causes dangerous mining production, but also damages the ecological environment of the gully runoff basin, even causes the cutoff of downstream rivers.



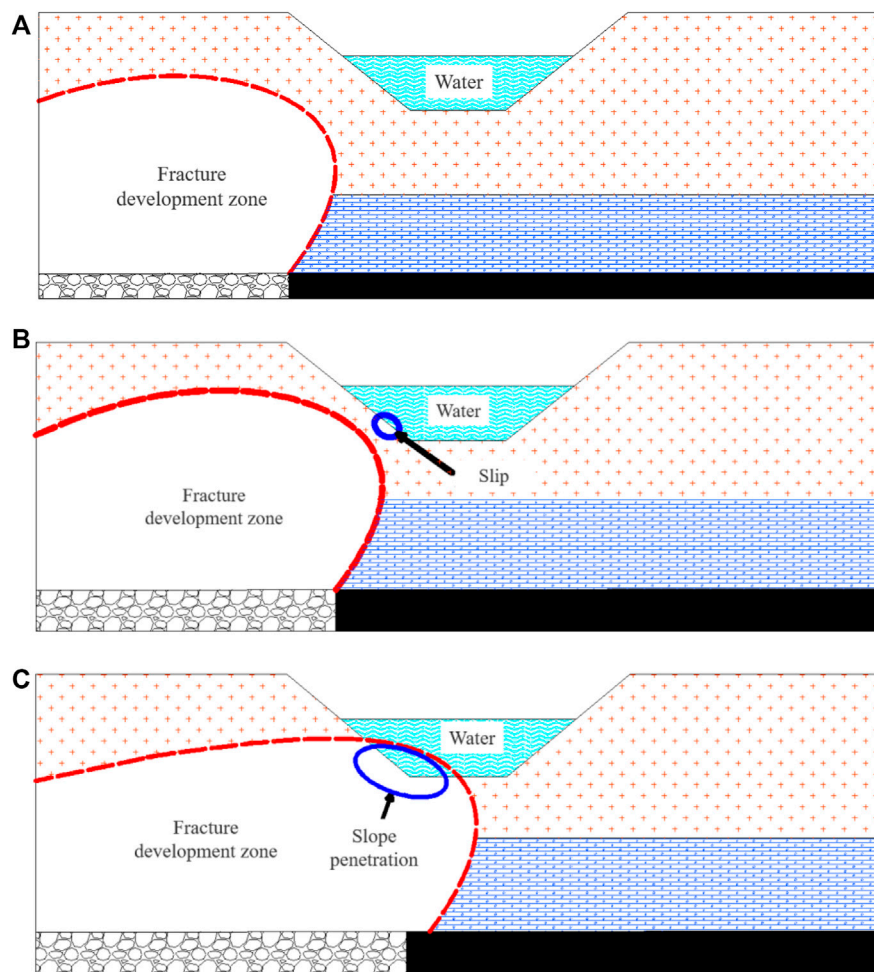


**FIGURE 12**  
Development process of mining-induced fractures. (A) Early stage of cross-gully mining (B) Interim stage of cross-gully mining (C) Late stage of cross-gully mining.

## 5.2 Setting of safety protection pillar for mining under slope

Through the experimental analysis of the movement characteristics of the mining slope, when the development height of mining-induced fractures in overburden ( $H_{\max}$ ) after coal mining is greater than the burial depth of the coal seam ( $h_b$ ) at the gully bottom, the overburden movement of the slope are obviously different from those of conventional mining, and the  $K_{\max}$  can be calculated as follows:

$$K_{\max} = \frac{H_{\max}}{h_b} \quad (2)$$

If  $K_{\max} < 1$ , the mining-induced fracture of overburden in the slope has not developed to the bottom of the gully. The slope is located in the bending subsidence zone, which belongs to the subsidence deformation mining slope, and the surface water at the bottom of the gully is not connected with the fractured zone. In addition, when there is a certain thickness of rock (soil) protective layer under the gully bottom, the seasonal surface

runoff of the valley poses a small threat to the safety of coal mining below.

If  $K_{\max} \geq 1$ , the development height of mining-induced fractures in the overlying strata of the slope is above the gully bottom. When the burial depth of the coal seam is shallow, the mining-induced fracture can develop to the surface. The slope-valley system is seriously affected by mining and belongs to the fractured mining slope. When the height of the caving zone is greater than the burial depth of the coal seam at the gully bottom, the slope-valley system is more seriously affected by mining. Part of the rock strata at the lower slope will collapse, forming the caved mining slope. Whether it is a fractured or caved mining slope, the surface water at the bottom of the gully will be connected with the fracture zone, threatening the safety of the working face.

In the actual mining process, only the coal seam mining factors are fixed, the valley shape, overburden structure combination, hydrogeology and other characteristics are changeable. Based on the simulation results, a generalized model of safety coal pillar setting under the slope is established, as shown in Figure 13, and the following simplified assumptions are made:

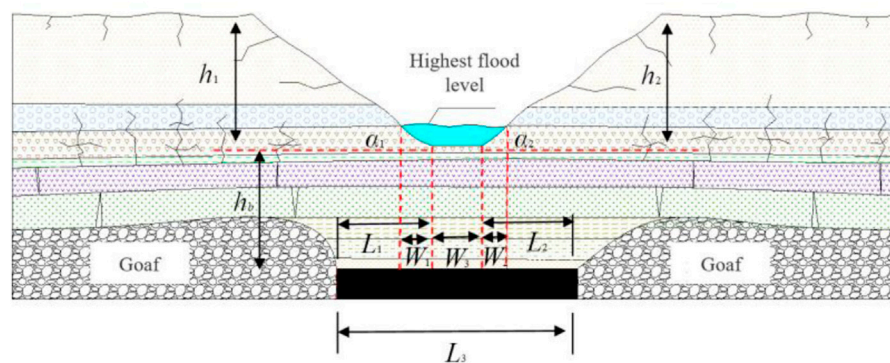


**FIGURE 13**  
Generalization Model of safety coal pillar for Mining under Slope.

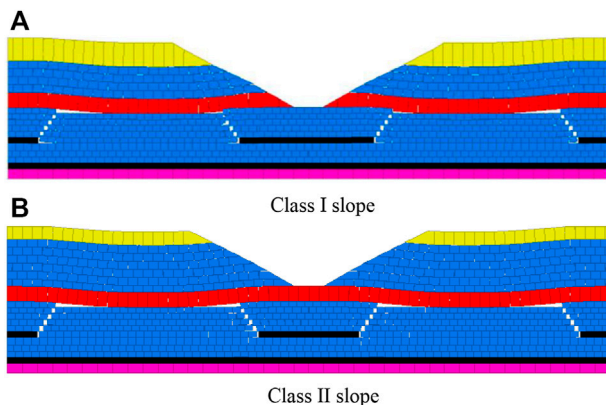


**FIGURE 14**  
Overburden evolution characteristics with safety pillar. (A) Class I slope. (B) Class II slope.

- (1) The gully bottom is the flat bottom interface of surface runoff, and the upper boundary of the water body is determined according to the highest flood level in history.
- (2) The overburden and rock strata at the bottom of the slope are horizontal layers.
- (3) In the advancing process from the adjacent area to the slope, the development height of mining-induced fractures in overburden has exceeded the bottom surface of valley surface runoff.

In Figure 13,  $v$  is the vertical height from the gully bottom interface to the mining seam roof;  $\alpha_1$  and  $\alpha_2$  are the slope angles of the slopes on both sides of the valley;  $W_1$  and  $W_2$  are the horizontal widths of the water body overflowing the slope bottom on both sides of the valley when the valley surface runoff reaches the highest flood level;  $W_3$  is the valley width;  $L_1$  and  $L_2$  refer to the horizontal safe distance between the working face and the slope bottom when mining the coal seam under the slope, and  $L_3$  refers to the width of the waterproof protective coal pillar.

According to the generalized model of safety coal pillar setting for mining under the slope, the most important thing is to determine the width of the safety coal pillar ( $L_3$ ) for gully runoff. To prevent the connection of the gully surface and overburden mining-induced fractures through horizontal slipping cracks at the rock stratum at the slope bottom, there is a safe distance between the working face and the slope. The safe distance of the working face is taken as the index to determine the  $L_3$ . The overburden movement and mining-induced fracture development characteristics of coal seam mining under slope are the comprehensive results of various influencing factors. In this study, the influence characteristics of four main factors on overburden movement and mining-induced fracture development are analyzed, and the single factor expression between the main factors and the safety distance is fitted based on the results of numerical simulation. To ensure the safety and reliability of the fitting, the maximum value calculated by the above three fitting formulas is taken as the safety distance of the working face. It is assumed that the working face under the gully slope on both sides of the gully is mined towards the gully. According to the gully topography and the generalization model of safety coal pillar width under gully surface runoff in Figure 13, the above analysis of the safety distance is considered, and the width of the safety coal pillar ( $L_3$ ) can be expressed as follows:

① Class I slope:

$$L_3 = \max \{L_{a1}, L_{h1}, L_D\} + \max \{L_{a2}, L_{h2}, L_D\} + W_3 + W_2 + W_1 \quad (3)$$

② Class II slope

$$L_3 = \max \{L'_{a1}, L'_{h1}, L'_D\} + \max \{L'_{a2}, L'_{h2}, L'_D\} + W_3 + W_2 + W_1 \quad (4)$$

The precondition for water hazard threat caused by gully runoff is that the development height of mining-induced fractures has exceeded the gully bottom interface, that is,  $K_{\max} \geq 1$ . Although local block overturning of the slope will produce reverse fractures to connect with the gully surface during the mining backward the gully, the areas of local block overturning of the slope mainly occur in the middle and upper parts of the slope, and the vertical distance from the gully bottom is large. Therefore, reverse fractures are not the

main channel for gully runoff water inrush. Therefore, referring to the Code for coal pillar retention and coal mining in buildings, water bodies, railways and main shafts, the width of the protective coal pillar can be designed according to the rock movement angle  $\delta$  during the mining backward the gully.

Assuming that there are gully slopes on both sides of the valley, the mining toward the gully is conducted for one side, and the mining backward the gully is conducted for the other side. According to the generalized model of safety coal pillar width established in Figure 13, the safety coal pillar width  $L_3$  can be expressed as:

① Class I slope:

$$L_3 = \max \{L_{a1}, L_{h1}, L_D\} + (h_w + h_b) \cot \alpha_2 + W_3 + W_2 + W_1 \quad (5)$$

② Class II slope

$$L_3 = \max \{L'_a, L'_{h1}, L'_D\} + (h_w + h_b) \cot \alpha_2 + W_3 + W_2 + W_1 \quad (6)$$

where  $L_a$  is the safety distance based on the change of slope angle of Class I slope model, m;

$L'_a$  is the safety distance based on change of slope angle of Class II slope model, m;  $L_h$  is the safety distance based on the Class I slope model when the slope height changes, m;  $L'_h$  is the safety distance based on the Class II slope model when the slope height changes, m;  $H_b$  is the minimum burial depth of the gully bottom coal seam, m;  $M$  is the mining height of coal seams, m;  $D$  is the minimum buried mining ratio at the gully bottom ( $D=H_b/M$ );  $L_D$  is the safety distance based on the change of minimum buried mining ratio at the gully bottom of the Class I slope model, m;  $L'_D$  is the safety distance based on the change of the minimum buried mining ratio at the gully bottom of the Class II slope model, m; According to the analysis results of the width of the safety coal pillar during the mining above the valley runoff, coal pillars of corresponding size should be set in the simulated excavation process, as is shown in Figure 14, and the deformation and failure conditions of Classes I and II slope with safety coal pillars under mining can be obtained.

## 6 Conclusion

- (1) In this study, the location of the key layer in the overburden and the cutting characteristics of the overburden are considered, and the occurrence structure characteristics of the gully slope are classified based on the control of the key layer on the rock strata at the bottom of the slope. The Class I slope is represented by the slope with an incomplete key layer, and the Class II slope is represented by the slope with a complete key layer.
- (2) The changes in slope angle, slope height, coal seam mining height, and burial depth of coal seam in the gully bottom have different effects on the Class I slope model (with an incomplete key layer) and Class II slope model (with a complete key layer). When there is an incomplete key layer, the damage degree of slope rock is more significant. The greater the slope angle, coal seam mining height and slope height, the more obvious the influence on the strata movement and damage of the slope rock, but the influence of the slope height is weaker than that of the

slope angle and mining height. The larger the buried depth of coal seams at the bottom of the gully, the smaller the damage degree caused by the strata movement of the slope rock, and the smaller the scope of horizontal sliding cracks in the slope bottom.

- (3) Based on the results of numerical simulation, the relations between the safety distance of the mining face under Class I and Class II slope and the required slope angle  $\alpha$ , slope height  $h_0$  and the D ratio of the buried depth of the coal seam under the gully bottom and the mining height. Specifically, the safety distance has a non-linear logarithmic positive correlation with the slope angle  $\alpha$ , a linear positive correlation with the slope height  $h_0$ , and a quadratic polynomial negative correlation with the ratio D of the buried depth to the mining height of coal seam under the gully bottom. Based on the generalized model of the safe distance of the working face and the coal pillar setting, the method of setting the safety coal pillar is proposed in this study.

## Data availability statement

The datasets presented in this study can be found in online repositories. The names of the repository/repositories and accession number(s) can be found in the article/Supplementary Material.

## Author contributions

Conceptualization, YZ and CQ; methodology, CQ and XC; software, XC; formal analysis, ZC; data collection, ZC and JW; writing—original draft preparation, XW, CQ, and ZN; writing—review and editing, ZN.

## Funding

This work was supported by the financial supports of General Program of The National Nature Science Foundation of China (51474206, 51874282, and 51874278).

## Conflict of interest

The author YZ was employed by Shangyuquan Coal Mine of Shanxi Luneng Hequ Electric Coal Development Co., Ltd.

The remaining authors declare that the research was conducted in the absence of any commercial or financial relationships that could be construed as a potential conflict of interest.

## Publisher's note

All claims expressed in this article are solely those of the authors and do not necessarily represent those of their affiliated organizations, or those of the publisher, the editors and the reviewers. Any product that may be evaluated in this article, or claim that may be made by its manufacturer, is not guaranteed or endorsed by the publisher.

## References

- Chen, J., Liu, L., Zeng, B., Tao, K., Zhang, C., Zhao, H., et al. (2022). A constitutive model to reveal the anchorage mechanism of fully bonded bolts. *Rock Mech. Rock Eng.* 11, 8. doi:10.1007/s00603-022-03160-8
- Cheng, G., Yang, T., Liu, H., Wei, L., Zhao, Y., Liu, Y., et al. (2020). Characteristics of stratum movement induced by downward longwall mining activities in middle-distance multi-seam. *Int. J. Rock Mech. Min. Sci.* 136, 104517. doi:10.1016/j.ijrmms.2020.104517
- Du, F., and Gao, R. (2017). Development patterns of fractured water-conducting zones in longwall mining of thick coal seams—a case study on safe mining under the Zhuozhang river. *Energies* 10 (11), 1856. doi:10.3390/en10111856
- Gui, H., Qiu, H., Chen, Z., Ding, P., Zhao, H., and Li, J. (2020). An overview of surface water hazards in China coal mines and disaster-causing mechanism. *Arabian J. Geosciences* 13 (2), 67. doi:10.1007/s12517-019-5046-0
- Liu, Y., Qi, Q., Wang, A., and Jiang, B. (2021). Influence of valleys terrain on pressure of fully mechanized working faces in shallow coal seams. *Shock Vib.* 2021, 1–11. doi:10.1155/2021/8880041
- Mondal, D., Roy, P. N. S., and Kumar, M. (2020). Monitoring the strata behavior in the Destressed Zone of a shallow Indian longwall panel with hard sandstone cover using Mine-Microseismicity and Borehole Televiewer data. *Eng. Geol.* 271, 105593. doi:10.1016/j.enggeo.2020.105593
- Ning, J., Wang, J., Tan, Y., and Xu, Q. (2020). Mechanical mechanism of overlying strata breaking and development of fractured zone during close-distance coal seam group mining. *Int. J. Min. Sci. Technol.* 30 (2), 207–215. doi:10.1016/j.ijmst.2019.03.001
- Qi, X. R., Li, D., Chu, F., Zhang, J., and Zhang, J. (2019). Study of the height of water flowing fracture zone based on strain energy failure criterion. *Earth Environ. Sci.* 330, 022065. doi:10.1088/1755-1315/330/2/022065
- Qi, Y., Wang, W., Ge, J., Yang, Z., and Qi, Q. (2022). Development characteristics of the rock fracture field in strata overlying a mined coal seam group. *PLoS One* 17 (10), e0268955. doi:10.1371/journal.pone.0268955
- Sainoki, A., Mitri, H. S., Chinnasane, D., and Schwartzkopff, A. K. (2019). Quantitative energy-based evaluation of the intensity of mining-induced seismic activity in a fractured rock mass. *Rock Mech. Rock Eng.* 52 (11), 4651–4667. doi:10.1007/s00603-019-01861-1
- Swift, G. (2013). Relationship between joint movement and mining subsidence. *Bull. Eng. Geol. Environ.* 73 (1), 163–176. doi:10.1007/s10064-013-0539-7
- Tan, Y., Cheng, H., Lv, W., Yan, W., Guo, W., Zhang, Y., et al. (2022). Calculation of the height of the water-conducting fracture zone based on the analysis of critical fracturing of overlying strata. *Sustainability* 14 (9), 5221. doi:10.3390/su14095221
- Tian, C., Liu, Y., Yang, X., Hu, Q., Wang, B., and Yang, H. (2019). Development characteristics and field detection of overburden fracture zone in multiseam mining: A case study. *Energy Sci. Eng.* 8 (3), 602–615. doi:10.1002/ese3.536
- Wang, F., Tu, S., Zhang, C., Zhang, Y., and Bai, Q. (2016). Evolution mechanism of water-flowing zones and control technology for longwall mining in shallow coal seams beneath gully topography. *Environ. Earth Sci.* 75 (19), 1309. doi:10.1007/s12665-016-6121-4
- Wang, Z., Song, G., and Ding, K. (2020). Study on the ground movement in an open-pit mine in the case of combined surface and underground mining. *Adv. Mater. Sci. Eng.* 2020, 1–13. doi:10.1155/2020/8728653
- Xie, X., Hou, E., Wang, S., Sun, X., Hou, P., Wang, S., et al. (2021). Formation mechanism and the height of the water-conducting fractured zone induced by middle deep coal seam mining in a sandy region: A case study from the xiaobaodang coal mine. *Adv. Civ. Eng.* 2021, 1–11. doi:10.1155/2021/6684202
- Yang, T., Yang, Y., Zhang, J., Gao, S., Li, T., and Wu, H. (2021). Study on development law of mining-induced slope fracture in gully mining area. *Adv. Civ. Eng.* 2021, 1–9. doi:10.1155/2021/9990465
- Zeng, Y., Lian, H., Du, X., Tan, X., and Liu, D. (2022). An analog model study on water–sand mixture inrush mechanisms during the mining of shallow coal seams. *Mine Water Environ.* 41 (2), 428–436. doi:10.1007/s10230-022-00870-x
- Zhang, C., Mitra, R., Oh, J., Canbulat, I., and Hebblewhite, B. (2017). Numerical analysis on mining-induced fracture development around river valleys. *Int. J. Min. Reclam. Environ.* 32 (7), 463–485. doi:10.1080/17480930.2017.1293495
- Zhang, Q., and López, D. L. (2019). 38. Ohio, 566–580. doi:10.1007/s10230-019-00619-z Use of time series analysis to evaluate the impacts of underground mining on the hydraulic properties of groundwater of dysart woods, Ohio. *Mine Water Environ.* 3
- Zhou, Y., and Yu, X. (2022). Study of the evolution of water-conducting fracture zones in overlying rock of a fully mechanized caving face in gently inclined extra-thick coal seams. *Appl. Sci.* 12 (18), 9057. doi:10.3390/app12189057
- Zhu, T., Li, W., Wang, Q., Hu, Y., Fan, K., and Du, J. (2020). Study on the height of the mining-induced water-conducting fracture zone under the Q2l loess cover of the jurassic coal seam in northern Shaanxi, China. *Mine Water Environ.* 39 (1), 57–67. doi:10.1007/s10230-020-00656-z





## OPEN ACCESS

## EDITED BY

Danqi Li,  
Curtin University, Australia

## REVIEWED BY

Zhengyang Song,  
University of Science and Technology  
Beijing, China  
Huibin Sun,  
Shandong Jianzhu University, China

## \*CORRESPONDENCE

Yu Wu,  
✉ wuyu@cumt.edu.cn

## SPECIALTY SECTION

This article was submitted to  
Environmental Informatics and Remote  
Sensing,  
a section of the journal  
Frontiers in Earth Science

RECEIVED 11 January 2023

ACCEPTED 13 February 2023

PUBLISHED 23 February 2023

## CITATION

Geng H, Wu Y, Hao G, Hao Y, Li D and  
Zhou H (2023), Numerical study on heat  
storage efficiency of broken rock mass  
under different CO<sub>2</sub> injection conditions.  
*Front. Earth Sci.* 11:1142167.  
doi: 10.3389/feart.2023.1142167

## COPYRIGHT

© 2023 Geng, Wu, Hao, Hao, Li and Zhou.  
This is an open-access article distributed  
under the terms of the [Creative  
Commons Attribution License \(CC BY\)](#).  
The use, distribution or reproduction in  
other forums is permitted, provided the  
original author(s) and the copyright  
owner(s) are credited and that the original  
publication in this journal is cited, in  
accordance with accepted academic  
practice. No use, distribution or  
reproduction is permitted which does not  
comply with these terms.

# Numerical study on heat storage efficiency of broken rock mass under different CO<sub>2</sub> injection conditions

Haozhe Geng<sup>1</sup>, Yu Wu<sup>2\*</sup>, Guan Hao<sup>3</sup>, Yang Hao<sup>2</sup>, Decheng Li<sup>1</sup> and Haiyang Zhou<sup>1</sup>

<sup>1</sup>School of Mechanics and Civil Engineering, China University of Mining and Technology, Xuzhou, Jiangsu, China, <sup>2</sup>State Key Laboratory for Geomechanics and Deep Underground Engineering, China University of Mining and Technology, Xuzhou, Jiangsu, China, <sup>3</sup>School of Civil Engineering and Architecture, Nantong Institute of Technology, Nantong, Jiangsu, China

The application of energy storage technology can solve the problems of randomness and volatility in the development and use of renewable energy, such as wind and solar energy, and effectively improve energy utilization. Rock heat storage is one of the primary forms of sensible heat storage. The heat storage efficiency and heat storage capacity of rock packed bed are important indicators to measure the energy storage effect of a rock energy storage system. This paper takes CO<sub>2</sub> as the heat-carrying medium and broken granite grains as the packed bed matrix of the energy storage system. It establishes a porous medium thermal-hydraulic-mechanical coupling model of the broken rock bed. The heat injection and production process of the large-sized rock bed heat storage system is simulated using the COMSOL finite element software, and the heat storage efficiency and heat storage capacity of the broken rock bed is analyzed under different fluid injection pressures and injection temperatures. The results show that: 1) With the increase of CO<sub>2</sub> injection pressure, the heat storage and heat production speed of the heat storage system will increase, and the heat storage rate changes from two stages of “low rise - slow decline” to four stages of “rapid increase—stability—rapid decrease—stability”; 2) With the increase of CO<sub>2</sub> injection temperature, the maximum heat storage capacity of the rock bed heat storage system will increase. Due to the increase in the temperature gradient between CO<sub>2</sub> and the rock bed, the heat storage and the heat production time of the heat storage system will increase, and its speed will decrease.

## KEYWORDS

heat storage system, rock packed bed, thermal hydraulic mechanical couple, heat storage efficiency, heat storage capacity

## 1 Introduction

To achieve the strategic goal of “carbon peaking and carbon neutralization,” the development and utilization of renewable energy have become the top priority of China’s energy strategy. With the rapid development of renewable clean energy, wind and solar energy have become relatively mature and large-scale used renewable clean energy. The number and scale of installed power generation using them have increased year by year. However, wind power generation and solar power generation are not stable enough due to



the influence of seasons and the duration of sunshine, which has caused the phenomenon of large-scale “wind abandonment” and “sunshine abandonment” (Ha and Saha, 2004; Piwko et al., 2009). The key to solving the problem of “wind abandonment” and “light abandonment” is to solve the randomness and volatility of wind and solar power generation. Establishing large-scale energy storage systems can effectively solve this problem (Li et al., 2016). Rock is an ideal medium for heat storage with the advantages of low cost, a wide range of sources, and a large heat exchange area. The study of rock heat storage is important for solar energy storage, wind/photovoltaic grid-connected operation, and deep peaking of thermoelectric units (Liu et al., 2018).

Scholars have conducted numerous researches on rock packed bed seepage and heat transfer characteristics. BU (BU, 2012), Wang, M. L. (Wang et al., 1992) conducted seepage experiments on broken rock mass and studied the relationship between the permeability coefficient of broken rock mass and its state of pressure and porosity. Yang Wei (YANG et al., 2015) deduced the pressure field distribution law of one-dimensional steady gas seepage based on the gas permeability test of broken sandstone under pressure, and concluded that the degree of rock fragmentation is non-regular under different axial stresses, and the higher the degree of fragmentation, the lower the gas permeability. Markevich (Markevich and Cecilio 2015) measured the stability of the seepage process by varying the diameter, size, and proportion of the broken rock grains separately, calculated the Reynolds number of the packed structure, and analyzed its turbulent flow state. SHANG (SHANG, 2017) obtained the variation of seepage parameters of the broken coal rock mass under different surrounding pressures based on the triaxial seepage experiment by numerical simulation. Schumann (SCHUMANN, 1929) proposed an analytical method for solving the thermal interaction problem between a flowing fluid and a porous medium. Furnas (FURNAS, 1930) proposed that rock can be used as an ideal heat storage material for packed bed and then conducted a heat-transfer experiment on the heat-transfer flow characteristics of the packed bed. It was proposed that the effective heat-transfer coefficient increases with the increase of fluid flow when the heat-transfer fluid flows through a packed bed filled with broken solids. Ergun (ERGUN, 1952) and Allen (ALLEN et al., 2013; ALLEN et al., 2014) found that the shape and arrangement of the grains affect the heat transfer in the packed bed by influencing heat radiation, heat convection, and axial heat conductivity in the packed bed. Zavattoni (Zavattoni et al., 2011) analyzed the influence of axial porosity distribution or thickness effect of packing on overall heat transfer through numerical simulation.

Scholars have also conducted much research on the mechanistic aspects of thermal-hydraulic-mechanical coupling in rock. Terzaghi (TERZAGHI, 1943) first proposed the hydraulic-mechanical coupling problem and the consolidation theory of soil, and built the basic theoretical framework for the hydraulic-mechanical coupling problem. Biot (BIOT, 1941; BIOT, 1954) proposed the three-dimensional consolidation theory and extended it to the dynamic analysis of anisotropic porous media. Savage (SAVAGE and BRADDOCK, 1982) proposed the generalized Biot theory, which mainly applies to elastic and isotropic media. Chen (CHEN and TEUFEL, 1997) established a dual pore fluid flow model based on Biot theory and proposed that the critical

coupling factor is the pore volume variation of the matrix, fracture, and dual continuum and the relevant effective stress law. Vaziri (VAZIRI, 1988) deduced the theoretical expressions based on the elastic and thermal properties of multiphase soil system, and developed a set of finite element programs to meet the complex three-field coupling under the specified displacement and fluid pressure conditions. Tortike (TORTIKE and ALI, 1987; TORTIKE and ALI, 1991) established a three-dimensional thermal-hydraulic-mechanical coupling mathematical model of an elasto-plastic rock mass and conducted numerical simulation research, which concluded that the geomechanical response depends mainly on temperature variation, pressure variation, and local material response. Gatmiri (GATMIRI and DELAGE, 1997) proposed the concept of thermal porosity state surface, including the influence of thermal effect and stress state on volume change, and proposed a fully thermal-hydraulic-mechanical coupling theory for saturated porous media. Currently, most of the research on the thermal-hydraulic-mechanical coupling mechanism of rock is based on Terzaghi's effective stress principle and Biot's three-dimensional soil consolidation theory.

CO<sub>2</sub> as a heat transfer fluid has certain thermophysical and chemical properties (Li and Dai, 2014), is more chemically stable than water, is a weak solvent for rock minerals, has very low corrosion, and has lower viscosity and better fluidity (Pruess, 2008; Atrens et al., 2010). In 2000, Brown first proposed the use of supercritical CO<sub>2</sub> as a heat transfer fluid in enhanced geothermal systems (Brown, 2000; Pruess, 2006). And the use of CO<sub>2</sub> for fluid loss during heat storage and recovery can indirectly achieve the purpose of sequestering CO<sub>2</sub>. At present, CO<sub>2</sub> has achieved good results in oil drive (Leena, 2008), fracturing (WANG et al., 2020) and drilling (SHEN et al., 2010), and most of the research as heat transfer fluid is focused on geothermal extraction (WU et al., 2021), but there is less research in using CO<sub>2</sub> for heat storage.

In this paper, based on the above theory and mechanism research, aiming at the law of rock mass deformation, fluid flow, and heat transfer in the process of heat injection, a thermal-hydraulic-mechanical coupling mathematical model describing the energy storage process of the rock packed bed is established. The heat injection and production process of the rock bed heat storage system is simulated using COMSOL finite element software, and the effect of fluid injection pressure and temperature on the heat storage capacity and heat storage efficiency of the heat storage system is studied.

## 2 Rock bed heat storage system and experiment

During heat injection and production, the heat-carrying gas flows through the rock packed bed and exchanges heat with the rock. The stress and strain of the rock changes due to thermal expansion, which changes the pore structure of the packed bed, thus affecting the gas seepage movement. The change of the gas seepage also affects the convective heat exchange between rock and gas. At the same time, the change in gas temperature will change its density, viscosity, and other properties, affecting the gas seepage movement. The gas pore pressure will also change, affecting the stress-strain structure of the packed bed. Therefore, in the process of heat injection and

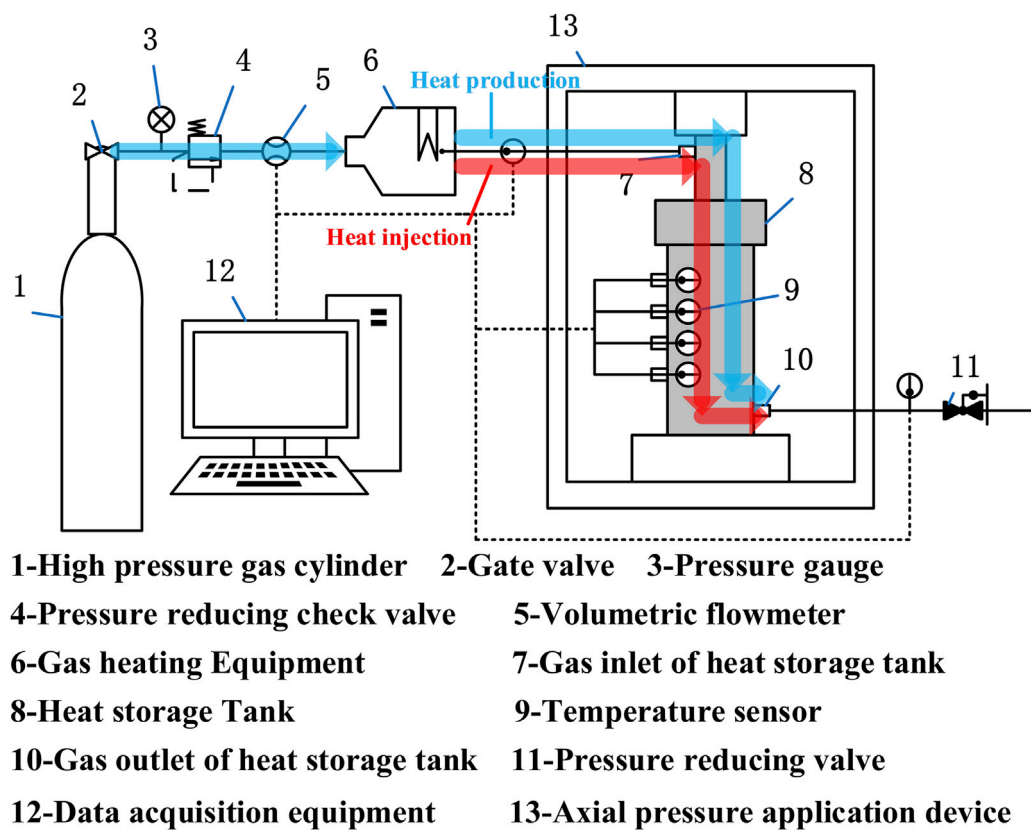


**FIGURE 1**  
Schematic diagram of the experimental system.

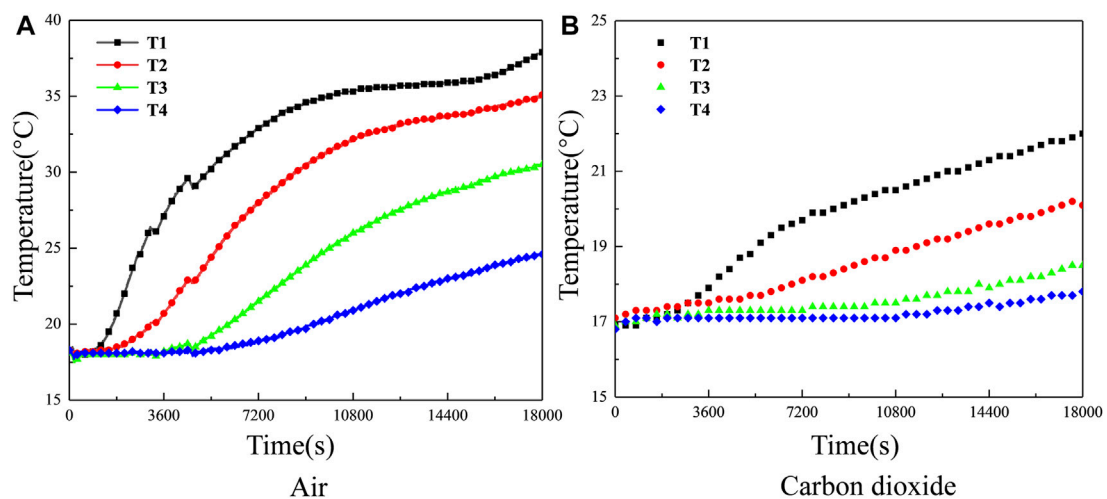


**FIGURE 2**  
Temperature change of each measuring point in heat injection experiments through different heat-carrying gas (A) Air (B) Carbon dioxide.

production of rock bed, the seepage movement of heat-carrying gas, rock deformation, and heat transfer involves the mutual coupling of the hydraulic field, mechanical field, and thermal field.

The schematic diagram of the experimental system is shown in Figure 1. The heat storage tank is filled with broken granite grains to form a rock packed bed, and axial pressure is applied to the packed

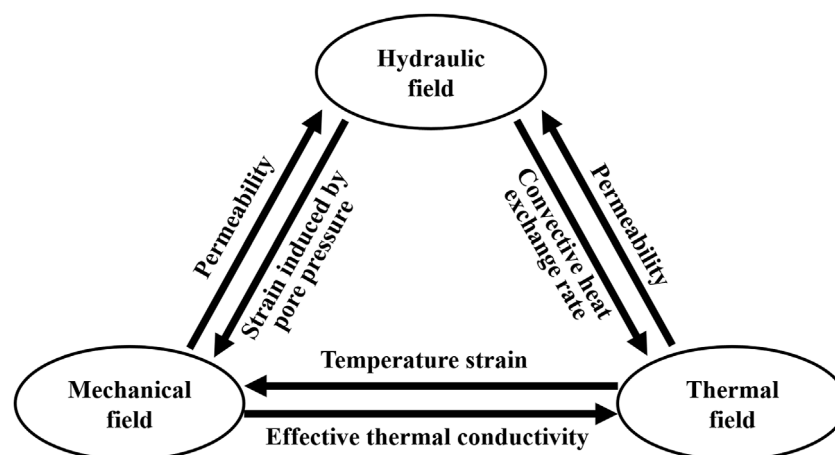


FIGURE 3  
Thermal-hydraulic-mechanical coupling in the heat storage system.

bed to maintain a certain energy storage density. In the heat injection experiment, the gas is injected into the storage tank through the heating device, and the high-temperature gas exchanges heat with the rock packed bed, and the heat is stored in the rock packed bed. In the heat production experiment, the low-temperature gas is injected directly into the storage tank, and the heat is extracted from the rock packed bed through heat exchange. Four temperature sensors are set inside the heat storage tank to record the axial temperature distribution inside the bed during the heat injection and production.

Air and CO<sub>2</sub> are used as heat-carrying gases, respectively. Figure 2 shows the temperature changes at each measuring point in the heat storage tank in the two groups of heat injection experiments. It can be seen that when CO<sub>2</sub> is used as heat-carrying gas, the temperature at T1 of the broken rock packed bed starts to increase within 0.5 h of heat injection. At 0.5 h of heat injection, the temperature at T2 also starts to increase, and the temperature at T3 and T4 starts to increase at 1.5 h. At 5 h of heat injection, the temperature difference at T1 of the broken rock packed bed reached about 20°C, and it also increased by nearly 10°C at the bottom T4. When air was used as the heat-carrying gas, the temperature at T1 and T2 of the broken rock packed bed changed at 1 h of heat injection, and at 3 h of heat injection, the temperature at T3 and T4 of the broken rock packed bed started to change. At 5 h of heat injection, the temperature difference at T1 of the broken rock packed bed is about 5°C, and the temperature difference at T4 is less than 1°C. It indicates that the heat-carrying capacity of CO<sub>2</sub> is much larger than air under the same conditions. Therefore, using CO<sub>2</sub> as the heat-carrying medium in heat injection and production is more appropriate.

### 3 Model establishment and solution

#### 3.1 Governing equations of thermal hydraulic mechanical coupling theory

The mutual coupling relationship of the temperature field, hydraulic field, and mechanical field involved in the heat storage system's heat injection and production process is shown in Figure 3.

The coupling between the three fields of THM is realized through the seepage motion of heat-carrying fluid, the deformation of broken rock, and the heat transfer between fluid and solid. Therefore, the governing equations of each physical field should be determined first.

##### 3.1.1 Deformation governing equation for pore media

According to the Terzaghi principle of effective stress (TERZAGHI, 1943), the stress of rock mass is:

$$\sigma_{ij} = \sigma_{ij}^* + \alpha p_f \delta_{ij} \quad (1)$$

where:  $\sigma_{ij}$  and  $\sigma_{ij}^*$  are the total stress tensor and effective stress tensor, respectively;  $\alpha$  is the Biot coefficient;  $p_f$  is the pore-fluid pressure;  $\delta_{ij}$  is the Kronecker constant.

The relationship between effective stress and strain affected by temperature effect is (BIOT, 1954):

$$\sigma_{ij}^* = 2G\varepsilon_{ij} + \lambda\delta_{ij}\varepsilon_v - K\alpha_T\delta_{ij}(T - T_0) \quad (2)$$

where:  $G$  is the shear modulus of elasticity;  $\lambda$  is the lame constant;  $K$  is the bulk modulus;  $\varepsilon_{ij}$  is the strain tensor;  $\varepsilon_v$  is the bulk strain;  $\alpha_T$  is the coefficient of thermal expansion.

The relationship between stress and strain affected by temperature effect and fluid pressure is as follows:

$$\sigma_{ij} = 2G\varepsilon_{ij} + \lambda\delta_{ij}\varepsilon_v - K\alpha_T\delta_{ij}T_s + \alpha p_f \delta_{ij} \quad (3)$$

The relationship between displacement and strain under small deformation, and deformation geometry equation is:

$$\varepsilon_{ij} = \frac{1}{2} (u_{i,j} + u_{j,i}) \quad (4)$$

$$\varepsilon_v = \varepsilon_{kk} = \varepsilon_{11} + \varepsilon_{22} + \varepsilon_{33} \quad (5)$$

without considering the inertial force effect, the equation of conservation of momentum is:

$$\sigma_{ij,j} + F_i = 0 \quad (6)$$

Through combination with Formula 3, 4, 5, 6, the stress field governing equation considering temperature, pressure, and displacement is obtained:

$$\mathbf{G}(\mathbf{u}_{i,jj} + \mathbf{u}_{j,ij}) + \lambda \mathbf{u}_{j,ji} - \alpha_T T_{s,i} + \alpha P_{f,i} + \mathbf{F}_i = \mathbf{0} \quad (7)$$

where:  $\mathbf{u}_i$  is the displacement component;  $\mathbf{F}_i$  is the volume force component.

### 3.1.2 Seepage governing equation for pore media

According to the law of conservation of mass, the fluid flow governing equation of porous media can be expressed as:

$$\frac{\partial(\phi \rho_f)}{\partial t} + \nabla(\rho_f \cdot \mathbf{v}) = Q_f \quad (8)$$

where:  $\rho_f$  is the fluid density ( $\text{kg}/\text{m}^3$ );  $\mathbf{v}$  is seepage velocity ( $\text{m}/\text{s}$ );  $\phi$  is the porosity of porous media;  $Q_f$  is the source (sink) item.

Since the fluid flow in porous media does not conform to Darcy flow, the Erugun non-Darcy flow permeability model equation was used (AKGIRAY and SAATCL, 2001):

$$\mathbf{v} = -\frac{k}{\mu_f} \frac{2}{\sqrt{1 + 4\left(\frac{k}{\mu_f}\right)^2 \beta \rho_f |\nabla p_f|}} \nabla p_f \quad (9)$$

$$k = \frac{d_p^2}{150} \frac{\varepsilon_p^3}{(1 - \varepsilon_p)^2} \quad (10)$$

$$\beta = \frac{1.75}{d_p} \frac{(1 - \varepsilon_p)}{\varepsilon_p^3} \quad (11)$$

where:  $k$  is the permeability ( $\text{m}^2$ );  $\mu_f$  is the dynamic viscosity of the fluid ( $\text{Pa} \cdot \text{s}$ );  $\beta$  is the Forchheimer parameter;  $p_f$  is the pore-fluid pressure;  $d_p$  is the effective (average) particle size of porous media;  $\varepsilon_p$  is porosity

Substitute Formula 9 into Formula 8 to get:

$$\frac{\partial(\phi \rho_f)}{\partial t} + \nabla \cdot \left( -\rho_f \frac{k}{\mu_f} \frac{2}{\sqrt{1 + 4\left(\frac{k}{\mu_f}\right)^2 \beta \rho_f |\nabla p_f|}} \nabla p_f \right) = Q_f \quad (12)$$

### 3.1.3 Heat transfer and convection governing equation for pore media

Fourier heat conduction considering seepage can be expressed as:

$$\mathbf{q} = -\lambda \nabla T + \rho_f c_f \mathbf{v} T \quad (13)$$

where:  $\mathbf{q}$  is the heat flux ( $\text{W}/\text{m}^2$ );  $\lambda$  is the coefficient of thermal conductivity ( $\text{W}/(\text{m} \cdot \text{K})$ );  $c_f$  is the specific heat capacity of  $\text{CO}_2$  ( $\text{J}/(\text{kg} \cdot \text{K})$ ).

The heat generated during the deformation of the porous media matrix is (JIANG, 2011):

$$Q_s = (1 - \phi) \alpha_T T \frac{\partial \varepsilon_v}{\partial t} \quad (14)$$

where:  $\alpha_T$  is the coefficient of thermal expansion.

The heat energy conservation equation of convection and heat conduction in porous media can be expressed as:

$$\phi \rho_f c_f \frac{\partial T_f}{\partial t} + \rho_f c_f \frac{-k}{\mu_f} \frac{2}{\sqrt{1 + 4\left(\frac{k}{\mu_f}\right)^2 \beta \rho_f |\nabla p_f|}} \nabla p_f \nabla T = \phi \lambda_f \nabla^2 T_f \quad (15)$$

where:  $\lambda_f$  is the gas thermal conductivity ( $\text{W}/(\text{kg} \cdot \text{K})$ ).

Considering the heat exchange between gas and rock, it is assumed that the heat equilibrium is maintained between the gas and the rock, and the thermal equilibrium equation is:

$$\begin{aligned} & (1 - \phi) \rho_s c_s \frac{\partial T_s}{\partial t} + (1 - \phi) T K_f \alpha_f \nabla \\ & \cdot \left( \frac{-k}{\mu_f} \frac{2}{\sqrt{1 + 4\left(\frac{k}{\mu_f}\right)^2 \beta \rho_f |\nabla p_f|}} \nabla p_f \right) + (1 - \phi) T K \alpha_r \frac{\partial \varepsilon_v}{\partial t} \\ & = (1 - \phi) \lambda_s \nabla^2 T_s \end{aligned} \quad (16)$$

where:  $\rho_s$  is rock density ( $\text{kg}/\text{m}^3$ );  $c_s$  is rock specific heat capacity ( $\text{J}/(\text{kg} \cdot \text{K})$ );  $\lambda_s$  is rock thermal conductivity ( $\text{W}/(\text{m} \cdot \text{K})$ );  $T_s$  is rock temperature (K).

Combined with 15, 16, the heat transfer control equation of porous media is obtained as follows:

$$\begin{aligned} & (\rho c)_{eff} \frac{\partial T}{\partial t} + (1 - \phi) T K_f \alpha_f \nabla \cdot \left( \frac{-k}{\mu_f} \frac{2}{\sqrt{1 + 4\left(\frac{k}{\mu_f}\right)^2 \beta \rho_f |\nabla p_f|}} \nabla p_f \right) \\ & + (1 - \phi) T K \alpha_r \frac{\partial \varepsilon_v}{\partial t} \\ & = \lambda_{eff} \nabla^2 T + \rho_f c_f \frac{-k}{\mu_f} \frac{2}{\sqrt{1 + 4\left(\frac{k}{\mu_f}\right)^2 \beta \rho_f |\nabla p_f|}} \nabla p_f \nabla T \end{aligned} \quad (17)$$

## 3.2 Model solving and verification

In order to verify the correctness of the model, the previously completed laboratory experiment (Wu et al., 2022) was set as a reference, the geometric model with the same size as the experiment was established, and the boundary conditions and related parameters with the same conditions were set.

Figure 4 shows the geometric model and the selected measuring point position. The model size is set to be consistent with the size of the heat storage tank in the experiment ( $150 \text{ mm} \times 350 \text{ mm}$ ). 3 mm wide fluid inlet and fluid outlet are set at the center of the upper and lower boundaries of the model. The model is solved by COMSOL Multiphysics software. The solution modules include the solid mechanics module under the structural mechanics branch, the free and porous media flow module and the porous media heat transfer module. The location of the measuring points corresponded to the location of the temperature sensors placed in the heat storage tank in the experiment.

Mechanical field boundary conditions: axial force is applied to the upper boundary of the model, and the rest of the boundaries are set as fixed boundaries to limit the boundary displacement.

Hydraulic field boundary conditions: The model's fluid inlet boundary and fluid outlet are set as the inflow and outflow boundary, respectively. The rest of the boundary is set as the zero flux boundary.

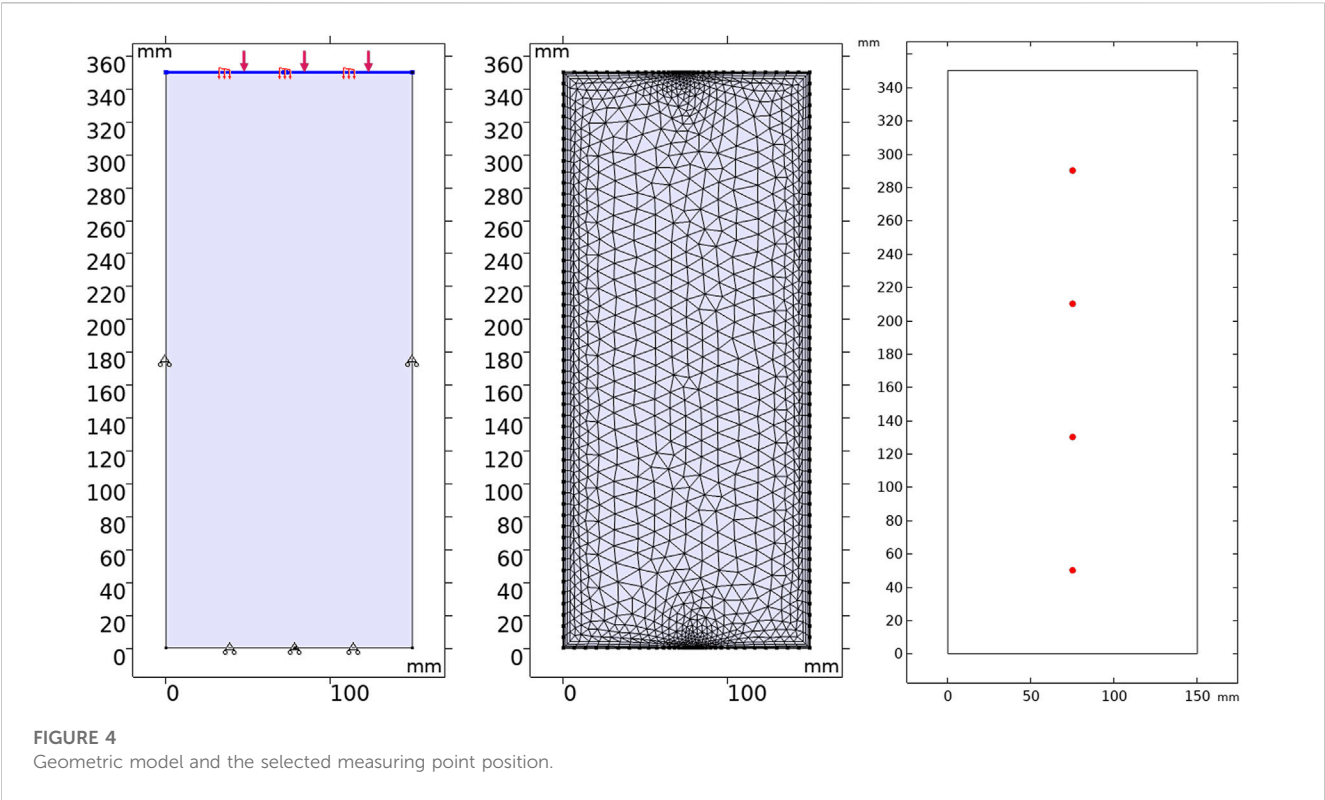


TABLE 1 Related parameters in model.

Parameters	Unit	Value
Thermal expansion coefficient of rock bed, $\alpha_T$	[1/K]	$2.4 \times 10^{-4}$
Initial temperature, $T_0$	[K]	293.15
Initial permeability, $k_0$	[m <sup>2</sup> ]	$6.1 \times 10^{-12}$
Rock density, $\rho_s$	[kg/m <sup>3</sup> ]	2,600
Rock bulk modulus, $K_s$	[MPa]	2000
Fluid specific heat capacity, $c_f$	[J/(kg·K)]	1,000
Fluid thermal conductivity, $\lambda_f$	[W/(m·K)]	0.8
Solid thermal conductivity, $\lambda_s$	[W/(m·K)]	3.49
Poisson's ratio, $\nu$		0.25
Young's modulus, $E$	[GPa]	45.4

Thermal field boundary conditions: the inlet boundary is set as the temperature boundary, the outlet boundary is set as the outflow boundary, and the rest are thermally insulated.

After reading the relevant literature (Shu et al., 2020; Dong et al., 2021), the thermophysical parameters of CO<sub>2</sub> and rock mass are determined, and the relevant parameters in the model are shown in Table 1. The temperature distribution in the model after different times of heat injection and production is shown in Figure 5. It can be seen that the high-temperature region in the heat storage system gradually increases with the increase of heat injection time. When the heat injection proceeds to 18,000 s, the heat storage system is

divided into three regions: high, medium, and low temperature. After 18,000 s, the heat production starts, the high-temperature region of the heat storage system gradually moves down, and the low-temperature region gradually occupies the entrance region and expands.

The calculation results were compared with the experimental results to verify the correctness of the model. Figures 6A, B shows the temperature variation curves with time at each measuring point during the heat injection process obtained from the model and experimental calculations. By comparing the two plots, it can be seen that the range and trend of temperature variation at each measuring point calculated by the model are in general agreement with those obtained from the experiment. In the 3 h heat injection process, the temperature at T1 increases first in the experiment and simulation, but the experimental curve increases at about 0.5 h after the heat injection experiment starts. It is considered that after the start of the heat injection experiment, the gas needs to pass through a long pipeline to reach the heat storage tank through the heating equipment, and it takes some time for the gas to heat the pipeline. With the heat transferred to the lower part of the heat storage tank, the temperature at T2, T3, and T4 also started to increase, and the range and trend of the simulated and experimental curves were basically the same in the following 2.5 h. After the heat injection experiment, the experimental pipeline is reconnected to conduct the heat production experiment, and the time without gas injection is about 10 min. It is the reason why the experimental curve appeared to fall first and then rise, while the simulation was only set to stop for 10 min, so the curve did not fluctuate. In the following heat production, the temperature at T1 of both the simulative and experimental curves dropped sharply, and the temperature at T2,



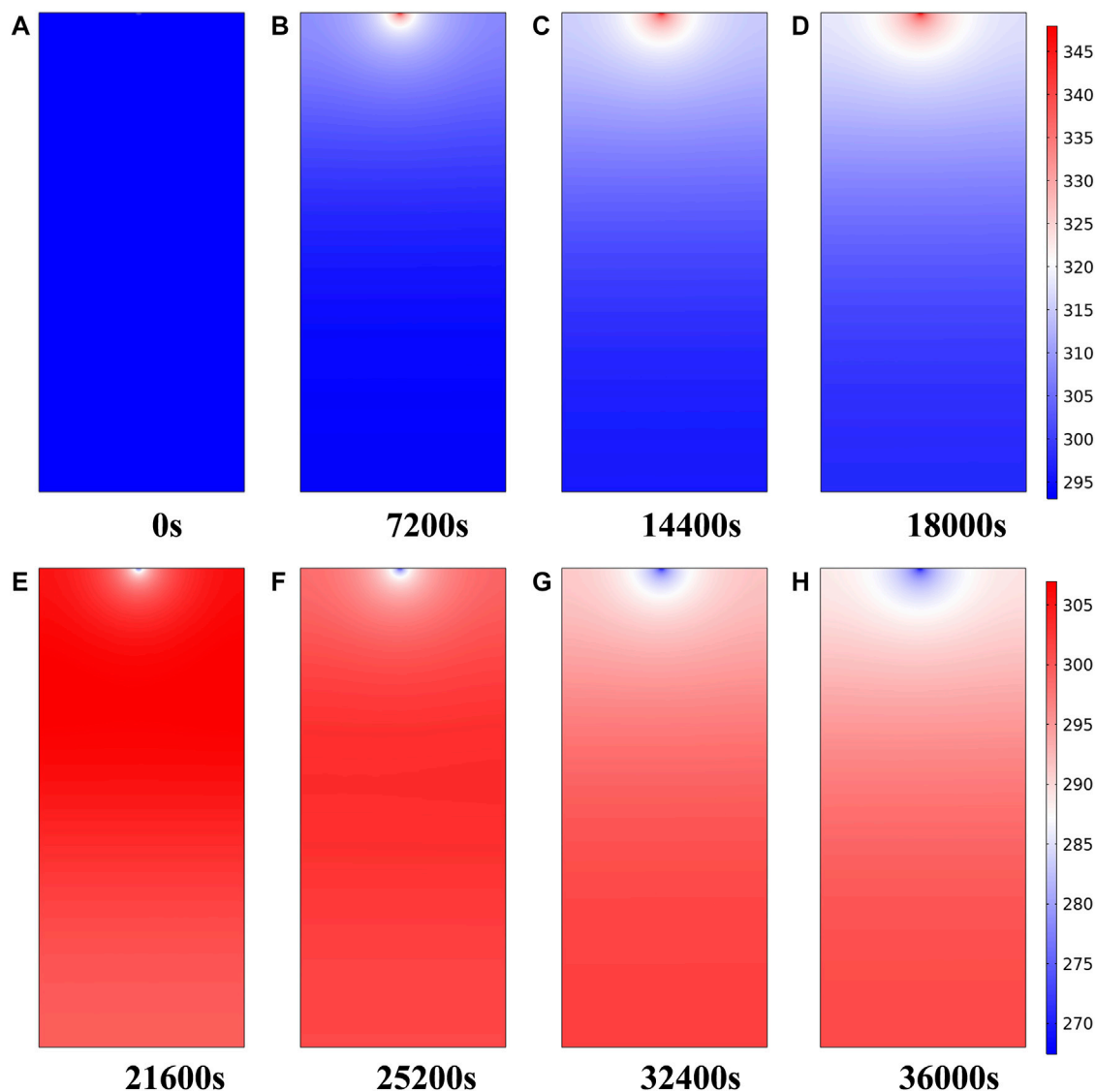


**FIGURE 5**  
Temperature distribution in the model during heat injection and production at different times (A) 0 s (B) 7200 s (C) 14000 s (D) 18000 s (E) 21600 s (F) 25200 s (G) 32400 s (H) 36000 s.

T3, and T4 increased first and then decreased. The curves of T1 intersected with the curves of T2, T3, and T4, and the declining process of T2 also intersected with the rising T3 and T4 curves, respectively.

The temperature change at measurement point T1 during 5 h of heat injection was taken for detailed numerical comparison, as shown in Figure 6C. It can be seen that the process of heating the gas flow line at the beginning of the experiment has a slight effect on the temperature increase of the packed bed. However, the temperature change in the middle period is in good agreement with the simulated temperature curve. The fluctuation of the experimental curve in the later period is because the gas flow is too fast during the experiment, and the actual outlet temperature of the heating equipment does not reach the set temperature, causing the gas temperature at the inlet of the heat storage tank to fluctuate. The temperature of the measuring points in the experiment and

simulation are in general agreement in terms of value, change range and change trend, which fully demonstrates the correctness of the model.

## 4 Simulation of rock bed heat storage system

### 4.1 Numerical model and simulation scheme

The geometric model is shown in Figure 7. The plane model is a rectangular interface with a length of 100 m, a width of 50 m, and a thickness of 5 m ( $z$ -direction). The blue line segment on the model's left side is the injection port, and the red line segment on the right side is the flow outlet, both of which are set to 1 m. The model is solved by COMSOL Multiphysics software. The solution

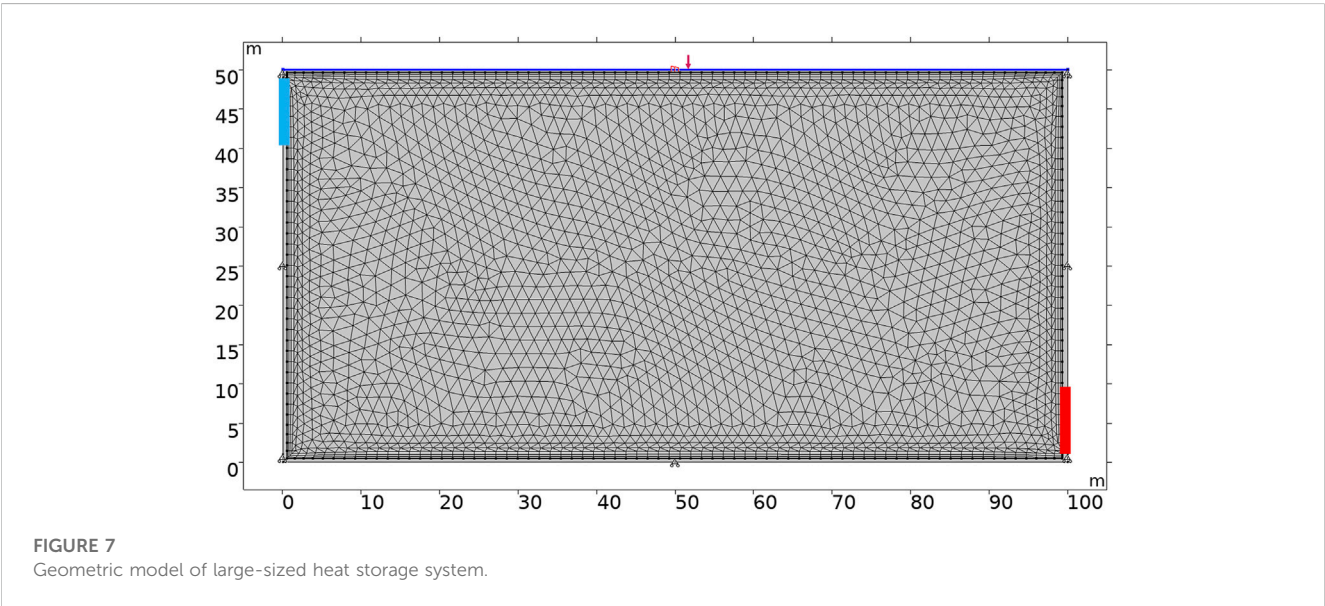
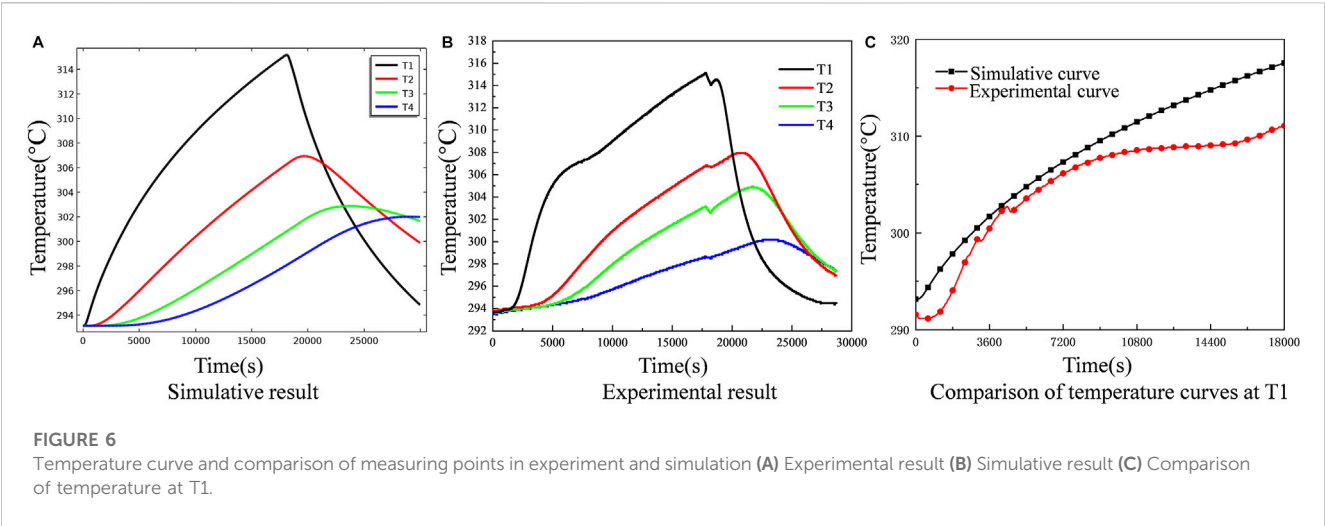
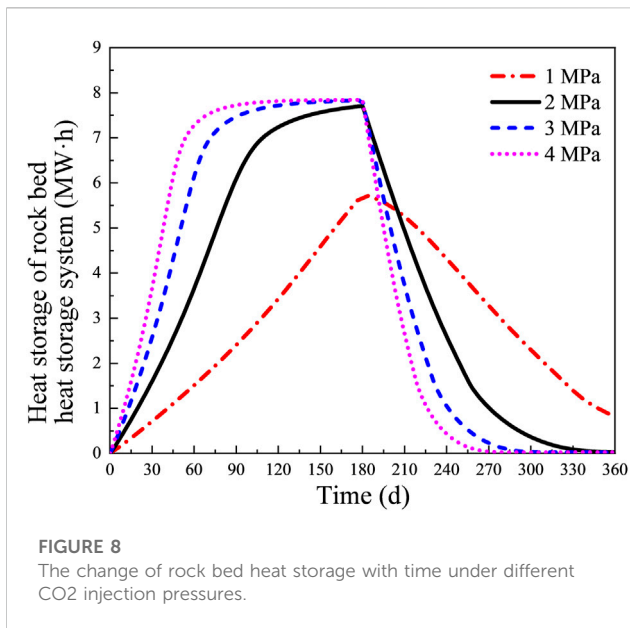


TABLE 2 Numerical simulation scheme.				
Number	Initial temperature of rock bed(K)	Injection pressure (MPa)	Heat injection temperature(K)	Heat production temperature(K)
I	293	2	373/473/573	283
II		1/2/3/4	473	

modules include the structural mechanics module, the groundwater flow module, and the heat transfer module. According to the previous introduction, it is known that the operation of the heat storage system is to “cut the peak and compensate the valley,” which is mainly divided into the heat injection stage and the heat production stage. Therefore, in order to study the thermal-hydraulic-mechanical coupling law in different stages, the heat injection and production processes are simulated separately.

In this model, an axial load is applied to the upper boundary, and the rest boundaries are set as fixed boundaries. For heat transfer, all boundaries are insulated except for the inflow and outlet. The physical and mechanical parameters of the rock bed and fluid in the model are shown in Table 1.

The outlet of the model is connected to the atmosphere, and the outlet pressure is 1 atm. The initial temperature of the rock bed heat storage system is set to 20°C. It is assumed that the heat storage system operates continuously 24 h a day, and the system operates for



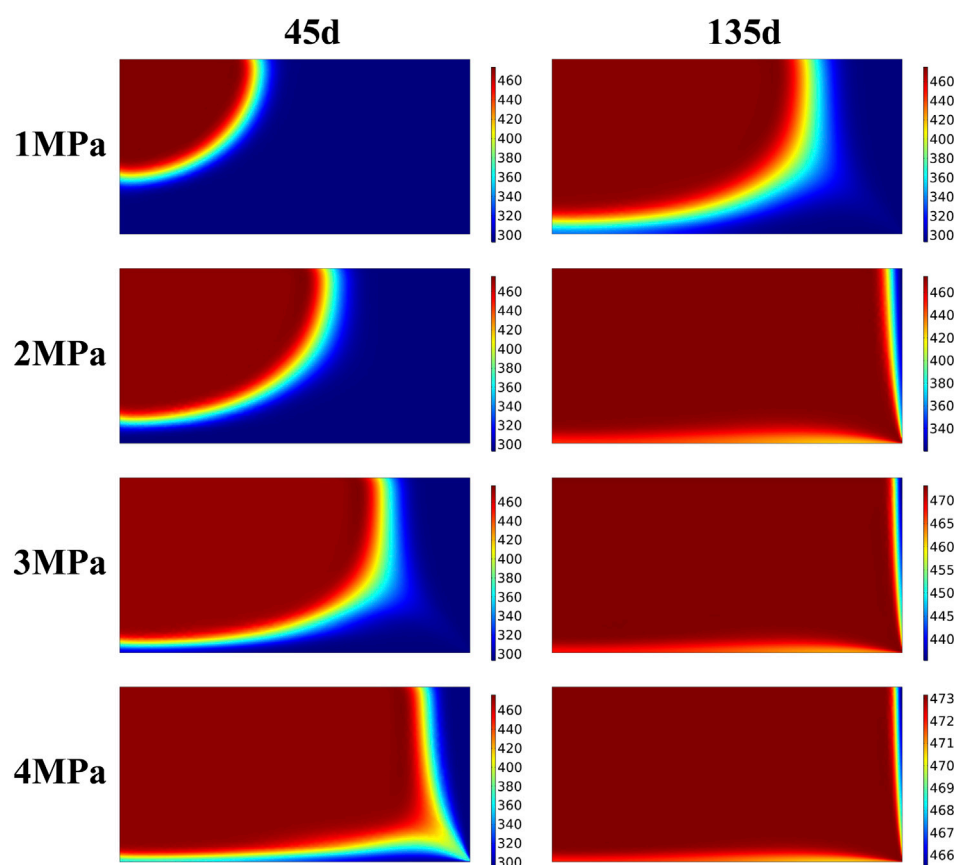
360 days as a cycle. In the spring and summer of the peak electricity abandonment period, the electricity is converted into thermal energy storage, and the heat is injected for 180 days at a temperature of

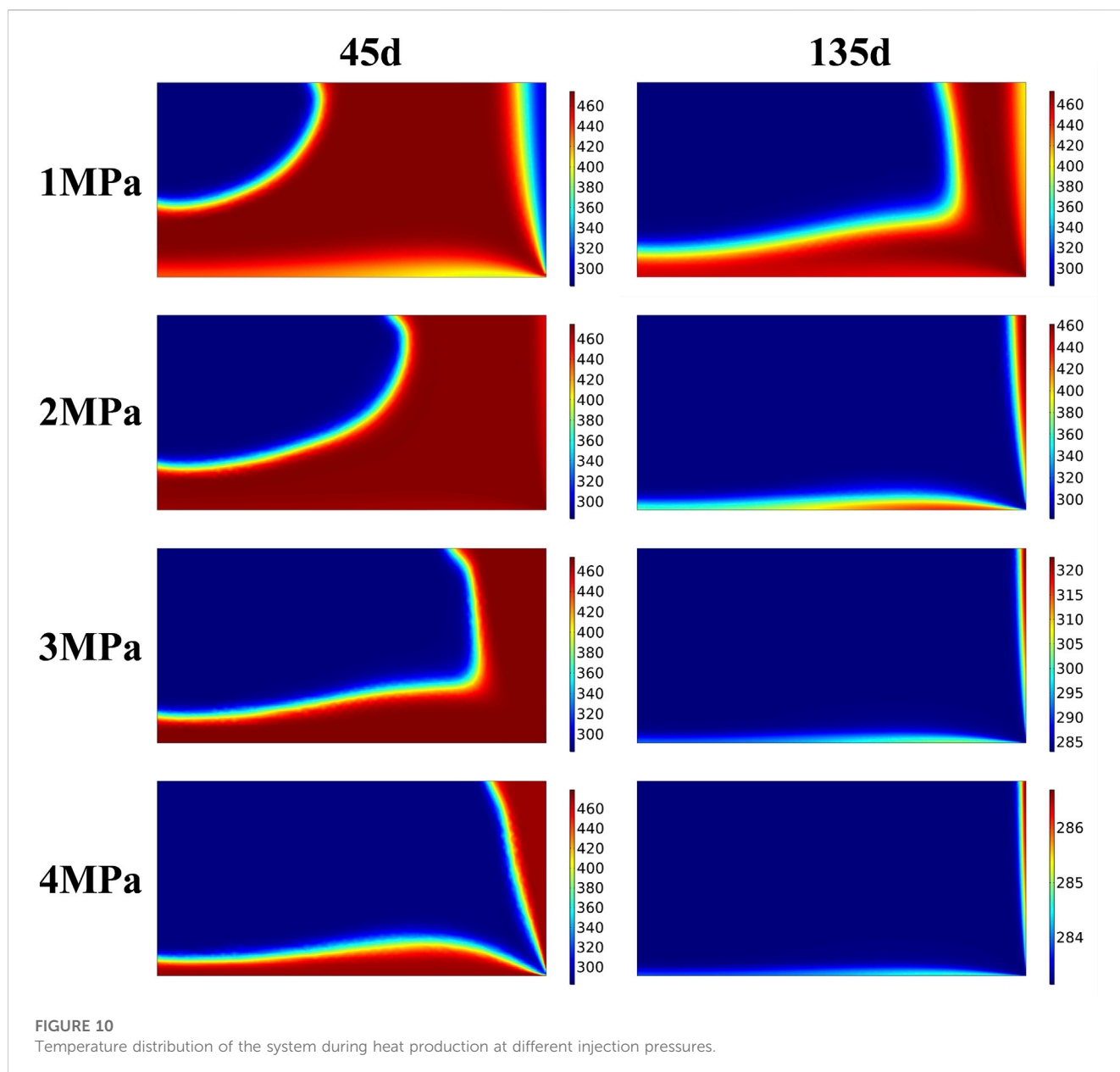
200°C. In the autumn and winter of the peak electricity consumption period, the stored heat energy is produced and converted into electricity again. The heat is produced for 180 days at a temperature of 10°C.

The numerical simulation scheme is shown in [Table 2](#).

## 4.2 The influence of CO<sub>2</sub> injection pressure on the heat storage capacity of rock bed

As shown in [Figure 8](#), the heat storage capacity of the rock bed heat storage system at 1–4 MPa CO<sub>2</sub> injection pressure changes with the heat injection time. It can be seen from the figure that the heat storage capacity increases gradually with the increase of injection pressure during the same 180 days of injection time, but its growth rate is different at different injection pressures. 1 MPa has the lowest growth rate, and at the 180th day of heat injection, the heat storage capacity of the system differs from other injection pressures by nearly 3 MW·h. When the fluid injection temperature is the same, the time for the system to reach temperature equilibrium is different under different injection pressures. The higher the injection pressure, the shorter the time for the rock bed to reach temperature equilibrium. It is because the heat-carrying capacity of CO<sub>2</sub> increases with the increase of injection pressure. Without considering the amount of CO<sub>2</sub> injected, higher injection pressure



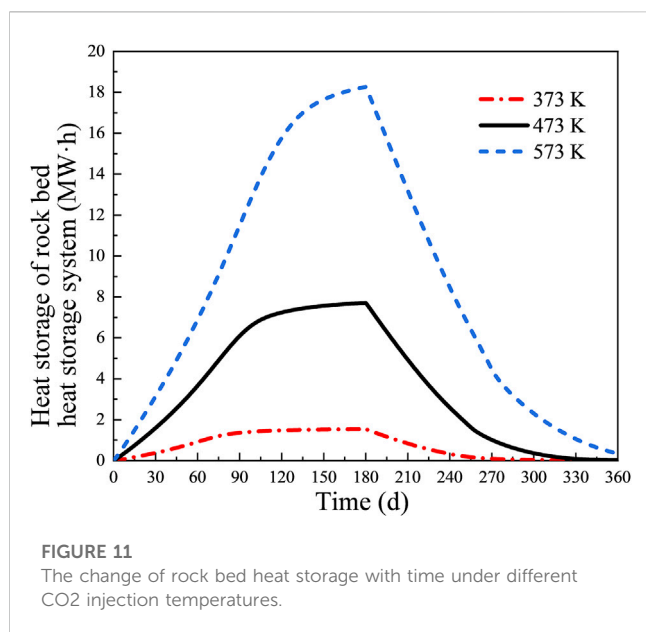


will reduce the time to reach the overall heat equilibrium of the rock bed heat storage system. However, in practical projects, in order to meet the demand for economic benefits, it is necessary to select appropriate injection pressure to avoid energy waste. In this model, 2 MPa is the appropriate injection pressure.

Under the same injection pressure, the change of the heat storage capacity can be roughly divided into four stages, namely, “rapid increase—stability—rapid decrease—stability.” 1 MPa injection pressure has only two stages, “slowly increase and slowly decrease,” without a stable stage. In the actual operation of the heat storage system, it can be divided into two modes: low injection pressure and high injection pressure. Although the total amount of heat storage is lower at low injection pressure, the heat input and output are relatively smooth. Under high injection pressure, the operation mode of the rock bed heat storage system can be set to four stages “heat storage—heat preservation—heat

extraction—shutdown.” Choosing different operation modes according to different needs to achieve the purpose of economic operation.

Figures 9, 10 show the temperature distribution nephogram of the rock bed when the heat storage system operates for 45 days, 135 days, 225 days, and 315 days under the injection pressure of 1 MPa–4 MPa, respectively. It can be seen that after increasing the injection pressure of CO<sub>2</sub>, the diffusion rate of the high-temperature region becomes faster. At 1 MPa injection pressure, there is still nearly half of the initial-temperature region in the rock bed at 45 days of injection time, while at 2 MPa injection pressure, the temperature of nearly 1/2 of the region is already above 400 K for the same injection time. When the injection pressure is increased to 3 MPa, the high-temperature region has grown to 2/3, and at an injection pressure of 4 MPa, the rock bed has roughly reached temperature equilibrium. Similarly, when the rock bed heat

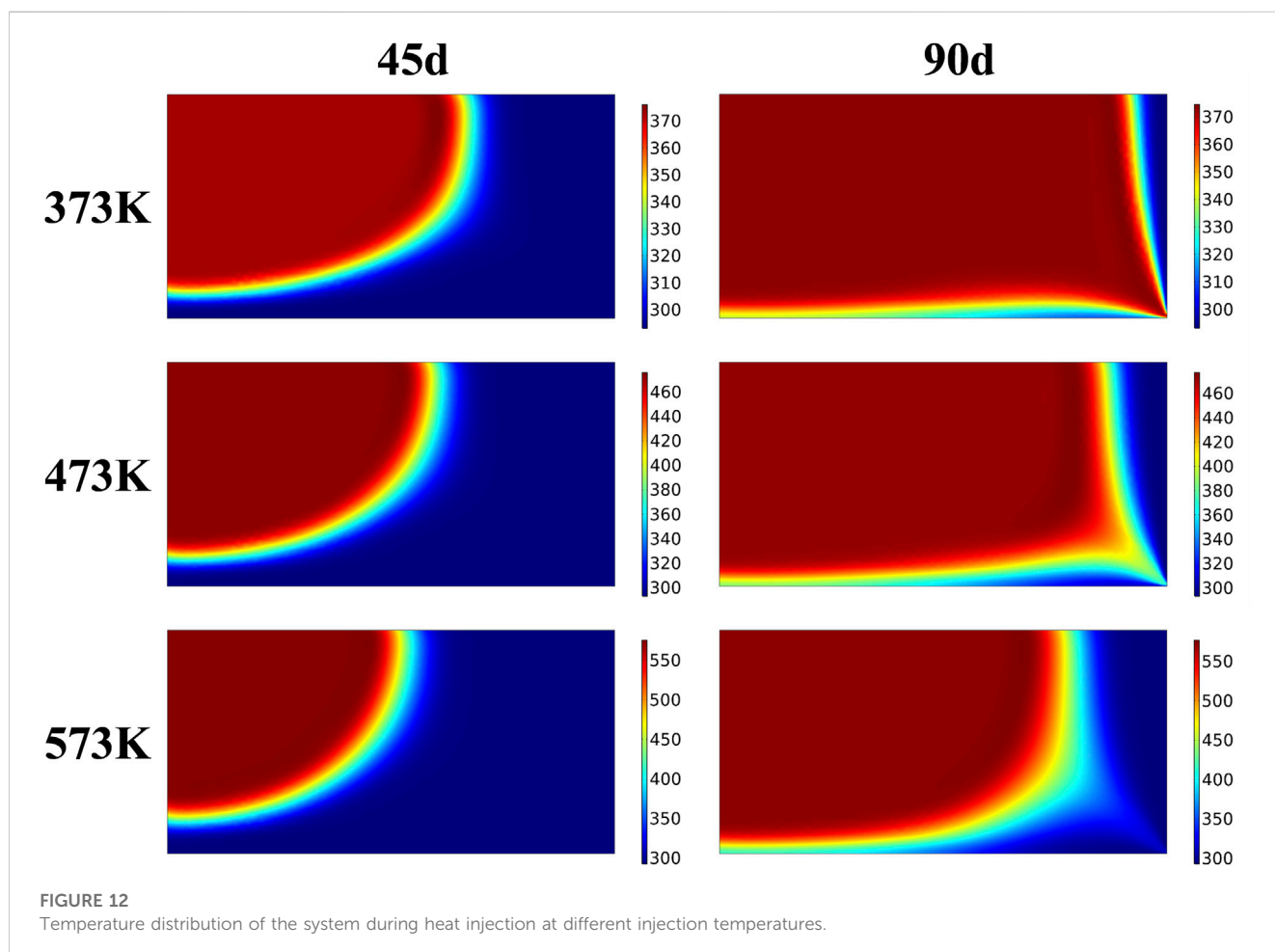


storage system was in operation for 225 days, i.e., 45 days of heat production, the temperature nephogram shows a “saddle” distribution at 1 MPa injection pressure, with the left injection

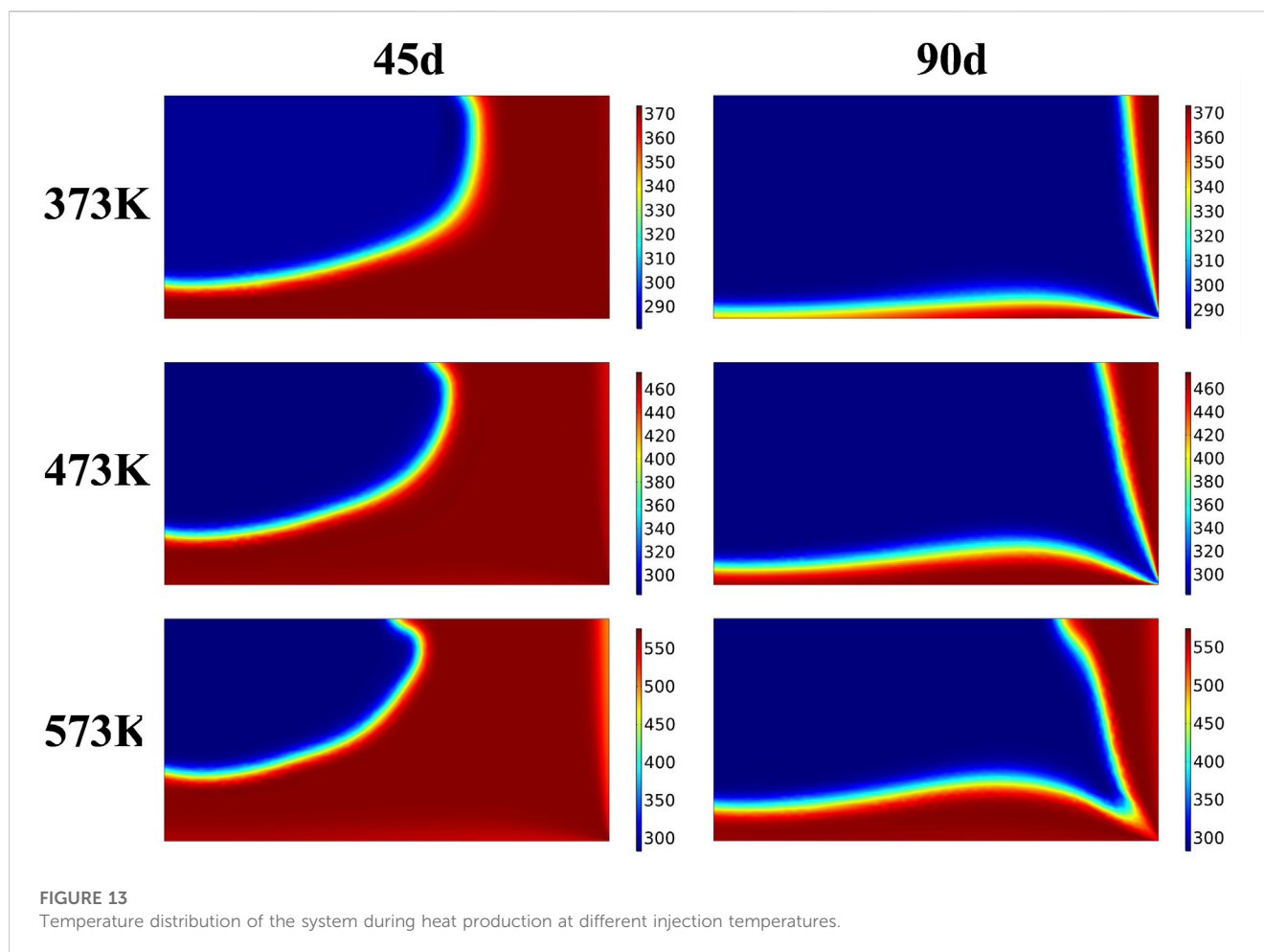
region and the right wall region being the low-temperature regions, and the middle region of the bed still having a higher temperature. With the increase of injection pressure, the cold fluid pushes the high-temperature region towards the outlet direction at the same heat production time. The rock bed is divided into three regions: high-temperature region, low-temperature region and thermocline. When the heat storage system operates for 315 days, the temperature of the rock bed basically decreases to 300 K at 2–4 MPa injection pressure, and the heat production process basically ends. In practical engineering, the design of the heat storage system can be optimized to extract the heat in the upper right region.

#### 4.3 The influence of CO<sub>2</sub> injection temperature on the heat storage capacity of rock bed

Figure 11 shows the variation of the heat storage capacity of the rock bed heat storage system with the heat injection time at different CO<sub>2</sub> injection temperatures under 2 MPa injection pressure. It can be seen that, in the same 180-day heat injection time, the heat energy storage capacity gradually increases with the increase of injection temperature. The trend of the heat energy storage curve of the rock bed under different







injection temperatures is roughly the same during the 180-day heat injection process, rising steadily first, reaching the upper limit of the heat energy storage capacity, and then entering the stable stage. In the 180-day heat production time, it is smoothly decreasing first and slowly decreases at last.

At the injection temperature of 373 K, the heat storage system basically reaches saturation at 90 days of heat injection, and the maximum heat storage capacity is 2 MW·h; at the injection temperature of 473 K, the rock bed heat storage system also basically reaches saturation at 90 days, and the maximum heat storage capacity is 8 MW·h; when the injection temperature is 573 K, the increase rate of heat storage capacity in the heat storage system starts to slow down at 150 days, and the maximum heat storage is about 18 MW·h. The above results are due to the fact that increasing the injection temperature increases the temperature gradient between CO<sub>2</sub> and the rock bed, which increases the time to reach heat equilibrium in the rock bed, and the stored heat increases simultaneously. In the actual heat storage system, it is necessary to choose a suitable injection temperature according to the injection pressure, which can reduce the time of heat storage of the whole system on the one hand, and avoid the waste of heat-carrying gas on the other hand, so as to achieve the maximum economic benefit.

Figures 12, 13 show the temperature distribution nephograms of the rock bed heat storage system with injection temperatures of 373 K, 473 K, and 573 K at 45 and 90 days of heat injection and 45 and 90 days of heat production, respectively. It can be seen that the proportion of the high-temperature region decreases with the increase of the injection temperature in the same heat injection time. It is because the increase in injection temperature increases the temperature gradient between CO<sub>2</sub> and rock increase, which increases the time for the rock bed to reach heat equilibrium. In the same heat production time, because the heat production gas temperature is the same, the difference in temperature nephogram is related to the highest temperature reached in heat injection. The bulge direction of the low-temperature region during heat production is basically the same as that during heat injection when using low heat injection temperature. In contrast, at high heat injection temperature, the bulge direction of the low-temperature region during heat production tends to the right wall, which is especially obvious on the 45th day of heat production at 473 K and 573 K. It is because the increase of heat injection temperature increases the temperature gradient between CO<sub>2</sub> and rock, thus increasing the thermal strain of rock and the deformation of the rock bed under thermal action, which leads to the change of the gas flow direction during heat production.

## 5 Conclusion

In this paper, a thermal-hydraulic-mechanical coupling model of porous media for broken rock bed is established, and the correctness of the model is verified by comparing it with an experiment. This paper simulated the heat injection and production process of a large-sized rock bed heat storage system, analyzed the influence of CO<sub>2</sub> injection pressure and temperature on the heat storage efficiency and heat storage capacity of broken rock bed, respectively, and obtained the following conclusions:

- (1) A porous media model was established based on the control equations of porous media deformation, seepage and heat transfer, and the heat injection and production process under the actual experimental condition was simulated. The numerical values and trends obtained from the simulation and experiment are in good agreement, which is of great significance for the simulation and analysis applicable to the field conditions and large-sized rock bed heat storage system.
- (2) Using the thermal-hydraulic-mechanical coupling model to simulate the heat injection and production process of a large-sized rock bed thermal storage system. The results show that, with the increase of CO<sub>2</sub> injection pressure, the time for the rock bed to reach the maximum heat storage capacity during heat injection decreases, and the time for heat production of the heat storage system also decreases. When the injection temperature is certain, the maximum heat storage capacity of the rock bed heat storage system is also certain. With the increase in CO<sub>2</sub> injection temperature, the maximum heat storage capacity of the rock bed heat storage system increases, but the temperature gradient between CO<sub>2</sub> and the rock bed increases, leading to an increase in heat injection and heat production time.
- (3) When the CO<sub>2</sub> injection pressure is low, the input and output of heat storage in the rock bed are relatively smooth, and the heat storage capacity only has two stages of “slow rise—slow fall,” so the heat storage system can be designed to operate in two stages of “heat storage—heat production” all year round, and the problem of low heat storage capacity can be solved by increasing the CO<sub>2</sub> injection temperature. When the CO<sub>2</sub> injection pressure is high, the heat storage capacity of the heat storage system has four stages “rapid increase—stability—rapid decrease—stability”. So under higher injection pressure, the operation mode of the rock bed heat storage system can be changed to “heat storage—heat preservation—heat production—shutdown”. Therefore, it is possible to choose different operation modes according to

the actual demand to achieve the purpose of economic operation.

## Data availability statement

The raw data supporting the conclusion of this article will be made available by the authors, without undue reservation.

## Author contributions

HG and YW designed the study and wrote the manuscript. HG, YW, GH, and YH obtained and analyzed data for the research. HG, DL, and HZ prepared the figures. All authors contributed to the discussion of research results and manuscript revision.

## Funding

This work was supported by the National Natural Science Foundation of China (Grant No. 51674247).

## Acknowledgments

The authors thank State Key Laboratory for Geomechanics and Deep Underground Engineering for providing experimental equipment. It is also grateful for the financial support provided by the National Natural Science Foundation of China.

## Conflict of interest

The authors declare that the research was conducted in the absence of any commercial or financial relationships that could be construed as a potential conflict of interest.

## Publisher's note

All claims expressed in this article are solely those of the authors and do not necessarily represent those of their affiliated organizations, or those of the publisher, the editors and the reviewers. Any product that may be evaluated in this article, or claim that may be made by its manufacturer, is not guaranteed or endorsed by the publisher.

## References

- Akgiray, O., and Saatci, A. M. (2001). A new look at filter backwash hydraulics. *Water Sci. Technol. Water Supply* 1 (2), 65–72. doi:10.2166/ws.2001.0022
- Allen, K. G., Von Backstr, M. T. W., and Kr Ger, D. G. (2013). Packed bed pressure drop dependence on particle shape, size distribution, packing arrangement and roughness. *Powder Technol.* 246, 590–600. doi:10.1016/j.powtec.2013.06.022
- Allen, K. G., Von Backstr, M. T. W., and Kr Ger, D. G. (2014). Packed rock bed thermal storage in power plants: Design considerations. *Energy Procedia* 49, 666–675. doi:10.1016/j.egypro.2014.03.072
- Atrens, A. D., Gurgunri, H., and Rudolph, V. (2010). Electricity generation using a carbon-dioxide thermosiphon. *Geothermics* 39, 161–169. doi:10.1016/j.geothermics.2010.03.001
- Biot, M. A. U. R. I. C. E. A. (1941). General theory of three-dimensional consolidation. *J. Appl. Phys.* 12 (2), 155–164. doi:10.1063/1.1712886
- Biot, M. A. U. R. I. C. E. A. (1954). Theory of stress-strain relations in anisotropic viscoelasticity and relaxation phenomena. *J. Appl. Phys.* 25 (11), 1385–1391. doi:10.1063/1.1721573

- Brown, D. (2000). "A hot dry rock geothermal energy concept utilizing supercritical CO<sub>2</sub> instead of water[C] IIAnon," in Proceedings of the Twenty-Fifth Workshop on Geothermal Reservoir Engineering (Stanford, CA, USA: Stanford University), 6.
- Bu, W. (2012). Experimental study of permeability of broken rock sampled from strata containing faults[J]. *J. Exp. Mech.* 27 (04), 469–473.
- Chen, H. Y., and Teufel, L. W. (1997). Coupling fluid-flow and Geomechanics in dual-porosity modeling of naturally fractured reservoirs [M]. oil field.
- Dong, X., Geng, H. Z., Hao, G., Li, P., Teng, Y., Zhang, W., et al. (2021). Numerical simulation on heat recovery efficiency of different working fluids in high-temperature rock mass[J]. *Geofluids* 2021, 1468825.
- Ergun, S. (1952). Fluid flow through packed columns [J]. *J. Mater. Sci. Chem. Eng.* 48 (2), 89–94.
- Furnas, C. C. (1930). Heat transfer from a gas stream to a bed of broken solids—ii<sup>1-2</sup>. *Industrial Eng. Chem.* 22 (7), 721–731. doi:10.1021/ie50247a008
- Gatmiri, B., and Delage, P. (1997). A formulation of fully coupled thermal-hydraulic-mechanical behaviour of saturated porous media—numerical approach. *Int. J. Numer. Anal. Methods Geomechanics* 21 (3), 199–225. doi:10.1002/(sici)1096-9853(199703)21:3<199::aid-nag865>3.0.co;2-m
- Ha, L. T., and Saha, T. K. (2004). "Investigation of power loss and voltage stability limits for large wind farm connections to a subtransmission network[C]," in Power Engineering Society General Meeting (IEEE).
- Jiang, Tao (2011). *Damage analysis of water injection layer and casing based on thermal hydraulic mechanical coupling model[D]*. Northeast Petroleum University, Daqing, China.
- Leena, K. (2008). World wide EOR survey[J]. *Oil Gas J.* 106 (15), 47–59.
- Li, J. L., Jin, W. T., Hui, D., and Zhang, Y. (2016). The typical application and technology trend of large-scale energy storage in renewable energy generation [J]. *Electr. Energy Manag. Technol.* (14), 7.
- Li, S., and Dai, Y. (2014). Thermo-economic comparison of Kalina and CO<sub>2</sub> transcritical power cycle for low temperature geothermal sources in China[J]. *Appl. Therm. Eng.* 70 (1), 139–152. doi:10.1016/j.applthermaleng.2014.04.067
- Liu, G. J., Han, L. P., Wang, Y. P., and Jiang, J. Z. (2018). Research progress of solid thermal storage technology [J]. *Appl. Energy Technol.* (03), 1–4.
- Markevich, N. J., and Cecilio, C. B. (2015). *Through-flow analysis for rockfill dam stability evaluations[C] Waterpower'91: A New View of Hydro Resources*. San Francisco: ASCE, 1991, 1734–1743.
- Piwko, R., Miller, N., Sanchez-Gasca, J., Yuan, X., Dai, R., and Lyons, J. (2009). "Integrating large wind farms into weak power grids with long transmission lines[C]," in 2006 CES/IEEE 5th International Power Electronics and Motion Control Conference (IEEE).
- Pruess, K. (2006). Enhanced geothermal systems(EGS) using CO<sub>2</sub> as working fluid: A novel approach for generating renewable energy with simultaneous sequestration of carbon[J]. *Geothermics* 35, 351–367. doi:10.1016/j.geothermics.2006.08.002
- Pruess, K. (2008). On production behavior of enhanced geothermal systems with CO<sub>2</sub> as working fluid[J]. *Energy Convers. Manag.* 49, 1446–1454. doi:10.1016/j.enconman.2007.12.029
- Savage, W. Z., and Braddock, W. A. (1982). A model for hydrostatic consolidation of Pierre shale. *Int. J. Rock Mech. Min. Sci. Geomechanics Abstr.* 28 (5), 345–354. doi:10.1016/0148-9062(91)90073-u
- Schumann, T. E. W. (1929). Heat transfer: A liquid flowing through a porous prism. *J. Frankl. Inst.* 208 (3), 405–416. doi:10.1016/s0016-0032(29)91186-8
- Shang, H. (2017). *Experimental study on fluid-solid coupling seepage stability of broken coal and rock[D]*. Xi'an University of Science and Technology, Xi'an, China. (in Chinese).
- Shen, Z., Wang, H., and Li, G. (2010). Feasibility analysis of coiled tubing drilling with supercritical carbon dioxide. *Petroleum Explor. Dev.* 37 (06), 743–747. doi:10.1016/s1876-3804(11)60008-6
- Shu, B., Zhu, R., Elsworth, D., Dick, J., Liu, S., Tan, J., et al. (2020). Effect of temperature and confining pressure on the evolution of hydraulic and heat transfer properties of geothermal fracture in granite. *Appl. Energy* 272, 115290. doi:10.1016/j.apenergy.2020.115290
- Terzaghi, K. T. (1943). *Theoretical soil mechanics*. M. INC, Cambridge, Mass., USA.
- Tortike, W. S., and Ali, S. M. F. (1987). *A framework for multiphase nonisothermal fluid flow in a deforming heavy oil reservoir[Z]*.
- Tortike, W. S., and Ali, S. (1991). Prediction of oil sand failure due to steam-induced stresses [J]. *J. Can. Petroleum Technol.* 30 (01), 87–96.
- Vaziri, H. H. (1988). *Coupled Fluid Flow And Stress Analysis Of Oil Sands Subject To Heating[J]*. Journal of Canadian Petroleum Technology 27 (05).
- Wang, H. Z., Li, G. S., Zheng, Y., Sepehrnoori, K., Shen, Z. H., Yang, B., et al. (2020). Research status and prospects of supercritical CO<sub>2</sub> fracturing technology[J]. *Acta Pet. Sin.* 41 (01), 116–126.
- Wang, M. L., Miao, S., Maji, A. K., and Hwang, C. L. (1992). Effect of water on the consolidation of crushed rock salt: Engineering mechanics, 531–534.
- Wu, Y., Geng, H. Z., Hao, G., and Li, D. (2022). Experimental study on heat exchange efficiency of rock bed heat storage system based on broken rock mass. *ENERGY Rep.* 8, 12456–12465. doi:10.1016/j.egy.2022.08.274
- Wu, Y., Li, P., Hao, Y., Wanniarachchi, A., and Peng, S. H. (2021). Experimental research on carbon storage in a CO<sub>2</sub>-Based enhanced geothermal system[J]. *Renew. Energy*, 175.
- Yang, W., Wang, S., and Chen, J. (2015). Preliminary study on laws of steady state seepage of gas in over-broken rock mass[J]. *Coal Technol.* 34 (006), 189–191. (in Chinese).
- Zavattoni, S., Barbato, M., Pedretti, A., and Zanganeh, G. (2011). CFD simulations of a pebble bed thermal energy storage system accounting for porosity variations effects: SolarPaces-2011. *Granada, Spain*.



## OPEN ACCESS

## EDITED BY

Liang Chen,  
China University of Mining and  
Technology, China

## REVIEWED BY

Gang Lin,  
École Normale Supérieure, France  
Qihong Wu,  
Chengdu University, China

## \*CORRESPONDENCE

An Chen,  
✉ 20140025@kust.edu.cn  
Kexin Yin,  
✉ kexin.yin@nuaa.edu.cn

## SPECIALTY SECTION

This article was submitted to  
Environmental Informatics  
and Remote Sensing,  
a section of the journal  
Frontiers in Earth Science

RECEIVED 20 November 2022

ACCEPTED 13 March 2023

PUBLISHED 23 March 2023

## CITATION

Meng J, Chen A, Yin K and Zhou C (2023),  
Study on the clogging mechanism of  
upward inclined drainage holes in  
cut slopes.  
*Front. Earth Sci.* 11:1103323.  
doi: 10.3389/feart.2023.1103323

## COPYRIGHT

© 2023 Meng, Chen, Yin and Zhou. This is  
an open-access article distributed under  
the terms of the [Creative Commons  
Attribution License \(CC BY\)](https://creativecommons.org/licenses/by/4.0/). The use,  
distribution or reproduction in other  
forums is permitted, provided the original  
author(s) and the copyright owner(s) are  
credited and that the original publication  
in this journal is cited, in accordance with  
accepted academic practice. No use,  
distribution or reproduction is permitted  
which does not comply with these terms.

# Study on the clogging mechanism of upward inclined drainage holes in cut slopes

Jian Meng<sup>1,2</sup>, An Chen<sup>2,3,4\*</sup>, Kexin Yin<sup>5\*</sup> and Caihui Zhou<sup>6</sup>

<sup>1</sup>Kunming Prospecting Design Institute of China Nonferrous Metals Industry Co., Ltd., Kunming, China,

<sup>2</sup>Faculty of Land Resources Engineering, Kunming University of Science and Technology, Kunming, China,

<sup>3</sup>Yunnan Key Laboratory of Geohazard Forecast and Geocological Restoration in Plateau Mountainous Area, Kunming, China, <sup>4</sup>Key Laboratory of Geohazard Forecast and Geocological Restoration in Plateau Mountainous Area, Ministry of Natural Resources of the People's Republic of China, Kunming, China,

<sup>5</sup>Department of Civil and Airport Engineering, Nanjing University of Aeronautics and Astronautics, Nanjing, China, <sup>6</sup>Yunnan Geological Exploration and Development Corporation, Kunming, China

Since groundwater is one of the main factors that affect the stability of highway slopes in mountainous regions, a smooth drainage is of importance for the safety of cut slopes. After years of service, the cut slopes of highway are often characterized with drainage problems or even drainage failures that threaten the stability and safety. In this paper, the clogging mechanism of drainage holes in highway cut slopes is firstly clarified through on-site survey. The soil and blockage samples are collected from typical slopes for laboratory tests and analysis, and the results reveal that all the blockages are made of fine-grained particles from the slopes. Scanning electron microscope (SEM) images indicate that the blockages penetrate the drainage pipe wrappings to form the clogging. The combined effect of clayey soil, chemicals, and biological clogging exacerbate the clogging process around the drainage pipes. Laboratory tests are also performed to simulate the CaCO<sub>3</sub> crystal clogging around the drainage holes, and the microstructure of the clogged geotechnical screens and geotextiles is observed by scanning electron microscope as well. The results confirm that the amount of CaCO<sub>3</sub> crystal attached to the drainage pipe surface increases with the time. The single-layer structure of screens does not facilitate the three-dimensional clogging as in the case of geotextiles. After soaking in diluted hydrochloric acid at a pH of 5.0, there is no significant decrease of CaCO<sub>3</sub> crystals attached on the screens and geotextiles. However, the CaCO<sub>3</sub> decrease is apparent after soaking in the hydrochloric acid at a pH of 3.0. The clogging of drainage holes can be classified into two stages according to the laboratory tests and acid soaking, and the relationship and characteristics between the two stages are summarized.

## KEYWORDS

highway cut slope, underground water, drainage hole, clogging mechanism, CaCO<sub>3</sub> crystal, microstructure

## 1 Introduction

The stability slope is a major issue for the highway engineering in mountainous area (Pantelidis, 2009; Subramanian et al., 2017; Latief and Zainal, 2019; Liu et al., 2021; Tsao et al., 2021). Since groundwater is one of the main factors that affect the deformation and stability of slopes, ensuring a smooth drainage is essential for the safety slopes (Castro et al., 2020; Nistor et al., 2020; Zhang et al., 2020; He et al., 2021). Water-rich slopes widely exist in highway engineering in South China. Due to the large annual precipitation, long rainy season, and high

groundwater level, the rock-soil body of the slope is often immersed below the groundwater level for a long period. The physical, chemical, and mechanical erosion induced by the groundwater have a coupled effect on the stability of rock-soil body in the slope (Jiao et al., 2005; Wu et al., 2008). Under the long-term action of groundwater, some components in the rock-soil materials may be washed away (Gu et al., 2015). As a result, the structural plane strength that determines the stability of the rock-soil body decreases, and the stability of the slope declines finally. The hydrodynamic pressure generated by the groundwater seepage increases the sliding force of the rock-soil mass within the slope. At the same time, the buoyancy effect of the high groundwater level decreases the slipping resistance of the rock-soil mass, which in turn leads to a decrease on the stability (Santoso et al., 2011; Zhang et al., 2011; Kaczmarek and Popielski, 2019).

In addition to the regular reinforcements, drainage devices on the surface or in the deep part of the cut slopes are often installed. For instance, the upward inclined drainage holes are the most widely used method (Cahyadi et al., 2018; Hongyue et al., 2019; Sun et al., 2021). Upward inclined drainage holes are usually installed by drilling holes with a small upward inclination from the slope surface into the deep part and inserting plastic drainage pipes into the holes for draining water (Guo et al., 2018). The plastic pipes could be unperforated to allow a water drainage from the end part inside the slope or collect drainage from the perforated section. Perforated drainage pipes are specially designed to prevent clogging or failure (Cao et al., 2021), for instance, to have a geotextile wrapped around (Mininger, 2010; Guo et al., 2018). After several years' running, cut slopes of early-built highways are often with problems of poor drainage or even drainage failures, resulting in unguaranteed stability and safety (Guo et al., 2018; Zhang et al., 2020). Therefore, studying the formation and development mechanism of the clogging in upward inclined drainage holes is of great significance for investigating new technologies to prevent or delay the clogging process, and to extend the effectiveness of drainage holes. It is also important for the stability of the cut slopes.

So far there is no literature to present detailed research on the clogging mechanism of the upward inclined drainage holes. In this paper, the slope drainage holes were investigated firstly by the on-site survey to locate the serious and typical drainage clogging sections for further study. The representative clogged drainage holes under different geological conditions were compared to determine the similarities and differences of the clogging mechanisms. The rock-soil mass, blockage soils, and water in the typical sections with clogged drainage holes were sampled and then analyzed in laboratory. Then, the chemical clogging tests were conducted with a consideration on the design and operation conditions of the upward inclined drainage holes, in order to reveal the chemical clogging mechanism and the development rules. The clogging of drainage holes can be classified into two stages according to the on-site survey, chemical clogging tests, and comprehensive analysis.

## 2 On-site survey and analysis

### 2.1 On-site survey

The highway section studied herein is on the Beijing-Hong Kong-Macau Expressway, starting from Xiaotang at the junction of

Hunan and Guangdong and ending at Gantang in the western suburbs of Shaoguan, with a total length of 109.9 km. The section was constructed from October 1998 to April 2003. An on-site survey of this studied area shows that the expressway is in a region with complicated geology conditions. The lithology conditions are highly heterogeneous, which is mainly consist of sandstone, siltstone, and argillaceous sandstone, with locally distributed shale, carbonaceous shale, and heavily weathered coal seam. The groundwater is mainly fissure water, and water seepage and mudflow widely exist on some parts of the slope. The middle section is karst-developed limestone with high liquid limit soils overlying. The studied section is rich in groundwater, and there is an outcrop of groundwater on many slopes along the expressway. In addition, karst caves and collapses can be found in the local region, and most of the groundwater is fissure water or karst water. The frequent landslides and other undesirable geological hazards are common to encounter such as debris flow or collapse in the research area, which pose high potential risks to the stability of the slopes and the serviceability of the highway.

The slopes studied in the paper are characterized with poor drainage or drainage failure, and the old drainage holes have worked more than 10 years (see Figure 1). Most of the clogged drainage holes are blocked with fine-grained soil, and chemical crystallization can be found in the blockages. Most of the drainage holes show traces of algae and other organisms on the surface. Preliminary analysis during the on-site survey shows that the main reasons for the clogging and drainage failure of the upward inclined holes are summarized as follows.

- 1) The composition of the rock-soil mass varies greatly, and the transfer of particles and chemical crystals within the slope can easily induce mechanical or chemical clogging in the drainage holes and on the geotextile.
- 2) There are obvious seasonal variations in the groundwater level of the slope. The upward inclined drainage holes work intermittently, i.e., only in rainy seasons or non-rainy seasons with sudden heavy rainfall. Thus, the geotextile is exposed to the atmosphere for a long period of time. Biological activities and variations in the redox environment can easily cause chemical and biological clogging on the geotextile. The mutual effect between physical, chemical, and biological clogging eventually accelerates the clogging process of the drainage holes.
- 3) Since the geotextile wrapped around the drainage pipes cannot be cleaned or replaced after the installation, the clogging continues until the drainage holes fail to work. In this way, the geotextile wrapped cannot prevent the clogging in the long time of running.

Most of the drainage holes in the research area are characterized by different degrees of clogging, and nine typical slope sections with serious drainage clogging were selected for further research. The drainage clogging in the selected slopes distributed in the three typical geological sections was statistically analyzed. As shown in Table 1, the slopes in all three sections show serious clogging problem. Cracks appear on the slopes, and groundwater seeps out through these cracks due to the failed drainage holes. The cracks and groundwater seepage decrease the stability of the slopes.

Based on the analysis on the long-time running drainage holes, most of the serious clogging occurred after about 3 years of working.





**FIGURE 1**  
Inclined drainage holes with poor drainage and clogging problem: (A) red clogging soil with plants; (B) brown clogging soil; (C) soft drainage pipe with red clogging soil; (D) clogging materials after rainfall; (E) totally clogging drainage holes; (F) red clogging soil near the drainage holes

**TABLE 1** Cut slopes with clogged drainage.

No.	Marked work point number	Section with clogged drainage	Brief description of clogging
1	K1849+980~K1850+240 Right side slope	K1850+20~150 Primary slope	Water seepage and mudflow off the slope
2	K1858+930~K1859+260 Right side slope	K1858+950~K1859+000 Primary slope	Water seepage and mudflow off the slope
3	K1863+080~430 Left side slope	K1863+100~250 Primary slope	Water seepage and water flow from the retaining wall
		K1863+100~250 Secondary slope	Water seepage at the foot of the secondary slope
		K1863+100~250 Tertiary slope	Water seepage off the sidewall and anchor head of the slope
4	K1873+180~+350 Left side slope	K1873+270~310 Tertiary slope	Spalling of the mortared flagstone
5	K1876+280~670 Right side slope	K1876+430~+480 Primary slope	Local water seepage and mudflow, lush vegetation on the primary platform
		K1876+380~480 Secondary slope	Frequent water seepage and mudflow
6	K1881+160~300 Left side slope	K1881+200~240 Secondary slope	Water seepage in the middle and lower parts
		K1881+180~230 Foot of the slope	Water gushing at the roadbed side drainage ditch
7	K1918+225~385 Left side slope	K1918+225~385 Primary slope retaining wall	Perennial water flow at the lower and middle parts
8	K1925+550~875 Left side slope	K1925+550~875 Primary retaining wall	Multiple poor groundwater drainage
		K1925+550~875 Primary slope	Abundant water in the drainage ditch during the rainy season and water gushing off the masonry on both sides
9	K1941+000~440 Left side slope	K1941+000~440 Primary retaining wall	Severe water seepage

The average clogging time is 3.2 years according to a standard that the holes cannot drain water after a rainfall (see [Table 2](#)). New drainage holes are constructed on the clogging zone for later study and the stability of the slopes.

To analyze the typical clogging, three soil and three water samples were collected from each typical slope with clogged drainage holes for laboratory tests. The inner pipes were extracted from the representative clogged drainage holes, and the

**TABLE 2** The information of the clogged drainage holes.

No.	Section with clogged drainage	The total number of drainage holes (–)	Average time to clogging (year)
1	K1850+20–150 Primary slope	86	2.81
2	K1858+950~K1859+000 Primary slope	34	3.01
3	K1863+100–250 Primary slope	98	2.51
	K1863+100–250 Secondary slope	98	2.88
	K1863+100–250 Tertiary slope	49	2.76
4	K1873+270–310 Tertiary slope	26	3.13
5	K1876+430~+480 Primary slope	30	2.93
	K1876+380–480 Secondary slope	60	3.21
6	K1881+200–240 Secondary slope	24	2.55
	K1881+180–230 Foot of the slope	16	2.01
7	K1918+225–385 Primary slope retaining wall	106	2.35
8	K1925+550–875 Primary retaining wall	160	3.35
	K1925+550–875 Primary slope	216	3.62
9	K1941+000–440 Primary retaining wall	220	4.11

blockage materials in the clogged drainage holes were also sampled for laboratory tests and analysis.

## 2.2 Analysis of drainage hole clogging mechanism

### 2.2.1 Analysis of blockage particles

Soil samples of the three typical slopes and their drainage hole blockages were collected for granulometric analysis. The particle size distribution curves were then obtained. Three slope soil samples and three drainage hole blockage samples were collected from each typical slope for testing, and the average values of every three samples were adopted for further analysis. The particle diameter of the slope soil varies greatly, while the blockages mostly consist of fine particles. Thus, both the sieving and densitometer methods were used to analyze the particle size distribution of the soil particles. As shown in [Figure 2](#), the particle distribution curves from the average data of the three typical slope soil samples and the corresponding drainage hole blockages are compared: i.e., the right-side slope of K1858+930~K1859+260, the right-side slope of K1876+280–670, and the left-side slope of K1925+550–875 are presented here. The mark number K1858+930~K1859+260, K1876+280–670, and K1925+550–875 are renamed hereafter as K1858, K1876, and K1925, respectively.

According to the results from the above tests, the particle composition of the soil samples and drainage blockages of the three selected slopes is as follows.

- 1) The right-side slope of section K1858 is made of silty clay with grain size distribution shown in [Figure 2A](#), in which the average soil content with a diameter below 0.075 mm is 66.0%. The drainage hole blockages are mainly clay, and

the content of soils with a diameter below 0.075 mm is 88.4% ([Figure 2A](#)).

- 2) The right-side slope of section K1876 is made of clay with grain size distribution shown in [Figure 2B](#), in which the average content of particles below 0.075 mm is 69.5%. The drainage hole blockages are fine-grained soil ([Figure 2B](#)) with a diameter lower than 2 mm, of which the total content of particles below 0.075 mm is 83.2%.
- 3) The soil sample from the left slope of section K1925 is silt, mainly composed of sand and clay, and the content of soil particles below 0.075 mm is 39.8% ([Figure 2C](#)). The drainage hole blockages are mainly silt and clay, and the content of particles below 0.075 mm is 71.4% ([Figure 2C](#)).

Except for the left slope of the section K1925, the fine particle content in the soil of the other two slopes with clogged drainage holes is high, and the content of fine particles below 0.075 mm is above 65%. Although the fine particle content of the left slope of section K1925 is 26.2%–29.7% lower than the other two slopes (K1858 and K1876), the corresponding drainage hole blockages of all the three slopes are mainly fine-grained soil at high contents (71.4%–77.4%). The fine particle content in the drainage hole blockages is larger than that of the slope soil. Therefore, the drainage blockages are formed due to the fine particles from the side slope soil that are transported and accumulated by groundwater.

### 2.2.2 Chemical analysis of side slope soil and drainage blockage

Comparative compositional analysis of the slope soil and blockage samples was performed using X-ray fluorescence (XRF), which was simple to operate, non-destructive, fast, and accurate ([Dos Anjos et al., 2000](#); [Silva et al., 2019](#); [Ravansari et al., 2020](#)).

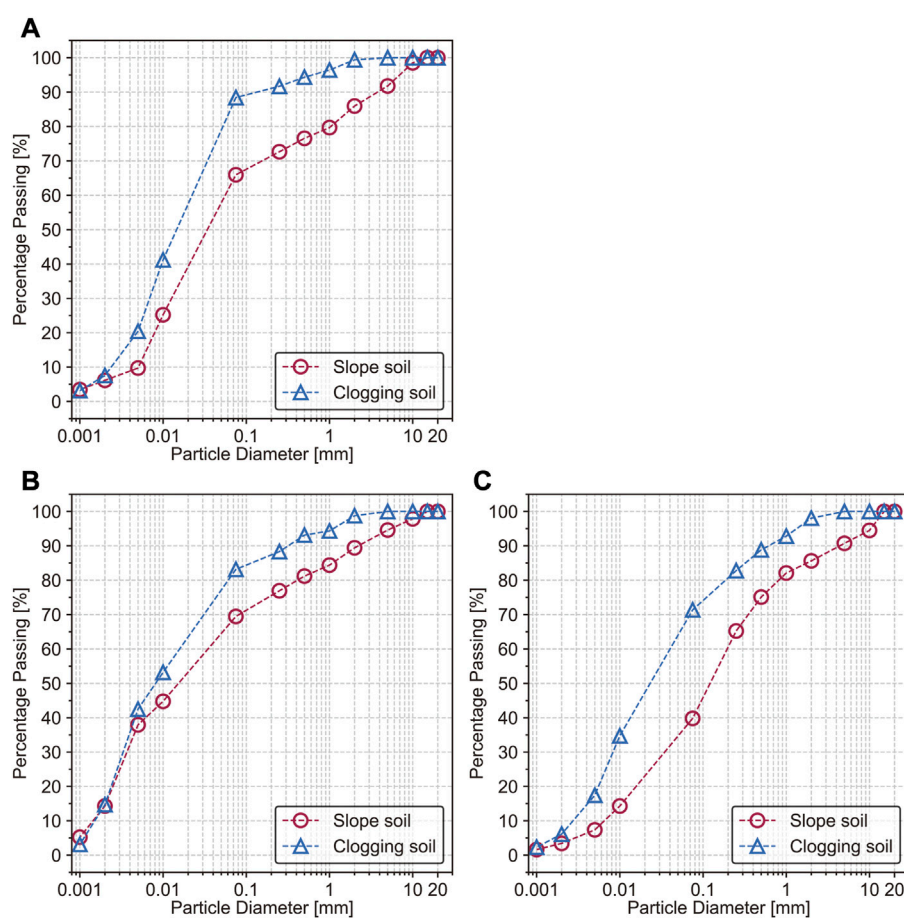


FIGURE 2

The particle size distribution of the three selected slope soil samples and their corresponding drainage hole blockages: (A) section K1858+930~K1859+260; (B) section K1876+280~670; (C) section K1925+550~875.

TABLE 3 Slope soil composition.

Sample	SiO <sub>2</sub>	Al <sub>2</sub> O <sub>3</sub>	Na <sub>2</sub> O	MgO	K <sub>2</sub> O	CaO	MnO	Fe <sub>2</sub> O <sub>3</sub>	TiO <sub>2</sub>	P <sub>2</sub> O <sub>5</sub>	LOI
1858-S	57.2	21.9	0.09	1.87	2.66	0.04	0.02	5.65	0.66	0.05	9.3
1876-S	48.4	18.5	0.13	0.29	1.56	6.2	0.03	10.3	0.17	0.08	13.65
1925-S	50.81	18.4	0.08	1.08	1.24	1.57	0.44	8.51	0.32	0.15	16.42

TABLE 4 Blockage composition.

Sample	SiO <sub>2</sub>	Al <sub>2</sub> O <sub>3</sub>	Na <sub>2</sub> O	MgO	K <sub>2</sub> O	CaO	MnO	Fe <sub>2</sub> O <sub>3</sub>	TiO <sub>2</sub>	P <sub>2</sub> O <sub>5</sub>	LOI
1858-B	19.40	5.50	0.14	0.06	0.24	0.22	0.109	58.71	0.03	0.20	15.41
1876-B	18.05	8.06	0.08	0.16	0.16	46.36	0.004	0.08	0.02	0.01	26.02
1925-B	20.81	7.69	0.20	0.08	0.33	2.25	0.464	49.38	0.14	0.09	18.56

Compositions of the three typical slope soil samples and drainage hole blockages are shown in Table 3 and Table 4, respectively.

According to the on-site survey, the drainage holes of section K1858 are located in a pelitic sandstone section, those of section

K1876 in the limestone section, and those of K1925 in the interbedded strata of shale, mudstone, and sandstone. A comparison of the compositions of soil samples from the three slopes and their drainage hole blockages indicates that.



TABLE 5 Water quality analysis.

No.	Ca <sup>2+</sup> (mg/L)	Mg <sup>2+</sup> (mg/L)	SO <sub>4</sub> <sup>2-</sup> (mg/L)	PH
K1876-1	104.31	15.72	298.82	7.07
K1876-2	126.18	14.51	19.55	7.72
K1876-3	97.58	13.30	184.40	7.17

- 1) The composition of the drainage hole blockages in the three selected sections is the same as the slope soil, mainly silicon and aluminum oxides. Therefore, the clay content in the drainage hole blockages is high. Clay can promote mechanical clogging in the drainage hole. The fine-grained soil is the main material for mechanical clogging of drainage holes, which is also consistent with the results of particle distribution tests.
- 2) The calcium oxide content of the blockages in the limestone section K1876 is significantly higher than that in the corresponding slope soil, which may be attributed to the calcium precipitation around the drainage hole with intermittent groundwater outflow, i.e., the chemical clogging. At the same time, an analysis on the clogging materials in the newly running drainage holes finding that there is nearly no increase on the CaCO<sub>3</sub> crystals, indicating that the chemical clogging is developing in a low rate.
- 3) The iron oxide content of blockages in sections K1858 and K1925 is significantly higher than that in the slope. Therefore, Fourier Transform Infrared Spectroscopy (FTIR) analysis of the

samples is necessary to determine the iron composition (Hahn et al., 2018).

FTIR analysis on the blockage samples from sections K1858 and K1925 shows that the Fe in the blockage from section K1858 is possibly a mixture of Fe(OH)<sub>3</sub> and α-Fe<sub>2</sub>O<sub>3</sub>•H<sub>2</sub>O. While the Fe in samples from K1925 is possibly Fe(OH)<sub>3</sub>. On-site analysis of the water quality shows that the contents of free CO<sub>2</sub>, erosive CO<sub>2</sub>, and total dissolved solids are 50.18 mg/L, 34.17 mg/L, and 547.08 mg/L, respectively, making it moderately corrosive (pH = 4.5). The wire skeleton of flexible drainage pipes is generally corroded, and the same high Fe content is not detected in the blockages without flexible drainage pipes. Therefore, most of the Fe in the blockage comes from the wire skeleton of the flexible drainage pipes (Figure 1C), which is consistent with the conclusion that the ferrous blockage is mainly iron hydroxide and its transformations as indicated in the literature (Wu et al., 2007; Wu et al., 2008). Therefore, flexible drainage pipes have poor suitability for the research slope area.

A large number of calcium oxides is found in the blockages of the limestone section K1876. Water samples were collected from the slopes in this section for quality analysis to identify the chemical clogging mechanism of the drainage holes. The water quality analysis results of the slopes in the limestone section K1876 are shown in Table 5. The results show that all the groundwater within the slopes is SO<sub>4</sub><sup>2-</sup>-Ca<sup>2+</sup>-Mg<sup>2+</sup> water, mostly neutral or alkaline water. However, the contents of SO<sub>4</sub><sup>2-</sup>, Ca<sup>2+</sup>, and Mg<sup>2+</sup> vary significantly in the sampling places.

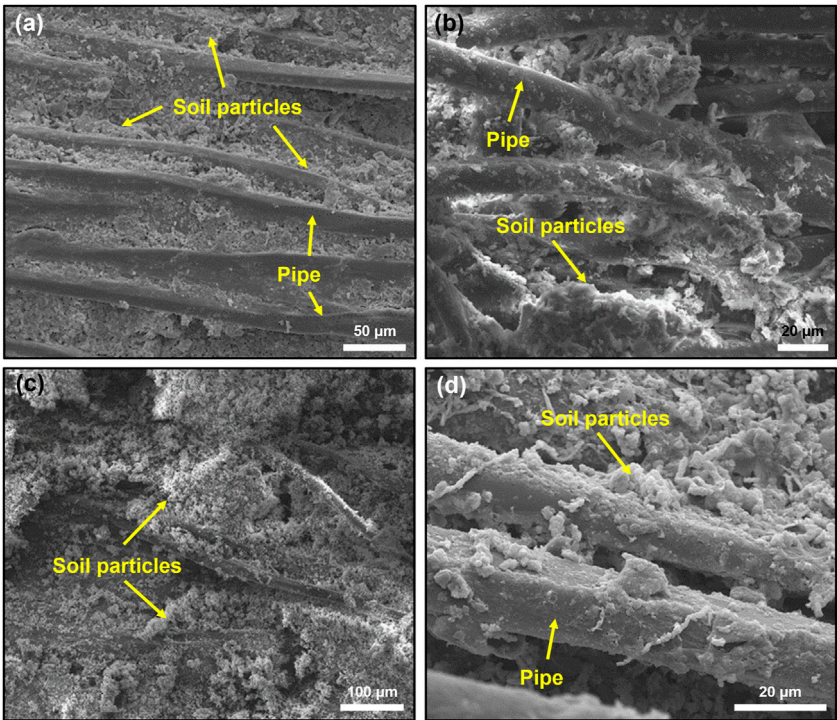
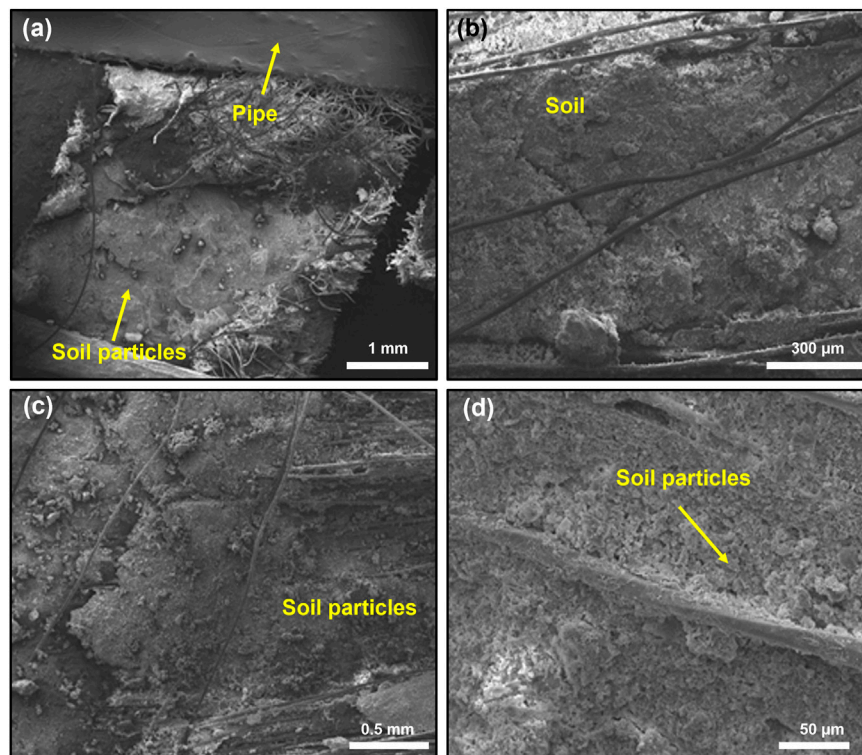
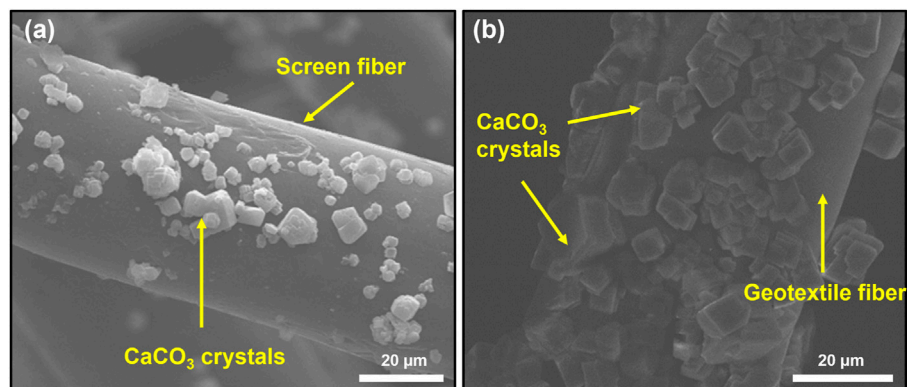


FIGURE 3 SEM images at the outer pipe end: (A), (B) inner surface; (C), (D) outer surface.



**FIGURE 4**  
SEM images of the inner pipe end: (A), (B) inner surface; (C), (D) outer surface.



**FIGURE 5**  
The attachment of  $\text{CaCO}_3$  crystals on: (A) screen; (B) geotextile.

### 2.2.3 Scanning electron microscope test

Scanning electron microscope (SEM) is an effective method to investigate the microstructure of soils (Yin et al., 2019; Yin et al., 2021a; Yin et al., 2021b; Yin et al., 2021c; Yin, 2021). In order to further study the microstructure of the clogged drainage holes, SEM scans were performed on the inner and outer surfaces of the clogged drainage pipes at both ends (i.e., the outer and the inner pipe end). The images of the inner surface of the clogged

drainage pipes are shown in Figures 3A, B, and the outer surface images are presented in Figures 3C, D. The SEM results show significant differences between the blockages on the inside and outside surfaces of the outer section of the drainage pipes. The fiber on the inner surface is still clearly visible, while that on the outer surface is completely covered by the blockage. Therefore, the blockage materials gradually penetrate from the outer surface of the drainage pipes to the inner surface, and eventually reach



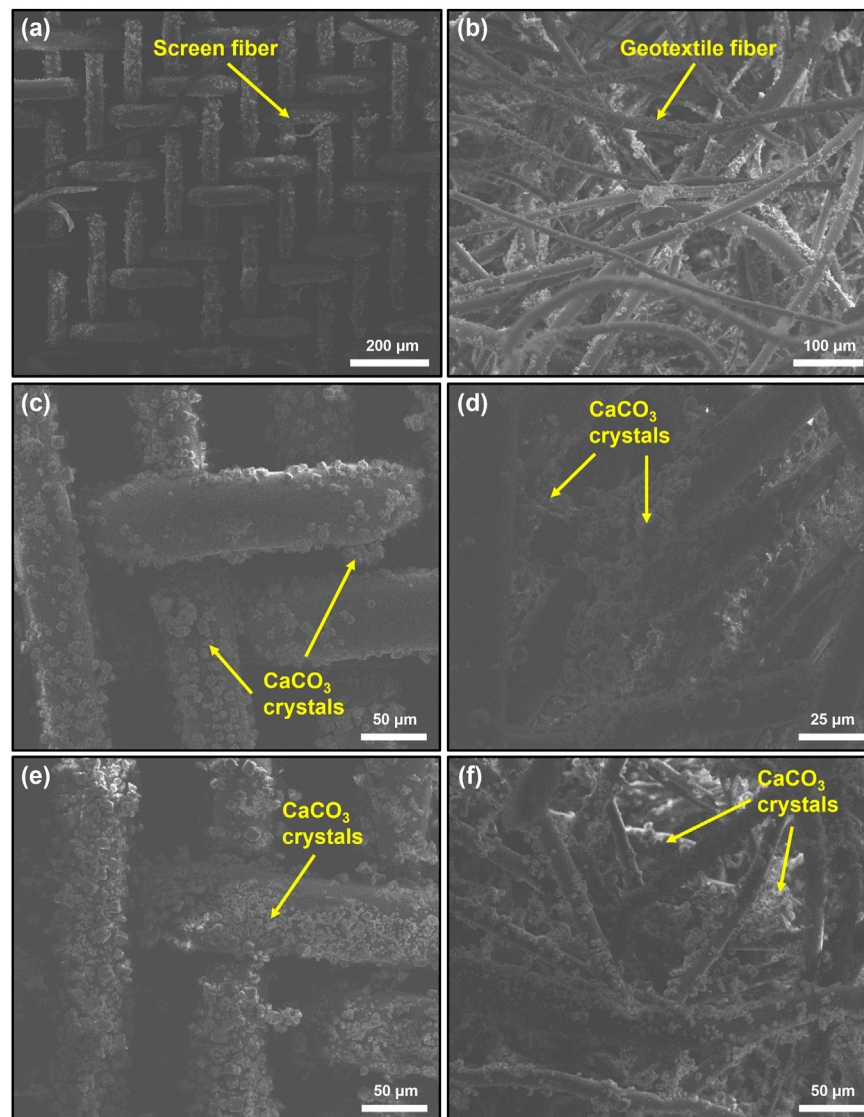


**FIGURE 6**

The screens and geotextiles under different titrations: (A), (B): 3 titrations; (C), (D): 6 titrations; (E), (F): 9 titrations.

saturation on the whole fiber. Thus, blockage materials are prevented from entering the interior and just adhering to the outer surface of the drainage pipes.

Scanning images of the inner and outer surfaces of the inner pipe end are collected in Figure 4. Similar to the scans of the outer ends, at the inner end, fibers are visible on the inner surface but not on the outer surface. SEM images indicate more blockage at the inner end than the outer end of the drainage pipe (see Figure 3 and Figure 4). Therefore, the clogging of the drainage pipe at the inner pipe end is more severe than that at the outer end.

From the SEM images, we can see that the clogging develops from the materials wrapped (geotextile and screen). The fine particles transferred by the underground water accumulate on the wrapped geotextile and screen. More clogging is formed in the bottom of the drainage holes due to the transportation effect of the underground water.

### 3 Chemical clogging test

Since most of the drainage holes work for a short time throughout the year, chemical clogging is often neglected. Few studies focused on the chemical clogging in the side slopes, especially in limestone regions (Luquot et al., 2014). The above analysis on the clogging materials provide proofs for that chemical clogging in limestone regions is mainly in the form of  $\text{CaCO}_3$ . Hence, it is necessary to perform model tests in the laboratory, to investigate the  $\text{CaCO}_3$  chemical clogging mechanism as well as to know the distribution, arrangement and microstructure of the  $\text{CaCO}_3$  crystal. Experiments of chemical clogging with different materials can offer useful information on drainage hole clogging improvements and delay or prevention of the chemical clogging.

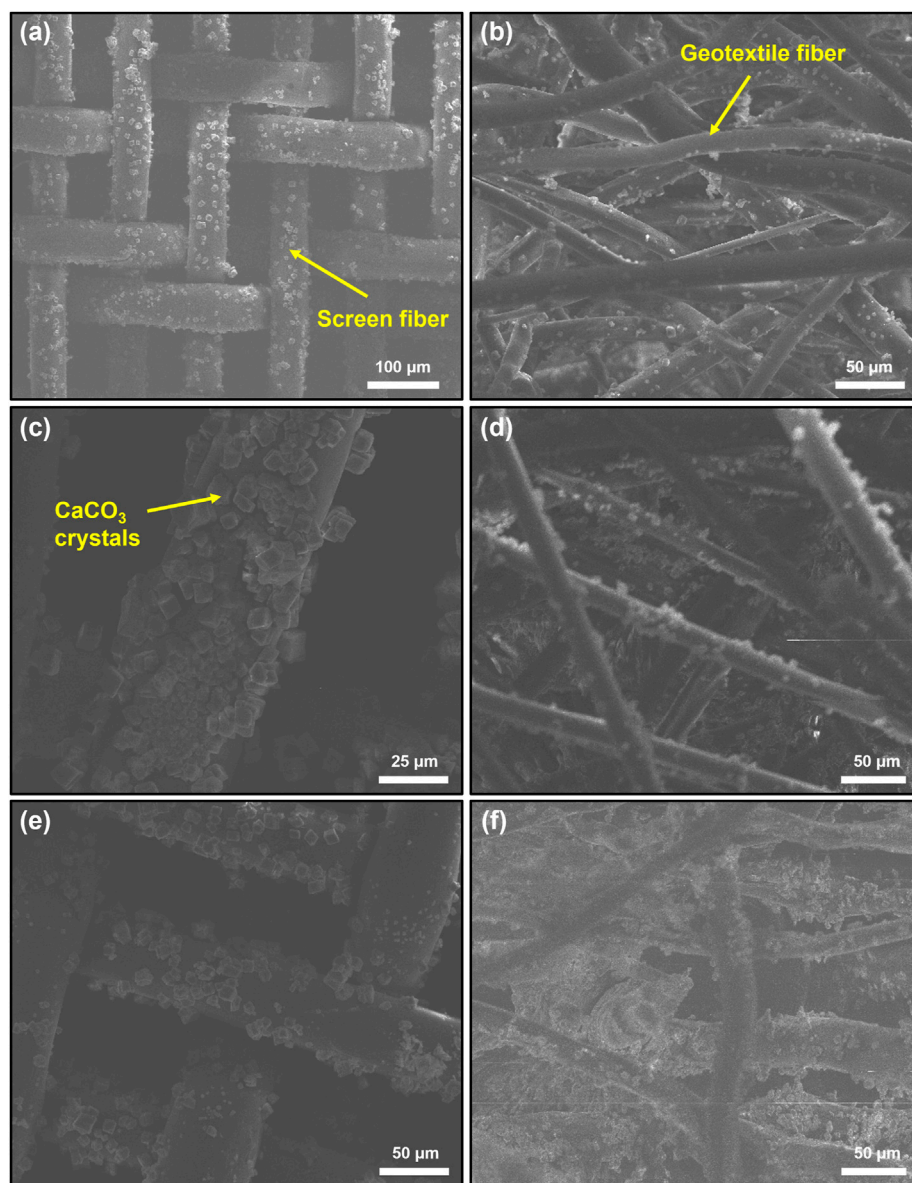
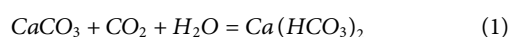


FIGURE 7

SEM images of the screens and geotextiles after: (A), (B): 3 titrations of acid washing; (C), (D): 6 titrations of acid washing; (E), (F): 9 titrations of acid washing.

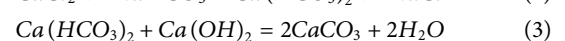
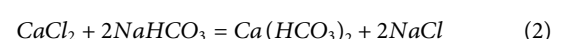
### 3.1 Experiment principle

Under the action of water and  $\text{CO}_2$ , the abundant calcium ions in the groundwater undergo chemical dissolution, and the reaction equation is as follows:



$\text{Ca}(\text{HCO}_3)_2$  has a much higher solubility than  $\text{CaCO}_3$ . With abundant groundwater and  $\text{CO}_2$ , the water discharge from the side slope drainage holes generally contains more  $\text{Ca}(\text{HCO}_3)_2$ . However, the highly unstable  $\text{Ca}(\text{HCO}_3)_2$  can be reduced to  $\text{CaCO}_3$  precipitation under decreased pressure or increased temperature, which can easily block the drainage holes due to their mutual adhesion. In order to simulate the effects of calcium precipitates on the clogging process and

the clogging degree in the drainage holes (especially the outer wrapping of drainage pipes) of cut slopes, the highly soluble  $\text{CaCl}_2$  solution was selected to provide  $\text{Ca}^{2+}$ , and  $\text{NaHCO}_3$  solution was used to promote  $\text{Ca}^{2+}$  in generating  $\text{Ca}(\text{HCO}_3)_2$  precipitation. Then, a certain amount of  $\text{Ca}(\text{OH})_2$  was added to induce the conversion of  $\text{Ca}(\text{HCO}_3)_2$  into the more stable  $\text{CaCO}_3$ . The chemical formulas for the above reactions are as follows.



The above process was applied to the geotechnical screen and geotextile wrapped around the drainage pipes to simulate the calcareous blockage process. The geotechnical screen and geotextile were saved and sampled in steps, and SEM scanning

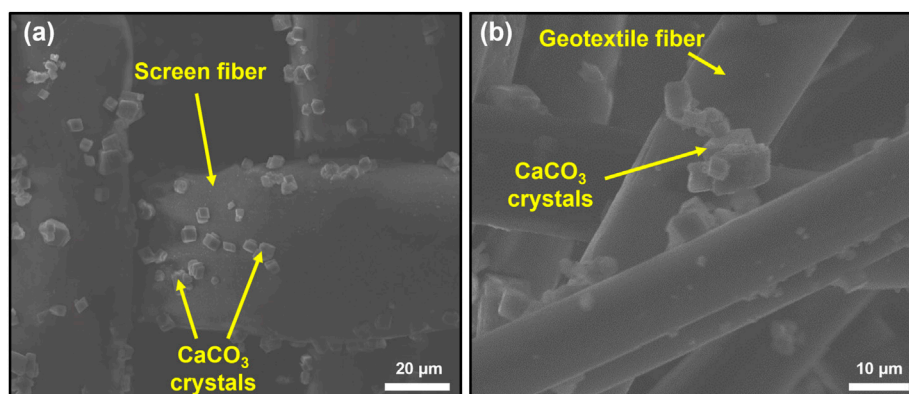


**FIGURE 8**  
SEM images of the (A) screens and (B) geotextiles after 6 titrations of acid washing.

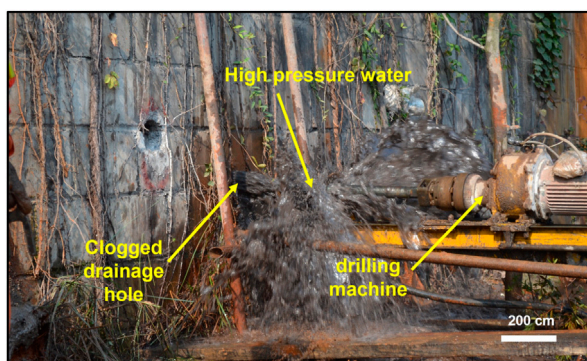


**FIGURE 9**  
Drainage holes washing.

was performed to analyze the form and extent of clogging. Diluted acid was used to clean the screen and geotextile with chemical blockage, and the cleaning effect was observed as well. The reaction between the diluted acid and  $\text{CaCO}_3$  is as follows:



## 3.2 Experimental setup

### 3.2.1 Equipment and chemicals

Several containers were needed to hold various chemical reagents for the experiment. Synthetic fiber screens (200 mesh) and geotextiles of different sizes were cut into  $5.0 \text{ cm} \times 5.0 \text{ cm}$  for the experiment. The  $\text{CaCO}_3$  crystallization adhered to the screens and geotextiles needed to be titrated with different acids and then compared. After the experiment, the screen and geotextile will be sampled for SEM scanning, which aims to reveal the internal microstructure and clarify the chemical clogging mechanism in the drainage holes and pipes. In addition,  $\text{CaCl}_2$ ,  $\text{Ca}(\text{OH})_2$ ,  $\text{Ca}(\text{HCO}_3)_2$ , and  $\text{HCl}$  solutions of the required concentrations were prepared according to the experimental needs.

### 3.2.2 Experiment procedure

The detailed steps of the experiment are described as follows.

- 1) A 0.05 mol/L  $\text{CaCl}_2$  solution, a 0.50 mol/L  $\text{NaHCO}_3$  solution, a saturated  $\text{Ca}(\text{OH})_2$  solution, and  $\text{HCl}$  solutions at pH of 3, 4, and five were prepared with distilled water.
- 2) The screen and geotextile were soaked in the 0.50 mol/L  $\text{NaHCO}_3$  solution and then titrated with 0.05 mol/L  $\text{CaCl}_2$  solution, followed by  $\text{Ca}(\text{OH})_2$  solution. The screen and geotextile were dried after the reaction and then gently washed with distilled water to remove the soluble materials before being dried again. Two pieces of the screen and geotextile squares were sealed and stored: one for SEM scanning tests and the other for titration with a diluted acid. The rest of the screen and geotextile were used for subsequent experiments.
- 3) The dried screen and geotextile in Step 2 were titrated with the 0.50 mol/L  $\text{NaHCO}_3$  solution until saturation and then titrated with the 0.05 mol/L  $\text{CaCl}_2$  solution and  $\text{Ca}(\text{OH})_2$  solution. The screen and geotextile were dried after the reaction and washed with distilled water to remove the soluble materials before being dried again. One of the screens and geotextiles was sealed and kept for SEM scanning, and the rest were used for subsequent experiments.
- 4) Step 3 was repeated until all screens and geotextiles were tested.
- 5) The screens and geotextiles in the above procedures saved for titration with diluted acid were subjected to diluted acid titration. Specifically, screens and geotextiles that underwent one precipitation test were titrated once, and those that underwent multiple precipitation tests were titrated an equal number of times to their number of precipitation. The phenomena that occurred during the test were observed, and the amount of diluted acid consumed was recorded. Then, the screens and geotextiles were dried and saved for SEM scanning.
- 6) Saturated  $\text{CaCl}_2$ ,  $\text{NaHCO}_3$ , and  $\text{Ca}(\text{OH})_2$  solutions were prepared at room temperature that is consistent with the *in situ* temperature, due to the changes of temperature will have impact on the chemical reactions (i.e., the higher temperature the faster reaction). Two screens and two geotextiles were soaked in  $\text{NaHCO}_3$  solutions and then titrated with saturated  $\text{CaCl}_2$  and



TABLE 6 Statistics of the drainage holes washing.

No.	Section with clogged drainage	Old failure holes (Recovered holes)	New holes (Recovered holes)
1	K1850+20–150 Primary slope	86 (12)	22 (9)
2	K1858+950–K1859+000 Primary slope	34 (9)	12 (5)
3	K1863+100–250 Primary slope	98 (6)	24 (11)
	K1863+100–250 Secondary slope	98 (22)	12 (7)
	K1863+100–250 Tertiary slope	49 (16)	12 (6)
4	K1873+270–310 Tertiary slope	26 (6)	9 (4)
5	K1876+430–+480 Primary slope	30 (16)	12 (7)
	K1876+380–480 Secondary slope	60 (22)	15 (8)
6	K1881+200–240 Secondary slope	24 (3)	6 (4)
	K1881+180–230 Foot of the slope	16 (2)	4 (4)
7	K1918+225–385 Primary slope retaining wall	106 (27)	20 (7)
8	K1925+550–875 Primary retaining wall	160 (25)	12 (10)
	K1925+550–875 Primary slope	216 (19)	30 (8)
9	K1941+000–440 Primary retaining wall	220 (42)	30 (14)
Success washing rate		18.6%	47.3%

Ca(OH)<sub>2</sub> solutions until the reaction was completed. The screens and geotextiles were dried and then washed with distilled water to remove the soluble materials before being dried again. One piece was saved for SEM scanning, and the other was titrated with diluted acid until the reaction was completed. The experimental phenomena were recorded.

- 7) All tested screens and geotextiles were subjected to the SEM scanning tests.

### 3.3 SEM results of chemical clogging

The screen and geotextile after the first two steps in Section 3 were scanned by SEM to observe the attachment of CaCO<sub>3</sub> crystals. Both the screen and the geotextile have CaCO<sub>3</sub> crystals attached to the fiber surface (see Figure 5). Under the *in situ* condition, as the working time of the drainage holes goes on, precipitated CaCO<sub>3</sub> crystals are accumulating on the screen and geotextile due to their high cohesiveness, thus exacerbating the clogging. From the distribution of the chemical clogging, it can be concluded that the wrapped materials with single-layer structure and larger pore size is more effective than these with multi-layer structure and smaller pore size to prevent the clogging.

The CaCO<sub>3</sub> crystal precipitation around the drainage holes with increasing *in situ* operation time was simulated by varying the number of CaCl<sub>2</sub> and Ca(OH)<sub>2</sub> titration. The images of the screens and geotextiles after titration are shown in Figure 6. A comparison of the microstructure of CaCO<sub>3</sub> precipitation indicates that the CaCO<sub>3</sub> crystals attached to the surface of the screen and the geotextile fibers increase with the increasing number of titrations. The CaCO<sub>3</sub> crystals continuously attach to and accumulate on the fibers, leading to blockage. With time going on, the crystal precipitation increases, and then chemical clogging intensifies.

The screens and geotextiles attached with CaCO<sub>3</sub> crystals were soaked in a diluted hydrochloric acid at a pH of 5.0 for 5 min, to observe the cleaning effect of acid washing on the chemical blockages. As presented in Figure 7, the decrease of CaCO<sub>3</sub> crystals attached to the screen and geotextile fibers was not significant after the acid washing with a pH = 5.0.

Since the decrease in the attached CaCO<sub>3</sub> crystals is not so significant after soaking in acid at the pH of 5.0, stronger hydrochloric acids are employed. SEM images of the screen and geotextile soaked with hydrochloric acid at a pH of 3.0 after 6 titrations are shown in Figure 8. The decrease in CaCO<sub>3</sub> crystals attached to the fibers is more significant after soaking in the stronger hydrochloric acid (pH = 3.0) for the same time (i.e., 5 min). Therefore, acid washing is effective for the Fe chemical blockage and Ca blockage.

## 4 Test of *in situ* drainage holes washing

The clogged drainage holes in the study area were washed from the outside to the inside with high-pressure water at a pressure of about 0.1 MPa (see Figure 9). After the washing, the cleaning effects on the old and new constructed drainage holes were counted and compared separately. The recovery of drainage after a rain is taken as the judging standard for the success of hole washing. The statistical success of hole washing is shown in Table 6. The data in brackets in the table is the number of drainage holes successfully washed. The operation time of the old drainage holes in this site is more than 10 years, and now it is in the late clogging stage, while the operation of the new drainage hole is working only for 2–3 years, i.e., the initial clogging stage. It can be seen from the statistical data that the drainage holes in the initial clogging stage are mainly physical blockage, and the success rate of washing reaches 47.3%. There

are blockage bonded together in the drainage holes located in the late clogging stage, due to the coupled effect of chemical and biological blockages. The Late clogging stage shows the characteristics of the three-dimensional comprehensive blockage. Therefore, the drainage effect of hole washing is not so effective, with a lower success rate of 18.6%.

## 5 Conclusion

In this paper, the degree and mechanism of drainage hole clogging in highway cut slopes were preliminarily clarified through an on-site survey. The soil and blockage samples from the selected slopes were collected for laboratory tests and analysis. The conclusions are summarized as follows.

- 1) All drainage holes in the research sections are characterized by different degrees of clogging. The blockages are correlated with the slope stratum lithology, the soil particle size, and the groundwater. All the blockages are made of fine-grained particles, and the clogging of slope drainage holes in slopes with clayey soil and other fine-grained soil is usually more severe. Slope drainage holes with flexible drainage pipes are also generally clogged with the hindered groundwater discharged, indicating its poor suitability for the slopes. The blockages contain abundant iron oxides, which are found to be related to the oxidation of the steel wire skeleton inside the flexible drainage pipes by FTIR analysis.
- 2) SEM images show more blockages at the inner end of the drainage pipes than at the outer end and more blockages on the outside than on the inside of the drainage pipes, in agreement with the movement of underground water and the fine particles. The blockages penetrate deep inside the drainage pipe wrappings, and the combined effect of clayey soil, chemical clogging, and biological clogging exacerbate the clogging of drainage pipes with the increase in time.
- 3) In addition to the same oxides as that in the side slopes, the blockages in the research area also have a high content of calcium oxides, indicating chemical clogging of calcium precipitates.

The chemical clogging in the research area is mainly in the form of  $\text{CaCO}_3$  crystals attached to the outer surface of the wrapping fibers, which exacerbates the clogging with its continuous accumulation. As a commonly used wrapping material for drainage pipes, the pore size of nylon screens is larger than that of geotextile. The single-layer structure of screens does not facilitate three-dimensional clogging without crystals attached to the interior. In contrast, geotextiles facilitate three-dimensional clogging with crystals attached to the different fibers. The three-dimensional clogging is difficult to clean through traditional washing methods. Therefore, under the same conditions, the chemical clogging of screens needs more time to form and is easier to clean than the chemical clogging of geotextiles.

- 4) Indoor tests were also conducted to simulate the  $\text{CaCO}_3$  crystal precipitation clogging around the drainage holes in the research area, and the microstructure of the clogged screens and geotextiles was observed by using SEM. The main conclusions are in following: All chemical clogging on the screens and geotextiles is in the form of  $\text{CaCO}_3$  crystal attachment and accumulation on

the fiber surface, leading to severe clogging. The higher the number of titrations on the screens and geotextiles, the more  $\text{CaCO}_3$  crystals is attached to the fiber surface. This study verifies that the amount of  $\text{CaCO}_3$  crystals attached to the surface of the wrapping outside the drainage pipes increases with the operation time. Therefore, the effect of chemical clogging should be considered for the long-term operation of drainage holes. The decrease in  $\text{CaCO}_3$  crystals attached to the screens and geotextiles is not significant after soaking in diluted hydrochloric acid at the pH of 5.0 but significant after soaking in hydrochloric acid at the pH of 3.0. Therefore, stronger acids perform better in removing part of the calcium clogging and delaying the chemical clogging. Considering the protection of environment, the acid washing method is not suggested to apply in the *in situ* engineering. The single-layer structure of screens does not facilitate three-dimensional clogging like in the geotextiles. In the meantime, the pore size of screens is larger than that of geotextiles. Therefore, chemical clogging on screens needs more time to form and is easier to clean than that in the geotextiles.

- 5) It can be seen from this study that drainage holes clogging can be divided into two typical stages: the initial stage and the late stage. The initial stage is dominated by physical blockage, which is manifested as fine grained soil that forming blockage around the drainage holes along with the groundwater migration. The physical blockage induced by fine grained soil is also a major component of the blockage. This stage is generally formed in an operation period of 2–3 years, and the drainage holes are often completely undrained. But there is usually a better hole washing effect on the drainage holes at this stage. With the increase of the operation time, the drainage holes are intermittently drained or even not drained, chemical and biological clogging become more obvious. The drainage holes located in the late stage make the blockage bond together to form a better whole because of chemical and biological blockage. Fine grained soil becomes difficult to destroy after bonding with chemicals, so the success rate of drainage hole washing at this stage is very low.
- 6) The structure of the drainage hole makes the clogging inevitable, to make the permanent drainage effect better, it is necessary to invent a drainage hole that is less easily clogged or better washed. The existing drainage hole blockage is based on the drainage hole wrapping material, so improving the wrapping material or even cancelling the wrapping material will be an effective direction to reduce the drainage hole blockage or make the drainage hole easier to wash.

## Data availability statement

The raw data supporting the conclusion of this article will be made available by the authors, without undue reservation.

## Author contributions

JM, conceptualization, methodology, writing—original draft preparation, formal analysis; AC, conceptualization and methodology; KY, formal analysis, writing—original draft preparation, writing—review and editing; CZ, writing—review and editing. All authors have read and agreed to the published version of the manuscript.



## Funding

This research is supported by the Talent Cultivation Project at Kunming University of Science and Technology (KKZ3201621012).

## Conflict of interest

Author JM was employed by the Company Kunming Prospecting Design Institute of China Nonferrous Metals Industry Co., Ltd. Author CZ was employed by Yunnan Geological Exploration and Development Corporation.

## References

- Cahyadi, T., Widodo, L., Fajar, R., and Baiquni, A. (2018). "Influence of drain hole inclination on drainage effectiveness of coal open pit mine slope," in *IOP conference series: Earth and environmental science* (IOP Publishing), 012060.
- Cao, Y., Xu, M., Ni, P., and Mei, G. (2021). Physical and numerical modelling of infiltration from drainage holes for perforated storm sewer. *Acta Geotech.* 17, 527–543. doi:10.1007/s11440-021-01247-0
- Castro, J., Asta, M. P., Galve, J. P., and Azañón, J. M. (2020). Formation of clay-rich layers at the slip surface of slope instabilities: The role of groundwater. *Water* 12 (9), 2639. doi:10.3390/w12092639
- Dos Anjos, M., Lopes, R., De Jesus, E., Assis, J., Cesareo, R., and Barradas, C. (2000). Quantitative analysis of metals in soil using X-ray fluorescence. *Spectrochim. Acta Part B At. Spectrosc.* 55 (7), 1189–1194. doi:10.1016/s0584-8547(00)00165-8
- Guo, Y., Leng, W., Nie, R., Zhao, C., and Zhang, X. (2018). Laboratory evaluation of a new device for water drainage in roadside slope along railway systems. *Geotext. Geomembranes* 46 (6), 897–903. doi:10.1016/j.geotexmem.2018.08.005
- Gu, T. F., Zhu, L. F., Hu, W., Wang, J. D., and Liu, Y. M. (2015). Effect on slope stability due to groundwater rising caused by irrigation: a case study of Heifang Platform in Gansu. *China. Geosci.* 29 (2), 408–413 (in Chinese).
- Hahn, A., Vogel, H., Andó, S., Garzanti, E., Kuhn, G., Lantzsich, H., et al. (2018). Using Fourier transform infrared spectroscopy to determine mineral phases in sediments. *Sediment. Geol.* 375, 27–35. doi:10.1016/j.sedgeo.2018.03.010
- He, Y., Sun, R., Xu, Z., and Tang, W. (2021). The dynamic change and effect of rainfall induced groundwater flow. *Water* 13 (19), 2625. doi:10.3390/w13192625
- Hongyue, S., Feixiang, S., Yuequan, S., Huan, X., and Dongfei, W. (2019). Study on negative pressure drainage method of down dip borehole in slope. *J. Eng. Geol.* 27 (3), 585–591.
- Jiao, J. J., Wang, X. S., and Nandy, S. (2005). Confined groundwater zone and slope instability in weathered igneous rocks in Hong Kong. *Eng. Geol.* 80 (1–2), 71–92. doi:10.1016/j.enggeo.2005.04.002
- Kaczmarek, Ł. D., and Popielski, P. (2019). Selected components of geological structures and numerical modelling of slope stability. *Open Geosci.* 11 (1), 208–218. doi:10.1515/geo-2019-0017
- Latief, R. H., and Zainal, A. K. E. (2019). Effects of water table level on slope stability and construction cost of highway embankment. *Eng. J.* 23 (5), 1–12. doi:10.4186/ej.2019.23.5.1
- Liu, Z., Liu, P., Zhou, C., and Zhang, L. (2021). A theoretical framework for optimization of three-dimensional slope stability monitoring. *Eng. Geol.* 295, 106436. doi:10.1016/j.enggeo.2021.106436
- Luquot, L., Roetting, T. S., and Carrera, J. (2014). Characterization of flow parameters and evidence of pore clogging during limestone dissolution experiments. *Water Resour. Res.* 50 (8), 6305–6321. doi:10.1002/2013wr015193
- Mininger, K. T. (2010). *Lifespan of horizontal wick drains used for landslide drainage*. Colorado School of Mines.
- Nistor, M. M., Rahardjo, H., Satyanaga, A., Hao, K. Z., Xiaosheng, Q., and Sham, A. W. L. (2020). Investigation of groundwater table distribution using borehole piezometer data interpolation: Case study of Singapore. *Eng. Geol.* 271, 105590. doi:10.1016/j.enggeo.2020.105590
- Pantelidis, L. (2009). Rock slope stability assessment through rock mass classification systems. *Int. J. Rock Mech. Min. Sci.* 46 (2), 315–325. doi:10.1016/j.ijrmms.2008.06.003
- Ravansari, R., Wilson, S. C., and Tighe, M. (2020). Portable X-ray fluorescence for environmental assessment of soils: Not just a point and shoot method. *Environ. Int.* 134, 105250. doi:10.1016/j.envint.2019.105250
- Santoso, A. M., Phoon, K. K., and Quek, S. T. (2011). Effects of soil spatial variability on rainfall-induced landslides. *Comput. Struct.* 89 (11–12), 893–900. doi:10.1016/j.compstruc.2011.02.016
- Silva, E. A., Weindorf, D. C., Silva, S. H., Ribeiro, B. T., Poggere, G. C., Carvalho, T. S., et al. (2019). Advances in tropical soil characterization via portable X-ray fluorescence spectrometry. *Pedosphere* 29 (4), 468–482. doi:10.1016/s1002-0160(19)60815-5
- Subramanian, S. S., Ishikawa, T., and Tokoro, T. (2017). Stability assessment approach for soil slopes in seasonal cold regions. *Eng. Geol.* 221, 154–169. doi:10.1016/j.enggeo.2017.03.008
- Sun, H. Y., Ge, Q., Yu, Y., Shuai, F. X., and Lü, C. C. (2021). A new self-starting drainage method for slope stabilization and its application. *Bull. Eng. Geol. Environ.* 80 (1), 251–265. doi:10.1007/s10064-020-01918-4
- Tsao, M. C., Lo, W., Chen, W. L., and Wang, T. T. (2021). Landslide-related maintenance issues around mountain road in dasha river section of central cross island highway, taiwan. *Bull. Eng. Geol. Environ.* 80 (2), 813–834. doi:10.1007/s10064-020-01967-9
- Wu, J., Wu, Y., and Lu, J. (2008). Laboratory study of the clogging process and factors affecting clogging in a tailings dam. *Environ. Geol.* 54 (5), 1067–1074. doi:10.1007/s00254-007-0873-9
- Wu, J., Wu, Y., Lu, J., and Lee, L. (2007). Field investigations and laboratory simulation of clogging in Lixi tailings dam of Jinduicheng, China. *Environ. Geol.* 53 (2), 387–397. doi:10.1007/s00254-007-0654-5
- Yin, K., Fauchille, A. L., Di Filippo, E., Kotronis, P., and Sciarra, G. (2021a). A review of sand-clay mixture and soil-structure interface direct shear test. *Geotechnics* 1 (2), 260–306. doi:10.3390/geotechnics1020014
- Yin, K., Fauchille, A. L., Di Filippo, E., Othmani, K., Branchu, S., Sciarra, G., et al. (2021b). The influence of mixing orders on the microstructure of artificially prepared sand-clay mixtures. *Adv. Mater. Sci. Eng.* 2021, 1–15. doi:10.1155/2021/8552224
- Yin, K., Fauchille, A. L., Othmani, K., Sciarra, G., Kotronis, P., Benoit, Y., et al. (2019). "Influence of sample preparation on the multi scale structure of sand-clay mixtures," in *E3S Web of conferences* (EDP Sciences), 01007.
- Yin, K. (2021). Influence of clay fraction on the mechanical behavior of a soil-concrete interface. Nantes, France: Thesis. École centrale de Nantes.
- Yin, K., Liu, J., Lin, J., Vasilescu, A. R., Othmani, K., and Di Filippo, E. (2021c). Interface direct shear tests on JEZ-1 mars regolith simulant. *Appl. Sci.* 11 (15), 7052. doi:10.3390/app11157052
- Zhang, L., Zhang, J., Zhang, L., and Tang, W. H. (2011). Stability analysis of rainfall-induced slope failure: A review. *Proc. Institution Civ. Engineers-Geotechnical Eng.* 164 (5), 299–316. doi:10.1680/geng.2011.164.5.299
- Zhang, S., Xu, Q., Peng, D., Zhu, Z., Li, W., Wong, H., et al. (2020). Stability analysis of rock wedge slide subjected to groundwater dynamic evolution. *Eng. Geol.* 270, 105528. doi:10.1016/j.enggeo.2020.105528



## OPEN ACCESS

## EDITED BY

Liang Chen,  
China University of Mining and  
Technology, China

## REVIEWED BY

Andrey Kuranov,  
Timan-Pechora Research Center, Russia  
Ilya Vinokurov,  
A.P. Karpinsky Russian Geological  
Research Institute, Russia  
Oleg Smirnov,  
All Russian Research Institute of Geology  
and Mineral Resources of the World  
Ocean, Russia

## \*CORRESPONDENCE

Ruiming Xu,  
✉ x472794773@gmail.com

RECEIVED 22 March 2023

ACCEPTED 20 April 2023

PUBLISHED 17 May 2023

## CITATION

Prischepa OM, Kireev SB, Nefedov YV,  
Martynov AV, Lutsky DS, Krykova TN,  
Sinita N and Xu R (2023), Theoretical and  
methodological approaches to  
identifying deep accumulations of oil and  
gas in oil and gas basins of the  
Russian Federation.  
*Front. Earth Sci.* 11:1192051.  
doi: 10.3389/feart.2023.1192051

## COPYRIGHT

© 2023 Prischepa, Kireev, Nefedov,  
Martynov, Lutsky, Krykova, Sinita and Xu.  
This is an open-access article distributed  
under the terms of the [Creative  
Commons Attribution License \(CC BY\)](https://creativecommons.org/licenses/by/4.0/).  
The use, distribution or reproduction in  
other forums is permitted, provided the  
original author(s) and the copyright  
owner(s) are credited and that the original  
publication in this journal is cited, in  
accordance with accepted academic  
practice. No use, distribution or  
reproduction is permitted which does not  
comply with these terms.

# Theoretical and methodological approaches to identifying deep accumulations of oil and gas in oil and gas basins of the Russian Federation

O. M. Prischepa, S. B. Kireev, Yu. V. Nefedov, A. V. Martynov,  
D. S. Lutsky, T. N. Krykova, N. Sinita and Ruiming Xu\*

Department of Geology of Oil and Gas, Saint-Petersburg Mining University, Saint-Petersburg, Russia

A large number of oil and gas accumulations at deep and ultra-deep depths, recently revealed in the world due to the development of drilling technologies, forces a revision of theoretical ideas on many issues, including conditions of oil and gas formation and hydrocarbon conservation in zones of high pressures and temperatures, as well as evaluating the possibility of conservation and formation of reservoirs. Among the most discussed, in this regard, are the issues determining the processes and rate of oil and gas formation at deep and ultra-deep depths, which differ significantly from those at small and medium depths: Thermobaric conditions responsible for the possibility of formation, phase distribution and conservation of hydrocarbons, geochemical indicators—type of kerogen, and its transformation, responsible for the phase distribution and staging of generation peaks—lithological composition of kerogen-bearing strata—the rate and scale of dip and uplift and the timing of exposure to high temperatures—the formation of overlapping saline strata and the presence of deep conductive faults that significantly affect temperature and pressure gradients. Analysis of the influence of the above factors on the prospects of deep-lying complexes taking into account new studies and achievements, mainly in the sedimentary basins of China (Tarim, Jungar, Ordos, Sichuan), the Gulf of Mexico and offshore Brazil (Santos) allowed typifying the sedimentary basins and major depressions of Russia, with the allocation of areas with high and ultra-low depth potential for hydrocarbon studies. Thermobaric and historical and geological criteria have been developed and a methodology for detailed study of promising areas has been proposed, including a complex of geochemical studies of hydrocarbons, extracts of bitumoids (pyrolytic, chromatographic) and lithological and petrophysical core studies aimed at assessing the prospects of oil and gas content of deep complexes in Russian sedimentary basins and the subsequent localization of the most promising areas for deep drilling.

## KEYWORDS

ultra-deep depths, oil and gas, deep accumulations, deep origin, high temperature, high pressure

# 1 Introduction

A number of global events in the field of prospecting and exploration of oil and gas accumulations are attracting more and more attention to the theoretical issues of oil and gas formation, taking into account the possibility of using the scientific results obtained in practice, reinforcing them with actual discoveries replacing the raw material base of traditional objects that is being eliminated as a result of extraction.

Among the most significant events that have substantially affected the state of the raw material base of hydrocarbons in the world, it is necessary to include such as:

- Scientific foundation of the oil and gas potential and development of technologies for the development of the raw material base of low-permeable and “shale” oil and gas-saturated reservoirs (which made it possible to radically change the energy balance and, for example, let the United States become the gas exporter due to the share of its production of more than 70% of such facilities (Alekseev et al., 2017);
- Development of deep drilling technologies and obtaining numerous facts of detecting accumulations of oil and gas at great depths, as well as new data that significantly clarify ideas about the thermobaric conditions of formation and the possibility of preservation of hydrocarbons (Dvoynikov et al., 2022).

The identification of oil and gas deposits at deep and ultra-deep depths (5–8 km or more) allowed us to establish that the boundary values of the thermobaric conditions for the formation and preservation of hydrocarbon deposits differ significantly from those assumed (*a priori*) earlier and justified experimentally (according to the postulates of the sedimentary migration (organic) theory of the origin of oil and gas. Some assumptions previously used as key ones directly in the practice of geological exploration have ceased to be relevant. First of all, this concerns the temperature, and, consequently, the depth interval of the processes of generation of hydrocarbons of various phase composition and their intensive transformation, up to complete destruction, as well as the influence of abnormally high and abnormally low pressure on the preservation of formed accumulations of oil and gas. The second important aspect determining the possibility of the presence of hydrocarbon accumulations at deep depths is the possibility of preserving the primary void space of reservoir rocks or the formation of fractured and secondary reservoirs, as well as the influence of epigenetic transformations on their formation (Gubin, 2004; Belozarov and Gubaydullin, 2020; Khafizov et al., 2020; Kosenkova et al., 2022). At the same time, an alternative and effective approach that could replace the traditionally used and proven to be highly predictive is basin modeling, which is based on algorithms of balance equations and models for the conversion of organic matter into hydrocarbons, developed in the USSR by the efforts of Sokolov V.A., Wassojevich N.B., Neruchev S.G., Rogozina E.A. and others (Dobryanski and Andrejev, 1954; Neruchev et al., 1976; Sokolov V.A., 1980) and European and American researchers (Tissot and Welte, 1981; Peters et al., 1994) have not been proposed. Despite a huge number of experiments to study the effects of

temperatures and pressures on inorganic compounds, to study the effect of methane inflow on the transformation of organic matter in order to substantiate the production of complex hydrocarbon compounds, to substantiate possible forms (radicals) of finding hydrocarbon compounds at deep and ultra-deep depths (Kudryavtsev, 1951; Kudryavtsev, 1971; Porfiriev, 1987; Ermolkin et al., 2008) a significant practical contribution to the search for oil accumulations and they did not have, because they were not adapted into any technology of search and exploration, which proved its effectiveness. Of course, the impossibility of obtaining direct observations at ultra-deep depths and conducting experiments that fully simulate natural thermobaric conditions, and most importantly the influence of time, continues to “excite” the minds of some researchers in the direction of the “deep origin” of oil and gas today. The most important facts obtained in recent years, which must be taken into account, along with the timing of hydrocarbon deposits at deep and ultra-deep depths to certain geological conditions, were the systematic identification in “special” conditions of deep depths of very rich in organic matter of oil and gas source formations that for one reason or another did not realize their full potential, or the identification of anomalous zones of high pressures, ensuring the preservation of liquid hydrocarbons (not complete cracking) in sedimentary basins with high immersion rates and “avalanche-like” sedimentation.

The concept of “deep origin” considering the possibility of synthesis of hydrocarbons from inorganic substances (carbonates, CO<sub>2</sub> and other carbon-containing substances) at deep depths at high temperatures and pressure allows the formation of accumulations of oil and gas at much deeper depths than those assumed by organic theory and, no less importantly, in which there are no oil and gas producing strata, primarily enriched with organic substance.

The problem of theoretical research in the direction of studying “deep oil”, which was developed in particular by N.A. Kudryavtsev (Kudryavtsev, 1951; Kudryavtsev, 1971) and V.B. Porfiriev (Porfiriev, 1961; Porfiriev, 1987), was the impossibility of using the models of oil and gas formation proposed by them to solve practical problems, which led to a damping of interest in these developments and, conversely, high efficiency and the possibility of provability (experimental) of oil and gas formation processes using balance equations developed by N.B. Vassojevich, S.G. Neruchev, E.A. Rogozina et al. (Neruchev et al., 1976), the quantitative forecast, the forecast of the phase composition and the “explainability” of the formation of most of the identified deposits allowed “organics” to dominate in the study of standard depths.

Dobryanski and Andrejev, 1954). noted that despite the huge scale of accumulated and buried organic matter (according to Ammosov, and then Neruchev S.G. (Neruchev et al., 1986). exceeding hundreds of billions of times the volume of all accumulations of oil and gas already discovered on Earth), the ambiguity of the accumulation mechanisms does not allow us to draw conclusions “how much oil will be collected”. S.G. Neruchev himself drew attention to the ambiguity of the accumulation coefficients in his calculations. According to V.B. Porfiriev the presence of areas of discrepancy between the scales and types of hydrocarbons to the potential of the oil and gas producing strata is noted, and the presence of deposits at depths greater than the depths of the oil and gas source formations is established, which determines the need to search for the causes of oil and gas potential in such areas

and depth intervals (Aguilera et al., 2014; Guliyev et al., 2017; Liu et al., 2017).

It is established that the processes of oil and gas formation at deep depths differ significantly from the processes modeled in surface conditions (DeCelles and Giles, 1996; Eberth et al., 2001; Egorov, 2015; Egorov et al., 2021). Ultra-deep hydrocarbon systems are characterized by specific features of fluid migration (Samvelov, 1995; Cao and Bai, 2014; Kerimov et al., 2018), which affects the development of accumulation zones and the preservation of hydrocarbon accumulations due to the dominance of such mechanisms as migration along the planes of conducting disjunctiva, zones of increased fracturing of decompression, contacts of diapir embeddings, eruptives of mud volcanoes (DeCelles and Giles, 1996; Kerimov and Osipov, 2016; Ganguli et al., 2018; Li et al., 2020).

Currently, the contradiction between “theory” and “experiment” (i.e., between science and practice) has worsened due to the discovery of a number of oil fields below (deeper) the so-called “oil window”, where oil can be generated from organic residues (an oil window of 50°C–150°C, i.e., depths, as a rule, from 2.3 to 4.6 km; immediately below—a “gas window”, 150°C–200°C).

A large number of drilled deep and ultra-deep wells in the oil and gas basins of the world testify to a wide range of temperatures and pressures, as well as a complex multi-stage history of the thermal evolution of deep-submerged horizons. Temperatures, thermal evolution and pressure are the determining factors of the formation of hydrocarbons, differences in their phase composition, the possibility of their preservation, and these parameters are especially significant at deep and ultra-deep depths, which today are considered as one of the most important areas of theoretical and practical study of many oil and gas basins in China, the shelf of Brazil, the Gulf of Mexico and other sedimentary basins with a large thickness of the cover.

Based on a large amount of new data on the influence of temperatures, pressures, and the history of diving to deep depths, the concepts of the factors determining the formation, phase composition and preservation of hydrocarbons have been significantly refined. Thus, the phase composition of hydrocarbons in the deep layers of sedimentary basins of different types varies significantly and is determined by temperature, heating rate, pressure and types of the initial oil and gas source rocks containing organic matter deposited with the rock. At the same time, temperature is the most important factor controlling the formation of hydrocarbons and their phase state. Along with the temperature, factors that are almost ignored at shallow depths have a significant impact—this is the time (exposure) and the rate of temperature increase (Neruchev et al., 1986).

Thus, according to the nature of changes in the temperature regime of deep and ultra-deep horizons, sedimentary basins can be distinguished (Ren et al., 2020):

- 1- With late (young in age) rapid deflection, low geothermal gradient and, accordingly, low temperatures;
- 2- With late rapid deflection, high geothermal gradient, and, accordingly, high (but short-lived exposure time) temperatures;
- 3- With moderate (gradual) deflection, average geothermal gradient and late rise and, accordingly, cooling;
- 4- With early (ancient) intense deflection, rapid heating and subsequent lifting and cooling.

It has been established that under conditions of rapid temperature rise (type 1, 2, and 4), but a short heating time in

deep and ultra-deep horizons, the conditions for the existence of oil and gas condensate deposits persist (Ren et al., 2020).

The most important thing for deep horizons is the close correlation between temperature and reservoir pressure, which determines the conditions of oil and gas formation and preservation of oil and condensate.

By the nature of the correlation between temperature and pressure at deep depths, all sedimentary basins can be divided into three groups:

- I - high temperature and high pressure;
- II - low average temperature and high pressure;
- III - average temperature and low pressure (Ren et al., 2020).

It has also been revealed that excessive pressure prevents both the formation of hydrocarbons and the cracking of previously formed (reformation of liquid hydrocarbons into gaseous and simple compounds), which have fallen into zones of high pressures and temperatures for the second time. For all these types and combinations of thermodynamic regimes, the prospects for the oil and gas potential of deep and ultra-deep horizons differ significantly.

The temperature regime of deep horizons is determined by the endogenous regime (the influence of processes occurring at deep depths) and a whole group of processes and phenomena occurring at significantly lower depths, directly in the sedimentary part of the section, often associated with epigenetic transformations.

Endogenous regimes are the subject of extensive study of sedimentary basins at the early stages of regional studies. But with a more detailed study, the significance of the processes occurring at deep depths becomes less important, declarative and is rarely used for practical conclusion and determining the directions of further exploratory research.

Since the influence of processes occurring at ultra-deep depths is more noticeable for the base of sedimentary basins and section intervals located at deep depths, the influence of endogenous phenomena and processes is also one of the subjects of research. At the same time, the possibilities of studying the deep structure are extremely limited both by the depths of wells and by obtaining only indirect information when using geophysical observation methods and conducting laboratory experimental studies with modeling of natural processes. Such restrictions, on the one hand, generated a huge number of assumptions, including about the influence of deep processes on oil and gas formation, and on the other hand, due to the impossibility of establishing reliable links between the actual oil and gas potential and purely assumed “deep factors”, they did not allow them to be used in practice.

Approaches to the assessment of the oil and gas potential based on the concepts of the deep tectonic structure and processes occurring at significant depths according to studies (Sokolov, 1980; Malyshev, 2000; Malyshev, 2004; Egorov et al., 2021) are reduced to the use of the “evolutionary-genetic method, when modern sedimentary basins are considered as a system of conjugate paleobasins, consisting of their relics related to a certain tectonotype, formed in certain geodynamic regimes and those that have undergone a long geological evolution” (Egorov et al., 2021). At each stage of the development of paleobasins, favorable geological, geochemical and thermobaric conditions arose, affecting the processes of oil and gas formation, migration and accumulation and further redistribution of hydrocarbons between different complexes. Crucial importance in the modern distribution



of hydrocarbon accumulations is attached to the latest stage of the formation of the basin structure.

According to the research of B.A.Sokolov (Sokolov, 1980): “each of the basins of the primary evolutionary and genetic series is characterized by a certain oil and gas geological regime, which includes the conditions for the development of the basin due to the mobility and direction of tectonic movements, their contrast, the type of the Earth’s crust and the rate of accumulation of sediments, as well as heat flow.”

As noted by most researchers, oil and gas geological regimes are not the same in sedimentary basins located within continents, oceans and transition zones. Within the continents, sedimentary basins of platforms and mountain-folded regions have fundamentally different regimes (Malyshev, 2000; Egorov et al., 2021).

The scales of oil and gas formation differ significantly, which vary from high and very high within the margins of young plates and folded-platform basins in the marginal parts of cratons and to low in post-orogenic depressions on Precambrian median massifs and very low (less than 1%) in orogenic intermountain depressions on the Epivariscian folded base (Malyshev, N.A. (2004).

According to modern concepts, in some sedimentary basins, due to the presence of wide salt layers in the section, relatively low geostatic pressure is provided (due to their relatively low density) and a “cooling” effect of the thermal field is observed (due to their relatively high thermal conductivity), which, despite the deep depths, leads to a delay in the transformation of organic matter in primary enriched (producing) rocks.

Large tectonic discontinuous disturbances, which serve as active conductors of deep heat and which, like salt layers, provide a “cooling” effect have an important effect on the temperature regime. This phenomenon has been little studied, but it is important along with understanding the contribution of the role of faults in the formation of secondary fracturing at deep depths, providing the possibility of reservoir formation, in addition to the preserved primary porosity (Prishchepa et al., 2022).

Separately, it should be noted the influence of high sedimentation rates (the so-called “avalanche” deposition) with variations in the accumulation of large capacities only in the Cenozoic, observed, for example, in the inland basins of China (Tarim, Dzungarian, Sichuan, Ordos) with massive identified deposits at deep depths and established oil and gas source rocks at deeper depths than at low sedimentation rates, which probably lead to stretching of the zones of transformation of organic matter (catagenesis), and the effect of the presence of zones of abnormally high reservoir pressures, which, in turn, have a significant impact on the catagenetic transformation of organic matter and the stability of the liquid hydrocarbon phase by inhibiting and significantly slowing down the processes of thermal destruction of organic components (Khafizov et al., 2020).

It is noted that (Kerimov and Osipov, 2016; Kerimov et al., 2018; Khafizov et al., 2020; Ren et al., 2020; Aleksandrova et al., 2023) the key factors of the transformation of OM into oil and the intervals of the location of the “oil window” are the rates of sedimentation and deflection (lowering) of the basin. The rate of deflection of the basin or the rate of elevation of its side structures determines the nature of sedimentation in the basin, due, in turn, to the size of negative relief forms, the rate of introduction of addition of material, its composition and mass. Depending on the individual contribution of these factors at each stage of evolution, the basin may be characterized by uncompensated, compensated and hypercompensated sedimentation (Kerimov et al., 2018).

The sedimentation rate is generally defined as the ratio of the sediment thickness (for the rates of deflection of the bottom of the basin, the sediment thickness together with the thickness of the water layer) and the absolute time of their formation, respectively, in meters per million years; the dimension of the resulting value is m/million years. Standard speeds are 5–10 m/1 million years. High and ultra-high sedimentation rates exceeding 100–1000 m/1 million years, respectively, characterize “avalanche-like” sedimentation (Kerimov et al., 2018).

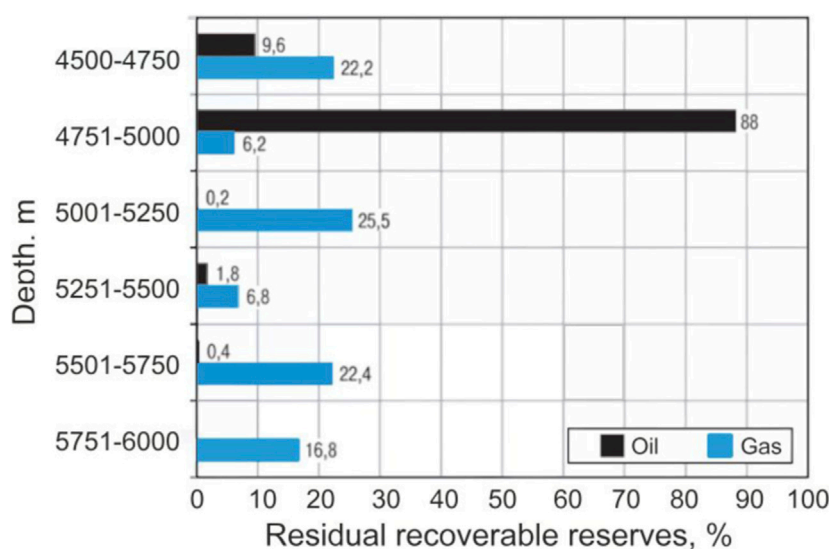


FIGURE 1

Distribution of residual recoverable oil and gas reserves of deep-lying deposits by depth intervals (Osipov, 2021).

**TABLE 1 Characteristics of deep-lying horizons of oil and gas basins of the Russian Federation.**

Oil\gas bearing basin	Age of the deep interval of the sedimentary cover	Max. capacity of deep horizons	Tectonic appurtenance of deep horizons	Regional cap rocks providing fluid systems with abnormal reservoir pressure (ARP)
West Siberian	Mz-Pz	More than 10 km	Plate and preplate	Clays
Pre-Caspian	Pz	More than 10 km	Plate	Salts
Volga-Ural	R-Pz	Up to 5 km	Plate and preplate	Clays
Timan-Pechora	Pz	5–10 km	Plate and preplate	Clays, salts
Lena-Tunguska	R-Pz	Up to 5 km	Plate and preplate	Clays

**TABLE 2 Oil and gas province of the Russian Federation with the development of sedimentary complexes at deep depths.**

Oil\gas bearing mega provinces, provinces and subprovinces	Age of the sedimentary cover	Sedimentary cover capacity, km	Age of oil and gas complexes
Oil\gas bearing mega provinces of ancient platforms			
Eastern European (Russian) mega province			
Volga-Ural oil and gas province	PZ	1.0–6.0	D, C, P
Timan-Pechora oil and gas province	PZ	1.0–7.0	O, S, D, C, P, T
Pre-Caspian oil and gas province	PZ, MZ, KZ	6.0–16.0	D, C, P, T, J, K
Baltic oil and gas province	PZ, MZ	1.0–3.5	O, S
East Siberian mega province			
Lena-Tunguska oil and gas province	PR, PZ, MZ	2.0–7.0	R, V
Lena-Vilyuiskaya oil and gas province	PZ, MZ	2.0–14.0	P, T, J
Yenisey-Anabarskaya oil and gas province	PZ, MZ	2.0–11.0	P, T, J, K
Oil\gas bearing mega provinces of young platforms			
West Siberian oil and gas province	MZ, KZ	1.5–5.5	J, K
Pre-Caucasian-Crimean (Scythian) oil and gas megaprovince	MZ, KZ	2.0–6.0	P, T, J, K, N
Oil and gas provinces of folded territories			
Pre-Caucasian oil and gas subprovince	MZ, KZ	4.0–12.0	T, J, K, N
Pre-Ural oil and gas subprovince	PZ	4.0–14.0	O, S, D, C, P
Predverkhoyanskaya oil and gas subprovince	PZ, MZ	2.0–14.0	J
Oil and gas provinces of folded territories			
Transcaucasian oil and gas province	MZ, KZ	3.0–10.0	K, N
Far Eastern oil and gas province	KZ	2.0–6.0	N
Oil and gas provinces of the Arctic and Far Eastern seas of Russia			
Barents Sea gas and oil province	PZ, MZ	3.0–18.0	T, J
North Kara potential oil and gas province	PZ, MZ	2.0–12.0	D, C, K
Laptevskaya potential oil and gas province	PR, PZ, MZ, KZ	1.0–8.0	R, V, S, D, C, P, T, J
East Arctic potential oil and gas province	PR, PZ, MZ, KZ	0–8.0	R, V, S, D, C, P, T, J, K
South Chukotka potential oil and gas province	MZ		C, P, K
Okhotomorskaya oil and gas province	KZ		
Pre-Pacific oil and gas province	KZ	3.0–8.0	N <sub>1</sub>

A certain correlation has been established between the rate of deflection in the sedimentation basin, the rate, gradients of precipitation accumulation rates, on the one hand, and the facies-geochemical situation in the basin and the scale of hydrocarbon generation by oil and gas source rocks, on the other. In the catagenetic evolution (transformation) of organic matter, which begins with its accumulation and burial, as in all sedimentary processes, the sedimentation rate plays a leading role. Qualitative observations and quantitative analysis show that the concentration of OM in sediments increases with an increase in the rate of fossilization, but, reaching some optimum, then decreases (Fomin, 2011; Kerimov et al., 2018; Kontorovich et al., 2021).

In the Russian Federation, despite the rather high geological and geophysical study of oil and gas-bearing areas with a long history of exploration and development (North Pre-Caucasus, Volga-Ural, Pre-Caspian, Timan-Pechora and West Siberian, Lena-Tunguska oil and gas provinces), it can be stated that the number of discoveries at deep and ultra-deep depths (more than 5 km) is estimated units (Osipov, 2021) (Figure 1).

At the same time, in sedimentary basins, a fairly significant volume of rocks is located at deep and ultra-deep depths.

If we consider regions with developed infrastructure and a long history of study, the undisputed leader in the volume of sedimentary cover located deeper than 5 km is the Pre-Caspian oil and gas province (hereinafter referred to as “OGP”) the eastern part of which is located in the Republic of Kazakhstan. Within the West Siberian basin, the deepest part of the sedimentary cover is

developed in the central part and in the northern (aquatic), plunging towards the North Kara Depression, but in general, the proportion of deep-lying horizons is only 10%–15% (Figure 2).

Most of the sedimentary asymmetric basins have significant volumes of deep-lying rocks, mainly accumulated in the marginal parts of the platforms (foothill deflections—Pre-Ural, Pre-Caucasian, Pre-Verkhoyansky marginal deflections) along the mountain structures and characterized in that they are blocked by powerful and often filled with a high rate of accumulation (“avalanche”) sediments associated with the time of formation in adjacent areas of the corresponding orogenic structures (Samvelov, 1995; Kontorovich et al., 1998; Leonov et al., 2015; Litvinenko et al., 2017; Abukova and Volozh, 2021; Egorov et al., 2021) (Tables 1, 2).

The areas of development of deep-submerged sediments of the second type are mainly associated with ancient avlakogenes and, accordingly, the phases of their active deflection up to the beginning of inversion (Pre-Timansky, Pechora-Kolva, Vyatka, Kamsko-Belsky, Srednerussky, Pachelma, Moscow, Pripyat-Dnieper-Donetsk avlakogenes). Such areas, in general, are often characterized by an increased heat flow, since they are located above deep active structures and a wide development of tectonic discontinuities. The influence of faults as “cooling” channels on deep horizons has been established, for example, when comparing the temperatures of deep depths in neighboring areas of the TPP, in particular wells drilled within the Vuktyl shaft in the fault zone (West-Vuktyl No. 1 at a depth of 5,604 m, temperature—98.5°C, in the North-Vuktyl No. 214—5,025 m—90°C, Vuktylskaya

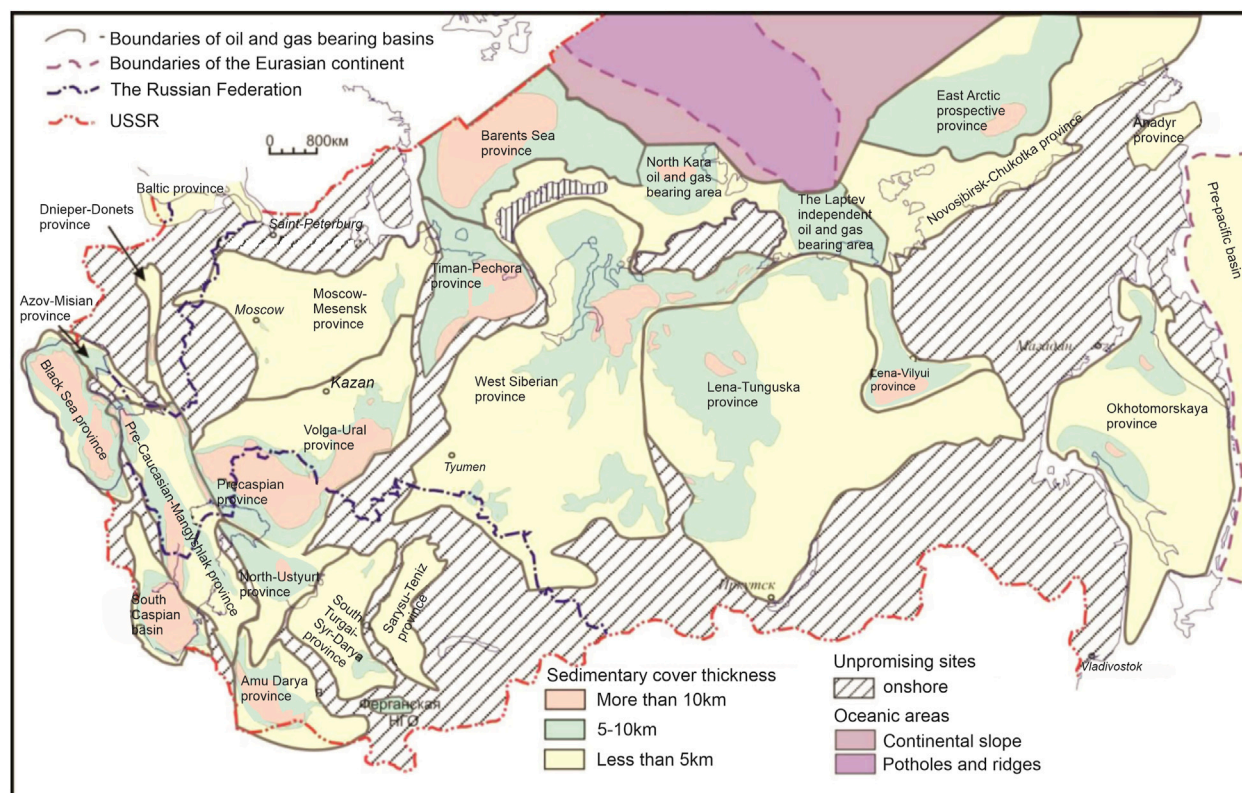


FIGURE 2

Map of oil and gas geological zoning of Russia and adjacent countries with selected areas with sediments at deep depths (Leonov et al., 2015).

No.58–6244 m—127°C, respectively, the geothermal gradient was 17°C–18°C/km), and in the Pechora-Kolva avlakogene in the Kolva ultra-deep well at a depth of 6,840 m, the temperature was 165°C, at a depth of 6,900 m—200°C, respectively, the geothermal gradient was 2.5°C–2.9°C/100m, i.e., significantly higher than in the fault zone. The deepest deposits represented by condensate and gas were found at a depth of 4,800–5,000 m. At the same time, within the Paleozoic part of the Pechora-Kolva avlakogene at depths from 4,500 to 4,800 m, 15 hydrocarbon deposits were identified, with differentiation from oil and gas condensate to oil.

Sedimentary basins such as the Pre-Caspian, Timan-Pechora, and East Barents Sea basins belong to areas with precipitation at deep depth deposited under avalanche sedimentation conditions.

The Pre-Caspian OGP also belongs to the sedimentary basins of the Russian Federation with a wide salt development in the section, followed by the Lena-Tunguska and Yenisei-Khatanga. There are some areas of deep-submerged sediments with the development of salts in the Timan-Pechora OGP.

In some areas of the ancient East European platform, in the areas of development of deep-submerged horizons—the Pre-Ural regional trough, the Dnieper–Donetsk depression—gas deposits were formed under conditions of immersion rates from 25 to 60 m/million years, occasionally more, and the gradients of the deflection rates exceeded 50 m/million years. At the same time, the main role in gas accumulation was played by the degassing of reservoir waters

during inversion tectonic movements and the destruction of oil from previously formed oil and gas deposits. Thus, in the Timan-Pechora sedimentary basin, areas of deep depths are associated, first of all, with the marginal part of the plate—the Pre-Ural marginal trough and the ancient (Riphean) Pechora-Kolva avlakogene (separating from the Paleo-Ural orogen and the younger (Early Hercynian) Varandei-Adzva, where the depths of the Lower Paleozoic part of the section exceed 8,000 m (and in deflection and more (up to 10,000 m) (Figure 3).

Analysis of sedimentation rates within the depressions of the Timan-Pechora sedimentary basin (ancient platform) shows a change from 15–30 m/million years in the gas-bearing Verkhnepetchorskaya and Denisovskaya depressions, up to 60–70 m/million years in the oil-bearing Khoreyverskaya.

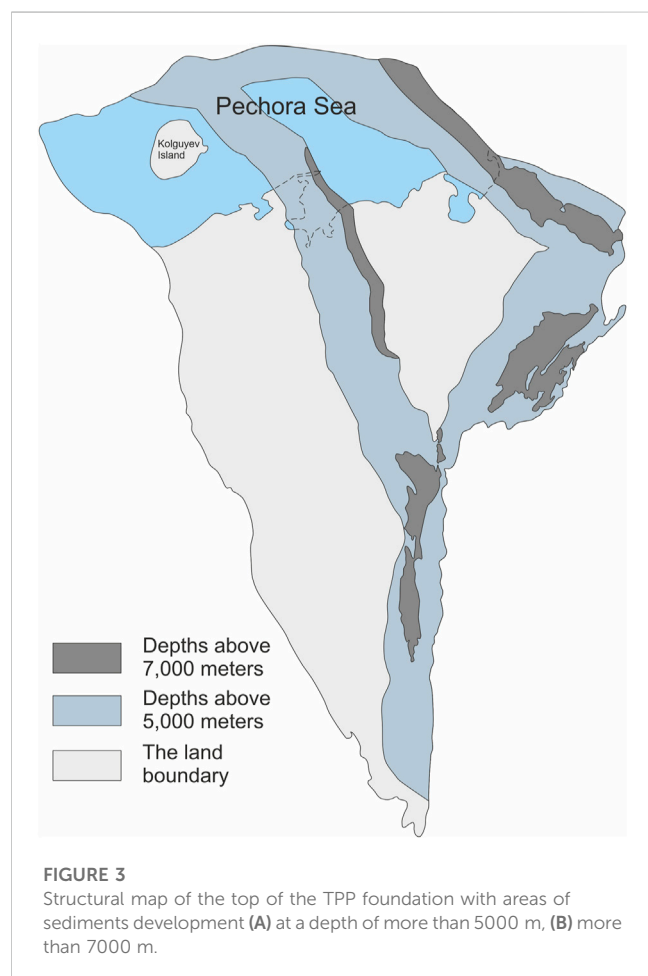
The study and development of the Arctic shelf, at least in areas remote from the coast, is postponed for a long period, probably beyond the middle of the current century, and therefore one can hardly expect much interest in their study in the next 30 years, despite the huge potential of deep horizons and their widespread development in provinces such as the Barents Sea, North Kara, Laptev Sea and East Siberian Sea (Dvornikov and Leusheva E.L. 2022). At the same time, the deep-submerged horizons of the water extensions of the Timan-Pechora, West Siberian and Pre-Caspian provinces will certainly be the subject of close study, especially when substantiating the prospects of oil-bearing capacity or the possibility of identifying condensate-enriched gas deposits.

Today deep horizons of some sedimentary basins (Ajdukiewicz et al., 2010; Gu et al., 2019; Huang et al., 2016; Lee and Geological Survey (U.S.), 1985; Li et al., 2021; Liu et al., 2012; Liu et al., 2015; Li et al., 2020; Adriano et al., 2022; Smith, 2018; Wang et al., 2014; Wei et al., 2019; Yang et al., 2021; Zhang et al., 2015; Zhu et al., 2021) are considered as the main directions of geological exploration for oil and gas within their limits.

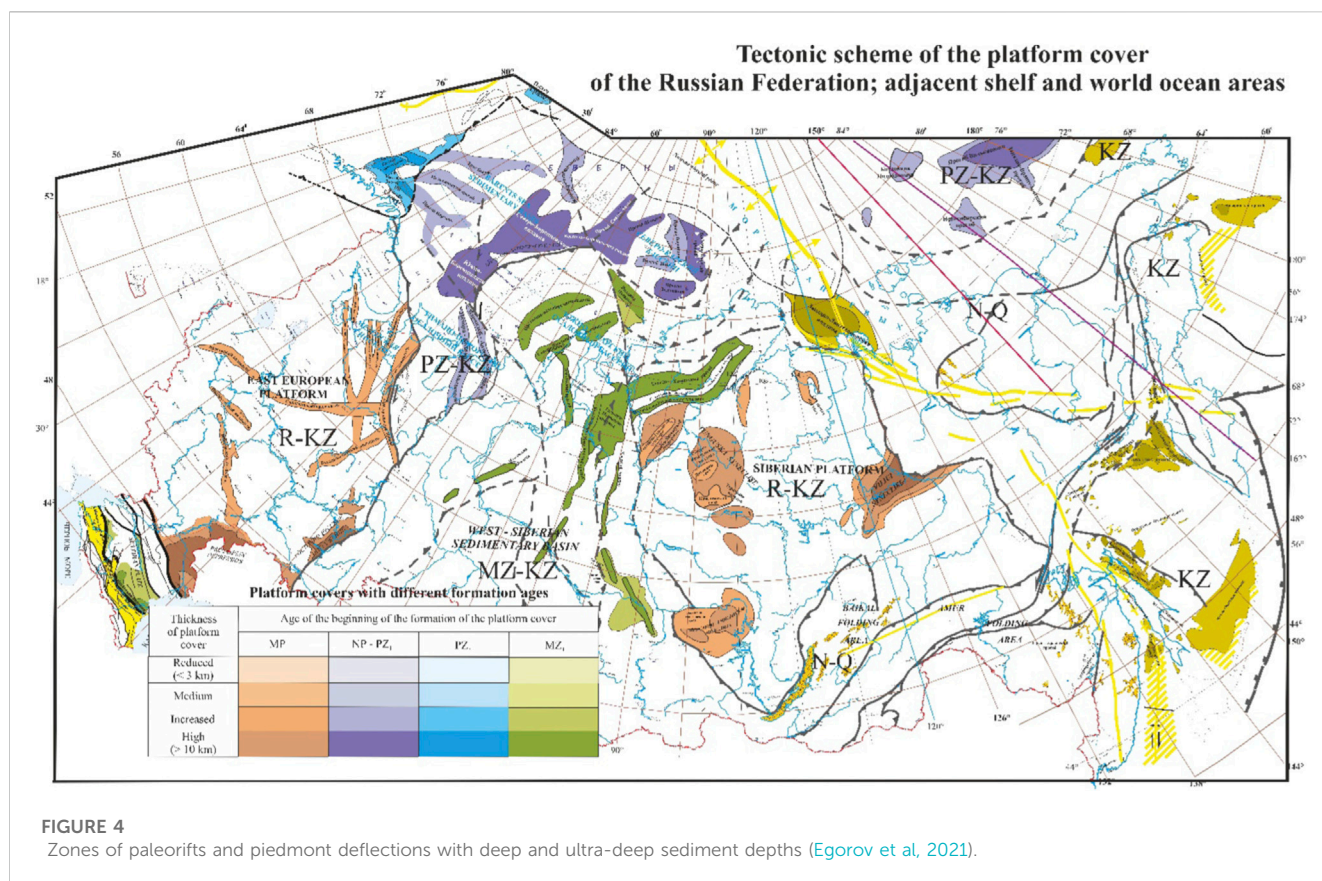
From the point of view of the tectonic position, it should be noted that in the Russian Federation there are several internal basins very similar to the Tarim and Dzungarian depressions of China, where deep-submerged sediments with identified accumulations of oil and gas are widely developed (Figure 4). There are known works comparing the geological structure of the depressions of China with the Zaisan, Zee-Bureinskaya and other depressions of the east of the Russian Federation. The problem is that in these depressions, even judging by relatively outdated seismic surveys, a large thickness of the sedimentary cover and, accordingly, a wide development of deep horizons are not expected. In this direction, it is possible to compare and consider, first of all, the prospects of such depressions as the Amur.

To develop criteria for the prospects of deep-submerged horizons, it is necessary to solve a number of theoretical issues, among the priority of which it is necessary to include such as:

- Conditions of formation (mechanisms of accumulation) and preservation of oil deposits at deep depths;
- Conditions of formation and preservation of reservoir rocks;
- Forms of migration and evolution (epigenetic processes) of hydrocarbons at deep depths;
- Geochemical conditions of formation, accumulation and preservation of hydrocarbons at deep depths.







The practice of geological exploration in the world and especially in China has proved the existence of liquid hydrocarbons in deep and ultra-deep horizons, including at high temperature and high pressure (Meihejef, 1993). Oil reservoirs preserved at temperatures above 200°C were found in the deep horizons of the Gulf of Mexico basin (Wang, 1992). In recent years, significant practical results have been achieved in the study of deep and ultra-deep horizons within the superimposed basins of inner China (Sun et al., 2013; Jia and Pang, 2015). Commercial inflows of oil and gas from reservoirs at depths of more than 7,000 m have been identified in the Sichuan, Tarim and Dzungarian basins. The most impressive results were obtained when studying ultra-deep horizons in the Shunbei region of the Tarim basin (Gu et al., 2019), where temperature and pressure were recognized as the most important factors affecting the conditions of formation, accumulation and preservation of hydrocarbons (Hao et al., 2002; Ren et al., 2008; Zhao et al., 2011; Liu et al., 2012; Zhang et al., 2015). However, for a wider range of sedimentary basins, including the Russian Federation, the influence of temperatures and thermal evolution on the phase state of hydrocarbons and the conditions of formation in deep and ultra-deep horizons has yet to be clarified.

The analysis of the revealed mechanisms of accumulation and conservation of hydrocarbons in deep and ultra-deep horizons of sedimentary basins of the world facilitates approaches to the development of a methodology for determining the areas of prospecting and exploration of deep-lying deposits.

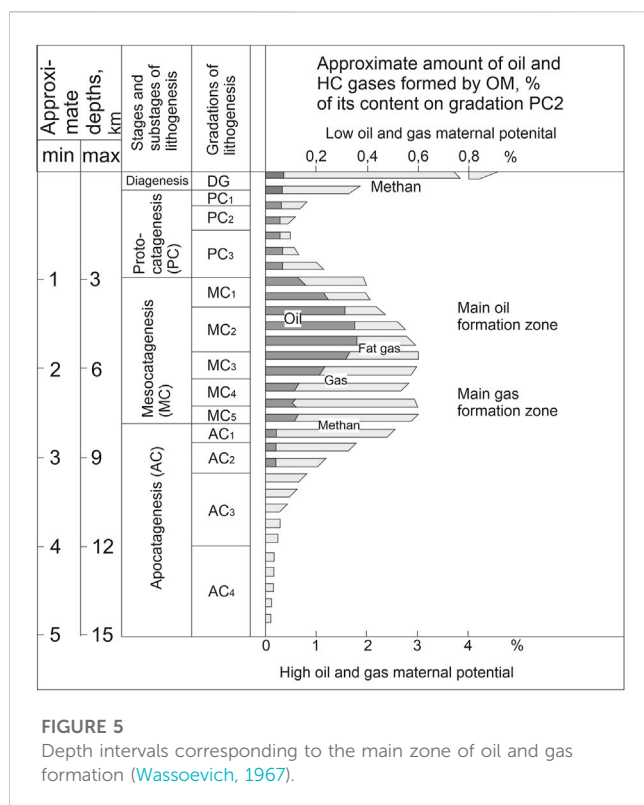
At the regional level, in order to determine the prospects for deep and ultra-deep horizons, along with traditional basin analysis, the study of the history of immersion and the nature of temperature changes, an analysis and the correlation of paleotemperature with pressure should be carried out (Kosenkova et al., 2022; Petrakov et al., 2022; Zakharov et al., 2022).

## 2 Dependence of the phase composition of hydrocarbons on the history of immersion and the influence of temperatures

Temperature is the most important factor determining the evolution of organic matter, the formation (generation) of hydrocarbons and the distribution of their phase state after accumulation (Wassoevich, 1967; Kontorovich et al., 2021).

With an increase in the depth of burial and temperature, the maturity of rocks and organic matter increases systematically.

According to researches (Wassoevich, 1967; Neruchev et al., 1976; Tissot and Welte, 1984; Kontorovich et al., 1991; Peters et al., 1994; Kontorovich et al., 1998; Bazhenova et al., 2008; Dakhnova et al., 2011; Jarvie, 2012; Kontorovich et al., 2021) the boundary temperature conditions were determined, as well as the pressures at which liquid and gaseous hydrocarbons are formed. At the same time, the actual depths of their formation were determined by the temperature gradient determined by the thermal conductivity of



rocks and the geothermal background, and, no less importantly, by the type of organic matter (sapropel, humus and mixed types according to researchers of the “Soviet” geochemical school or types I-II or III according to Peters et al., 1994). Thus, in the well-known work of N.B. Wassoevich in 1967, two scales are given - minimum and maximum depths (Figure 5) (the second is often not mentioned by representatives of the school of abiogenic origin of oil) from 2 to 8 km and gas formation from 4 to 12 km or more. Accordingly, without idealizing the tools and methods that were in the arsenal of researchers more than 50 years ago, it is necessary to note the great intuition and foresight of researchers who state, mainly, the possibility of reaching the stage of highly mature and super-mature OM (dry gas formation) at deep and ultra-deep depths, but do not deny the possibility, under certain temperature conditions and for of a certain type of OM, preservation of residual oil and condensate formation at these depths during full-scale gas formation.

According to the sedimentary migration theory (SMT), the “temperature window” of the formation of liquid hydrocarbons varies in the range of 60–90–120°C–150°C, the degree of transformation of OM, determined by the reflectivity of vitrinite (Ro) varies in the range of 0.60%–1.35% (Tissot and Welte, 1984) and according to the stage of catagenesis (used in the Russian Federation) is in the zone of mesocatagenesis of stages MK1–MK3. At the same time, most of the identified oil accumulations in the world are located in the temperature range of 65.5°C–149.0°C (Pusey, 1973). According to the SMT, hydrocarbons should not exist in a liquid state, even despite differences in the type of organic matter, in formations with temperatures above 150°C, i.e., at a standard temperature gradient at depths over 5 km!! Below this

mark, liquid hydrocarbons should be subjected to cracking—thermal decomposition with the formation of hydrocarbon gases, hydrogen, and carbon dioxide and sulfur compounds. And when temperatures reach 200°C (on average at a depth of more than 6 km), liquid hydrocarbons should completely decompose (Lu et al., 2002). At the same time, the lower boundary of the main gas formation zone is determined by depths of 6–8 km (or up to 9 km according to N.B. Wassoevich), i.e., in the temperature range up to 200°C–250°C.

However, some new geological discoveries that were made recently make it necessary to be more careful about determining the maximum temperatures and depths of oil and gas formation. For example, liquid hydrocarbons have been found in reservoirs with temperatures exceeding 200°C in China in the Wumishan formation in the Jizhong Basin in the Bohai Gulf Basin, in the United States at the Puckett field in the Valerille Basin and the Gomez field in the Delaware Basin, at the Marun field in the Persian Gulf (Ren et al., 2020). The temperature in the productive horizon of the Marun oil field exceeded 230°C (Sun et al., 2013). The temperature range of the distribution of liquid hydrocarbons in deep and ultra-deep horizons is very different from the temperatures considered by the classical SMT, as evidenced by the existence of liquid hydrocarbons at a very high temperature. The results of the studies show that traces of oil saturation with liquid hydrocarbons were detected in formations with a depth of 7,544–9,600 m, with catagenesis estimated higher than AK2-3, Ro reaching 3.0% and a reservoir temperature of 200°C–250°C (Price, 1993).

Statistics on Chinese basins over the past 40 years show a steady increase in depths estimated as the lower limit of the existence of oil deposits, and sometimes even faster than theoretical assumptions (Kosenkova et al., 2022) (Figure 6).

Thus, the solution to the question of the prospects of oil and gas potential of deep horizons lies in the field of explaining the established fact of a significant difference in the temperature of completion of oil and gas formation, varying in different basins and regions, depending on the time (speed) of heating, pressure, types of OM and other factors.

Some works (Kosenkova et al., 2022) note important differences in the conditions of formation of oil and gas deposits and the factors of their control between basins developed on ancient and young platforms at deep and ultra-deep depths. On ancient platforms, the boundaries of the distribution of liquid hydrocarbons are much higher in section and in intervals with lower temperatures than in the basins of young platforms or Mesozoic-Cenozoic folded and transitional regions. In the latter, oil deposits can sink to a depth of 7 km. The zone of accumulation of exclusively methane deposits in young basins has not yet been reached; it is assumed that it can be developed at a depth of 9–10 km (Gu et al., 2019; Kosenkova et al., 2022). At the same time, the marginal parts of the ancient platforms in the area of articulation with folded systems, due to the high rates of deflection and immersion in the orogenic stage of development, differ significantly in the paleotemperature conditions of deep depths, which is observed almost along the entire length of the Pre-Ural marginal deflection framing the Eastern European platform in three independent sedimentary basins at once (Timan-Pechora, Volga-Ural and the Pre-Caspian region).

The temperature and depth of completion of oil formation vary greatly in different types of basins (Figure 6).

## 2.1 The influence of paleotemperature on the phase state of hydrocarbons in ancient basins

At deep depths of the basins of ancient platforms, a significant number of deposits of liquid hydrocarbons—oil and/or gas condensate—have been revealed. Such accumulations are established, first of all, in zones of extremely low temperature gradients determined by geological conditions, the first of which include the presence of salts, late and rapid deflection, where Paleozoic sediments were at low temperatures for a long time.

Such areas include the Pre-Caspian bowl, where the geothermal gradient is only 16°C/km (Gulieyu et al., 2017; Khafizov et al., 2020), and the lower boundary of oil formation drops to a depth of 8–9 km, the Pre-Ural deflection of the marginal part of the Pechora Plate (the geothermal gradient is only 14°C–17°C/km. In the Tarim basin of China, the reservoir temperature at a depth of 8,000 m is only 160°C–170°C, and oil detected at a depth of more than 7 km (Liu et al., 2015; Huang et al., 2016; Ma, 2016) (7,200–7,863 m) in the Ordovician formation in the Shunbei region has no signs of degradation (Sun et al., 2013) (Figure 7). Ordovician sediments in the Shunbei area of the Tarim basin have been in low temperature conditions for a long time, which was crucial for the preservation of the light part of liquid hydrocarbons.

In the Dzungarian basin, a fairly low geothermal gradient is observed in a number of wells in the central part of the basin (2.0°C–2.3°C/100 m), and accordingly, conditions for the formation of oil have been preserved at depths up to 6 km, and condensate at deeper depths. Thus, in the work (Prischepa et al., 2022), a pattern of decreasing the density of crude oil with depth was revealed (at a depth of <3,100 m—average density oil 0.84–0.9 g/cm<sup>3</sup>, at a depth of

3,100–3,900 m—light oil 0.8–0.82 g/cm<sup>3</sup>, and below 4,400 m—mainly condensate. An important pattern is noted in the distribution of gas in the central part of the Dzungarian basin. Thus, the methane content varies from 60%–95% with a decrease in it at deep depths (below 4,500 m <80%). The content of ethane and propane, on the contrary, gradually increases with increasing depth (Prischepa et al., 2022). The dryness coefficient of natural gas in the study area is 0.7–1.0 and it gradually decreases with increasing depth.

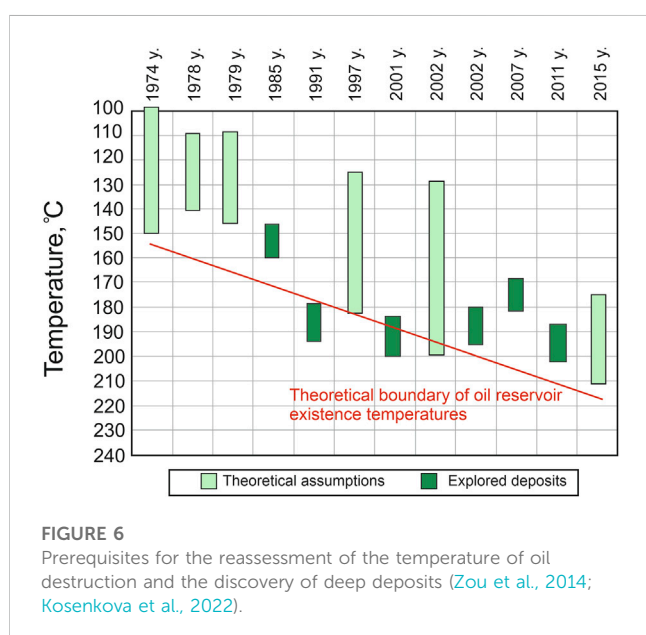
On the other hand, along with geochemical conditions, an extremely important positive factor for hydrocarbons of deep depths is a significant expansion of the reservoir conservation depth range in conditions of a low geothermal gradient.

In one of the most representative (in terms of the number of wells) that have opened deep and ultra-deep horizons, in the sedimentary basin of the Gulf of Mexico (HPHT, 2020; Iskaziev et al., 2021) out of more than 30,000 wells drilled in the period of 2000–2016. 31 wells reached a depth of 9,000 m and more than 60 wells reached a depth of 8,000 m (the total of the sea and rocks, with most of these wells drilled at a sea depth of more than 3,000 m) (Figure 3). For wells with a depth of more than 6,000 m, the average geothermal gradient differs significantly in wells drilled in a zone of relatively shallow sea depths (up to 3,000 m), but with a small proportion of salts in the section or their absence from 24°C to 26°C/km to 12°C–12.8°C/km for wells drilled at a deeper depth of the sea (more than 3,000 m) and with a significant development of salts in the section. Very low downhole temperatures were detected in the deepest 8 wells (9,700–10,000 m) from 93°C to 138°C, which indicates the conditions for finding such horizons in the conditions of the completion of the “oil window”. One of the important factors determining the preservation of oil from cracking at high temperatures is pressure. The deep horizons of the Gulf of Mexico basin are characterized by abnormally high reservoir pressures with a coefficient of 1.6–2.0 (Figure 8).

For Paleozoic basins, such as the Pre-Caspian bowl, a low geothermal gradient (1.2–2.2 C/100 m) determined the reservoir temperature no more than 200°C even for the deepest horizons (14–16 km), which can be considered as the main factor in the possibility of the existence of deep-lying oil and gas deposits in the basin in the Paleozoic and possibly in the Upper Proterozoic deposits. The key factor is not the achievement of temperatures at which crude oil is completely cracked, and the oil and gas producing strata remain in the range of oil generation.

## 2.2 Influence of paleotemperature on the phase state of hydrocarbons in young basins

For the basins of young platforms, it was found that under conditions of rapid temperature increase and even with a high geothermal gradient, deposits of crude oil and gas condensate are formed and preserved at deep depth. For example, in the basin of the Bohai Bay, which belongs to the Cenozoic basins, where a high geothermal gradient is established, rapid deflection and, accordingly, rapid temperature rise in the late Cenozoic led to thermal transformation of the source rocks, causing a rapid transition





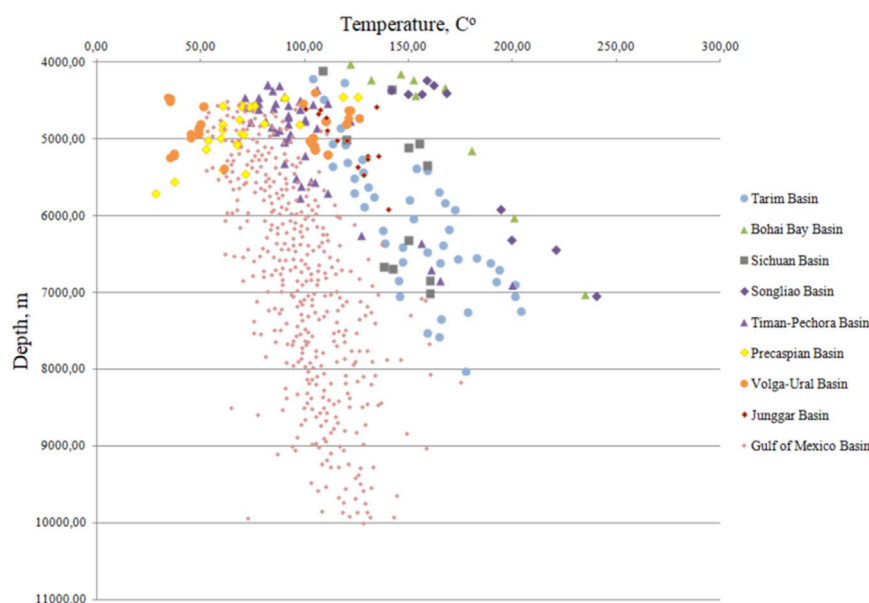


**FIGURE 7**

The dependence of temperature on depth in the oil and gas basins of the world, opened by IIs at deep depths (Wang et al., 2014; Ma, 2016; Liu et al., 2017, HPHT 2020).

from oil formation to gas formation. Thus, in the basin of the Bohai Bay, a condensate-saturated reservoir was detected at a depth of 5,641–6,027 m with a reservoir temperature of 201°C (Zhao et al., 2011). According to modern data, at a depth below 4,500 m, the reflectivity coefficient of vitrinite  $R_o$  exceeded 1.5%, which indicates the stage of intense gas formation. At a depth of 5,141 m, the temperature reached 180°C, but due to the short duration of heating—less than 10 million years (Zhou et al., 2017), the condensate did not degrade.

The cracking of crude oil is controlled by the properties of crude oil and the history of thermal evolution. Experiments show that the boundaries of the beginning of oil degradation differ greatly in temperature. So, if under standard conditions this occurs in the range from 165°C to 190°C, then under certain conditions (extremely high pressure) oil is preserved at higher temperatures in the range from 230°C to 240°C (Sun et al., 2013; Liu et al., 2017). Under the condition of rapid burial and low temperature due to the low geothermal gradient in the Cenozoic basins, the depth of oil formation is in a very wide range, with a maximum of more than 8,000 m or even more than 10,000 m (Sun et al., 2013; Liu et al., 2017; Ren et al., 2020).

For intermountain basins and foothill depressions, such as the southern part of the Pre-Caspian basin, the Panon basin, due to rapid immersion and short heating time (<10–15 million years), the temperature of the “oil window” is significantly higher than in other basins at comparable depths.

For Mesozoic basins (for example, the Barents Sea, West Siberian) with a low rate of deflection in the Cenozoic, or subjected to uplift and denudation since the Cenozoic, the effective heating time is stretched, and the temperature of the “oil window” and “gas window” decreases, and the depth of the location of oil and gas deposits is extremely limited.

## 2.3 Influence of heating time on the phase state of hydrocarbons

The heating time also has an important influence on the temperature range and phase state of hydrocarbons. Temperature and heating time are the key reasons for the difference in temperature ranges of phase states of hydrocarbons in different basins. In the case of a short heating time, the oil is stored at a very high temperature. Liquid hydrocarbons can be stored at a maximum depth of up to 8,000 m and reservoir temperature >200°C; gas deposits—at a maximum depth of 10,000–12,000 m and reservoir temperature up to 300°C–350°C (Tuo, 2002). Oil in a basin with a short heating time and a temperature in the range from 300°C to 315°C was discovered in a deep ocean basin in the northeast Pacific Ocean (Wang, 1992).

For basins with a high deflection rate in the Cenozoic, the effective heating time is very short, and crude oil can exist at very high temperatures. For example, in China, condensate gas deposits were found in the Bohai Bay basin at a temperature of 201°C at a depth of 6,027 m (Sun et al., 2013); liquid hydrocarbons were detected at a depth of 5,011 m in the Inghehai Basin at a reservoir temperature of 240°C and  $R_o$  of only 1.20% (Hao et al., 2002). With the same rate of increase in reservoir temperature, the temperature of the initial cracking of oil varies greatly from region to region, and the temperature of the complete cracking of oil also differs slightly.

As a rule, the temperature at which the liquid phase undergoes thermal cracking is at least 170°C, and the thermal stability largely depends on the composition of the crude oil, in addition to the temperature and heating time. The temperature of the formation of the oil phase is 178°C–214°C (Liu et al., 2017).



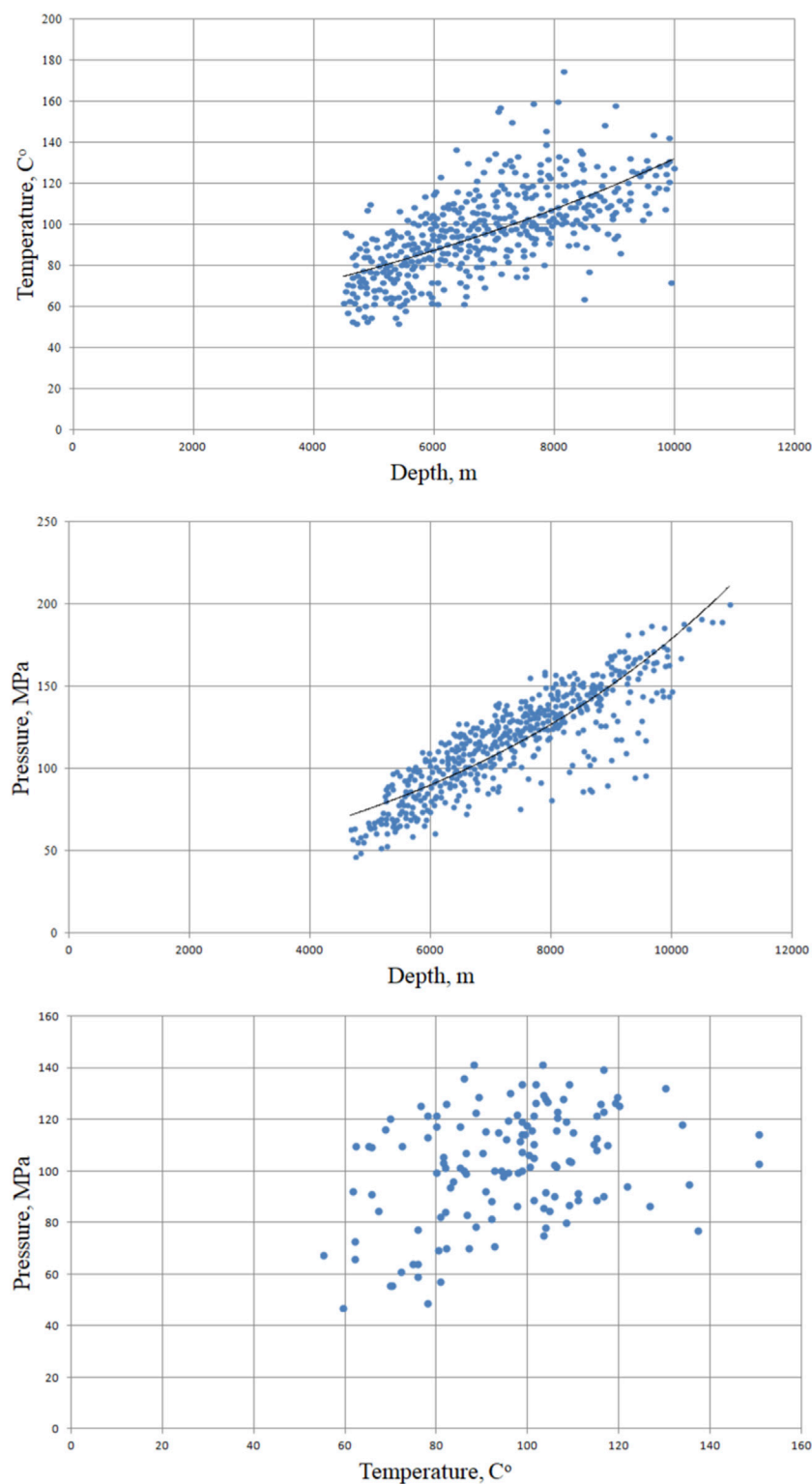


**FIGURE 8**

Thermodynamic conditions at deep depth in wells of the Gulf of Mexico. Based on materials (HPHT, 2020).

The heating rate also has an obvious effect on the temperature range of the liquid phase. An increase in the heating rate from 1°C/Ma to 10°C/Ma can increase the temperature of the

independent oil phase by 17°C–27°C. With an increase in the heating rate in conditions of deep depth and high temperature, hydrocarbons can exist in the oil phase, and the temperature limit

for storing condensate in a supercritical state is about 240°C (Kerimov and Osipov, 2016; Liu et al., 2017; Kerimov et al., 2018; Ren et al., 2020).

### 3 The relationship between pressure and temperature

An important role in the control of the phase state of hydrocarbons and the distribution of oil and gas reserves depending on the ratio of temperature and pressure is revealed. These two factors are closely related and interact with each other.

According to data analysis, the correlation between temperature and pressure at deep depths is complex and varies significantly in different types of basins and even in different structural units of the same basin. This ratio can be divided into three types: the type of high temperature and high pressure, the type of low average temperature and high pressure, and the type of medium temperature and low-medium pressure (Ren et al., 2020) (Figure 9).

#### 3.1 Basin type with high temperature and high pressure

High reservoir temperatures (>150°C) and high reservoir pressures (>60 MPa) in deep and ultra-deep depths are the most typical and characteristic of both ancient and young basins. According to classical concepts, the degree of transformation of organic matter should be extremely high and oil can only be located at a relatively shallow depth. But high pressure prevents the

conversion of hydrocarbons into oil and gas producing strata, which is why the temperature does not reach the threshold value of cracking crude oil. (Gu et al., 2019). At the same time, another extremely important positive moment was revealed, associated with the possibility of formation of fracture zones in such conditions, as well as the formation of an additional capacity due to a large driving force due to pressure drop during migration from the oil and gas producing strata. Such examples are known in the Timan-Pechora, Pre-Caspian and Lena-Tunguska basins (Cherdantsev and Zharkov, 2021; Zhukov and Kuzmin, 2021; Prischepa et al., 2022).

The influence of abnormally high pressure plays an important role in controlling the thermal evolution of deep-lying oil and gas source formations. Some researchers as Price and Wenger (1992) believe that an increase in pressure can prevent the thermal release of organic matter and the formation of oil and gas. At the same time, the correlation between the reflectivity of vitrinite and the depth in the overpressure range (2,400–4,500 m) in the northern part of the Green River basin in the United States did not reveal any significant effect of overpressure on the reflectivity of vitrinite (Law, 2002). The study of Domanik deposits of the TPP (Prischepa et al., 2013) showed, with large pressure variations, significant variations in determining the reflectivity of vitrinite and the degree of transformation of organic matter in neighboring wells and even within the section of one well, depending more on the lithological composition. Excessive pressure prevents thermal degradation and formation of hydrocarbons from kerogens, as well as high-temperature cracking of hydrocarbons (Helgeson et al., 2009; Gu et al., 2019).

In sedimentary basins with a low geothermal gradient and a deep depth of occurrence of oil and gas producing strata, high pressure affects the thermal evolution and the degree of transformation. Thus, in the study (Gu et al., 2019), Ro was observed to be more

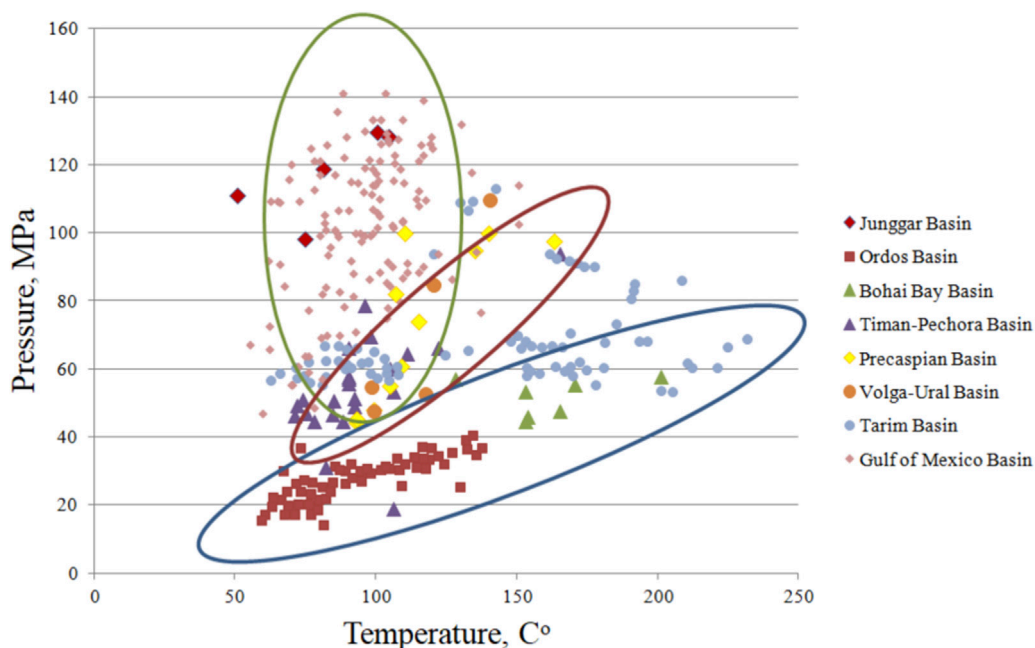


FIGURE 9

Correlation between reservoir temperature and reservoir pressure in deep oil and gas deposits.

than 0.5% lower than the normal value. High pressure helps to prolong the formation time of liquid hydrocarbons in the strata at deep and ultra-deep depths and prevents the conversion of liquid hydrocarbons into gaseous hydrocarbons.

The presence of excessive pressure leads to the fact that even deep-lying oil and gas producing strata (hereinafter referred to as “OGPS”) that have entered the stage of metamorphism in a sedimentary basin with a high geothermal gradient remain in a favorable stage of hydrocarbon formation and accumulation of oil and gas. At the Lake Washington oil field in the Gulf of Mexico basin, tertiary formations with a depth of more than 6,540 m have a reservoir temperature of more than 200°C, but hydrocarbons remain in the liquid phase due to abnormally high pressure (130 MPa) (Ajdukiewicz et al., 2010).

Typical examples are the Shunbei, Tabei, and Anyue gas fields in the Tarim Basin. In the Shunbei region, for deep-lying (more than 8,000 m) productive sediments of the Ordovician, the geothermal gradient is 2.12°C/100 m, the reservoir temperature is 160°C–170°C, and the reservoir pressure is more than 80 MPa. At the Anyue gas field, the gas reservoir of the Lunwangmiao formation at a depth of 4,600–5,400 m is characterized by a reservoir temperature of 140°C–161°C, a reservoir pressure of 56–59 MPa and a pressure anomaly coefficient of 1.06–1.65 (Wang et al., 2014).

### 3.2 Basin type with low temperature and abnormally high pressure

In the most common case, both temperature and pressure are a function of the depth of occurrence and, accordingly, at deep and ultra-deep depths, high pressures must correspond to high temperatures. The causes of temperature anomalies were discussed above, mainly in the direction of their lowered values, caused by both a reduced geothermal background and a “cooling” effect in the case of the presence of salts in the section, a powerful layer of overlapping water in the water areas and zones of tectonic disturbances. Accordingly, in such areas, a lower temperature will be shown relatively to the “standard” at the appropriate depths. A feature of sedimentary basins with oil deposits at deep depths is often abnormally high pressures with an anomaly coefficient of 1.5 or more.

This type of basins (structures) is characterized by a low reservoir temperature (usually up to 150°C) and increased reservoir pressure (usually >80 MPa) than most basins at comparable depths of 5,000–8,000 m.

Since pressure can suppress the degree of thermal transformation of hydrocarbons for this type of structures, the generation stages and the possibility of preserving liquid and gaseous hydrocarbons occur later and at deeper depths. Abnormally high pressure can also slow down the compaction of overlying sediments, which contributes to the formation and preservation of deep and ultra-deep zones with high residual porosity (Ren et al., 2020; Volozh et al., 2021; Zakharov et al., 2022). Typical examples are the Keshen gas fields of the Tarim basin, Kelasu and Dabey in the Kulkainsky depression of the Dzungarian basin (Lu et al., 2018).

The Kela-Keshen gas field (Tarim basin) is an ultra-deep accumulation in the zone of abnormally high pressures at a depth of 6,500–8,000 m, with a reservoir pressure of 90–136 MPa,

an anomaly coefficient of 1.60–1.85 and a low reservoir temperature of less than 150°C. The same is noted for the neighboring Keshen 2 block, where the initial reservoir pressure was 116 MPa, the pressure anomaly coefficient is 1.79, and the reservoir temperature is 168°C. The Keshen gas field was formed due to the Jurassic coal-bearing gas-producing strata of the Baicheng depression. The maturity coefficient of natural gas at the gas field is 2.28%–3.68%, on average 3.10%, which indicates the overripe nature of natural gas.

Similar thermobaric conditions were found in the central part of the Dzungarian basin located to the north. So, at depths from 4,600 to 5,900 m, the reservoir pressure was 67–115 MPa, the anomaly coefficient was 1.45–2.04, and the reservoir temperatures varied in the range of 100°C–140°C, i.e., they were low enough for such depths. The reservoir, according to the researchers, was formed under the influence of rapid burial and rapid formation of hydrocarbons, as well as a significant difference in pressure in oil and gas producing strata and reservoirs with a correspondingly strong driving force of migration and accumulation of hydrocarbons (Wei et al., 2019).

### 3.3 Medium temperature and low pressure type

Sedimentary basins with low pressure (<50 MPa) and moderate temperature at deep depths (<150°C) are specific, first of all, for ancient platforms or their marginal parts, but are also noted on young platforms. They have extremely limited opportunities for vertical and lateral redistribution of hydrocarbons due to the low pressure drop. The most favorable conditions for the preservation of oil and gas accumulations at deep depths are provided by relatively young uplift and erosion. In such conditions, a significant potential is associated with the oil and gas producing strata from which previously generated hydrocarbons did not migrate. Typical examples are the Lena-Tunguska OGP of the Siberian Platform with a large burial depth in the Proterozoic and Paleozoic periods and a relatively small depth at present, limited areas of the northern part of the West Siberian OGP, and, for example, the Ordos basin in China. The Ordos basin was subjected to severe uplift and erosion, which let the residual potential of the OGPS to be preserved.

Despite the similarity of temperature–pressure relations, when comparing the sedimentary basins of the Siberian Platform and the Ordos basin, they differ significantly in the hydrocarbon potential of the deep-lying horizons. Thus, in the Lena-Tunguska OGP, the widely developed phenomena of uplift and erosion in the period after the Early Ordovician, when the basin reached the maximum depth of immersion and maximum paleotemperature, which allowed the formation of hydrocarbons from black shales of the Riphean and Vendian age, led mainly to unsatisfactory conditions for the preservation of deposits at deep depths, since the ancient (Late Riphean–Vendian) reservoirs were violated (Bochkarev and Krinichkin, 1988). At the same time, due to the low geothermal gradient, the ancient OGPS were still at the stage of oil formation at the time of the beginning of the inversion. Later, when the basin experienced slow uplift and was largely eroded, the reservoir temperature decreased. A positive factor for deep horizons was the widespread distribution of salts in the lower Cambrian of the

East Siberian Platform, which in this case did not work as a subsurface cooling system, but created good conditions for the preservation of ancient oil and gas deposits, which is confirmed by numerous discoveries at moderate depths and are assumed to be within the entire Riphean-Vendian (Precambrian) part section (Bochkarev and Krinochkin, 1988; Qiu et al., 2018) (Figure 10).

Inversion movements and the influence of erosion processes are noted as important factors that cause the formation of reservoirs in ancient (Paleozoic) strata filled with hydrocarbons before their immersion to deep depth in subsequent historical periods. The possibility of preserving deposits is provided, as already discussed earlier, by a high rate of immersion and high pressures that do not let cracking to begin. Thus, the influence of erosion processes with an emphasis on carbonate rocks is noted for many formations and sedimentary basins where oil deposits have been identified at deep depths. The influence of stratigraphic inconsistencies on the improvement of reservoir properties as a result of leaching by meteoric waters is noted in works.

Discussing the criteria of oil and gas potential along with the effect of “cooling” of the depths, due to the presence of conducting (through) faults, it is impossible not to say about their role in the formation and distribution of reservoirs. Thus, at deep depths, control of the distribution of oil-saturated reservoirs by faults is noted, which is used as a search sign (Figure 10). Based on the analysis of the factors of hydrocarbon accumulation in the deep reservoirs of the oil and gas fields of the Dzungarian basin (Shiksi, Mobei, and Mosuovanan), it was concluded that the oil and gas source rocks were connected by faults with the reservoirs (Prischepa

et al., 2022), which let hydrocarbons to migrate. Consequently, faults not only contribute to the formation of fractures at deep depths (Prischepa et al., 2022), but also to the flow of oil and gas through them.

Conditions for the formation of reservoirs (areas with improved FCS) at deep depths are an important issue along with the formation and preservation of hydrocarbons (Kosenkova et al., 2022; Kuandykov et al., 2022). A major generalization on the distribution of porosity and permeability at deep depths was made in Ehrenberg's work, in which an extensive database was statistically processed, including more than 35,000 values for terrigenous sections and 13,300 for carbonates (Ehrenberg and Nadeau, 2005). A decrease in porosity with depth was traced in the range up to 3,500–4,500 m, after which a “flattening” of the trend is observed, which allows us extrapolating the values of absolute porosity to more than 5,000–6,000 m at the level of 8% for carbonate reservoirs and 10% for terrigenous ones. Due to the significantly greater chemical activity of carbonate reservoirs, epigenetic processes during immersion pay great attention to them. It is noted that for FCS, the influence of reservoir temperatures (and paleotemperature) is much more important than the absolute values of the depths of occurrence (Kuandykov et al., 2022).

A significant addition to understanding the prospects of deep horizons is the direct study of the geochemistry of oil and the comparison of parameters with the geochemistry of extracted bitumen core samples. Thus, the use of the isomerization parameters of C29 sterane for deep oil and shallow oil deposits makes it possible to determine the similarity of the source of oil and

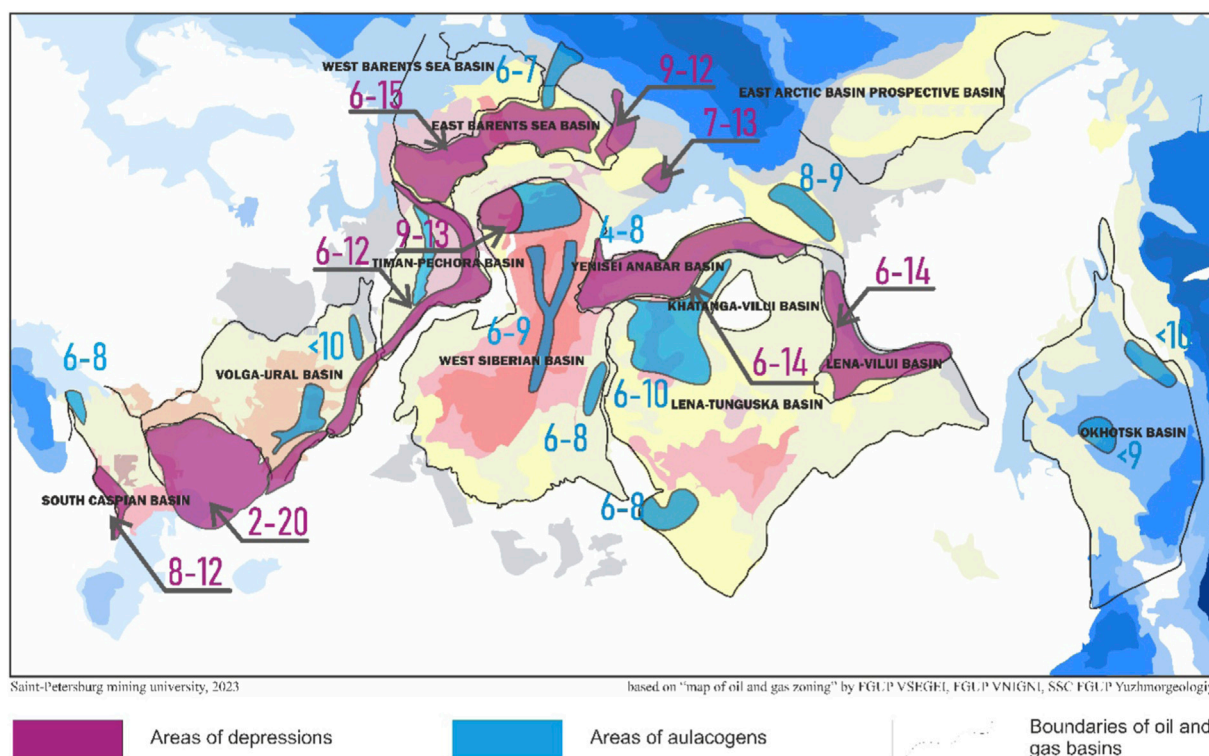


FIGURE 10

Schematic distribution of deep-lying sedimentary complexes in oil and gas basins of the Russian Federation.



gas formation, and the ratio of  $\beta\beta$  sterane  $C_{29}/(\beta\beta+\alpha\alpha)$  characterizes the depth, since it decreases with increasing depth. This is probably influenced by the degree of thermal evolution, which increases with increasing thermal maturity and, according to (Osipov, 2021), significantly affects the migration of hydrocarbons. During the migration of oil and gas, the ratio of  $\beta\beta$  sterane  $C_{29}/(\beta\beta+\alpha\alpha)$  increases with the distance of migration. Thus, the ratio of  $\beta\beta$  sterane  $C_{29}/(\beta\beta+\alpha\alpha)$  is gradually increasing from deep-lying to shallow oil and indicates oil migration controlled by faults and distance.

Based on the analysis and the proposed classification, a sequence (methodology) for studying deep and ultra-deep horizons of sedimentary basins of the Russian Federation, including two main blocks, has been developed (Figure 11):

1. Study of thermodynamic conditions (temperature, pressure) and assessment of their influence on the possibility of formation and preservation of hydrocarbon accumulations at deep depths.
2. Assessment of geochemical conditions for the formation and preservation of hydrocarbon accumulations at deep depths.

The first block, in turn, includes the study of:

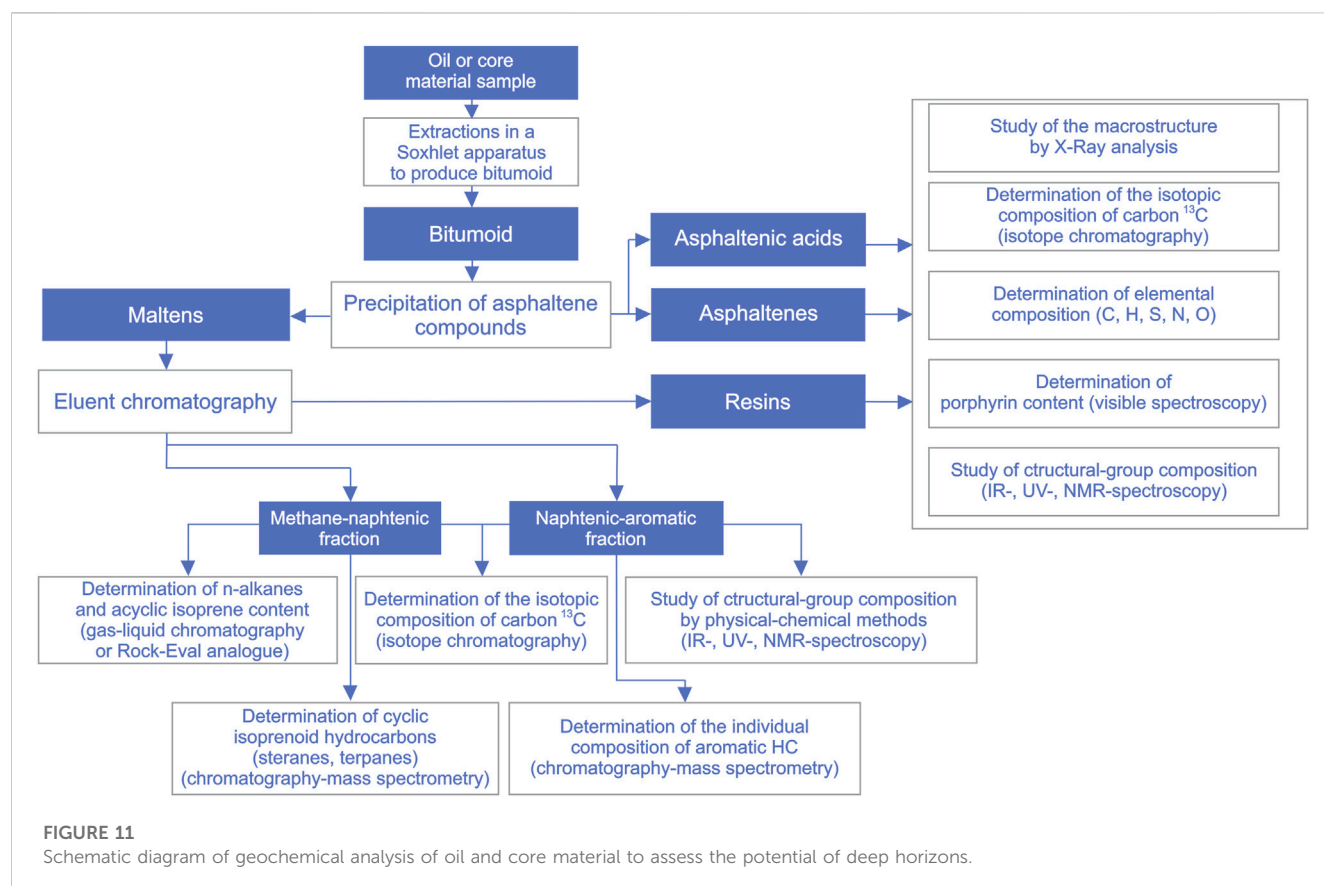
- Geodynamic characteristics of the sedimentary basin (including tectonic conditions for the formation of underlying sedimentary cover levels);

- Sedimentary basin immersion history (immersion rates and sedimentation rates);
- The nature of the temperature distribution and geothermal gradient with an emphasis on deep depths;
- Paleotemperature history (time of exposure to temperatures);
- Lithological composition of rocks, distribution of depths and areas of development of salts and salt-containing strata;
- Conducting or screening properties of tectonic disturbances penetrating to deep depths;
- Studying the possibility of preserving the primary properties of reservoirs (porosity) at deep depths;
- Studying the time and scale of formation and preservation of fracturing.

The second block of research includes a number of sequential procedures containing clarification of the features of the geological structure of the thickness section intervals that can be diagnosed as oil and gas-producing, the study of geochemical features and biomarkers of oil and gases, oil-saturated reservoirs, bitumoids and kerogen of the core of wells from deep depths and the study of reservoir properties of hydrocarbon-containing strata.

Such sequential steps include:

1. Identification of characteristic features of attribution to high-carbon deposits (study of TOC content).
2. Determination of the stratigraphic interval of the distribution of deposits primarily enriched with organic matter, referred to as OGPS.



3. Determination of lithological composition (microscopic and petrographic studies of sections) and lithotyping of sediments.
4. Mapping of the current concentration of organic carbon and catagenetic maturity of organic matter by bituminological and pyrolytic studies.
5. Assessment of geochemical parameters (laboratory study of extracts of bitumoids and pyrolytic studies of core samples), distribution and degree of transformation of organic matter of high-carbon deposits, their association with different lithotypes and zones differ in facies conditions of formation.
6. Assessment of thermodynamic conditions. Isolation of temperature parameters and pressures of zones of HC manifestation and preservation of different composition.
7. Geochemical characteristics of oil and bitumen extracts (analytical studies, including: pyrolysis (Rock-Eval), study of the kinetics of thermal decomposition of kerogen, one-dimensional (GC-MS), two-dimensional (GC × GC-MS) chromatomass spectrometry and isotope mass spectrometry (EA-IRMS).
8. Biomarker analysis with the identification of the oil-extract connection.
9. Assessment of the possibility of preserving the porosity (petrophysical parameters) of the selected OGPS lithotypes.
10. Evaluation of petrophysical properties with fracturing.
11. Recalculation of the organic carbon content in rocks at the beginning of catagenesis using balance equations for three main types of organic matter.
12. Determination of the movable part of bitumoids (separation into residual kerogen and parautachthonous bitumoids) preserved in Domanik oil and gas bearing deposits after migration of generated hydrocarbons.
13. Assessment of oil and gas resources of deep and ultra-deep horizons according to a set of geological and geochemical indicators.
14. Assessment of the possibility of using the developed approach to the deeply submerged horizons of sedimentary basins of the Russian Federation

Geochemical characteristics of oil and bitumen extracts can be obtained by using a complex of modern analytical studies, including: pyrolysis (Rock-Eval), study of the kinetics of thermal decomposition of kerogen, one-dimensional (GC-MS), two-dimensional (GC × GC-MS) chromatomass spectrometry and isotope mass spectrometry (EA-IRMS).

According to the results of pyrolytic studies, the total content of organic carbon (TOC) in rocks can be estimated. The obtained pyrolytic parameters S1, S2, and Tmax are used to estimate the generation potential.

The Russian Federation has store of considerable experience in studying kerogen-saturated sections of such oil-producing strata as the Bazhenov, Domanik, Kuma, and Khadum formations, located at relatively shallow depths and almost unexplored at deep depths. Meanwhile, even fragmentary data indicate a significant and not fully realized potential of these strata at deep depths. Thus, in the Timan-Pechora basin, “cooled” zones with a geothermal gradient of 15°C–18°C/km and a residual TOC for marls and clay

limestones of the Upper Devonian from 0.5% to 1% were identified within the junction zone of the marginal part of the platform and the Pre-Ural marginal deflection. According to the results of GIS, intervals of oil-producing, fluid-saturated rocks are being distinguished.

In connection with the development of ideas about events that contribute to the accumulation of carbon-enriched “high-bituminous” horizons, the information about global anoxic events in the World Ocean is important information for their diagnosis. The isotopic composition measured by the values of isotopic densification  $\delta^{13}\text{C}_{\text{carb}}$  and  $\delta^{13}\text{C}_{\text{org}}$ . Carbonate and organic carbon of sedimentary rocks allows us to diagnose sedimentation conditions and to isolate biotic and facies conditions for the formation of enriched rocks with OM.

The saturation of reservoirs with movable oil (both natural reservoirs and technically stimulated ones) can be determined by high values of pyrolytic parameters S0 + S1, productivity index (PI), oil saturation index (OSI) and reduced Tmax, relative to the average distribution in the section.

According to the results of kinetic studies of thermal decomposition of kerogen, most samples are characterized by a spectrum characteristic of type II kerogen. As the degree of catagenesis increases, the shape of the spectrum changes and the maximum shifts towards higher activation energies. Information about the facies-genetic type of OM and its thermal maturity can be obtained by studying the composition of biomarkers and isotopic composition data. Based on the values of molecular parameters, characteristic biomarker ratios Pr/Ph and C29/C27, conclusions are drawn about the assessment of the conditions for the OM formation of the studied deep sediment bitumoids.

The second block of the proposed methodology assumes the obtained analytical data, which should be compared with the data of thermodynamic modeling to assess the possibility of the existence of individual components of liquid oil, gaseous reservoir fluid and solid kerogen mass under various thermobaric conditions (Shimansky et al., 1994; Kerimov et al., 2018; Kontorovich et al., 2021).

It is most rational to take the interpretation of equilibrium processes described in R. Helgeson's work as the basis of the thermodynamic model (Helgeson et al., 2009).

The Helgeson model suggests a sequence of biomass conversion processes with a step-by-step transformation of shales containing bitumoids and kerogen, oil and gas, formed, among other things, in areas of high pressures, temperatures and depths.

For further research, it is important that this equilibrium system of equations will also help to describe the processes postulated within the framework of abiogenic concepts, which are characterized by a reversible dependence.

This case implies a reverse pyrolysis process. At the same time, endogenous deep hydrocarbons, with a decrease in temperature and pressure, form the oil and gas familiar to us, successively passing into carbon shales, shungite and graphite during the ascent.

Thus, the proposed method of thermodynamic modeling, based on the basic chemical reactions associated with chemical

and physical transformation in an equilibrium system of solid, liquid, gas and further construction of the dependences of the reduced Gibbs energies on temperature and pressure in the reservoir, taking into account the imperfection of the system, will allow us obtaining an array of results that let not only determine the equilibrium composition of the components of this a three-phase system at various depths, but also to confirm or refute the possibility of regressive metamorphism, characterized by the possibility of phase “solidification” of oil in areas of ultra-high pressures or abnormally low temperatures with the formation of pseudocrystal kerogens.

Thermodynamic calculations are based on the assumption that all the transformations described above proceed in accordance with the basic postulates of Hess’s law, Kirchhoff’s law and the second law of thermodynamics.

At the same time, it is possible to represent oil, gas and solid kerogen in the form of chemical compounds of a given stoichiometry, and, consequently, to bring their thermodynamic state functions for further calculations. For example, light and heavy oils can be represented as compounds of the type—(C<sub>10</sub>H<sub>22</sub>), solid kerogens—(C<sub>128</sub>H<sub>68</sub>O<sub>7</sub> and C<sub>292</sub>H<sub>288</sub>O<sub>12</sub>), gases (alkanes (C<sub>n</sub>H<sub>2n+2</sub>) (Helgeson et al., 2009). The structural formulas of “mature” and “immature” kerogen are shown in Figures 12, 13.

The transformations of sulfur-containing and nitrogen-containing heteroatomic compounds of kerogen will not be considered in the proposed model. This assumption makes the above described system idealized, however, in accordance with the data published in (Helgeson et al., 2009), the possibility of applying such a simplification is shown.

Thus, the equilibrium reactions between the phases can be written as:

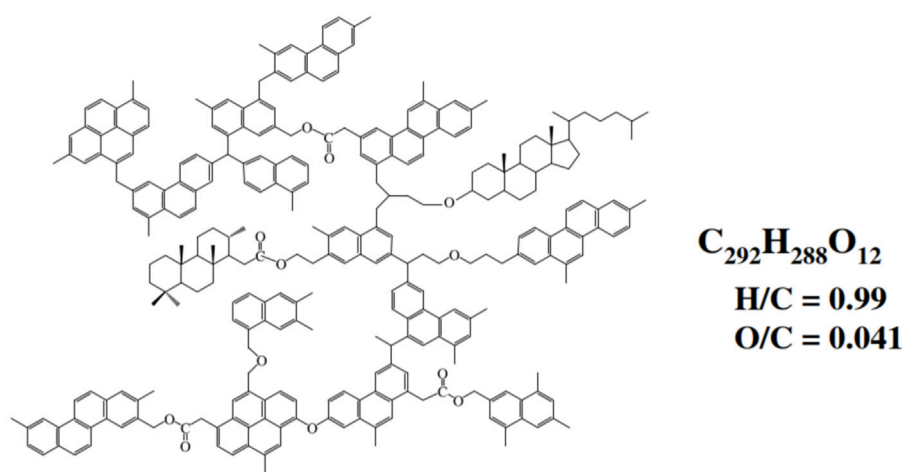


FIGURE 12

Structural formula of “immature” kerogen (Helgeson et al., 2009).

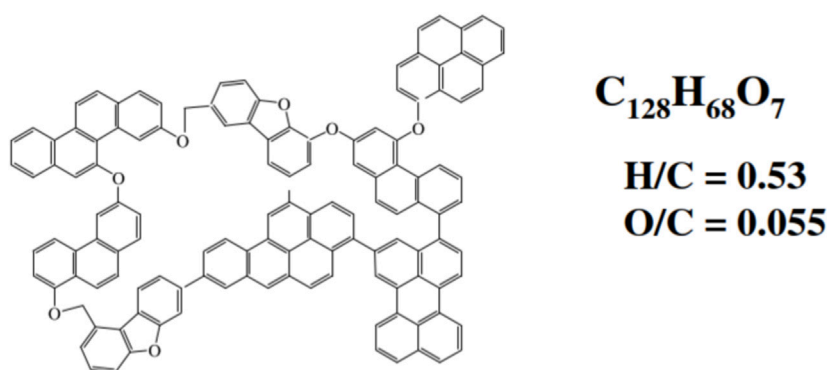


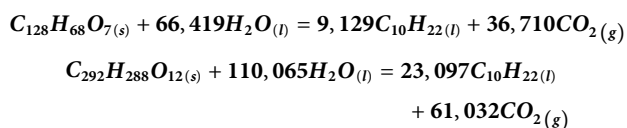
FIGURE 13

Structural formula of “mature” kerogen (Helgeson et al., 2009).

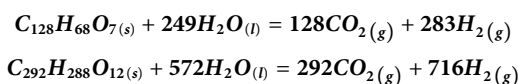
TABLE 3 Isotherms of equilibrium constants for the proposed reactions.

Reaction no.	Dependence of the equilibrium constant on the activities and fugitives of the components
1	$\log K = 9,129 \log(a_{C_{10}H_{22}}) + 36,710 \log(f_{CO_2})$
2	$\log K = 23,097 \log(a_{C_{10}H_{22}}) + 61,032 \log(f_{CO_2})$
3	$\log K = 128 \log(f_{CO_2}) + 283 \log(f_{H_2})$
4	$\log K = 292 \log(f_{CO_2}) + 716 \log(f_{H_2})$
5	$\log K = 12,8 \log(a_{C_{10}H_{22}}) - 113,8 \log(f_{H_2})$
6	$\log K = 29,2 \log(a_{C_{10}H_{22}}) - 189,2 \log(f_{H_2})$
7	$\log K = 12,45 \log(a_{C_{10}H_{22}}) + 3,5 \log(f_{CO_2}) - 102,95 \log(f_{H_2})$
8	$\log K = 28,61 \log(a_{C_{10}H_{22}}) + 6 \log(f_{CO_2}) - 170,6 \log(f_{H_2})$
9	$\log K = -\log(a_{C_{10}H_{22}}) + 10 \log(f_{CO_2}) + 31 \log(f_{H_2})$
10	$\log K = \log(a_{CO_2}) - \log(f_{CO_2})$

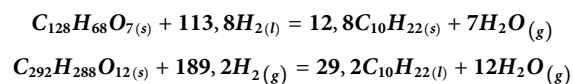
Hydrolytic disproportionation of kerogen:



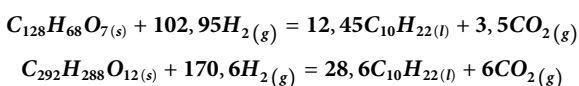
Metastable state in the kerogen—water system:



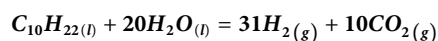
Metastable state in the kerogen—oil—water system:



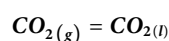
Metastable state in the kerogen—oil—gas system:



Metastable state in the oil—gas—water system:



Metastable state in the gas—water system:



The obtained isotherms for the equilibrium constants for the proposed reactions are shown in Table 3.

By solving the proposed system of equations for various temperatures and pressures, it is possible to obtain dependences of the quantitative ratio of the components described above on the depth of occurrence, which in turn

will allow us predicting the critical boundaries (depth) of the place of possible oil and gas accumulations in atypical geological conditions.

## 4 Conclusion

- 1) Deep and ultra-deep horizons of sedimentary basins differ significantly in temperature and paleotemperature conditions, reservoir pressures, the rate of deposition of sediments and the time of exposure to high temperatures from horizons located at medium and shallow depths, where most of the previously discovered hydrocarbon deposits are located (up to 4.5–5 km).
- 2) Sedimentary basins with widely developed deep and ultra-deep hydrocarbon deposits are fairly confidently typified by their prospects in terms of the ratio of temperature and reservoir pressures, geothermal gradient, presence (or forecast) and richness at great depths of strata, organic matter, and belonging to a certain geodynamic (tectonic) situation.
- 3) One of the significantly underestimated factors for large depths, and not included in the technology of basin modeling, is the time factor (which refers to both the rate of immersion and the time of exposure to high temperatures and the time of manifestation of peaks in the generation of liquid and gaseous hydrocarbons). The effective heating time significantly affects the phase composition of ultra-deep hydrocarbon accumulations.
- 4) The phase composition of hydrocarbons is controlled by temperature, heating time, heating rate, pressure and the type of organic matter of the oil and gas producing rock. The possibility of detecting oil deposits at deep and ultra-deep depths of 8–10 km is determined by both a low geothermal gradient and abnormally high pressures. Under the condition of



rapid heating in a high-temperature environment, gas condensates may exist. The detection of gas deposits in conditions of progressive cracking of oil or at relatively low temperatures is not limited by ultra-high pressures and is possible up to a depth of 10–12 km.

## Data availability statement

The original contributions presented in the study are included in the article/supplementary material, further inquiries can be directed to the corresponding author.

## Author contributions

Conception the Research: OP. Methodology: OP, SK, and DL. Design: YN, TK, and NS. Collection and assembly of data: OP, SK, YN, AM, TK, and RX. Data analysis and interpretation: OP, AM, DL, TK, and NS. Writing-original draft: PM. Writing-review and editing: OP, SK, and YN. All authors read and provided significant inputs into

all drafts of the editorial, agreed to be accountable for all aspects of the work and approved the final draft of the editorial for publication.

## Conflict of interest

The authors declare that the research was conducted in the absence of any commercial or financial relationships that could be construed as a potential conflict of interest.

## Publisher's note

All claims expressed in this article are solely those of the authors and do not necessarily represent those of their affiliated organizations, or those of the publisher, the editors and the reviewers. Any product that may be evaluated in this article, or claim that may be made by its manufacturer, is not guaranteed or endorsed by the publisher.

## References

- Abukova, L. A., and Volozh, Yu. A. (2021). Geofluidodynamics of deep-submerged zones of oil and gas accumulation of sedimentary basins. *Geol. Geophys.* 62 (8), 1069–1080. doi:10.15372/gig2021132
- Adriano, M. S., Figueiredo, J. P., Coelho, P. H. G. R., and Borghi, L. (2022). Tectonic and stratigraphic evolution of the Santos Basin rift phase: New insights from seismic interpretation on Tupi oil field area. *J. S. Am. Earth Sci.* 116 (116), 103842. doi:10.1016/j.jsames.2022.103842
- Aguilera, R. F., Ripple, R. D., and Aguilera, R. (2014). Link between endowments, economics and environment in conventional and unconventional gas reservoirs. *Fuel* 126 (3), 224–238. doi:10.1016/j.fuel.2014.02.063
- Ajdukiewicz, J. M., Nicholson, P. H., and Esch, W. L. (2010). Prediction of deep reservoir quality using early diagenetic process models in the Jurassic Norphlet Formation, Gulf of Mexico. *AAPG Bull.* 94 (8), 1189–1227. doi:10.1306/04211009152
- Aleksandrova, T., Nikolaeva, N., Afanasova, A., Romashev, A., Aburova, V., and Prokhorova, E. (2023). Extraction of low-dimensional structures of noble and rare metals from carbonaceous ores using low-temperature and energy impacts at succeeding stages of raw material transformation. *Minerals* 13, 84. doi:10.3390/min13010084
- Alekseev, A. D., Zhukov, V. V., Strizhnev, K. V., and Cherevko, S. A. (2017). Research of hard-to-recovery and unconventional oil-bearing formations according to the principle 'in-situ reservoir fabric. *J. Min. Inst.* 228, 695–704. doi:10.25515/PMI.2017.6.695
- Bazhenova, T. K., Shimansky, V. K., Vasilyeva, V. F., Shapiro, A. I., Gembitskaya, L. A., and Klimova, A. I. (2008). *Organic geochemistry of the Timan-Pechora basin*. St. Petersburg: VNIGRI.
- Belozherov, I. P., and Gubaydullin, M. G. (2020). Concept of technology for determining the permeability and porosity properties of terrigenous reservoirs on a digital rock sample model. *J. Min. Inst.* 244, 402–407. doi:10.31897/pmi.2020.4.2
- Bochkarev, V. S., and Krinochkin, V. G. (1988). "Precambrian and paleozoic formations of western siberia," in *Tectonics of platform areas* (Netherlands: Elsevier).
- Cao, B., and Bai, G. (2014). "Global distribution of petroleum reserves in deep reservoirs," in 2014 AAPG Annual Convention and Exhibition At, Houston, Texas, 6–9 April 2014.
- Cherdantsev, G. A. A., and Zharkov, A. M. (2021). Prospects for the oil and gas content of the Upper Permian deposits of the southwestern part of the Vilyui syncline based on the analysis of sedimentary environments and geochemical conditions of oil and gas content. *J. Min. Inst.* 251, 698–711. doi:10.31897/PMI.2021.5.9
- Dakhnova, M. V., Bazhenova, T. K., Lebedev, V. S., and Kiselev, S. M. (2011). Isotopic criteria for predicting the phase composition of hydrocarbons in Riphean and Vendian deposits of the Lena-Tunguska petroleum province. *Russ. Geol. Geophys.* 52 (8), 945–953. doi:10.1016/j.rgg.2011.07.015
- DeCelles, P. G., and Giles, K. A. (1996). Foreland basin systems. *Basin Res.* 8 (2), 105–123. doi:10.1046/j.1365-2117.1996.01491.x
- Dobrynski, A. F., and Andrejev, P. F. (1954). Thermodynamics of processes of formation and change of oils in nature. *Eesti NSV Tead. Akad. Toim.* 3 (2), 193–204. doi:10.3176/toimetised.1954.2.03
- Dvoynikov, M. V., and Leusheva, E. L. (2022). Modern trends in hydrocarbon resources development. *J. Min. Inst.* 258, 879–880.
- Dvoynikov, M. V., Sidorkin, I., Yurtaev, S. L., Grokhovtsev, I., and Ulyanov, D. S. (2022). Drilling of deep and ultra-deep wells for prospecting and exploration of new raw mineral fields. *J. Min. Inst.* 258, 945–955. doi:10.31897/PMI.2022.55
- Eberth, D. A., Brinkman, D. B., Chen, P.-J., Yuan, F.-T., Wu, S.-Z., Li, G., et al. (2001). Sequence stratigraphy, paleoclimate patterns, and vertebrate fossil preservation in jurassic-cretaceous strata of the junggar basin, xinjiang autonomous region, people's republic of China. *Can. J. Earth Sci.* 38 (12), 1627–1644. doi:10.1139/e01-067
- Egorov, A. S. (2015). *Features of the deep structure and composition of the geostructures of the Earth's crust in the continental part of the Russian territory*. Russian: Journal of Mining Institute, Publishing House of the NMSU.
- Egorov, A. S., Prischepa, O. M., Nefedov, Y. V., Kontorovich, V. A., and Vinokurov, I. Y. (2021). Deep structure, tectonics and petroleum potential of the western sector of the Russian arctic. *J. Mar. Sci. Eng.* 9 (3), 258. doi:10.3390/jmse9030258
- Ehrenberg, S. N., and Nadeau, P. H. (2005). Sandstone vs. carbonate petroleum reservoirs: A global perspective on porosity-depth and porosity-permeability relationships. *AAPG Bull.* 89 (4), 435–445. doi:10.1306/11230404071
- Ermolkin, V. I., Kochofa, A. G., Sorokova, E. I., and Trunova, M. I. (2008). Phase zonality of hydrocarbons in the ultra-deep horizons of the Earth's crust. *Bull. Peoples' Friendsh. Univ. Russ. Ser. Eng. Res.* (3), 36–40.
- Fomin, A. N. (2011). *Catagenesis of organic matter and oil and gas potential of Mesozoic and Paleozoic deposits of the West Siberian basin*. Novosibirsk: INGG SO RAN.
- Ganguli, S. S., Vedanti, N., Pandey, O. P., and Dimri, V. P. (2018). Deep thermal regime, temperature induced over-pressured zone and implications for hydrocarbon potential in the Ankleshwar oil field, Cambay basin, India. *J. Asian Earth Sci.* 161, 93–102. doi:10.1016/j.jseas.2018.05.005
- Gu, Y., Wan, Y., Huang, J., Zhuang, X., Wang, B., Li, M., et al. (2019). Mutual correlation attentive factors in dyadic fusion networks for speech emotion recognition. *Pet. Geol. Exp.* 41 (2), 157–166. doi:10.1145/3343031.3351039
- Gubin, I. A. (2004). The problem of assessing the filtration-capacitance properties of the reservoir in connection with epigenetic changes. *J. Min. Inst.* 159 (2), 7–10.
- Guliyev, I. S., Kerimov, V. Yu., Osipov, A. V., and Mustaev, R. N. (2017). Generation and accumulation of hydrocarbons at great depths under the earth's crust. *SOCAR Proc.* (1), 4–16. doi:10.5510/ogp20170100302
- Hao, F., Zou, H., Ni, J., Zeng, Z., and Wang, M. (2002). Evolution of overpressured systems in sedimentary basins and conditions for deep oil/gas accumulation. *Earth Science-Journal China Univ. Geosciences* 27 (5), 610–615.
- Helgeson, H. C., Richard, L., McKenzie, W. F., Norton, D. L., and Schmitt, A. (2009). A chemical and thermodynamic model of oil generation in hydrocarbon source rocks. *Geochimica Cosmochimica Acta* 73 (3), 594–695. doi:10.1016/j.gca.2008.03.004

- HPHT (2020). *HPHT production in the Gulf of Mexico*. New Orleans: U.S. Department of the Interior Bureau of Ocean Energy Management New Orleans Office.
- Huang, J., Deliao, Y., and Yu, H. (2016). Petroleum geology features and accumulation controls for ultra-deep oil and gas reservoirs. *Petroleum Geol. Exp.* 38 (5), 635–640. doi:10.11781/sydz201605635
- Iskaziev, K. O., Syngaevsky, P. E., and Khafizov, S. F. (2021). Deep oil. Offshore fields in the Gulf of Mexico in the Norflot Formation. Development history and prospects. *Kazakhstan J. oil gas industry* 3 (2), 3–26. doi:10.54859/kjogi89466
- Jarvie, D. (2012). Shale resource systems for oil and gas: Part 2: Shale-Oil resource systems. *AAPG Mem.* 97, 89–119. doi:10.1306/13321447M973489
- Jia, C., and Pang, X. (2015). Research processes and main development directions of deep hydrocarbon geological theories. *Acta Pet. Sin.* 36 (12), 1457–1469. doi:10.7623/syxb201512001
- Kerimov, V. Yu., Mustae, R. N., and Osipov, A. V. (2018). Peculiarities of hydrocarbon generation at great depths in the crust. *Dokl. Earth Sci.* 483 (3), 1413–1417. doi:10.1134/s1028334x18110193
- Kerimov, V. Yu., and Osipov, A. V. (2016). *Oil and gas content of great depths and promising areas of geological exploration for oil and gas in deeply submerged horizons in the territory of the Russian Federation*. RU: Delovoy zhurnal Neftegaz.
- Khafizov, S. F., Osipov, A. V., Dantsova, K. I., Monakova, A. S., and Barshin, A. V. (2020). “Factors that determine the formation and preservation of accumulations of liquid hydrocarbons at depths of more than 5 km.”. *Geomodel*.
- Kondrasheva, N. K. (2018). “Evaluation of the effectiveness of using oil shale,” in *Innovation-based development of the mineral resources sector: Challenges and prospects - 11th conference of the Russian-German raw materials* (Boca Raton, Florida, United States: CRC Press).
- Kontorovich, A. E., Danilova, V. P., Kostyeva, E. A., and Stasova, O. F. (1998). Geochemistry and Genesis of paleozoic oilfields of western siberia. *Geochemistry* 36 (1), 3–17.
- Kontorovich, A. E., Ivanov, I. A., Kovešnikov, A. E., Krasnov, V. I., and Perozio, G. N. (1991). “Geological conditions of oil and gas potential of the upper part of the Paleozoic section of Western Siberia,” in *Theoretical and regional problems of oil and gas geology* (Novosibirsk: Nauka).
- Kontorovich, A. E., Burstein, L. M., and Livshits, V. R. (2021). Theory of naphthidogenesis: A quantitative model of the evolution of aquagenic organic matter in catagenesis. *Geol. Geophys.* 62 (8), 1026–1047. doi:10.15372/gig2021119
- Kosenkova, N. N., Syngaevsky, P. E., and Khafizov, S. F. (2022). Review of the modern ideas about the hydrocarbon accumulations formation processes at the great depth. *Neft. khozyaystvo - Oil Ind.* (5), 6–12. doi:10.24887/0028-2448-2022-5-6-12
- Kuandykov, B. M., Syngaevsky, P. E., and Hafizov, S. F. (2022). Formation and preservation of reservoirs at great depths. *Bull. oil gas industry Kazakhstan* 4 (2), 11–26. doi:10.54859/kjogi100605
- Kudryavtsev, N. A. (1951). Against the organic hypothesis of the origin of oil. *Oil Ind.* (9), 17–24.
- Kudryavtsev, N. A. (1971). Oil is abiogenic. *Nat. M., Sci.* (3), 70–72.
- Law, B. E. (2002). Basin-centered gas systems. *AAPG Bull.* 86 (11), 1891–1919.
- Leonov, Yu. G., Volozh, Yu. A., Antipov, M. P., Bykadorov, V. A., Patina, I. S., and Lodzhnevskaya, M. I. (2015). Oil of deep horizons of sedimentary basins of Russia and neighboring countries. *Monit. Sci. Technol. Sci. Tech.* J. 25 (4), 6–15.
- Li, J., Zhang, Z., Zhu, G., Zhao, K., Chi, L., Wang, P., et al. (2021). Geochemical characteristics and the origin of superdeep condensates in Tarim basin, China. *ACS Omega* 6 (11), 7275–7285. doi:10.1021/acsomega.0c04932
- Li, Y., Lobusev, A. V., Bochkarev, A. V., Wang, Q., and Liu, R. (2020). The nature and modeling of the oil reservoir fractures in X field of the Tarim basin (China). *Geol. Geophys. Dev. Oil Gas Fields* (3), 27–34. doi:10.30713/2413-5011-2020-3(339)-27-34
- Litvinenko, V. S., Kozlov, A. V., and Stepanov, V. A. (2017). Hydrocarbon potential of the Ural–African transcontinental oil and gas belt. *J. Petroleum Explor. Prod. Technol.* 7 (1), 1–9. doi:10.1007/s13202-016-0248-4
- Liu, J., Jin, Z., and Ma, A. (2015). Hydrocarbon phase in the deep cambrian of the Tarim Basin. *Pet. Geol. Exp.* 37 (6), 681–688. doi:10.11781/sydz201506681
- Liu, Y., Tian, Y., Yang, C., Xiao, D., Liao, Q., Shen, C., et al. (2017). Hydrocarbon phase limit and conversion process in the deep formation from Qikou Sag of Bohai Bay rift lacustrine basin, China. *J. Nat. Gas Geoscience* 2 (4), 229–238. doi:10.1016/j.jnggs.2017.12.003
- Liu, Z., Zhu, W., Sun, Q., Jin, B., Xu, X., Zhang, H., et al. (2012). Blockade of autocrine TGF- $\beta$  signaling inhibits stem cell phenotype, survival, and metastasis of murine breast cancer cells. *Shiyou Xuebao/Acta Pet. Sin.* 33, 1–8. doi:10.4172/2157-7633.1000116
- Lu, S., Xue, H.-T., and Zhong, N.-N. (2002). Chemical kinetic study of the oil preservation threshold. *Petroleum Explor. Dev.* 29 (6), 1–3.
- Lu, X., Zhao, M., Liu, K., Zhuo, Q., Fan, J., Yu, Z., et al. (2018). Forming condition and mechanism of highly effective deep tight sandstone gas reservoir in Kuqa foreland basin. *Shiyou Xuebao/Acta Pet. Sin.* 39 (4), 365–378. doi:10.7623/syxb201804001
- Ma, A. (2016). Kinetics of oil-cracking for different types of marine oils from Tahe Oilfield, Tarim Basin, NW China. *J. Nat. Gas Geoscience* 1 (1), 35–43. doi:10.1016/j.jnggs.2016.03.001
- Malyshev, N. A. (2004). *Tectonics, evolution and oil and gas content of sedimentary basins of the European North*. Yekaterinburg: Ural Branch of the Russian Academy of Sciences, Komi Scientific Center.
- Malyshev, N. A. (2000). *Tectonics, evolution and oil and gas potential of sedimentary basins of the European North of Russia*. Russia: Doctoral dissertation. MSU.
- Meihejef (1993). The oil bearing temperature conditions on deep strata. *Pet. Geol. Form.* 14 (3/4), 1–4.
- Neruchev, S. G., Rogozina, E. A., Parparova, G. M., Zelichenko, I. A., Silina, N. P., Lebedev, B. A., et al. (1986). *Oil and gas formation in Domanik deposits*. Leningrad, USSR: Nedra.
- Neruchev, S. G., Vassoevich, N. B., and Lopatin, N. V. (1976). *On the catagenesis scale in connection with oil and gas formation Combustible Minerals*. Moscow, USSR: Nauka.
- Osipov, A. V. (2021). Characteristics of hydrocarbon reserves in deep accumulations of oil and gas provinces of the Russian Federation. *Neft. khozyaystvo - Oil Ind.* (5), 8–10. doi:10.24887/0028-2448-2021-5-8-10
- Pang, X.-Q., Jia, C.-Z., and Wang, W.-Y. (2015). Petroleum geology features and research developments of hydrocarbon accumulation in deep petroliferous basins. *Petroleum Sci.* 12 (1), 1–53. doi:10.1007/s12182-015-0014-0
- Peters, K. E., Kontorovich, A. E., Huizinga, B. J., Moldowan, J. M., and Lee, C. Y. (1994). Multiple oil families in the West Siberian basin. *AAPG Bull.* 78 (6), 893–909. doi:10.1306/a25fe3dd-171b-11d7-8645000102c1865d
- Petrakov, D. G., Penkov, G. M., and Zolotukhin, A. B. (2022). Experimental study on the effect of rock pressure on sandstone permeability. *J. Min. Inst.* 254, 244–251. doi:10.31897/PMI.2022.24
- Porfiriev, V. B. (1961). *On the nature of oil*. *Geol. collection*. Lviv: LSU Publishing House.
- Porfiriev, V. B. (1987). The nature of oil, gas and fossil coals: Selected works: In 2 vols. *Sciences* 1–2, 440.
- Price, L. C. (1993). Thermal stability of hydrocarbons in nature: Limits, evidence, characteristics, and possible controls. *Geochimica Cosmochimica Acta* 57 (14), 3261–3280. doi:10.1016/0016-7037(93)90539-9
- Price, L. C., and Wenger, L. M. (1992). The influence of pressure on petroleum generation and maturation as suggested by aqueous pyrolysis. *Org. Geochem.* 19 (1–3), 141–159. doi:10.1016/0146-6380(92)90033-t
- Prischepa, O. M., Averyanova, O. Yu., and Zharkov, A. M. (2013). Oil and gas deposits of domanic type – A reserve to maintain hydrocarbons production in commercially developed areas. *Georesursy* 54 (4), 18–22. doi:10.18599/grs.54.4.3
- Prischepa, O. M., Nefedov, Y., Nikiforova, V., and Ruiming, X. (2022). Raw material base of Russia’s unconventional oil and gas reserves (hydrocarbons shale strata). *Front. Earth Sci.* 10, 1. doi:10.3389/feart.2022.958315
- Pusey, W. C. (1973). How to evaluate potential gas and oil source rocks. *World oil* 176 (5), 71–75.
- Qiu, N., Liu, W., Xu, Q., Liu, Y., and Chang, J. (2018). Temperature-pressure field and hydrocarbon accumulation in deep-ancient marine strata. *Diqiu Kexue - Zhongguo Dizhi Daxue Xuebao/Earth Sci. - J. China Univ. Geosciences* 43 (10), 3511–3525. doi:10.3799/dqkx.2018.286
- Ren, Z., Cui, J., Qi, K., Yang, G., Chen, Z., Peng, Y., et al. (2020). Control effects of temperature and thermal evolution history of deep and ultra-deep layers on hydrocarbon phase state and hydrocarbon generation history. *Nat. Gas. Ind. B* 7 (5), 453–461. doi:10.1016/j.ngib.2020.09.003
- Ren, Z., Liu, L., and Cui, J. (2008). Application of tectonic thermal evolution history to hydrocarbon accumulation timing in sedimentary basins. *Oil Gas Geol.* 29 (4), 502–506. doi:10.11743/ogg20080413
- Samvelov, R. (1995). Hydrocarbon deposits at deep depths: Features of formation and placement. *Geol. oil gas* (9), 5–15.
- Shen, Y., Lü, X., Guo, S., Song, X., and Zhao, J. (2017). Effective evaluation of gas migration in deep and ultra-deep tight sandstone reservoirs of Keshen structural belt, Kuqa depression. *J. Nat. Gas Sci. Eng.* 46 (46), 119–131. doi:10.1016/j.jngse.2017.06.033
- Shimansky, V. K., Neruchev, S. G., Bazhenova, T. K., Prischepa, O. M., and Smirnov, S. V. (1994). “Geochemical modelling of Timan-Pechora oil and gas basin on the basis of balance and kinetic models petroleum Exploration and Production in Timan-Pechora Basin and Barents Sea,” in *Collected reports of international conference august 15-17, 1994* (St. Petersburg, Russia: VNIGRI).
- Sokolov, B. A. (1980). *Evolution and oil and gas content of sedimentary basins*. Kazakhstan: M. Nauka.
- Sun, L., Zou, C., Zhu, R., Zhang, Y., Zhang, S., Zhang, B., et al. (2013). Formation, distribution and potential of deep hydrocarbon resources in China. *Petroleum Explor. Dev.* 40 (6), 687–695. doi:10.1016/s1876-3804(13)60093-2
- Tissot, B. P., and Welte, D. H. (1984). *Petroleum Formation and occurrence*. Berlin: Springer-Verlag.

- Tissot, B., and Welte, D. (1981). *Fate of organic matter in sedimentary basins: Oil and gas generation*. Moscow, Russia: Oil formation and distribution: Mir.
- Torba, D. I., and Nikiforova, V. S. (2019). *Proceedings of the XIV international forumcontest of young researchers*. St. Petersburg, Russia: Litvinenko V. Oil recovery increase in kerogen of the Bazhenov formation by a thermal treatment technology," in Topical issues of rational use of natural resources
- Tuo, J. (2002). Research status and advances in deep oil and gas exploration. *Adv. Earth Sci.* 17 (4), 565–571. doi:10.11867/j.issn.1001-8166.2002.04.0565
- Volozh, Y. A., Gogonenkov, G. N., Miletenko, N. V., and Petrov, E. I. (2021). Oil resources development from deep horizons in historically oil producing regions. *Geol. Oil Gas* 6, 7–21. doi:10.31087/0016-7894-2021-6-7-21
- Wang, X. (1992). Ultra-deep drilling and hydrocarbon prediction. *Nat. Gas. Geosci.* 3 (6), 38–40.
- Wang, Z., Wang, T., Wen, L., Hua, J., and Baomin, Z. (2014). Basic geological characteristics and accumulation conditions of Anyue giant gas field, sichuan basin. *China Offshore Oil Gas* 28 (2), 45–52.
- Wassoevich, N. B. (1967). Theory of sedimentary-migratory origin of oil (historical review and current state). *Izv. USSR Acad. Sci. Ser.geol.* (11), 135–156.
- Wei, Q., Li, X., and Sun, K. (2019). Geochemical characteristics of deep-seated natural gas accumulation of the Keshen large gas field in the Kuqa depression. Tarim Basin. *Nat. Gas. Geosci.* 30 (6), 897–907.
- Weisberg, L. A., Kameneva, E. E., and Nikiforova, V. S. (2018). Microtomographic studies of the pore space of rocks as a basis for improving the technology of their disintegration. *Ob. Rud.* 2018 (3), 51–55. doi:10.17580/or.2018.03.09
- Yang, P., Liu, K., Liu, J., Yu, S., Yu, B., Hou, M., et al. (2021). Petroleum charge history of deeply buried carbonate reservoirs in the Shuntuoguole Low Uplift, Tarim Basin, west China. *Mar. Petroleum Geol.* 128, 105063. doi:10.1016/j.marpetgeo.2021.105063
- Zakharov, L. A., Martyushev, D. A., and Ponomareva, I. N. (2022). Predicting dynamic formation pressure using artificial intelligence methods. *J. Min. Inst.* 253, 23–32. doi:10.31897/PMI.2022.11
- Zhang, S., Huang, H., Su, J., and Liu, M. (2015). Ultra-deep liquid hydrocarbon exploration potential in cratonic region of the Tarim Basin inferred from gas condensate Genesis. *Fuel* 160, 583–595. doi:10.1016/j.fuel.2015.08.023
- Zhao, X., Jin, F., Wang, Q., Zhang, R., Wang, J., Bai, X., et al. (2011). Niudong 1 ultra-deep and ultra-high temperature subtle buried hill field in Bohai Bay basin: Discovery and significance. *Acta Pet. Sin.* 32 (6), 915–927. doi:10.7623/syxb201106001
- Zhou, X., Zhang, R., Li, H., Wang, B., and Guo, Y. (2017). Major controls on natural gas accumulations in deep-buried hills in Bozhong Depression, Bohai Bay Basin. *J. China Univ. Petroleum Ed. Nat. Sci.* 41 (1), 42–50.
- Zhu, G., Milkov, A. V., Chen, F., Weng, N., Zhang, Z., Yang, H., et al. (2018). Non-cracked oil in ultra-deep high-temperature reservoirs in the Tarim basin, China. *Mar. Petroleum Geol.* 89, 252–262. doi:10.1016/j.marpetgeo.2017.07.019
- Zhu, G., Milkov, A. V., Li, J., Xue, N., Chen, Y., Hu, J., et al. (2021). Deepest oil in Asia: Characteristics of petroleum system in the Tarim basin, China. *J. Petroleum Sci. Eng.* 199, 108246. doi:10.1016/j.petrol.2020.108246
- Zhukov, V. S., and Kuzmin, Y. O. (2021). Experimental evaluation of compressibility coefficients for fractures and intergranular pores of an oil and gas reservoir. *J. Min. Inst.* 251, 658–666. doi:10.31897/PMI.2021.5.5
- Zou, C., Jinhu, D., and Chunhuan, Xu. (2014). *Formation, distribution, resource potential, and discovery of Sinian–Cambrian giant gas field, Sichuan Basin. SW China: Petroleum Exploration and Development.*



## OPEN ACCESS

## EDITED BY

Liang Chen,  
China University of Mining and  
Technology, China

## REVIEWED BY

Wenshuai Li,  
Shandong University of Science and  
Technology, China  
Huibin Sun,  
Shandong Jianzhu University, China

## \*CORRESPONDENCE

Chen Cao,  
✉ caochen@lntu.edu.cn

RECEIVED 03 April 2023

ACCEPTED 25 May 2023

PUBLISHED 07 June 2023

## CITATION

Jia D, Zhi Z, Cao C and Zhang M (2023),  
Investigations into the failure  
mechanisms of coal bursts based on a  
real burst event in the Tangshan  
coal mine.  
*Front. Earth Sci.* 11:1199142.  
doi: 10.3389/feart.2023.1199142

## COPYRIGHT

© 2023 Jia, Zhi, Cao and Zhang. This is an  
open-access article distributed under the  
terms of the [Creative Commons  
Attribution License \(CC BY\)](#). The use,  
distribution or reproduction in other  
forums is permitted, provided the original  
author(s) and the copyright owner(s) are  
credited and that the original publication  
in this journal is cited, in accordance with  
accepted academic practice. No use,  
distribution or reproduction is permitted  
which does not comply with these terms.

# Investigations into the failure mechanisms of coal bursts based on a real burst event in the Tangshan coal mine

Dongxu Jia<sup>1</sup>, Zengzhu Zhi<sup>2</sup>, Chen Cao<sup>1\*</sup> and Ming Zhang<sup>3</sup>

<sup>1</sup>College of Mining, Liaoning Technical University, Fuxin, China, <sup>2</sup>Tangshan Coal Mine, Kailuan (Group) Limited Liability Corporation, Tangshan, China, <sup>3</sup>Research Center of Ministry of Emergency Management, Beijing, China

To investigate the failure mechanisms of coal bursts in the longwalls of underground coal mines, a case study based on the real coal burst in the Tangshan coal mine occurring on 2 August 2019 was carried out to analyze the cause and basic theories of the coal burst and, thus, propose approaches and methods to mitigate the damage. The coal burst occurred mainly due to the sliding of coal from the longwall ribs and the simultaneous uplifting of the floor. As a result of the longwall retraction, the roof above the coal seam was too stable to collapse, forming a long hanging roof behind the longwall. Because the longwall acted as a fulcrum, the hanging roof acted like a saw, exerting massive loads on the longwall. As a result, the roof in front of the longwall tended to slope upward, leaving the underlying coal seam unconfined. Due to the horizontal stresses, the longwall ribs collapsed into the longwall, causing the coal seam to break out. These findings could help improve the fundamental understanding of the failure mechanisms of coal breakouts and, thus, aid in the development of measures to prevent such occurrences.

## KEYWORDS

coal burst, mechanical model, roof reflection, normal stress unloading, horizontal ground stress, rib coal slippage

## 1 Introduction

As mineral resources are depleted at shallow depths, mining depths are increasing by 10–25 m annually, posing further challenges to mining operations (Xie et al., 2015). The high *in situ* stresses, and complex geological and geotechnical conditions in deep earth mining have led to unavoidable bursting events, such as coal bursts in underground coal mines (Lan et al., 2011). Both the frequency and magnitude of burst events have increased significantly. To date, approximately 146 known underground coal mines in China have experienced coal bursts. The database of 2,510 reported coal bursts showed that coal bursts usually occur in the longwall face, longwall face roadways and development roadways, with 86.3% of coal bursts occurring in the longwall face (Tan et al., 2019). Such events usually result in the coal rib entering the roadway, causing damage to mining equipment or even accidents and fatalities. The convergence of the drifts is usually 50%–70% or even up to 90% (Pan, 2018), which causes serious problems for safe mining.

The causes and failure mechanisms of coal burst eruptions are very complex. At first, foreign scientists put forward a series of theories, including the strength theory, the stiffness theory, the energy theory, and the burst proneness theory. Similarly, domestic scholars in



China have also suggested theories. Zang (1987) pointed out that the bursting of coal in the critical state occurs under high stress from mining activities nearby. Qi et al. (2019) proposed a mechanism of frictional sliding failure based on their field observations and tests. Failure during coal bursts may be due to discontinuities between the rock and the coal or weak fills in between. Pan and Zhang (1996) analyzed coal bursts in roadways, longwall faces, and geological structures, and proposed a critical resistance zone theory, in which the ratio of the slope of the stress-strain curve before the peak and after the peak ( $E/\lambda$ ) can be used as an important index for the occurrence of coal bursts. Dou et al. (2015) conducted extensive laboratory tests to analyze the strain rate evolution during the testing of coal specimens. They categorized the strain source as static or dynamic and proposed the theory of superimposed static and dynamic strains. Miao et al. (1999) analyzed the yield failure of slab rock at the coal rib and developed a model for crack propagation in the coal rib due to coal excavation. Jiang et al. (2014) proposed an earthquake burst theory for thick coal seams based on case studies of the Yima and Nantun coal mine bursts. Jiang and Zhao (2015) summarized the interactions between the geological structures, *in situ* stresses, and coal outbursts based on the coal outburst in the Yima coal mine in Henan province. Pan (2019) developed a theory for coal eruptions that divided the event into three successive phases, namely, the triggering, energy transfer, and eruption phases.

With the advancement of coal rock fractals, fracture mechanics, loss mechanics, and other rock mechanics, as well as computer science, many domestic and foreign researchers have researched the mechanisms of coal bursts based on these theories. Xie and Pariseau (1993) proposed a fractal theory for coal burst events. Yin et al. (2002) characterized brittle rock using a nonlinear model to develop a model for energy loss during coal burst events. Pan and Yang (2004) conducted extensive laboratory tests and indicated that coal bursts could occur sequentially in the elastic, non-linear, and volumetric expansion phases. Tan et al. (2019) proposed theories of deep mine strain, geologic structural slip, and competent hanging roof bursts based on their field and laboratory test data. Ma et al. (2016) reported that coal bursts in circular roadways would most likely exhibit butterfly-shaped failure in the plastic failure zone and, thus, proposed a “butterfly-shaped failure theory”.

As can be seen from the aforementioned discussion, the factors influencing the mechanism of coal bursts are massive and complex. Unfortunately, there remains no conclusive knowledge regarding the causes and failure mechanisms of coal bursts, especially for coal bursts occurring at the coal ribs in the longwall panel roadways. Therefore, this study was mainly a case study based on a real coal burst incident that occurred in the Tangshan coal mine on 2 August 2019. This study aimed to analyze the failure mechanism of the coal burst at the coal rib and propose some measures to prevent the occurrence of such bursts. This study provides a theoretical basis for the prevention and control of this kind of ground impact pressure.

## 2 General information on the Tangshan coal mine

The Tangshan coal mine is owned by the Kailuan Mining Group. It was built in 1878 and put into operation in 1881, with 145 years of mining activity. The annual production is 3 million

tons. The mine is located in the Kailuan mining area, which is on the southeastern side of the Yan Mountain-Southern Foot-Yan Mountain-Sedimentary Rock geological unit. The coal seam is located in the caprock and fold structures in Li County, which were formed by rock alterations in Yan Mountain. The main geological faults in the mining area dip toward NE-SW and run parallel to the ground surface (Yang, 2011). The fault is numbered FI, FII, FIII, FIV, and FV from north to south, with the FV fault in the central and southern areas being the most massive (Jiang et al., 2012). The fold structure dips southward with anticlines and meanwhile dips westward with a series of anticlines. Due to the complexity of the geological structures in the mining area, a series of sub-mining areas have been categorized.

We carried out *in situ* stress measurements at the transport roadways in longwall panel 8,250 and at the bottom of the No. 10 shaft (Table 1). The maximum and minimum main stress inclination angles are close to 0°, corresponding to horizontal stress, while the intermediate principal stress inclination angle is close to 90°, corresponding to vertical stress. The maximum principal stress orientation of each measurement point is between 255.14° and 266.90° in the NEE-SWW direction. The maximum principal stress is between 31.30 MPa and 33.33 MPa, while the vertical stress *in situ* is between 20.48 MPa and 22.09 MPa. The maximum principal stress is about 1.5 times the vertical stress of the overburden.

At present, the main mining areas are in the Yuexu and Nanwu mining districts, with no development and mining activities taking place in other areas. Coal seam Nos. 5, 8, and 9 are mined; in some areas, seam Nos. 8 and 9 are mined at the same time. According to the coal burst susceptibility database, coal seam Nos. 5, 8 and 9 in the Nanwu and Yuexu areas and the coal pillars in the ventilation drift exhibit weak susceptibility to burst, with the roof having weak susceptibility and the floor having weak or no susceptibility.

## 3 Coal burst incident in the Tangshan coal mine on August 2, 2019

### 3.1 General information about the area of incident

On August 2, 2019, a massive coal burst occurred at the Tangshan coal mine at the connecting channel of the F5010 ventilation roadway and the crosscut of the F5009 transport roadway (Figure 1). Seven fatalities and five injuries were reported.

Longwall panel F5009 was located on the west side of the field where the coal pillars of the ventilation section were located. The east side of the field was the T<sub>2</sub>150 conveyor roadway, and the west side was longwall 3,654. To the south was the potential mining area in F5010 and mining areas T<sub>2</sub>155, T<sub>2</sub>154, T<sub>2</sub>153, and T<sub>2</sub>152. To the north were the F5009 coal transport road and the F5009 material transport road. The roadway heights were between 12.6 and 16.6 m. The crosscut in the F5009 material transport roadway was 110 m in length. It was located in the No. 5 seam, and the ceiling was reinforced with rock bolts and a steel arch. The average thickness of the coal seam was 2.6 m, and the average dip angle was 17°. This roadway was developed in June 2017 and referenced with an

TABLE 1 *In situ* stress measurements in the Tangshan coal mine.

Measurement location	Borehole number	Principal stress category	Principal stress value/MPa	Dip Direction/(°)	Dip angle/(°)
Transport roadway in panel 8,250 (depth: 800.3 m)	1	Maximum $\sigma_1$	33.00	259.30	2.01
		Intermediate $\sigma_2$	22.09	-18.57	-75.60
		Minimum $\sigma_3$	19.60	169.81	-14.25
	2	Maximum $\sigma_1$	33.33	264.57	0.86
		Intermediate $\sigma_2$	22.19	-1.11	78.76
		Minimum $\sigma_3$	21.47	174.40	11.21
Bottom of the No. 10 shaft (depth: 706.2 m)	1	Maximum $\sigma_1$	31.73	255.14	2.10
		Intermediate $\sigma_2$	20.48	-8.76	70.92
		Minimum $\sigma_3$	19.83	164.42	18.95
	2	Maximum $\sigma_1$	31.33	256.10	0.53
		Intermediate $\sigma_2$	21.22	-12.39	69.72
		Minimum $\sigma_3$	20.55	165.99	20.27
	3	Maximum $\sigma_1$	31.30	266.90	3.49
		Intermediate $\sigma_2$	21.04	4.26	64.54
		Minimum $\sigma_3$	20.05	175.26	25.18

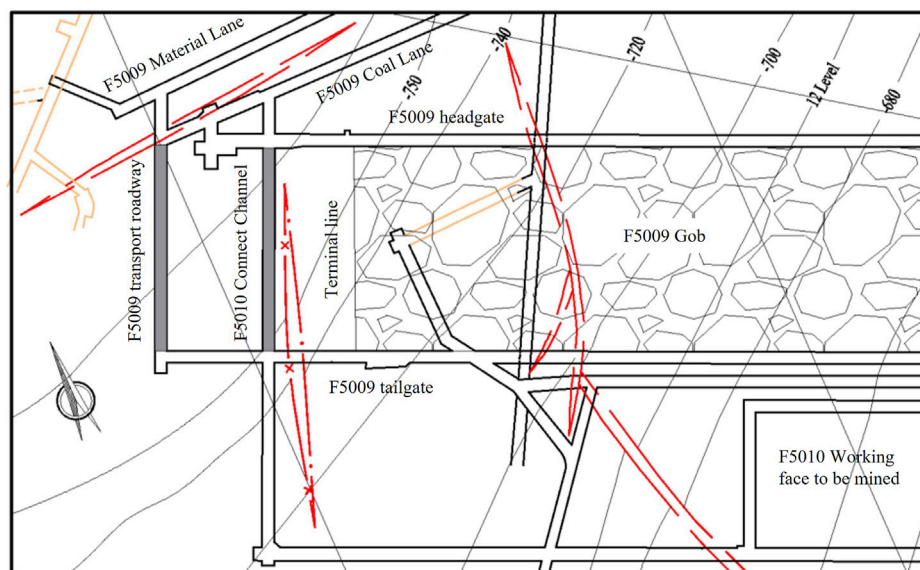


FIGURE 1  
Location of the coal burst of “8.2” in the Tangshan coal mine.

elevation of  $-755.2$  m compared to the F5009 wind connection and an elevation of  $-777.6$  m compared to the F5009 transport road connection. It was developed by machinery and drilling and blasting operations.

Longwall field F5010 was located on the west western side of the ventilation shaft coal pillar area. The eastern side of the field was the T<sub>2</sub>150 conveyor belt route and the western side was the 3654-field

mining area. To the south were the T<sub>2</sub>155, T<sub>2</sub>154, T<sub>2</sub>153, and T<sub>2</sub>152 mining areas. To the north were the mining areas of F5009, the coal transport roadway, and the material transport roadway of F5009. The height of the roadways was between 12.6 and 16.6 m. The connecting channel of F5010 178 m in length and was connected to the ventilation roadway of F5010, the ventilation roadway of F5009, the chain roadway of F5009, and

**TABLE 2** Mechanical properties of No. 5 coal seam and its roof.

Rock layer	Rock type	Lithological characteristic	Thickness/m	UCS/MPa
In-direct roof	Slight gray fine sandstone	Composition is mainly quartz and feldspar, siliceous colloid, and has poor sort ability	17.5	143.0
Direct roof	Dark gray fine sandstone	The main components are mainly quartz and feldspar, hard and striped	3.7–6.0	105.1
Fake roof	Sandy mudstone	Muddy composition, siliceous, with fossilized plant leaves	0–0.4	-
No. 5 coal seam	Coal	Black glossy-semi-bright coal, with strip and flake structure, low ash, and low sulfur	2.5	8.5
Direct floor	Sandy mudstone	Composition mud with silica, harder, flat fracture, with plant root fossils	0.4–1.4	-
In-direct floor	White fine sandstone	Main component quartz, banded, siliceous colloidal, with horizontal lamination	5.2	101.3

Note: “-” indicates no relevant data.

the coal transport roadway of F5009. All roadways were secured with rock bolts and steel mesh. The dimensions of the roadways were  $4.5 \times 3.0$  m, and the average inclination angle was  $12^\circ$ . On May 27, roadway support began from the longwall face and extended to the F5010 connecting duct in seam No. 5. On June 18, a support connected to the F5009 ventilation roadway and on July 11 to the F5009 chain roadway. On July 13, a connection was made to the F5009 coal transport roadway and development was complete. The incident occurred in coal seam No. 5, and the roof was sandstone 20-m thick. The UCS of the sandstone was over 100 Mpa. The floor consisted of a combination of sandy mudstone and fine sandstone (Table 2). It is noteworthy that coal seam No. 5 and its blanket showed a weak susceptibility to bursting.

### 3.2 Results of the incident investigation

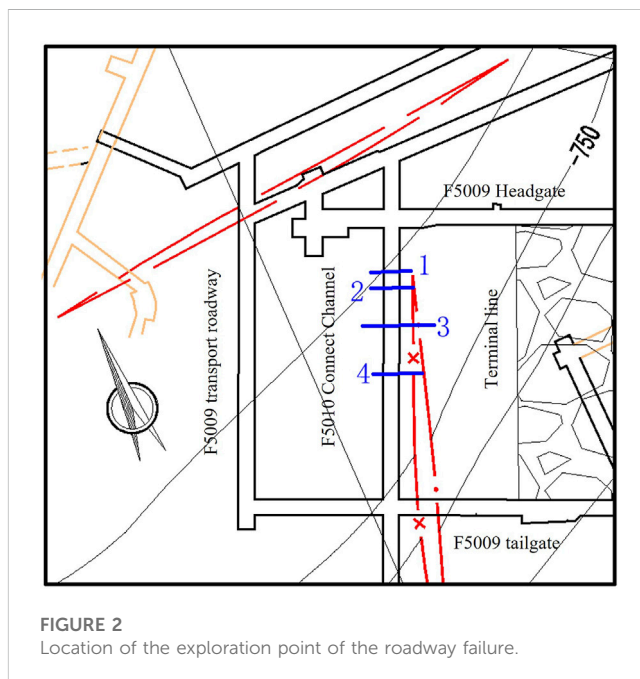
Immediately after the incident, a group of experts was formed. The group conducted extensive research and analysis on the ground and concluded that several causes led to this disaster.

Among these was the complexity of the geological structures and high stresses in the Tangshan coal mine. The accident area was located at the boundary of the FV fault and the stresses in place were very high. The area was also located in the axis zone of the fold syncline and, thus, was subject to a very high local stress concentration. The principal stress was determined to be between 31.30 Mpa and 33.33 Mpa, and the lateral pressure factor constant was between 1.38 and 1.6.

Moreover, the incident area is susceptible to coal bursts. The ceiling and floor of the No. 5 coal seam are weakly susceptible to fracturing. The operating depth in the incident area was nearly 800 m. The weight of the overburden exceeded the UCS of the coal sample. The ceiling of the No. 5 coal seam consisted of hard fine sandstone >20 m in thickness. The UCS of the coal sample was >100 Mpa, and it was reported that the coal tended to accumulate elastic energy.

Additionally, the accident area has a peninsular coal column with high load concentrations. The area was located next to the coal pillar of the ventilation shaft and some mining areas in seam Nos. 5, 8, and 9 in the Tie'er zone. Meanwhile, the F5009 longwall panel also created new mining areas. As a result, there was a superposition of several stresses in the pillar in the area of the incident.

The concentration of stresses induced by mining operations was also high. After the complete retraction of the longwall panel F5009,



there was a superposition of stresses in the surrounding roadways, resulting in a high stress concentration. The connecting duct of F5010 is 31 m away from the barrier pillar of F5009, and the coal pillars in the incident area were exposed to a high stress concentration. Moreover, in addition to longwall F5009, the chain and ventilation roadways of F5009 caused further stress concentrations on the coal pillars. Meanwhile, the retrograde mining direction led to the formation of a hanging competent roof, which also transferred massive stresses to the coal pillar. The connecting channel of F5010 and the crosscut of F5009 are oriented perpendicular to the main stress direction, which is unfavorable to the stability of the roadway. A fault 2.5 m high was found to be present at F5009-F6 located 5 m from the connecting channel of F5010. The induced stresses due to the fault structure amplified the stress concentration in the connecting channel of F5010.

Finally, disturbance by development in the roadway also had an effect. A development area in ventilation road 3654E located 80 m from the accident site affected the stability of the rock strata. Mining

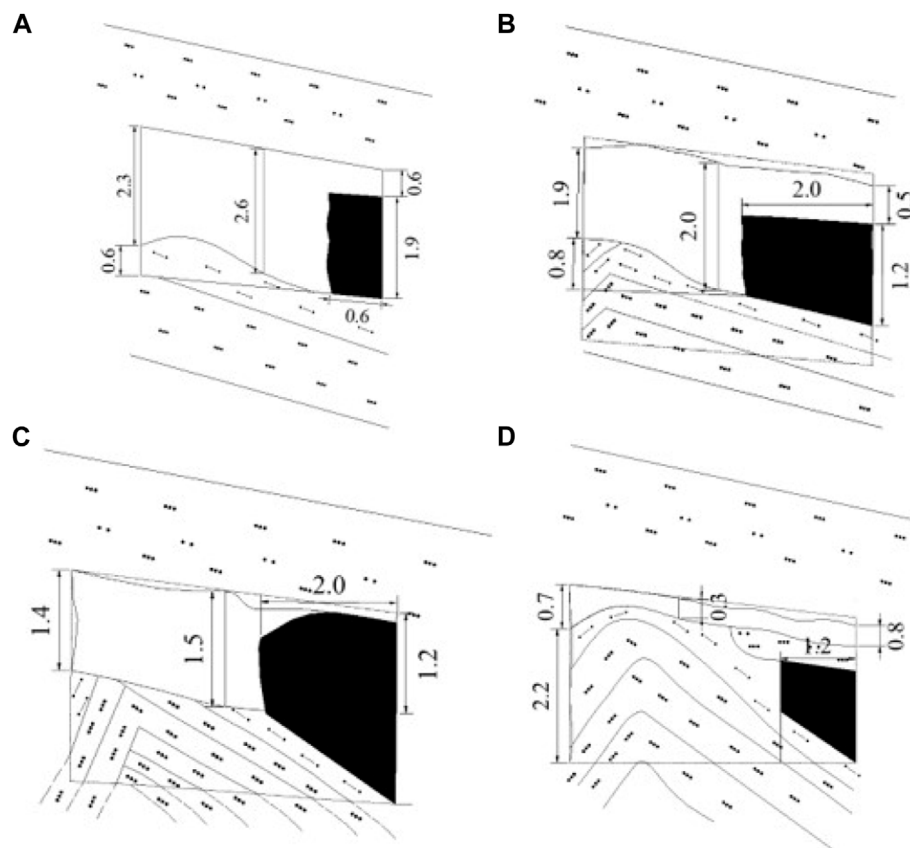


**FIGURE 3**  
Destroy sketch maps for each point of the F5010 connection channel. (A) Location 1. (B) Location 2. (C) Location 3. (D) Location 4.

activities in the 3654E roadway also affected the stability of the coal pillars and could have triggered the failure of the pillars.

## 4 Analysis of the failure mechanism of the incident

### 4.1 Damage in the underground roadway

The site investigation was conducted in the F5010 connecting channel after the coal burst incident. The locations of all incidents are shown in Figure 2.

The incident occurred at 32.1 m from the lower section of the connecting channel F5010. The roadway is 2.6 m high, and the upper rib is 2.3 m high, while the lower rib is only 0.6 m high. The lower rib has deformed inward by approximately 0.6 m so that the remaining width of the roadway is only 3.5 m. The upper section has a slight ground elevation, as can be seen in Figure 3A.

Another site is located 36.8 m from the lower section of connecting channel F5010. The roadway is 2 m high, and the upper rib is 1.9 m high, while the lower rib is only 0.5 m high. The rib has deformed about 2 m inward. The steel arch for the bottom support has deformed somewhat, as can be seen in Figure 3B.

The third site is 47.2 m from the lower section of connecting channel F5010. The roadway is 1.5 m high, and the upper rib is 1.4 m high. The rib has deformed inward about 2 m so that the roadway is completely closed 1 m from the lower rib (Figure 3C).

The last site is 61.3 m from the lower section of connecting channel F5010. The upper rib is 0.7 m high. The minimum height is 0.3 m and is 1.1 m from the upper rib. The area on the left side of the roadway experienced ground heave, which also resulted in some ground heave on the right side. The rib deformed inward by about 1.2 m, as can be seen in Figure 3D.

As can be seen in Figure 3, the greatest damage and failures occurred at the F5010 connector channel. The roadway was almost completely closed, and there was deformation of the ribs in the roadway and ground elevations.

### 4.2 Mechanism of coal burst failure

#### 4.2.1 High induced vertical stress in the longwall face

On-site tensions were disturbed by mine development and underground production activities. As a result, the two ribs of the roadway and the longwall were subjected to very high vertical stresses, which were higher than the original stresses on site (Song, 1988).



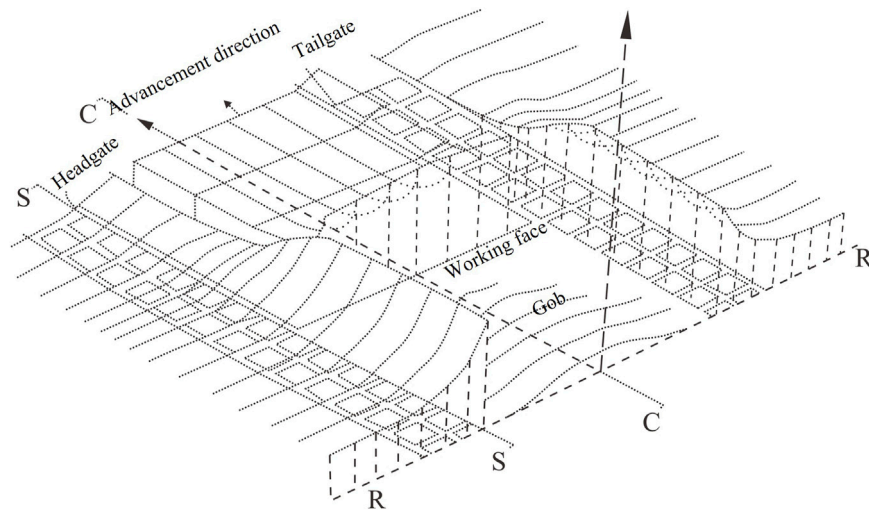


**FIGURE 4**  
Stope abutment pressure distribution.

The vertical stresses originated from different sources. The vertical stresses in the current longwall were mainly carried by the nearby coal seam. The vertical stresses in the adjacent longwall area were carried by the coal pillars. The rib pillars were subjected to the massive vertical stresses emanating from both mining areas. The vertical stresses resulted from the superposition of the two longwall areas, which led to the formation of the maximum vertical stress at the corner of the roadway, as shown in Figure 4.

Vertical stresses depend on the geological conditions of the roof and its mechanical properties. If the roof has a high load-bearing capacity, it will not collapse easily and consequently form a hanging roof. It is worth noting that the rock layers above the hanging roof were also supported by the nearby coal seam. As the longwall moves forward, periodic vertical stress concentration occurs dynamically. This was one of the main causes of the longwall coal burst incident. In this incident, the vertical stresses emanating from the transport roadway and the ventilation roadway overlapped with the vertical stresses in the F5009 longwall, resulting in a massive stress concentration that caused the incident.

#### 4.2.2 High load-carrying capacity of the coal seam

Mining activities led to the formation of massive cavities in the subsurface, causing a disturbance of the stress carried by the coal seam. As a result, stress was removed from at least one direction of the coal seam, resulting in biaxial or even uniaxial stress conditions in the coal seam. Under these complex stress conditions, internal fractures would propagate more easily and lead to ultimate failure. Therefore, four zones were distinguished in the coal seam, namely, the crack zone, the plastic zone, the elastic zone, and the *in situ* zone, from the near field to the far field.

The bearing capacity of the carbon specimen could be significantly improved if the specimen is clamped. Numerous results of true triaxial tests (Gao et al., 2017; Yin et al., 2018; Shen et al., 2019; Lu et al., 2020) confirmed that the maximum compressive strength of the coal specimen increases exponentially with increasing confining pressure. A true triaxial test of four coal

specimens was conducted according to the group standard from the Chinese Society of Rock Mechanics & Engineering, titled “Technical specification for true triaxial test of rock specimen (T/CSRME007-2021)”. The specimen information and results are shown in Table 3. The densities of the specimens are close to each other, but no significant relationship with their compressive strengths at different confining pressures was observed. As shown in Figure 5, the maximum compressive strengths of the coal specimens at different confining pressures were determined to be 53.08 Mpa, 64.64 Mpa, 82.04 Mpa, and 91.37 Mpa. This indicated that increasing the confining pressure could increase the compressive strength by 21.8%, 54.6%, and 72.1%, respectively.

After a mine is developed and mined, cavities will form. Crack zones, elastic zones, plastic zones, and *in situ* zones will form in the mined areas from the near field to the far field. According to the experience with the paste, the boundary between the elastic zone and the plastic zone is <2 m from the longwall face. This means that the horizontal *in situ* stress is equal to the original stress when the zone is >2 m away from the longwall. In the elastic zone, the bearing capacity of the coal seam increases significantly with increasing rock pressure. Therefore, the zone near the longwall experiences elastic deformation. The vertical deformation depends on the stress in place, the elastic modulus, and the mining height. In such a condition, where the hard and competent coal seam bears high stresses, the coal would tend to burst.

#### 4.2.3 Hanging roof tilt

Since the coal seam in the longwall is competent and could support a massive vertical load from the roof, the immediate roof above the seam would slope upward if the length of the hanging roof is sufficient (Figure 6).

The short black arrow in the figure indicates the direction of gravity of the overlying rock layers, while the long black arrow indicates the vertical load from the hanging roof due to mining activity based on data from field measurements. The coal seam at the longwall is strong enough to support a substantial load. Therefore,

TABLE 3 Results of true triaxial test coal specimens.

Number	Size (length × width × height)/mm	Density/kg·m <sup>-3</sup>	$\sigma_x$ /MPa	$\sigma_y$ /MPa	$\sigma_{zmax}$ /MPa
M-1	50.43 × 50.58×100.16	1,295	4	2	53.08
M-2	50.13 × 50.19×100.61	1,315	8	4	64.64
M-3	50.25 × 49.68×101.11	1,258	24	12	82.04
M-4	50.85 × 50.62×100.34	1,265	32	16	91.37

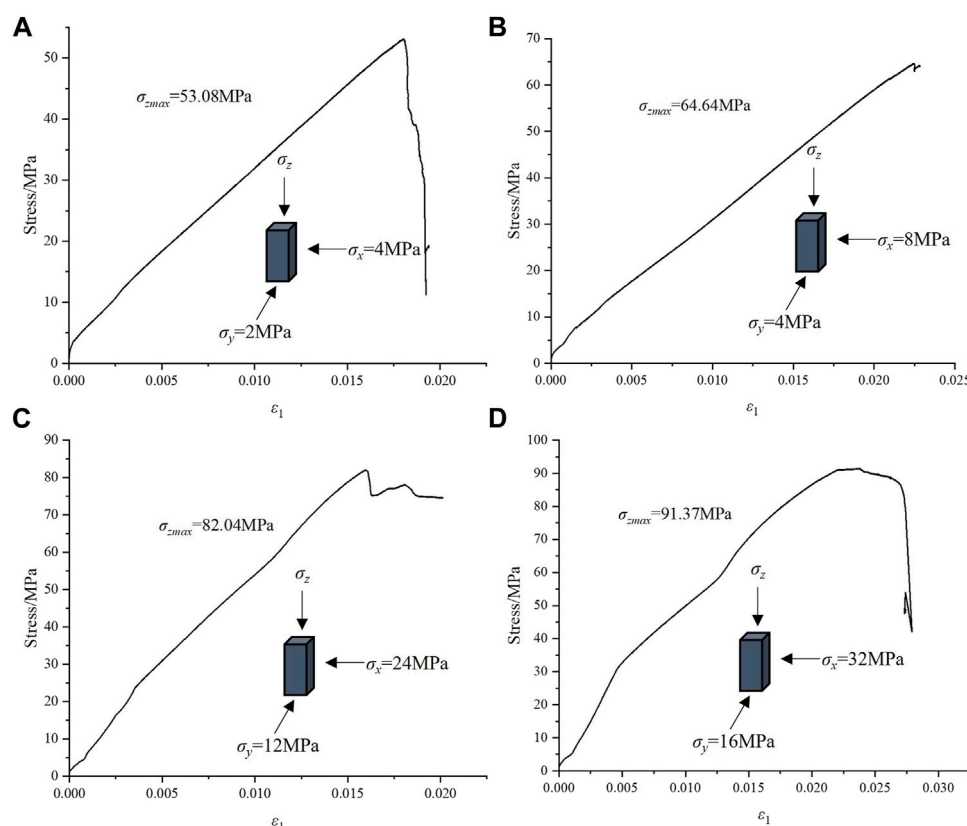


FIGURE 5  
bearing capacity increases greatly with increased confining pressure. (A) M-1. (B) M-2. (C) M-3. (D) M-4.

the roof above the seam would tilt upward if the longwall face moved forward a bit (blue arrow in the figure). The longwall would then act as a fulcrum. The hanging roof behind the longwall face would compress the coal seam at the longwall face, causing the roof above the coal seam in front of the longwall face to straighten.

## 5 Mitigation measures for coal bursts

### 5.1 Improvement of the mitigation system

In the Tangshan coal mine, a sophisticated coal burst containment system has been developed in recent years. Coal breakout containment is the most important task in the Tangshan coal mine and, so far, many pieces of high-tech

monitoring equipment have been used to monitor the voltage change, the deformation of the roadway, etc. In addition, equipment for stress relief and energy field mapping has also been purchased and implemented. A sophisticated damage mitigation system has been developed and a professional team of technicians has been established.

Based on work experience, a coal outburst mitigation procedure has been developed, which includes 29 coal burst control and mitigation measures. The main principle is to optimize the design so that coal burst incidents are less likely to occur. Then, real-time and field measurements and evaluations must be conducted continuously to prevent incidents. In the meantime, a mature flash relief measure has been developed that can be implemented as soon as a potential coal burst is detected. In addition, upper limits on mining depth, mine production, and

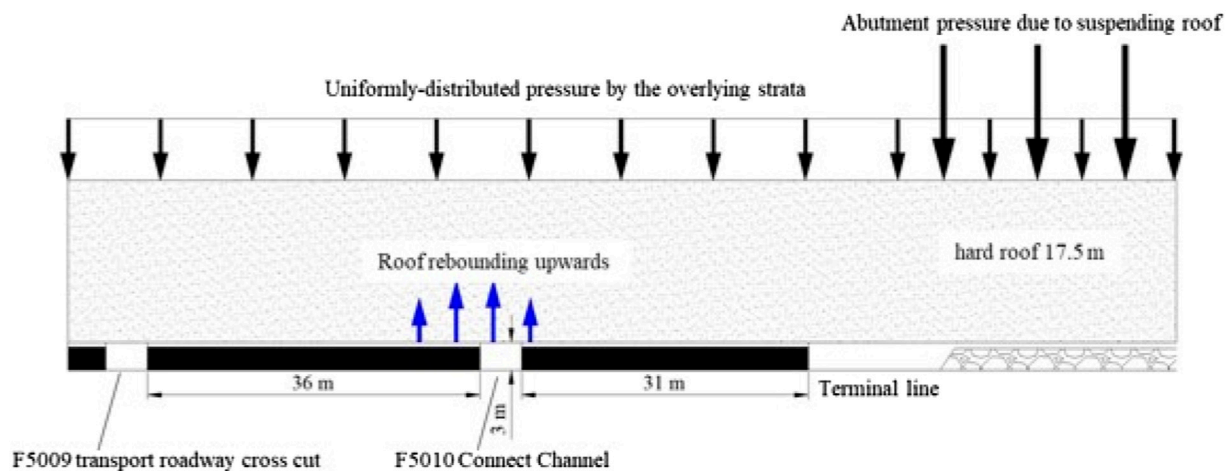


**FIGURE 6**  
Seesaw structure formed by the hard roof and high-bearing coal.

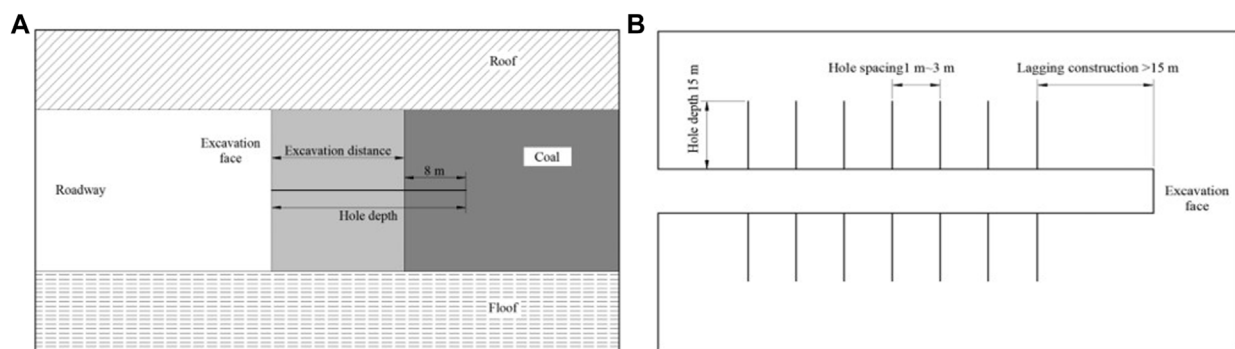


**FIGURE 7**  
Schematic diagram of the pre-pressure relief method. (A) Excavation front. (B) Excavation rear.

number of underground crews must be established. Attention should also be paid to rock reinforcement and ground support.

A mature early warning system for coal bursts has also been well developed at the Tangshan coal mine. Both local and global seismicity monitoring systems were implemented and are continuously operated by trained technicians. The time and location of each seismic event can be recorded. In addition, the drilling stress-releasing method, real-time stress monitoring, and electromagnetic radiation method are also used to monitor the risk of bursts. In particular, a system was installed to monitor seismicity in the ARAMIS M/E and KJ768 Zones. Three roof deformation monitoring systems were installed in the KJ24 zone. Three acoustic and electrical monitoring systems were installed in the YDD16 Zone and two in the KBD5 Zone. Five trained technicians were assigned to coal excavation mitigation and related risk monitoring only. Four mining engineers were assigned to mitigation activities and are responsible for monitoring data and operating the early warning system. A daily report on the monitoring of the coal burst is prepared and forwarded to the management team.

## 5.2 Optimization of mitigation measures

### 5.2.1 Optimization of local mitigation measures

Coal seam nos 5, 8, and 9 are mined simultaneously in the Tangshan coal mine. We propose to give priority to coal seam No. 5 to minimize the risks of coal burst in coal seam nos. 8 and 9. When the mine was designed, the main drift, main development tunnel, and access tunnels were constructed in the rock strata to minimize the risk of a burst. Some mining zones were mined simultaneously, and in one zone, at least one slab was left between two active slabs. In one zone, only one side was mined at a time. Thus, the disturbance of the stress distribution was minimized. The frequency of coal bursts depended on the speed of the longwall movement. The higher the speed, the more energetic events occurred. Therefore, an appropriate mining speed could significantly reduce the risk and frequency of coal bursts.

### 5.2.2 Optimization of stress-releasing practices

We propose a stress relief method to address the challenges associated with the pivot formed under high stress concentrations.

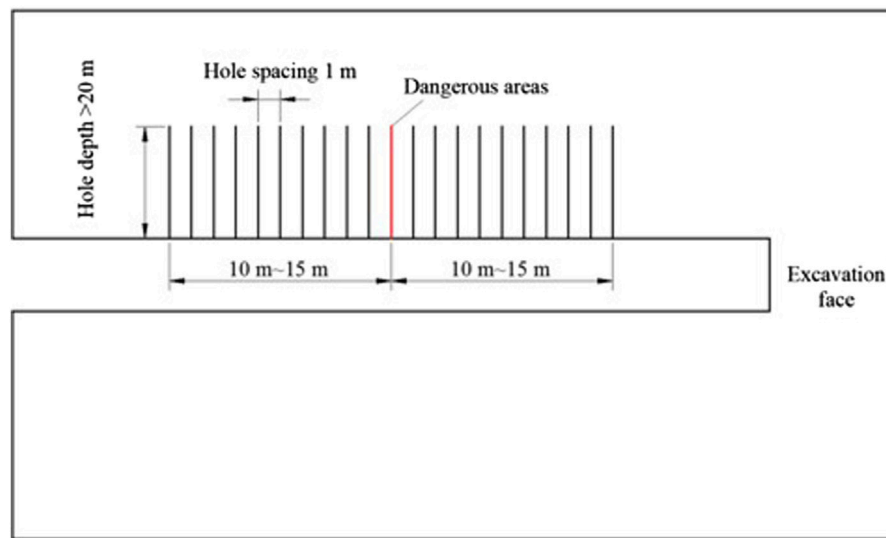


FIGURE 8

Schematic diagram of the pressure relief method.

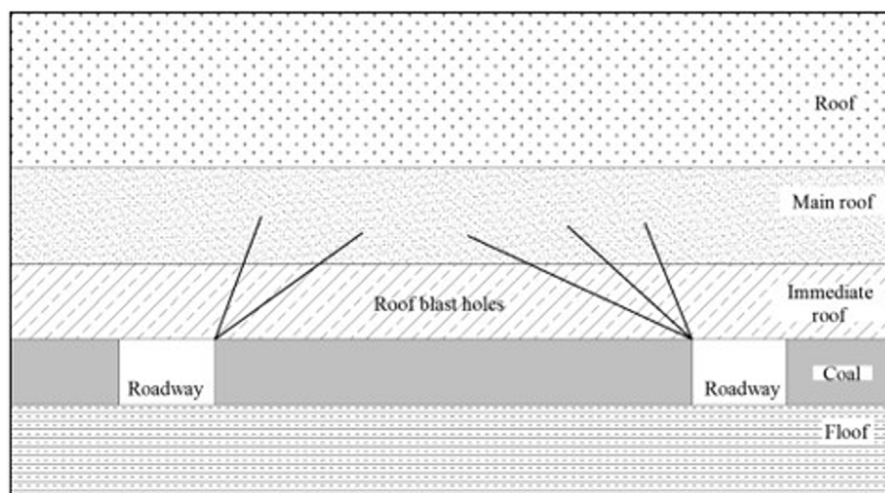


FIGURE 9

Schematic diagram of the roof blasting.

Preconditioning method: the borehole should not be less than 110 mm in diameter. During the development phase, 1–3 holes are drilled, depending on the assessment of coal burst risk, to ensure that stress relief is present in the rock 8 m from the development face (Figure 7A). Behind the mining face, holes should be drilled to a depth of 15 m and no less than 10 m from the mining face. The drill hole spacing should range from 1 to 3 m, depending on the assessment of the risk of a coal burst (Figure 7B). During the longwall retreat phase, 200 m in front of the longwall should be relieved, with an arrangement similar to that in the development stage.

Stress relief method: the borehole should not be less than 110 mm in diameter. In the development stage, the pattern is like a three-petaled flower. The depth of the borehole should exceed

20 m. If there is a risk behind the rock wall, the borehole should be drilled 10–15 m away from the monitoring points. The spacing between boreholes should be 1 m (Figure 8). During the longwall retraction phase, 200 m in front of the longwall should be relieved, with an arrangement similar to that in the development phase.

Considering the formation of a long, hanging roof after the longwall has moved somewhat forward, a method of long-hole drilling and blasting was proposed to relieve the stresses. In the areas at high risk for bursts where blasting was performed, long-hole drilling and blasting significantly relieved the stresses, ensuring a safe environment for subsequent mining activities. A hydraulic drill rig and a special drill bit were used to perform the long-hole drilling with a borehole diameter of no less than 72 mm. Three to five holes



were drilled every 10–15 m in the two roadways adjacent to the longwall (Figure 9). Angled holes were also drilled in the ceiling 1.5 m from the rib. The borehole spacing, angles, and depth could be adjusted depending on site conditions. After the explosives were installed, the drill holes were sealed with mud. The blasting was carried out in accordance with the Safe Mining Regulation.

### 5.2.3 Stress-relief facilities

Two drilling vehicles (CMS1-12--/22 (model B)), 15 pneumatic drills (ZQJC-200/5), 5 drills (ZQJC-500), 87 hand drills (FIV-HT), and 109 hydraulic support units were used to contain the coal burst. In addition, 400 self-rescuers (ZYJ-M6), 800 protective helmets (ANF-2), and 1000 PPE were available.

As a result of the prudent remedial measures, safe mining activities were carried out in the Y394, 0250, 0291, and Y251 longwall fields, producing ROM 4.45 million tons of coal, resulting in a profit of 276 million Chinese yuan.

## 6 Conclusion

- 1) The results of this study showed that coal sliding in the rib area was the main failure mechanism of coal burst in 8.2 incidents. The maximum deformation of the coal rib was up to 2 m, and significant floor heave was also observed near the failure rib.
- 2) The cause of the coal burst incident was identified. If the immediate roof was too competent, a long, hanging roof would form as the longwall moved forward slightly. This caused the roof above the coal seam in front of the longwall to tilt upward, releasing the confinement of the coal seam.
- 3) A number of effective measures to mitigate coal bursts have been proposed, with very promising results. The research results provide new ideas for coal outburst prevention and control that can effectively contain the occurrence of similar ground pressure and ensure safe production in mines.

## References

- Dou, L., He, J., Cao, A., Gong, S., and Cai, W. (2015). Rock burst prevention methods based on theory of dynamic and static combined load induced in coal mine. *J. China Coal Soc.* 40(7) 469–476. doi:10.13225/j.cnki.jccs.2014.1815
- Gao, Y., Liu, D., Zhang, X., and He, M. (2017). Analysis and optimization of entry stability in underground longwall mining. *Sustainability* 9 (11), 2079. doi:10.3390/su9112079
- Jiang, Y., Wang, H., Xue, S., Zhao, Y., Zhu, J., and Pang, X. (2012). Assessment and mitigation of coal bump risk during extraction of an island longwall panel. *Int. J. Coal Geol.* 95, 20–33. doi:10.1016/j.coal.2012.02.003
- Jiang, Y., Zhao, Y., Gauthier, A., Baptiste, C., Martinon, P., and Bresse, X. (2015). A comparative public health and budget impact analysis of pneumococcal vaccines: The French case. *Chin. J. Rock Mech. Eng.* 34 (11), 2188–2197. doi:10.1080/21645515.2015.1011957
- Jinag, F., Wei, Q., Wang, C., Yao, S., Zhang, Y., Han, R., et al. (2014). Analysis of rock burst mechanism in extra-thick coal seam controlled by huge thick conglomerate and thrust fault. *J. China Coal Soc.* 39 (7), 1191–1196. doi:10.13225/j.cnki.jccs.2013.1402
- Lan, H., Qi, Q., Pan, J., and Peng, Y. (2011). Analysis on features as well as prevention and control technology of mine strata pressure bumping in China. *Coal Sci. Tech.* 39 (1), 11–15. doi:10.13199/j.cst.2011.01.17.lanh.008
- Lu, J., Yin, G., Gao, H., Li, M., and Deng, B. (2020). Experimental study on compound dynamic disaster and drilling pressure relief of gas-bearing coal under true triaxial loading. *J. China Coal Soc.* 45 (05), 1812–1823. doi:10.13225/j.cnki.jccs.2019.0530
- Ma, N., Guo, X., Zhao, Z., Zhao, X., and Liu, H. (2016). Occurrence mechanisms and judging criterion on circular tunnel butterfly rock burst in homogeneous medium. *J. China Coal Soc.* 41 (11), 2679–2688. doi:10.13225/j.cnki.jccs.2016.0788
- Miao, X., An, L., Zhai, M., Zhang, X., and Yang, T. (1999). Model of rockburst for extension of slip fracture in palisades. *J. China Univ. Min. Technol.* (2), 15–19.
- Pan, J. (2019). Theory of rockburst start-up and its complete technology system. *J. China Coal Soc.* 44 (1), 173–182. doi:10.13225/j.cnki.jccs.2018.1156
- Pan, L., and Yang, H. (2004). Dilatancy theory for identification of premonitory information of rock burst. *Chin. J. Rock Mech. Eng.* (S1), 4528–4530. doi:10.3321/j.issn:1000-6915.2004.z1.056
- Pan, Y. (2018). *Rock burst in coal mine*. Beijing: Science Press.
- Pan, Y., and Zhang, M. (1996). The exact solution for rockburst in coal mine by instability rockburst theory. *Chin. J. Rock Mech. Eng.* S1, 504–510. CNKI: SUN: YSLX.0.1996-S1-017.
- Qi, Q., Li, Y., Zhao, S., Zhang, N., and Deng, W. (2019). 70 years development of coal mine rockburst in China: Establishment and consideration of theory and technology system. *Coal Sci. Technol.* 47(9) 1–40. doi:10.13199/j.cnki.cst.2019.09.001
- Shen, W., Duo, L., He, H., Gong, S., and Ji, X. (2019). Study on mechanism and prevention of rock burst under loading and unloading path in solid coal driving. *J. Min. Safe. Eng.* 36 (04), 768–776. doi:10.13545/j.cnki.jmse.2019.04.016

## Data availability statement

The original contributions presented in the study are included in the article/Supplementary Material. Further inquiries can be directed to the corresponding author.

## Author contributions

DJ was mainly responsible for the overall writing of the full text. ZZ and MZ were responsible for the theoretical analysis. CC was responsible for the innovative ideas in this article. All authors contributed to the article and approved the submitted version.

## Conflict of interest

Author ZZ was employed by Tangshan Coal Mine, Kailuan (Group) Limited Liability Corporation. Author MZ was employed by the Research Center of the Ministry of Emergency Management.

The remaining authors declare that the research was conducted in the absence of any commercial or financial relationships that could be construed as a potential conflict of interest.

## Publisher's note

All claims expressed in this article are solely those of the authors and do not necessarily represent those of their affiliated organizations, or those of the publisher, the editors, and the reviewers. Any product that may be evaluated in this article, or claim that may be made by its manufacturer, is not guaranteed or endorsed by the publisher.

- Song, Z. (1998). *Practical mine pressure control*. Xuzhou: China university of mining and technology press.
- Tan, Y., Guo, W., Xin, H., Zhao, T., Yu, F., and Liu, X. (2019). Key technology of rock burst monitoring and control in deep coal mining. *J. China Coal Soc.* 44 (1), 160–172. doi:10.13225/j.cnki.jccs.2019.5088
- Xie, H., Gao, F., and Ju, Y. (2015). Research and development of rock mechanics in deep ground engineering. *Chin. J. Rock Mech. Eng.* 34 (11), 2161–2178. doi:10.13722/j.cnki.jrme.2015.1369
- Xie, H., and Pariseau, W. G. (1993). Fractal characteristics and mechanism of rockburst. *Chin. J. Rock Mech. Eng.* (01), 28–37. CNKI:SUN:YSLX.0.1993-01-003.
- Yang, Z. (2011). *Investigation on law and prevention technology of coal bump in Kailuan Coal Mine*. [doctoral's Thesis] ([Beijing(China)]): China University of Mining and Technology).
- Yin, G., Liu, Y., Li, M., Deng, B., Liu, C., and Lu, J. (2018). Influence of true triaxial loading-unloading stress paths on mechanical property and permeability of coal. *J. China Coal Soc.* 43 (1), 131–136. doi:10.13225/j.cnki.jccs.2017.4500
- Yin, G., Zhang, D., Dai, G., and Wang, L. (2022). Damage model of brittle coal and rock burst damage energy index. *J. Chongqing Univ.* (09), 75–78+89. doi:10.3969/j.issn.1000-582X.2002.09.021
- Zang, M. (1987). Theory and numerical simulation of rock burst instability. *Chin. J. Rock Mech. Eng.* (3), 197–204. CNKI:SUN:YSLX.0.1987-03-001.



## OPEN ACCESS

## EDITED BY

Liang Chen,  
China University of Mining and  
Technology, China

## REVIEWED BY

Zhenlong Song,  
Southern University of Science and  
Technology, China  
Jiarui Chen,  
Huaiyin Institute of Technology, China

## \*CORRESPONDENCE

Fanang Dang,  
✉ dangfn@163.com

RECEIVED 15 June 2023

ACCEPTED 14 August 2023

PUBLISHED 30 August 2023

## CITATION

Wei L, Dang F and Ding J (2023), An  
investigation on the thixotropic  
parameters and mechanical properties  
of loess.  
*Front. Earth Sci.* 11:1240799.  
doi: 10.3389/feart.2023.1240799

## COPYRIGHT

© 2023 Wei, Dang and Ding. This is an  
open-access article distributed under the  
terms of the [Creative Commons  
Attribution License \(CC BY\)](#). The use,  
distribution or reproduction in other  
forums is permitted, provided the original  
author(s) and the copyright owner(s) are  
credited and that the original publication  
in this journal is cited, in accordance with  
accepted academic practice. No use,  
distribution or reproduction is permitted  
which does not comply with these terms.

# An investigation on the thixotropic parameters and mechanical properties of loess

Le Wei, Fanang Dang\* and Jiulong Ding

Xi'an Key Laboratory of Environmental Geotechnical Engineering of Loess Plateau, Xi'an University of Technology, Xi'an, China

The analysis of thixotropic mechanical properties of loess has a significant influence on the calculation of the strength of compacted loess foundation. In order to distinguish the consolidation growth strength of loess from the thixotropic strength, a resting thixotropic instrument is developed. The proposed device is capable of maintaining a constant volume pressure. To attain the goals, after selecting the representative Xi'an loess, the samples were pressed by the resting thixotropic instrument under constant volume pressure. Eight resting ages were also set. Moreover, the thixotropic mechanical properties of loess soil were studied at 6 months resting ages through uniaxial compression without lateral limit and triaxial CU test. The thixotropic triaxial shear strength ratio  $J_t$ , thixotropic triaxial shear strength recovery ratio  $K_t$  and thixotropic cohesion recovery ratio  $L_t$  were defined, the mechanical properties of which were investigated under different stress states. The obtained results demonstrated the obvious thixotropy of Xi'an loess, the strength of which was found to increase with an increase in the resting age. This is while, an increase in the resting age was observed to decrease its growth rate. Moreover, the unconfined thixotropic strength was found to increase by 1.75 times after resting for 160d, which corroborates the influence of thixotropic strength in designing the foundation bearing capacity of loess. Furthermore, the recovery ratio of unconfined thixotropic strength and the growth ratio of eccentric stress strength were found to be 0.187 and 0.115, respectively. In addition, the thixotropic triaxial shear strength ratio  $J_t$ , the recovery ratio of thixotropic triaxial shear strength ratio  $K_t$ , and the recovery ratio of thixotropic cohesion ratio  $L_t$  were observed to be 0.15, 0.527, and 0.5, respectively. The obtained results suggest the resting age of 40 days to be used as the inflection point for the recovery of thixotropic strength such as uniaxial compressive strength, peak deviator stress, shear strength and cohesion of loess. Despite the insignificant variation range of the friction Angle in the resting process, the contribution ratio of friction force in increasing the shear strength was also found to be much greater than that of the cohesion.

## KEYWORDS

loess, thixotropy, resting, pressure holding device, shear strength

## 1 Introduction

As a widely distributed material in northwest China, loess has been used as the basis of numerous projects. Accordingly, hill-digging, gully filling and urban construction projects are increasingly performed in recent years in such cities as Yan'an, Tongchuan, Lanzhou, etc. Which are surrounded with loess mountain areas. As a result, several high fill projects have

been introduced and carried out. However, almost no tall building has been yet constructed on loess foundation in the reclaimed areas which have been left for several years. To be more exact, loess has only been seen used in the construction of roads, parks or low-rise buildings, which can be argued to be due to loess being categorized as an extremely sensitive soil. Consequently, the reshaped loess foundation significantly lacks the required bearing capacity in an actual project. Therefore, when the foundation is filled with thick soil, there will be long-term post-construction settlement, which affects the safety or normal use of the building. During the foundation shelving period, some temporary low-load facilities can be built in shallow locations on the surface for economic development, such as underground energy storage warehouses that have emerged in recent years (e.g., Xue et al., 2023; Xue et al., 2023). As time develops, the filling is gradually compacted, leading the bearing capacity of the foundation to be constantly increased, which in turn, provides favorable conditions for the building height. At the same time, complex coupling effects, such as soil-water pressure and geothermal, will affect the structural stability of underground facilities with the development of time (e.g., Jiang et al., 2022; Liu et al., 2023; Xue et al., 2023; Yang et al., 2023). Hence, determining the variation law of the strength of the remolded loess foundation over time as well as the standard value of the bearing capacity of the foundation under different time nodes are significant issues in the urban expansion of the mountainous areas.

Strength of a compacted loess is found to increase as time develops. This improvement is partly due to the consolidation volume compression. In other words, on the one hand, when the dead weight or overlying load is unchanged, soil compaction makes the strength increase; a phenomenon which is called consolidation growth strength of loess. On the other hand, the increase in the strength is partly due to what is called the thixotropic strength of loess. In other words, it is caused by the rise in the cohesion and friction, which, in turn, are triggered by the regrowth of the calcium carbonate bridge between the particles when the external load and volume of the disturbed loess do not change. Currently, despite numerous studies on creep characteristics and consolidation strength of remolded loess, the thixotropic strength of loess has remained understudied. Moreover, while the increase in the soil strength has been mainly attributed to the consolidation process, the influence of thixotropy is not clear. Therefore, distinguishing the thixotropic from the consolidation strength of loess can improve the related mechanical theory. Moreover, a mechanical explanation can also be provided for the test deviation caused by other characteristics of loess. In addition, the bearing capacity of remolded loess foundation can also be determined over time, which provides practical suggestions to be used in construction projects.

The term “thixotropy” was first coined by Peterfi (1927) to describe the reversible transition between the fluid state and the elastic solid state of colloidal solutions. Later, a new definition of the thixotropic properties of geotechnical materials was offered by Burger and Blair (1949), according to which, reshaping disturbance can soften the soil, which can be hardened again after resting, with a tendency to develop to the original state. In another study, Boswell (1948) found that, except for clean sandy soil, varying degrees of thixotropy were demonstrated by other soil sediments. Moreover, thixotropy was shown by Kruyt (1952) to exist in most clay-water systems. Mitchell (1961) also discussed thixotropy to be

an isothermal, reversible and time-dependent process with constant soil composition and volume. Furthermore, according to ASTM (D653-14) 2014, while thixotropy can cause a disturbed material to harden for a relatively short time, it then turns into a high viscosity fluid after the disturbance. Moreover, the processes of resting hardening and disturbed softening were able to transform into each other.

The thixotropic mechanics of soil have also been studied by a number of scholars. For example, Skempton and Northey (1952) studied thixotropy by conducting shear tests on soil materials, the results of which revealed that, provided with sufficient resting age, the idealized pure thixotropic materials could recover their strength after disturbance to the initial level; however, this was shown to be difficult for most natural soils. In another study, investigating the thixotropy of quick-clay, Kerr and Drew (1968) found that soil strength could recover to water saturation strength after resting for 40 min under seismic disturbance. Nevertheless, Cabrera and Smalley (1973) believed that the thixotropy of the quick-clay was not significant at all. Measuring the thixotropy of Mexican soil using a conductivity method, Diaz-Rodriguez and Santamarina (1999) found the strength of the disturbed soil to be increased more than one time after resting. Zhang et al. (2017) measured the unconfined compressive strength of Zhanjiang soft clay before and after disturbance. The results revealed that, after resting for 500 days, while the strength was only recovered for 33% of that of the original soil before disturbance, it increased by 2.46 times compared with the original disturbed soil without resting. Frydman et al. (2007) also observed changes in the residual strength of the landslide surface of swamp after a certain time. In addition, using indoor ring shear test, Hu et al. (2017) found that the thixotropy of different-size particles influenced the movement of the landslide shear zone. Tang et al. (2021) defined the quantitative index system and classification method of the thixotropic mechanical properties of clay, introduced the concept of thixotropic sensitivity to describe the relationship between thixotropy and soil structure, proposed the structural recovery coefficient  $K$  and structural recovery index  $K_e$  to qualitatively describe the thixotropy of Zhanjiang remodeled clay, and classified the thixotropy by calculating and determining the  $K$  value boundaries  $K_I$  and  $K_{II}$ . The thixotropy is moderate when  $K$  is between  $K_I$  and  $K_{II}$ , and strong when  $K$  is greater than  $K_{II}$ . Ren et al. (2021) and Ren et al. (2022) studied the thixotropic mechanical properties and microstructure changes of offshore soft clay in China by means of falling cone test and scanning electron microscopy, and proposed a “probabilistic entropy” index to describe the size and quantity changes of particles or aggregates in soil particles, pointing out that thixotropy has a significant impact on the strength improvement of offshore soft clay. Thixotropic strength ratio has good correlation with soil moisture content, plasticity index, fluidity index and sensitivity. Peng et al. (2022) studied the thixotropy of marine clay containing illite with medium salt concentration and artificial kaolin with high purity under different liquid limits, and studied the undrained shear strength  $S_u$  and small strain shear modulus  $G_{max}$  of soil under different standing time through falling cone and bender element tests, and found that  $S_u$  increased by 330% after resting for 64 days,  $G_{max}$  increased by 386%, and the increase rate decreased with the increase of time. Salam et al. (2023) pointed out that the deposited clay, dredged sediment and clay-containing oil sand tailings all have thixotropy to a certain extent. After resting



for more than 100 days, the test found that the strength, sensitivity, pre-consolidation pressure and compressibility of different remolded soil samples in the laboratory were increased. Compared to tail sand, some components of clay can absorb some free water and make the thixotropy stronger.

The relationship between the soil thixotropy and actual engineering properties has also been widely researched (e.g., Solonenko, 1977; Cronin et al., 1999; Khaldoun et al., 2009; Mainsant et al., 2015; Yenes et al., 2020). For example, studying pile foundation, Andersen and Jostad (2002) found thixotropy to have a positive effect on engineering stability. Accordingly, after setting the pile driving or suction anchor in soil, part of the friction force was observed to be generated in the remolded clay, improving the shear strength. Furthermore, studying certain projects in the Ob Bay area (the north coast of Siberia), Romanov and Romanov (1997) also found that, due to the influence of soil thixotropy, the strength changed significantly after 10 days of foundation piling. Moreover, while the bearing capacity of the piles of around 10 days could reach 85% after 1 month, the mechanism of the increase in the strength has remained unclear. Therefore, the redistribution of pore pressure from thixotropic or remolded soils needs to be further defined.

Some scholars have also studied the test methods used in examining soil thixotropy and their shortcomings. Park et al. (2014), for example, found that the result obtained from blade shear test was lower than that of the falling cone test, which was argued to be due to the disturbance of the soil caused by blade insertion. Moreover, Seng and Tanaka (2012) showed significant errors in the results obtained by such conventional methods as unconfined compression test, standard penetration test, direct shear test and ring shear test; such errors were discussed to be caused by the significant disturbance applied on the soil structure in the sample preparation process. In another study, to ensure the safety and wellness of the soil structure, Osipov et al. (1984) used a liquid nitrogen container to freeze the sample and added an electric vibration damping frame in the sample preparation process, which accordingly, improved the rotary viscometer during the test. Also, to keep the conditions constant during the test, Rinaldi and Clari (2016) designed an adiabatic integrated test device, which was capable of monitoring the changes in shear modulus, temperature, resistance, capacitance and matric suction of soil in the remolding and resting state in real time. In addition, to reduce large fluctuations in the moisture content of soil remolding and resting state, Yang and Anderson (2016) also designed a double-conical plastic container, Iwase et al. (2021) studied the effects of clay mineral type and particle size on the hydrogel thixotropy of montmorillonite minerals by scanning electron-assisted dielectric microscopy and small-angle neutron scattering method, and pointed out that the hydrogel thixotropy strength depends on the particle size and aggregation degree of kryptonite when soil is shear.

Review of the research results suggests that, after the structure of loess is destroyed by disturbance, the strength growth of long-term resting under the action of overlying soil pressure can be divided into two parts, namely, the strength growth caused by consolidation volume compression (called the consolidation volume variable growth strength) and the one caused by thiotropy. Moreover, while the so-called thixotropic strength measured by previous scholars includes the strength of consolidation, the increase in the strength generated by consolidation is difficult to be



separated from the thixotropic strength. In addition, such conventional test methods of measuring the thixotropic strength as unconfined compression, are found to be simple and accordingly, unable to reflect the change of thixotropic strength in complex stress states. At the same time, studies on the thixotropic properties of soil materials have been mainly limited to clay or silt. This is to say that, few studies have been carried out on the thixotropic properties of loess, most of which are not in-depth enough to be able to calculate the bearing capacity of remolded loess foundation. Therefore, to distinguish the variable growth strength of the consolidated body from the thixotropic strength, the present study aims at developing a resting thixotropic instrument with constant volume pressure maintenance. Consequently, the proposed instrument is intended to ensure the moisture content, dry density and total volume of the soil to remain unchanged during the resting process of the sample. Moreover, the strength improvement of the remolded loess in the resting process is aimed to be only due to the thixotropy rather than the variable compaction of the consolidated body. Accordingly, capable of reflecting the shear strength index under complex stress, the triaxial undrained test (CU test) is used to select a representative Xi'an loess. Subsequently, to study the thixotropic mechanical properties of loess with resting ages of 6 months, thixotropic parameters related to the shear strength are compared with the obtained results from the unconfined compression tests.

## 2 Soil sample and resting thixotropic instrument with constant volume pressure maintaining

### 2.1 Test soil sample

The soil sample for the test was taken from a construction site 1 km north of the North Wall of Weiyang District, Xi'an, Shaanxi

**TABLE 1** Basic physical properties of loess in Xi'an.

Natural water content (%)	Natural density (g/cm <sup>3</sup> )	Relative density	Porosity	Plastic limit/ W <sub>p</sub> (%)	Liquid limit/ W <sub>L</sub> (%)	Plastic index/I <sub>p</sub>
25.4	1.73	2.71	0.49	19.4	30.8	11.4

**TABLE 2** Composition and classification of loess particles.

Mass fraction of different particle sizes/%			Classify	
>0.075 mm	0.075~0.005 mm	<0.005 mm	Classified by plastic diagram	Classified by particle composition
12.5	63.2	24.3	CL	clay

Province. It was Q<sub>2</sub> loess with a depth of 10–12 m. The basic physical property indexes of the soil sample are shown in [Table 1](#), the composition and classification of loess particles are shown in [Table 2](#):

## 2.2 Structure design of constant volume pressure maintaining resting thixotropy and preparation with soil samples

In order to distinguish the thixotropic strength from the consolidation growth strength, a resting thixotropic apparatus maintaining constant volume pressure was required to be devised. The instrument requires no unloading of the external pressure. No consolidation volume deformation of the sample was required during the resting process, as well. Accordingly, the change in the strength measured after a certain resting age can be argued to be only the growth strength caused by thixotropy of the soil sample, excluding the consolidation growth strength.

[Figures 1, 2](#) displays respectively the physical structure and principle of resting thixotropy with the constant volume pressure device designed in this paper. The instrument is composed of a back pressure loading device (black parts) and a constant volume pressure maintaining resting device (blue parts). The latter was composed of a 22 mm thick Q235 base steel plate, four M24 screws, a 22 mm thick Q235 top steel plate and a reaction I-steel, as well as a 5T hydraulic jack and plate. The function of the device was to apply the specified displacement or load to the sample at the initial stage of sample preparation. On the other hand, the former device was composed of an 8 mm thick Q235 base steel plate, four M12 screws, an 8 mm thick Q235 top reaction steel plate, a force transfer steel cylinder and a rigid model box with a movable roof, the function of which was to maintain the specified displacement or load applied to the sample at the initial stage of sample preparation. Moreover, the device also kept the volume, dry density and water content of the sample unchanged throughout the thixotropic resting age. To ensure sufficient stiffness, three rings of hoop Angle steel were used around the model box. The movable roof was made of an 8 mm steel plate. To ensure uniform deformation of each area of the soil section during compression, the size of the plate was fitted around the inner wall of the model box.

While the volume, dry density and water content of the soil sample remained unchanged when the soil sample was held in the

device, the position of the soil particles inside the sample demonstrated a slight creep displacement. Moreover, the pressure inside the soil body showed a similar stress relaxation phenomenon. Due to the above mentioned reasons, the instrument is called a pressure holding device rather than an isobaric one.

The principle of sample making was to make the top of the jack and the bottom of the rigid model box contact with the upper and lower end of the reverse pressure loading device. To this end, the external rigid back pressure loading device was utilized. The bottom of the jack and the top of the soil sample were connected through the movable roof and the force transfer parts of the rigid model box. Moreover, using the jack, the specified displacement or load was applied to the soil sample.

The soil samples were placed in the rigid model boxes with the movable roof fastened by the Angle steel hoops. The size of the internal section of the model boxes was 25 cm × 25 cm. The plastic wrap was laid on the inside wall of the model box first. Subsequently, the configured loose soil sample was poured into the layers. Next, the soil sample was wrapped tightly. In the process of soil compression, a small number of pinholes need be drilled on the outside of the plastic wrap covered with soil samples to exhaust air. When resting, due to the compaction of the soil, the inner side of the steel plate of the model box will be closely fitted with the plastic wrap, which will prevent the water in the soil pores from leaking through the pinhole and ensure the constant moisture content of the soil sample.

In order to ensure the uniform density of the sample, it is necessary to make all parts of the soil sample in the model box produce uniform compression during the compression process. First, the center of the jack is aligned with the center of the model box. In addition, a level device is placed on the top steel plate of the model box during the compression process. Every 1 cm compression, use the level device to detect whether the compression surface is tilted, and constantly calibrate the alignment to prevent the instrument from producing eccentric compression. When the soil in the model box is compressed to the specified dry density, the reaction force provided by the jack will prevent the soil from springback deformation. At this time, the top steel plate of the pressure holding device and 4 M12 screw kits are used to fix the model box. The sample volume in the box is changed from jack anti-force fixing to screw anti-force fixing. When the jack is removed later, the steel plate fixed by screw will still prevent the soil from springback deformation.

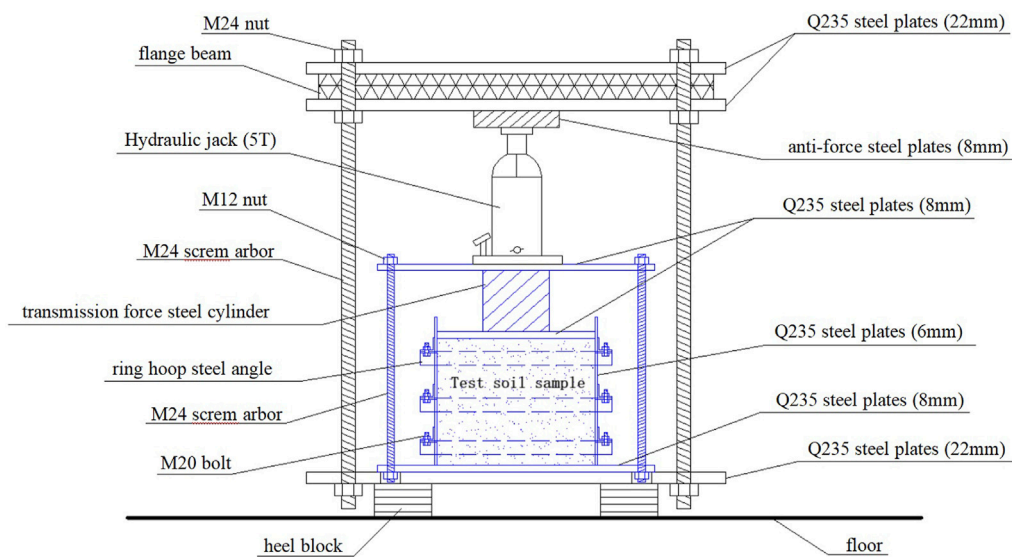


FIGURE 2  
The structural parts of thixotropy device.

After placing the soil samples at the test age under constant volume pressure, the model box was dismantled. Moreover, the soil samples with uneven structure near the edge of the model box were cut off. The test samples were also selected from nearest parts to the center of the homogeneous soil embryo.

## 2.3 Designing the test scheme

In this thixotropic test, the mechanical indexes of the undisturbed and the remolded loesses were compared at different resting ages. Moreover, the variation law of soil strength was obtained with the increase of time. As the original loess, the remolded one was made into soil samples with the same moisture content and dry density. After compressing the sample using the loading device, the resting ages of 0d (After the soil sample is compressed to the specified dry density, the model box is removed immediately to prepare the sample and test the strength without resting), 5d, 10d, 20d, 40d, 80d, 120d, and 160d were determined. Using the unconfined compression test as well as the triaxial consolidation undrained test (CU test), the  $q_u$  compressive strength and the stress-strain curves of the unaltered and the remolded loesses were measured under different confining pressures, respectively. Finally, the values of  $c$  and  $\varphi$  were obtained using Moerculen criterion.

## 3 Defining the thixotropic parameters of loess in complex stress state

### 3.1 Superiority of thixotropic parameters of triaxial shear strength

Zhang et al. (2017) defined the growth ratio of soil thixotropic strength based on the result obtained from the uniaxial compression test. Accordingly,  $A_t$  and  $B_t$  were the ratio of the unconfined strength between the remolded and

the undisturbed loess at a certain time after disturbance and the ratio of thixotropic strength to the total disturbance loss strength, respectively.

$$A_t = \frac{q_t}{q_u}, \quad (1)$$

$$B_t = \frac{q_t - q_0}{q_u - q_0}, \quad (2)$$

Where  $q_u$ ,  $q_0$  and  $q_t$  stand for the unconfined compressive strengths of the undisturbed loess, of the soil under full disturbance and of the soil at thixotropic resting age  $t$ , respectively.

Since the complex stress state of the soil buried deep underground may not be determined by the unconfined strength, only the uniaxial compressive action and not the triaxial shear action of the soil thixotropy can be examined. Therefore, the shear strength indexes  $c$  and  $\varphi$  of the soil obtained by the triaxial shear test are used as the parameters in this paper. Moreover, the three specific loess thixotropic parameters,  $J_t$ ,  $K_t$  and  $L_t$  were defined to describe the changing process of the shear strength and the cohesion of remolded loess during thixotropic process.

In this paper, the introduction of the triaxial shear strength rates  $J_t$ ,  $K_t$  and  $L_t$  can reflect not only the compressive action of the thixotropic soil, but also the triaxial shear action. Moreover, the thixotropic parameter can still be used in the face of the complex stress states when the shear strength index  $c$  and  $\varphi$  are introduced; a property which cannot be achieved through other thixotropic parameters.

### 3.2 Defining thixotropic parameters based on triaxial shear strength

The known shear strength, normal stress of shear plane, tangential stress of shear plane and included angle of fracture plane of viscous soil are:

$$\tau = c + \sigma \tan \phi, \quad (3)$$

$$\sigma = \frac{1}{2} (\sigma_1 + \sigma_3) + \frac{1}{2} (\sigma_1 - \sigma_3) \cos 2\alpha, \quad (4)$$

$$\tau = \frac{1}{2} (\sigma_1 - \sigma_3) \sin 2\alpha = \frac{1}{2} (\sigma_1 - \sigma_3) \cos \phi, \quad (5)$$

$$\alpha_f = 45^\circ + \frac{\phi}{2}, \quad (6)$$

The shear strength of soil under the limit equilibrium condition is:

$$\tau_f = c + \left[ \frac{1}{2} (\sigma_1 + \sigma_3) - \frac{1}{2} (\sigma_1 - \sigma_3) \sin \phi \right] \tan \phi, \quad (7)$$

The thixotropic triaxial shear strength ratio  $J_t$  of the remolded loess at the resting age  $t$  was defined as:

$$J_t = \frac{\tau_{f,t}}{\tau_{f,0}} = \frac{c_t + \left[ \frac{1}{2} (\sigma_1 + \sigma_3) - \frac{1}{2} (\sigma_1 - \sigma_3) \sin \phi_t \right] \tan \phi_t}{c_0 + \left[ \frac{1}{2} (\sigma_1 + \sigma_3) - \frac{1}{2} (\sigma_1 - \sigma_3) \sin \phi_0 \right] \tan \phi_0}, \quad (8)$$

The thixotropic triaxial shear strength recovery ratio  $K_t$  of the remolded loess at the resting age  $t$  was defined as:

$$K_t = \frac{\tau_{f,t} - \tau_{f,0}}{\tau_{f,u} - \tau_{f,0}} = \frac{(c_t - c_0) + \sigma_t \tan \phi_t - \sigma_0 \tan \phi_0}{(c_u - c_0) + \sigma_u \tan \phi_u - \sigma_0 \tan \phi_0},$$

$$= \frac{2(c_t - c_0) + (\sigma_1 + \sigma_3)(\tan \phi_t - \tan \phi_0) + (\sigma_1 - \sigma_3)(\sin \phi_0 \tan \phi_0 - \sin \phi_t \tan \phi_t)}{2(c_u - c_0) + (\sigma_1 + \sigma_3)(\tan \phi_u - \tan \phi_0) + (\sigma_1 - \sigma_3)(\sin \phi_0 \tan \phi_0 - \sin \phi_u \tan \phi_u)}, \quad (9)$$

The thixotropic cohesion recovery ratio  $L_t$  of the remolded loess at the resting age  $t$  was defined as:

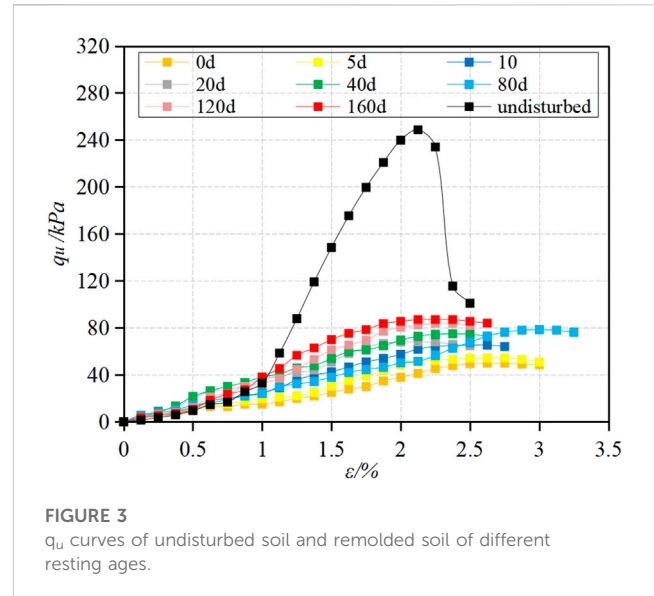
$$L_t = \frac{c_t - c_0}{c_u - c_0}, \quad (10)$$

Where,  $c_t$ ,  $\phi_t$  and  $\tau_{f,t}$  respectively represent the compressive properties of the remolded loess, and the cohesion, friction angle and ultimate shear strength of the samples prepared after  $t$  resting age are obtained by triaxial shear test. Moreover,  $c_0$ ,  $\phi_0$  and  $\tau_{f,0}$  respectively stand for the cohesion, the friction angle and the ultimate shear strength obtained by the triaxial shear test after the remolded loess is compressed and prepared immediately without resting. Also,  $c_u$ ,  $\phi_u$  and  $\tau_{f,u}$  denote the cohesion, the friction angle and the ultimate shear strength of the undisturbed loess obtained by the triaxial shear test, respectively.

## 4 Mechanical test results of thixotropy of loess

### 4.1 Unconfined experimental study on thixotropic properties of loess

Figure 3 shows the unconfined stress-strain curves of the undisturbed and the remolded loess at different resting ages. As can be seen in the figure, an increase in the resting age led to an increase in the unconfined compressive strength of the soil sample. The  $q_u$  of the eight different ages of 0d, 5d, 10d, 20d, 40d, 80d, 120d, and 160d were obtained to be 49.9, 54.5, 65.4, 67.8, 75, 78.5, 83.7, and 87.1 kPa, respectively. Moreover, with the  $q_u$  of the undisturbed loess of 248.7 kPa, the strengths of the eight reconstructive loesses in the resting age were found to be 0.20, 0.22, 0.26, 0.27, 0.30, 0.32, 0.34, 0.35 times that of the undisturbed loess. Furthermore, the  $q_u$  of 160 days was observed



to be 1.75 times greater than that of 0 days. The recovery range of the uniaxial thixotropic strength was also realized to be significant, which suggests considering the influence of thixotropic strength in designing the foundation bearing capacity of loess.

As can be observed in Figure 4, by the substitution of the  $q_u$  of the undisturbed and the remolded loess of different resting ages into Eq. 1, the relationship between the ratio of the unconfined thixal strength recovery  $A_t$  and the resting age can be obtained. Accordingly, the  $A_t$  values of 1.75 were obtained for the resting ages of 160d. It can also be found from Figure 4 that the  $A_t$  curve has a significant growth rate change before and after resting for 40d. In this paper, the point is set as the inflection point of thixotropic strength change. According to the design principle of the thixotropic device, two thixotropic effects of soil particle shape, position adjustment and clay consolidation aggregation will occur inside the structure when the soil is resting, which will increase the strength of the remolded soil. The inflection point of intensity change may be caused by the end of one of the thixotropic effects. It is known that soil particle shape and position adjustments continuously reduce the elastic potential energy generated by compression. Since the total volume of soil remains unchanged, the duration of this process is relatively short, but the flocculation between dispersed clay cements generated by soil remolding will last for a long time, so the inflection point of 40d thixotropic strength change may represent the final dissipation time of the elastic potential energy inside the soil.

The resting 40d,  $A_t$  value is 1.51, which is 86.3% of the resting 160d value. In addition, as shown in Figure 5, the relationship between the unconfined thixotropic strength recovery ratio  $B_t$  and the resting age can be obtained by substituting the  $q_u$  of the undisturbed and the remolded loess of different resting ages into Eq. 2. So, the resting ages of 160d and 40d yielded the  $B_t$  values of 0.187 and 0.127, the former value of which reached 67.9% of that of the latter.



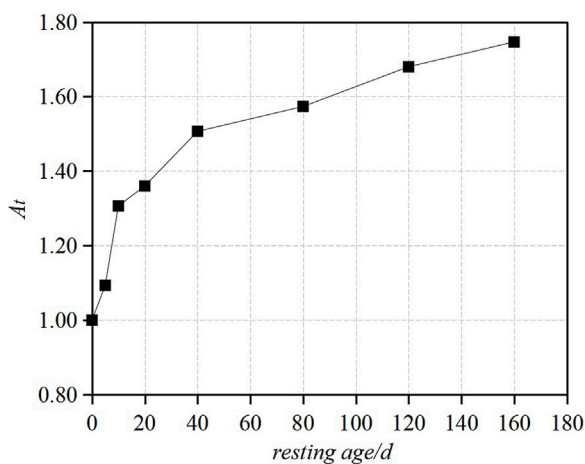


FIGURE 4  
 $A_t$  curve of thixotropic parameters.

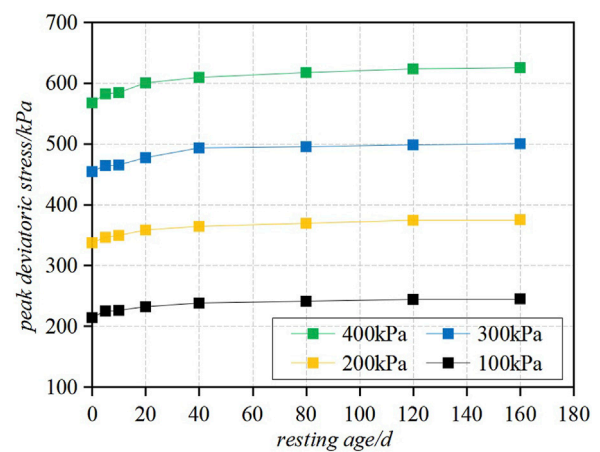


FIGURE 6  
Peak value of deviatoric stress at different resting ages.

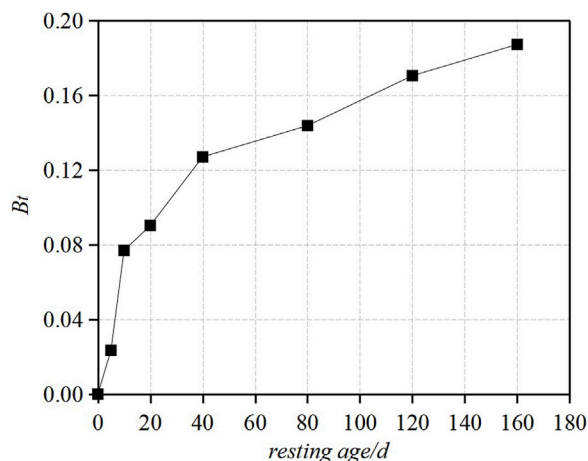


FIGURE 5  
 $B_t$  curve of thixotropic parameters.

## 4.2 Triaxial experimental study on thixotropy of loess

### 4.2.1 Recovery characteristics of peak deviatoric stress with time

According to the obtained results of the triaxial shear tests, both the remolded loess and the undisturbed loess demonstrated plastic failure, the mechanical properties of which were also shear strain hardening. Moreover, the peak value of the deviatoric stress at 15% axial strain was taken as the peak value. The relationship between the peak value of the deviatoric stress  $(\sigma_1 - \sigma_3)_{\max}$  under different confining pressures and different resting ages is shown in Figure 6. As can be observed, while the peak value increased with the growth of the resting age, the growth proportion decreased gradually. Moreover, while the growth rate was observed to be large in the first 40 days, it tended to be gentle between the 40 and 160 days.

Comparing the peak deviatoric stress of the reconstituted loess after 0d and 160d of resting demonstrated the increases of 31, 38, 46, and 58 kPa for the confining pressures of 100, 200, 300, and 400 kPa, respectively. Moreover, the growth rates of the peak deviatoric stress were found to be 14.5%, 11.3%, 10.1%, and 10.2%, respectively. Accordingly, the average of the growth rate at 160d was obtained to be 11.5%. Furthermore, the comparison of the peak value of deviatoric stress of the reconstructed soil samples after resting for 0 day and 40 days showed the increases of 24, 27, 39, and 42 kPa under different confining pressures, which were 11.2%, 8.0%, 8.6%, and 7.4%, respectively. Therefore, the average absolute growth rate of 40d was calculated to be 8.8%, which is 76.5% of the growth rate of 160d.

Under different confining pressures, the different values of the peak deviatoric stress between the undisturbed and the remolded loess at 0 days were 66, 86, 114, and 129 kPa, respectively. However, compared with the undisturbed loess, the peak recovery ratio of deviatoric stress was 47.0%, 44.2%, 40.4%, and 45.0% at 160d, respectively, with an average recovery ratio of 44.2%. Moreover, the peak recovery ratio of the deviatoric stress was 36.4%, 31.4%, 34.2%, and 32.6%, for 40d of resting respectively. In other words, with the average recovery ratio of 33.7%, it reached 76.1% of the recovery ratio at 160d. Therefore, 40 days of resting age can be considered as the inflection point of change time for recovery of peak deviatoric stress thixotropic strength of loess.

### 4.2.2 Recovery characteristics of strength parameters $c$ and $\varphi$ with time

Using triaxial CU tests, the peak values of deviatoric stress  $(\sigma_1 - \sigma_3)_{\max}$  of the soil samples were obtained under different confining pressures. Subsequently, plotted as Mohr circle shear strength inclines. The cohesion  $c$  and friction Angle  $\varphi$  of the unaltered and the remolded loess were also obtained at different resting ages. Accordingly, the values of  $c$  and  $\varphi$  of the unaltered loess were obtained to be 46.3 kPa and 24.2°. Moreover, the variation curves of  $c$  and  $\varphi$  of the remolded loess are shown in Figures 7, 8. Furthermore, an increase in the resting age was observed to lead to an increase in the cohesion. The increase was also found to be large

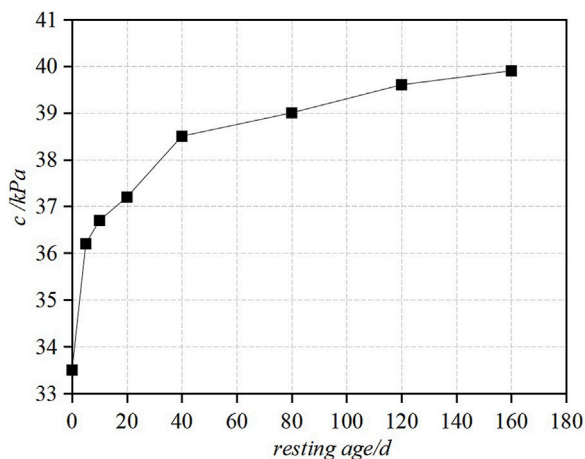


FIGURE 7  
Curve of cohesion.

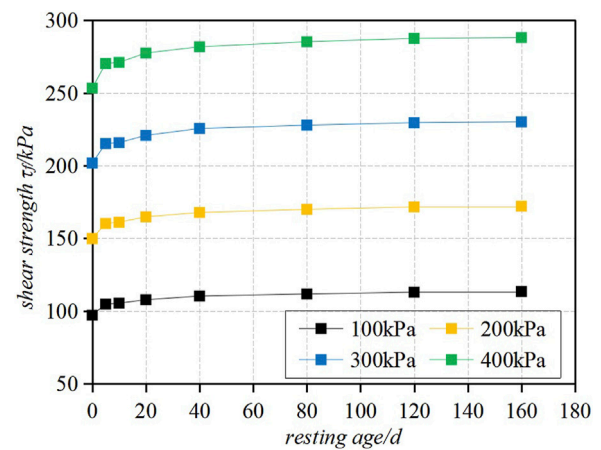


FIGURE 9  
Shear strength curves of remolded soil at different ages.

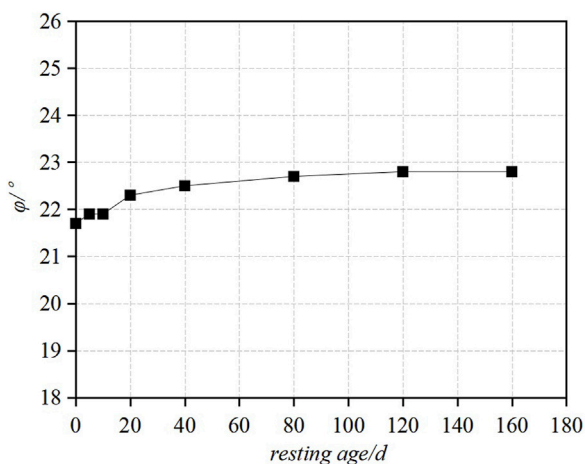


FIGURE 8  
Curve of angle of friction.

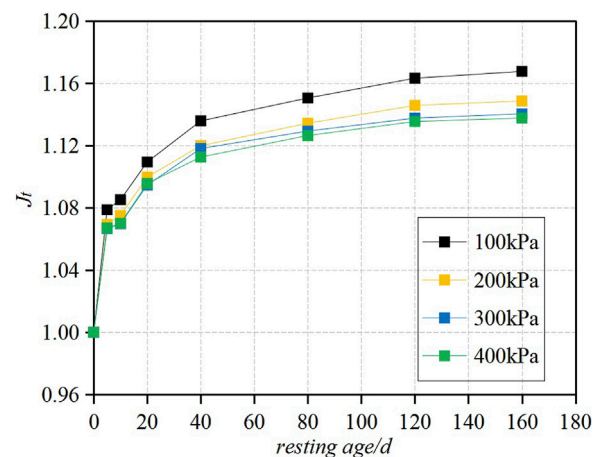


FIGURE 10  
 $J_t$  curve of thixotropic parameters.

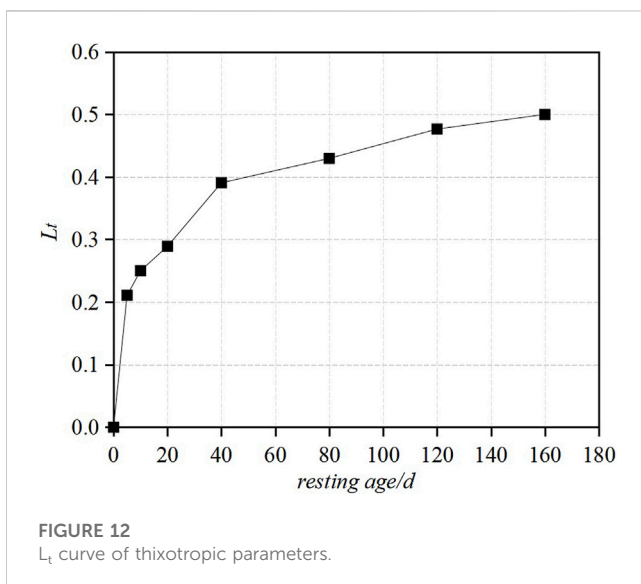
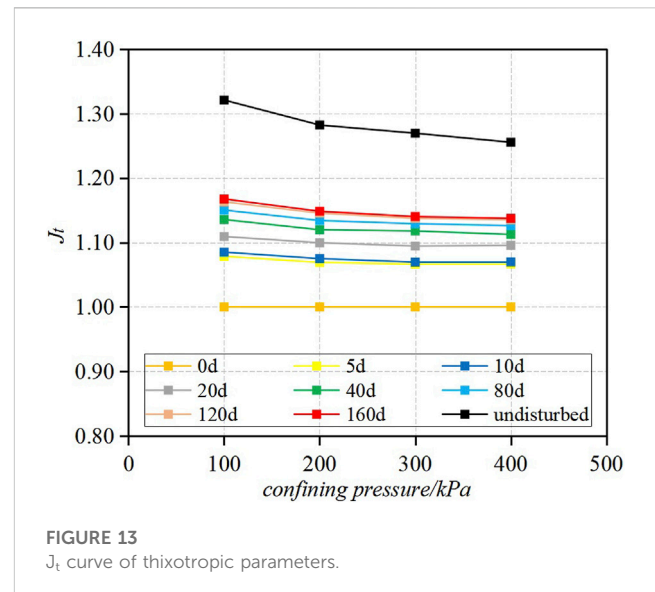
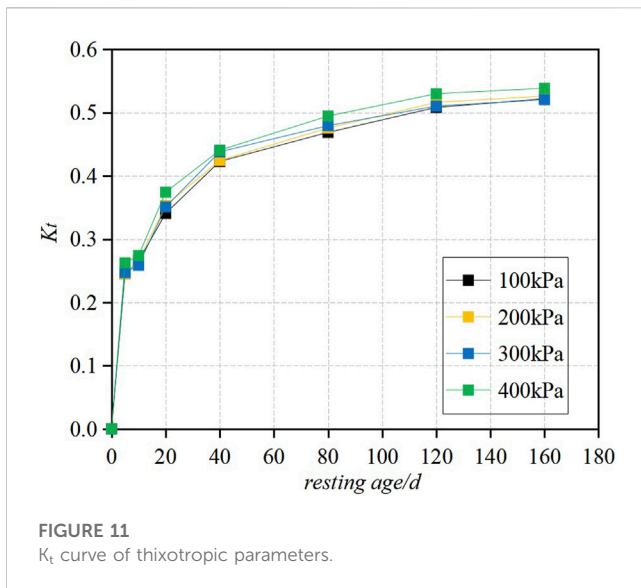
in the first 40d, with the strength increasing by about 5.0 kPa. In addition, while the increase rate tended to be gentle from 40 to 160d, with the intensity increasing by about 1.4 kPa, the increase in the friction angle  $\phi$  was found to be gentle, i.e., only  $1.1^\circ$  which tended to be stable. The  $c$  and  $\phi$  values of the undisturbed loess were found to be greater than those of the remolded loess, the difference between which at 160d was observed to be 6.4 kPa and  $1.4^\circ$ , respectively.

#### 4.2.3 Recovery characteristics of loess thixotropic parameters with time

As can be seen in Figure 9, the shear strength index was substituted into Eq. 7 to obtain the triaxial shear strength of the remolded loess at different resting ages and under various confining pressures. Subsequently, as shown in Figures 10–12, the  $J_t$ ,  $K_t$  and  $L_t$  were obtained by substituting the index into Eqs 8–10, respectively.

As can be seen, all the three thixotropic parameters demonstrated increasing trends with the growth of the setting age, with a large increase in the first 40d and a gradual one in 40–160d.

Moreover, the confining pressures of 100, 200, 300, and 400 kPa demonstrated the difference of 16.3, 22.3, 28.4, and 34.8 kPa in the shear strength between the reconstituted loess at 0d and 160d, respectively. Also, compared with 0d, the cohesion of the remold loess was found to increase by 6.4 kPa after resting for 160d. According to Eq. 3, the friction force also increased by 9.9, 15.9, 22, and 28.4 kPa under different confining pressures. In such conditions, the contribution ratios of the cohesion and the friction in increasing the shear strength were found to be 39.3% and 60.7%, 28.7% and 71.3%, 22.5% and 77.5%, and 18.4% and 81.6%, respectively. Moreover, despite the increase of the friction Angle being much smaller than that of the cohesion, due to the



larger normal stress on the shear surface, the contribution ratio of the former was observed to be much greater in increasing the shear strength than that of the latter.

In addition, the  $J_t$  ratios of thixotropic triaxial shear strength were found to be 1.17, 1.15, 1.14, and 1.14, respectively, with the average increase ratio of 15% at the 160d resting; the increase ratio is also obvious, indicating that the actual bearing capacity of the foundation with thixotropic strength recovery is higher than that of the foundation only considering the consolidation factor. When the calculated value is less than the actual value, the engineering design load is often conservative. Moreover, the comparison of the shear strength of the remolded soil samples resting at 0d and 40d revealed the stress to be increased under different confining pressures for 13.2, 18.0, 23.9, and 28.5 kPa, respectively. The thixotropic shear strength ratio  $J_t$  was also found to be 1.14, 1.12, 1.12, and 1.11, respectively. Accordingly, the average increase rate of the absolute

shear strength was revealed to be 12.3% at the 40d resting, which suggests reaching 82% that of resting at 160d.

Under different confining pressures, the triaxial shear strength difference between the undisturbed and the reconstituted loess was observed to be 31.2, 42.3, 54.4, and 64.7 kPa, respectively. Moreover, with an average of 0.527, the recovery ratio of the thixotropic triaxial shear strength at 160d was found to be 0.522, 0.526, 0.521, and 0.539, respectively. Furthermore, with an average value of 0.432,  $K_t$  was discovered to be 0.423, 0.424, 0.438, and 0.441 under different confining pressures after resting for 40 days, respectively, which was 82% of the growth rate after 160 days of resting. In addition, the thixotropic cohesion recovery ratio  $L_t$  was found to be 0.5 and 0.39 after resting for 160d and 40d, respectively; i.e., the latter being 78% of the former.

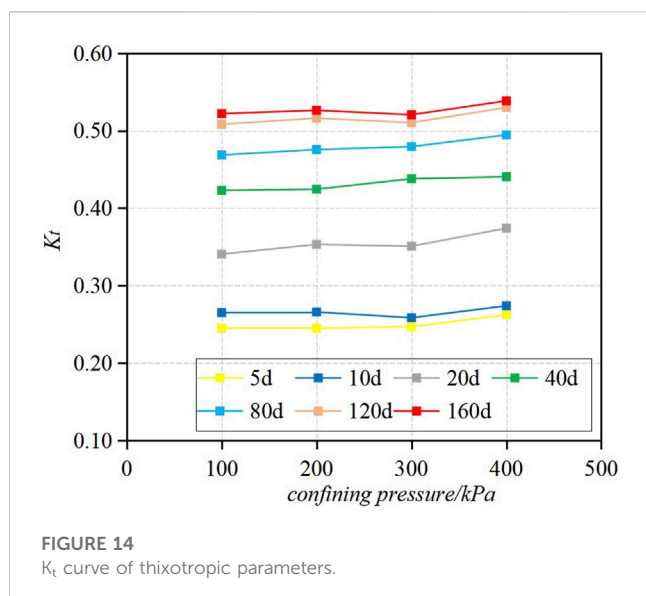
Comparing the results of  $J_{160}$  and  $J_{40}$ ,  $K_{160}$  and  $K_{40}$ , and  $L_{160}$  and  $L_{40}$ , the resting age of 40 days can be argued as the time inflection point of shear strength thixotropic properties of loess.

#### 4.2.4 Recovery characteristics of loess thixotropic parameters with confining pressure

The change curves of  $J_t$  and  $K_t$  are shown in Figures 13, 14. As can be seen, with the growth of the confining pressure, all of the  $J_t$  values demonstrated a downward trend at different resting ages. In other words, the larger the resting age is, the faster the downward trend becomes. This indicates that not only the growth rate of shear strength of soil decreased with an increase in the resting age, it also decreased with an increase in the confining pressure and the buried depth. Furthermore, while the  $K_t$  value of different resting ages was found to be positively correlated with the increase in the confining pressure, no significant relationship was observed with the development of resting age.

#### 4.2.5 Comparison of uniaxial compression and triaxial shear test results

According to the results of the thixotropic mechanics test, it can be found that the growth ratio of thixotropic strength under uniaxial



compression is much higher than that under triaxial test. This is because in uniaxial compression, there is no confining pressure, and the compressive strength mainly comes from the structural strength provided by the cohesion force. In the triaxial test, the confining pressure provides a lot of friction, which makes the structural strength relatively high compared with the unconfined test. When the micro-structure bonding caused by thixotropy increases the cohesion, the increase ratio of the cohesion in uniaxial compression is higher, but due to the participation of friction in triaxial test, the increase ratio of cohesion is relatively small.

## 5 Conclusion

A resting thixotropic instrument with the ability to maintain constant volume pressure was developed in the present study. The developed device was also capable of distinguishing the thixotropic strength from the variable growth strength of the consolidated body. During the resting process of the soil sample, the external pressure was not unloaded and the sample did not undergo consolidation volume deformation. Accordingly, the strength variation of the soil sample was argued to be only caused by thixotropy, and so, excluding the strength increase of the consolidated body.

Based on the unconfined compressive strength, the thixotropic strength ratio  $A_t$  and the thixotropic strength recovery ratio  $B_t$  were compared and defined. Accordingly, the thixotropic triaxial shear strength ratio  $J_t$ , thixotropic triaxial shear strength recovery ratio  $K_t$  and thixotropic cohesion recovery ratio  $L_t$  were introduced. Moreover, the introduced ratios were expressed the changes in shear strength and cohesion of loess during thixotropic process under complex stress state.

Xi'an loess was found to demonstrate obvious thixotropic characteristics. In line with this, an increase in the resting age was observed to lead to a significant increase in the unconfined compressive strength, peak deviator stress, shear strength and cohesion. Moreover, while the increase in the friction Angle was observed to be much smaller than that of the cohesion, the ratio of

friction in increasing the of shear strength was found to be much larger than that of the cohesion. In addition, an increase in the resting age was revealed to decrease the overall growth rate of the strength. The resting age of 160d was also resulted in the  $A_t$ ,  $B_t$ , the growth ratio of eccentric stress strength,  $J_t$ ,  $K_t$  and  $L_t$  to be 1.75, 0.187, 0.12, 0.15, 0.527, and 0.5, respectively. Accordingly, it can be argued that, in order to avoid conservatism when calculating the bearing capacity of the loess foundation, the influence of thixotropic strength needs to be considered.

Compared with 160d, uniaxial compressive thixotropic strength ratio  $A_t$ , the uniaxial compression thixotropic recovery strength ratio  $B_t$ , and the mean peak eccentricity stress of the Xi'an loess were shown to reach 86.3%, 67.9%, and 76.1% at the resting age of 40d, respectively. The shear strength ratio  $J_t$ , the shear strength recovery ratio  $K_t$  and the cohesion recovery ratio  $L_t$  were also found to reach 78%, 82%, and 82%, respectively. Therefore, the 40 days of resting age can be argued to be considered as the time inflection point of the loess thixotropic strength change. Furthermore, an increase in the confining pressure was observed to lead to a decrease in the thixotropic shear strength ratio ( $J_t$ ). This is while the decreasing range increased as the result of increasing the resting age. Finally, while the recovery ratio of thixotropic shear strength ( $K_t$ ) increased with increasing the confining pressure, no significant correlation was found with increasing the resting age.

## Data availability statement

The original contributions presented in the study are included in the article/Supplementary Material, further inquiries can be directed to the corresponding author.

## Author contributions

All authors listed have made a substantial, direct, and intellectual contribution to the work and approved it for publication.

## Acknowledgments

The authors are grateful to the financial support from the National Natural Science Foundation of China (51979225, 52078421, 42007264, and 51909204), the National Natural Science Foundation Youth Foundation (52009107), the China Postdoctoral Science Foundation (2019M663943XB), the Natural Science Basic Research Program of Shaanxi (2022JM-216), the Shaanxi Province Key Research and Development Plan Project (2022ZDLSF07-02), and the Shaanxi Provincial Department of Education Key Laboratory Project (20JS091).

## Conflict of interest

The authors declare that the research was conducted in the absence of any commercial or financial relationships that could be construed as a potential conflict of interest.



## Publisher's note

All claims expressed in this article are solely those of the authors and do not necessarily represent those of their affiliated

organizations, or those of the publisher, the editors and the reviewers. Any product that may be evaluated in this article, or claim that may be made by its manufacturer, is not guaranteed or endorsed by the publisher.

## References

- Andersen, K. H., and Jostad, H. P. (2002). "Shear strength along outside wall of suction anchors in clay after installation," in *The Twelfth International Offshore and Polar Engineering Conference*, Kitakyushu, Japan, May 26–31, 2002.
- ASTM (2014). *ASTM d653-14: Standard terminology relating to soil, rock, and contained fluids*. West Conshohocken, PA, USA: ASTM International.
- Boswell, P. G. H. (1948). A preliminary examination of the thixotropy of some sedimentary rocks. *Q. J. Geol. Soc.* 104 (1–4), 499–526. doi:10.1144/gsl.jgs.1948.104.01-04.23
- Burgers, J. M., and Blair, G. W. S. (1949). *Report on the principles of rheological nomenclature*. Amsterdam: North-Holland Publishing Company, International Council of Scientific Unions. Joint Committee on Rheology.
- Cabrera, J. G., and Smalley, I. J. (1973). Quickclays as products of glacial action: a new approach to their nature, geology, distribution and geotechnical properties. *Eng. Geol.* 7 (2), 115–133. doi:10.1016/0013-7952(73)90041-0
- Cronin, S. J., Neall, V. E., Lecointre, J. A., and Palmer, A. S. (1999). Dynamic interactions between lahars and stream flow: a case study from ruapehu volcano, New Zealand. *Geol. Soc. Am. Bull.* 111 (1), 28–38. doi:10.1130/0016-7606(1999)111<0028:diblas>2.3.co;2
- Díaz-Rodríguez, J. A., and Santamarina, J. C. (1999). "Thixotropy: the case of Mexico city soils," in XI Panamerican Conf. on Soil Mech. and Geotech. Eng. Foz Do Iguassu, Brazil, August 08–12, 1999, 441–448.
- Frydman, S., Talesnick, M., Geffen, S., and Shvarzman, A. (2007). Landslides and residual strength in marl profiles in Israel. *Eng. Geol.* 89 (1–2), 36–46. doi:10.1016/j.enggeo.2006.09.009
- Hu, W., Xu, Q., Wang, G., Scaringi, G., Mcsaveney, M., and Hicher, P. Y. (2017). Shear resistance variations in experimentally sheared mudstone granules: a possible Shear thinning and thixotropic mechanism. *Geophys. Res. Lett.* 44 (21), 11–040. doi:10.1002/2017gl075261
- Iwase, H., Kubota, M., Itoh, T., Ogura, T., Ebina, T., Ohtani, H., et al. (2021). Direct observation of the relationship between thixotropic behavior and shear-induced orientation of clay particles in synsthetic hectorite suspensions. *Langmuir* 37 (21), 6435–6441. doi:10.1021/acs.langmuir.1c00404
- Jiang, H., Mu, J., Zhang, J., Jiang, Y., Liu, C., and Zhang, X. (2022). Dynamic evolution in mechanical characteristics of complex supporting structures during large section tunnel construction. *Deep Undergr. Sci. Eng.* 1 (2), 183–201. doi:10.1002/dug2.12027
- Kerr, P. F., and Drew, I. M. (1968). Quick-clay slides in the USA. *Eng. Geol.* 2 (4), 215–238. doi:10.1016/0013-7952(68)90001-x
- Khalidoun, A., Moller, P., Fall, A., Wegdam, G., De Leeuw, B., M'heust, Y., et al. (2009). Quick clay and landslides of clayey soils. *Phys. Rev. Lett.* 103 (18), 188301. doi:10.1103/physrevlett.103.188301
- Krupt, H. R. (1952). *Colloid science, I, Irreversible systems*. Amsterdam, Houston, New York, London: Elsevier.
- Liu, J., Xue, Y., Fu, Y., Yao, K., and Liu, J. (2023). Numerical investigation on microwave-thermal recovery of shale gas based on a fully coupled electromagnetic, heat transfer, and multiphase flow model. *Energy* 263, 126090. doi:10.1016/j.energy.2022.126090
- Mainsant, G., Chambon, G., Jongmans, D., Larose, E., and Baillet, L. (2015). Shear-wave velocity drop prior to clayey mass movement in laboratory flume experiments. *Eng. Geol.* 192, 26–32. doi:10.1016/j.enggeo.2015.03.019
- Mitchell, J. K. (1961). "Fundamental aspects of thixotropy in soils," in *Transactions of the American Society of Civil Engineers* 126 (1), 1586–1620.
- Osipov, V. I., Nikolaeva, S. K., and Sokolov, V. N. (1984). Microstructural changes associated with thixotropic phenomena in clay soils. *Geotechnique* 34 (3), 293–303. doi:10.1680/geot.1984.34.3.293
- Park, D., Kutter, B. L., and DeJong, J. T. (2014). Effects of thixotropy and cement content on the sensitivity of soft remolded clay. *J. Geotech. Geoenviron.* 141 (2), 04014095. doi:10.1061/(asce)gt.1943-5606.0001221
- Peng, J., Luo, S., Wang, D., Cao, Y., DeGroot, D. J., and Zhang, G. (2022). Multiple thixotropisms of liquid limit–consistency clays unraveled by multiscale experimentation. *J. Geotechnical Geoenvironmental Eng.* 148 (1), 04021165. doi:10.1061/(asce)gt.1943-5606.0002705
- Peterfi, T. (1927). *Arch. Entwicklungsmech. Organ* 112, 660–695. doi:10.1007/bf02253780
- Ren, Y., Yang, S., Andersen, K. H., Yang, Q., and Wang, Y. (2021). Thixotropy of soft clay: a review. *Eng. Geol.* 287, 106097. doi:10.1016/j.enggeo.2021.106097
- Ren, Y., Yang, S., Zhang, S., Yang, Q., Wang, Y., He, B., et al. (2022). Experimental study of the thixotropic strength recovery and microstructural evolution of marine clays. *J. Geotechnical Geoenvironmental Eng.* 148 (8), 04022059. doi:10.1061/(asce)gt.1943-5606.0002833
- Rinaldi, V. A., and Clari, J. J., Jr. (2016). Time dependent stress–strain behavior of bentonite slurries; effect of thixotropy. *Powder Technol.* 291, 311–321. doi:10.1016/j.powtec.2015.12.036
- Romanov, S. V., and Romanov, D. A. (1997). Procedure for impressing reinforced-concrete piles into leader holes using soil thixotropy. *Soil Mech. Found. Eng.* 34 (1), 22–24. doi:10.1007/bf02465085
- Salam, M. A., Simms, P. H., and Örmeci, B. (2023). Ageing/thixotropy effects on strength and compressibility in Leda clay and polymer-amended clayey tailings. *Eng. Geol.* 317, 107088. doi:10.1016/j.enggeo.2023.107088
- Seng, S., and Tanaka, H. (2012). Properties of very soft clays: a study of thixotropic hardening and behavior under low consolidation pressure. *Soils Found.* 52 (2), 335–345. doi:10.1016/j.sandf.2012.02.010
- Skempton, A. W., and Northey, R. D. (1952). The sensitivity of clays. *Geotechnique* 3 (1), 30–53. doi:10.1680/geot.1952.3.1.30
- Solonenko, V. P. (1977). Les glissements de terrains et les effondrements dans les regions seismiques leur prediction. *Bull. Int. Assoc. Eng. Geol.* 15 (1), 4–8. doi:10.1007/bf02592633
- Tang, B., Zhou, B., Xie, L., and Yin, J. (2021). Evaluation method for thixotropy of clay subjected to unconfined compressive test. *Front. Earth Sci.* 9, 683454. doi:10.3389/feart.2021.683454
- Xue, Y., Liu, J., Liang, X., Li, X., Wang, S., Ma, Z., et al. (2023). Influence mechanism of brine-gas two-phase flow on sealing property of anisotropic caprock for hydrogen and carbon energy underground storage. *Int. J. Hydrogen Energy* 48 (30), 11287–11302. doi:10.1016/j.ijhydene.2022.05.173
- Xue, Y., Liu, S., Chai, J., Liu, J., Ranjith, P. G., Cai, C., et al. (2023). Effect of water-cooling shock on fracture initiation and morphology of high-temperature granite: application of hydraulic fracturing to enhanced geothermal systems. *Appl. Energy* 337, 120858. doi:10.1016/j.apenergy.2023.120858
- Xue, Y., Ranjith, P. G., Gao, F., Zhang, Z., and Wang, S. (2023). Experimental investigations on effects of gas pressure on mechanical behaviors and failure characteristic of coals. *J. Rock Mech. Geotechnical Eng.* 15 (2), 412–428. doi:10.1016/j.jrmge.2022.05.013
- Yang, S., and Andersen, K. H. (2016). Thixotropy of marine clays. *Geotech. Test. J.* 39 (2), 20150020–20150339. doi:10.1520/gtj20150020
- Yang, Z., Qi, W., Ding, Y., Jiang, Y., Yang, X., Yang, X., et al. (2023). Numerical investigation on the spewing mechanism of earth pressure balance shield in a high-pressure water-rich sand stratum. *Deep Undergr. Sci. Eng.* 2 (1), 74–87. doi:10.1002/dug2.12032
- Yenes, M., Monterrubio, S., Nespereira, J., and Casas, D. (2020). Apparent overconsolidation and its implications for submarine landslides. *Eng. Geol.* 264, 105375. doi:10.1016/j.enggeo.2019.105375
- Zhang, X. W., Kong, L. W., Yang, A. W., and Sayem, H. M. (2017). Thixotropic mechanism of clay: a microstructural investigation. *Soils Found.* 57 (1), 23–35. doi:10.1016/j.sandf.2017.01.002



## OPEN ACCESS

## EDITED BY

Liang Chen,  
China University of Mining and  
Technology, China

## REVIEWED BY

Zhenlong Song,  
Southern University of Science and  
Technology, China  
Jiarui Chen,  
Huaiyin Institute of Technology, China

## \*CORRESPONDENCE

Fanling Dang

✉ dangfn@163.com

Zhengzheng Cao

✉ caozz2008@126.com

RECEIVED 19 June 2023

ACCEPTED 25 July 2023

PUBLISHED 05 September 2023

## CITATION

Wei L, Dang F, Ding J, Wu X, Li J and  
Cao Z (2023) An analysis of thixotropic  
micropore variation and its mechanism  
in loess.

*Front. Ecol. Evol.* 11:1242462.  
doi: 10.3389/fevo.2023.1242462

## COPYRIGHT

© 2023 Wei, Dang, Ding, Wu, Li and Cao.  
This is an open-access article distributed  
under the terms of the [Creative Commons  
Attribution License \(CC BY\)](#). The use,  
distribution or reproduction in other  
forums is permitted, provided the original  
author(s) and the copyright owner(s) are  
credited and that the original publication in  
this journal is cited, in accordance with  
accepted academic practice. No use,  
distribution or reproduction is permitted  
which does not comply with these terms.

# An analysis of thixotropic micropore variation and its mechanism in loess

Le Wei<sup>1</sup>, Fanling Dang<sup>1\*</sup>, Jiulong Ding<sup>1</sup>, Xiaojuan Wu<sup>1</sup>,  
Jiayang Li<sup>1</sup> and Zhengzheng Cao<sup>2\*</sup>

<sup>1</sup>Xi'an Key Laboratory of Environmental Geotechnical Engineering of Loess Plateau, Xi'an University of Technology, Xi'an, China, <sup>2</sup>School of Civil Engineering, Henan Polytechnic University, Jiaozuo, Henan, China

The relationship between the thixotropic mechanism and the macroscopic thixotropic strength can be clarified by analyzing the changes in microstructure and pores in the loess thixotropic process. This approach is of significant importance for calculating the strength of compacted loess foundations. In the present study, a representative sample prepared from Xi'an loess was analyzed and eight resting ages were set. The micropore characteristics of the remolded loess and undisturbed loess at different resting ages were obtained using electron microscope observation and nuclear magnetic resonance testing. The results indicate that the thixotropy in the prepared loess samples is significant. It is also found that as the resting age grew, newly formed cements in the remolded loess continuously accumulated and filled in the microcracks between the aggregates. Consequently, the contact area of aggregates increased, thereby decreasing the width and length of the microcracks. The proportion of cementation pore and small microcracks gradually increased, while the proportion of large microcracks gradually decreased, indicating that thixotropy increased the cohesive force and friction force of soil structure at the mesoscale. This phenomenon also explains the increase of thixotropic strength at the macroscopic scale. The mesoscopic mechanism of loess thixotropic strength recovery is that the connection between soil particles is re-established after the break of the clay particle–water–charge system. Moreover, the elastic potential energy of soil particles generated by compression promoted the polymerization of clay particles dispersed in a pore water solution to produce flocculating aggregates during resting dissipation. The continuous consumption of clay particles expanded the processing time and flocs and continuously decreased the strength growth rate.

## KEYWORDS

loess, thixotropy, microscopic, microcrack, cementation

## 1 Introduction

Geological surveys indicate the widespread presence of large and thick loess strata in northern China. With the rapid economic development in the past few decades, numerous construction activities are under process on these loess foundations. Furthermore, recent economic developments have led to the rapid expansion of most cities. It is worth noting that some cities are located in loess gully mountain areas, wherein conducting mountain

digging and trench-filling projects is an enormous challenge to provide space for expansion. The excavated area in the loess foundation consists of undisturbed loess that has undergone millions of years of natural deposition. As a result, the strength of the loess foundation is typically high and stable. This allows for an accurate assessment of the bearing capacity of the foundation, ensuring the safety and stability of construction projects conducted in the area. However, the excavated area has a remolded loess foundation so its strength is far lower than that of the undisturbed loess foundation even after rolling and ramming processes, which are typically carried out to compact the area. Moreover, an area with a large fill thickness usually has long-term post-construction settlement, which is generally shelved for many years. Some underground space projects with lower loads may be constructed, such as underground warehouses or energy storage facilities (Xue et al., 2023a; Xue et al., 2023b). During the shelving of the foundation, while the soil settles and deforms, various coupling effects such as soil water pressure and geothermal energy can also occur, affecting the strength of the foundation soil (Liu et al., 2023; Yang et al., 2023). These coupling effects also affect the structural stability of underground space engineering during shelving (Jiang et al., 2022; Xue et al., 2023c). During the period of foundation shelving, the bearing capacity of the foundation increases continuously. This may be attributed to two primary reasons: creep consolidation and thixotropy of loess. Creep consolidation refers to the long-term compaction of loess, leading to an increase in the strength of the soil structure. Thixotropy, on the other hand, relates to the strengthening of chemical composition cementation within the soil structure when the soil body does not change. While there have been numerous studies on the consolidation of loess, further investigations are needed to better understand the thixotropy of loess.

The term “thixotropy” was initially coined by Peterfi (1927) to describe the interconversion of colloidal solutions between fluid and elastic solids. Since then, the concept of thixotropy has been widely used in the field of geotechnical materials to describe the gradual increase in soil strength over time after reshaping disturbance by Burgers and Blair (1949). Boswell (1948) conducted a study on thixotropic materials in various soils and found that except for pure sand lacking fine particles, geotechnical materials exhibit different degrees of thixotropy. A review of the literature reveals that the internal mechanism of the thixotropic process has been extensively analyzed. For example, Mitchell (1961) conducted experiments and demonstrated that the thixotropic effect of the soil–water mixture on the spacing of soil particles is much greater than that of chemical composition. Zhang et al. (2017) studied the thixotropy of Zhanjiang soft clay and indicated that variations in the internal force field of the soil affect the pore structure between particles, thereby affecting the strength of the soil over the resting ages. Day (1954) carried out experimental investigations and revealed that when the soil is disturbed, the internal energy and stress state of the structure changes over time. Accordingly, Mitchell (1961) proposed a new theoretical hypothesis for soil thixotropy, pointing out that thixotropy is a structural effect that relates to the arrangement of soil

particles, pore water distribution, and ion content. Furthermore, it was found that energy within the structure consistently dissipates during thixotropy. Díaz-Rodríguez and Santamarina (1999) indicated that the essential thixotropy mechanism originates from changes in the internal energy of soil, chemical reactions between minerals, mechanical loads, and transmission of electrons within the microstructure. Blake and Gilman (1970) and Rinaldi and Clari’ a (2016) indicated that when soil is disturbed, chemical bonds between particles are broken and the system enters a dispersed state. In this case, the repulsive force between soil particles exceeds the gravitational force, and the internal energy slightly strengthens. As energy is partially dissipated and the gravitational force surpasses the repulsive force, the energy level of the soil–water–electric system decreases, and dispersed particles fluctuate in the soil.

The thixotropic model has been gradually proposed and applied to calculate the strength of rock and soil materials. Dexter et al. (1988) proposed a simplified thixotropic model of the number of bonds between soil particles over time. At a resting age of 0d, the soil failure strength is related to the force and the corresponding failure surface area when the bond number between particles is broken. At the resting ages  $t$ , the structure strength is enhanced by the formation of new bonds between soil particles due to thixotropy, and the formation of new bonds is independent of compaction. Doglioni and Simeone (2013) pointed out that when soil is subjected to high effective stress, the position and shape of soil particles are not easy to change due to the restriction of neighboring particles. Heymann et al. (1996) proposed another model of thixotropic behavior change related to yield strength change, pointing out that thixotropic strength is an exponential function related to different material properties. Abu-Farsakh et al. (2015) introduced a time-dependent reduction parameter  $\beta$  into the thixotropic strength calculation formula proposed by Heymann et al., it is introduced into the finite element model to simulate the increase of soil thixotropic strength around the pile before and after thixotropic change. The calculated results are close to those of the instrument pile load test. In addition, some scholars have studied the thixotropy of geotechnical materials by using thixotropy models such as viscosity, viscoelasticity or viscoplasticity of suspension or gel (Barnes, 1997; Dullaert and Mewis, 2006; de Souza Mendes, 2009).

The thixotropic theory has been verified using advanced testing techniques. In this regard, Zhang et al. (2017) evaluated this theory by studying the microscopic thixotropy mechanism in Zhanjiang soft clay using electron microscopy observation and mercury injection tests. Osipov et al. (1984) utilized a rotating viscometer, analyzed changes in the microstructure of thixotropic soil before and after vibration, and indicated that relatively uniform and dispersed micro-cracks form in the soil during vibration. It was found that when the soil is under vibration, the size of micro-aggregates gradually increases over time, the pore size increases and the soil structure develops to the initial state. Jacobsson and Pusch (1972) studied the thixotropy of quick-clays using transmission electron microscopy, microsection, and nuclear spin echo. It was found that thixotropic structure recovery is related to the

reorientation of small particles and changes in pore water solution. [Aminpour \(2019\)](#) performed numerical simulations based on multifunctional molecular dynamics, explored the interaction between soil particles over time, and clarified the relationship between clay thixotropy at the macro- and micro-levels. Although significant progress has been made in understanding the microscopic characteristics of thixotropic, the existing technologies have some shortcomings. For example, scanning electron microscopy (SEM) may not accurately capture the exact location of the sample, and the mercury injection pore method can damage the sample structure. To address these challenges, environmental scanning electron microscopy (ESEM) and computed tomography (CT) were proposed ([Gagnoud et al., 2008](#); [Pardo et al., 2019](#); [Sun et al., 2019](#); [Sun et al., 2020](#)).

The relationship between mineral composition and thixotropic micromechanical properties of soil has also been explored extensively. [Skempton and Northey \(1952\)](#) studied the thixotropy of different clay minerals and found that bentonite exhibits the most pronounced structural change in a short time. This may be attributed to the high thixotropy nature of bentonite, while Illite has low thixotropy and kaolin has almost no thixotropy. Similar results were also obtained by [Shahriar et al. \(2018\)](#). [Jeong et al. \(2012\)](#) conducted experiments and found that higher soil activity corresponds to more prominent thixotropy. Furthermore, [Shahriar et al. \(2018\)](#) carried out thixotropic mechanical tests on six types of clay and found that the stronger the soil activity at resting ages of 1d and 8d, the greater the thixotropic-induced increases in strength. [Abdou and Ahmed \(2013\)](#) demonstrated that the thixotropic degree is positively correlated with soil activity by adjusting the bentonite content. [Andersen et al. \(2008\)](#) analyzed the thixotropic test data and revealed a correlation between the strength and activity level of the soil. [Zhang et al. \(2017\)](#) carried out experiments and demonstrated that highly active minerals have a larger specific surface area, which can increase more cationic exchange capacity and charge quantity to enhance thixotropy.

Additionally, the effect of salt concentration of pore water on the degree of thixotropy has been explored in detail. In this context, [Jeong et al. \(2012\)](#) studied the relationship between salt concentration and thixotropy in clay with high montmorillonite content and revealed that salt concentration significantly affects yield stress and plastic viscosity. [Lu et al. \(1991\)](#) found that soil samples made with fresh water exhibit slightly higher thixotropic strength compared to those made with salt water. [Perret et al. \(1996\)](#) prepared mud samples with different salt concentrations ranging from 0.1 to 30 g/L and found that samples with low salinity exhibit higher thixotropy. Similarly, [Abdou and Ahmed \(2013\)](#) prepared bentonite mud samples with different salt concentrations and found that low salt concentration results in high thixotropy, while high salt concentration leads to almost no thixotropy. [Olphen \(1977\)](#) demonstrated that high salt concentration in pore water may change the thickness of the double electric layer between soil particles, thereby reducing the interaction attraction between soil particles, and reducing the thixotropy. [Perret et al. \(1996\)](#) carried out experiments and indicated that when the salt concentration is

low, the bond energy between soil particles is strong. This phenomenon induces flocculation, thereby increasing the thixotropy degree.

The performed literature survey highlights a gap in the research on thixotropy specifically in loess samples. Most studies have focused on clay and mud samples, while there are limited in-depth investigations on the thixotropy behavior of loess. Moreover, studies on the thixotropic mechanism have prominently explored the micro level and the relationship between soil particles has been analyzed extensively. However, the transition relationship of thixotropy from micro-scale to macro-mechanical strength improvement cannot theoretically support the calculation of the bearing capacity of the remolded loess foundation, and further investigation is required in this area. Aiming at resolving these shortcomings, the present study utilized the electron microscopy technique to observe the mesoscopic void changes of the undisturbed and remolded loess of different resting ages at low multiples. Moreover, nuclear magnetic resonance technology was used to observe the aperture distribution proportions of the undisturbed and remolded loess of different resting ages at different scales to analyze the relationship between the thixotropy of loess and the changes in mesoscopic pores. The main objective of this article was to clarify the thixotropic mechanism of loess at mesoscopic scales. The results are expected to provide a basis for further understanding of the growth of macro-scale strength. Meanwhile, it is intended to propose an expression for the growth of macro-scale strength caused by the thixotropy-induced changes in the mesostructure of loess.

## 2 Test samples and the analysis method

### 2.1 Test soil sample

The test samples were prepared from a construction site 1km north of the North Wall of Weiyang District, Xi'an, Shaanxi Province, China. It was Q<sub>2</sub> loess with a depth of 10–12m. The physical properties of the soil sample are presented in [Table 1](#), the chemical composition and classification of the soil sample particles are presented in [Table 2](#), the concentration of different cements in the soil sample (%) are presented in [Table 3](#).

### 2.2 Test methods and sample preparation

To study the relationship between the microstructural changes and the macroscopic thixotropic strength of loess during the thixotropic process and analyze the variations in the microstructural mechanism of the thixotropic strength, the microstructure of the undisturbed and remolded loess samples was analyzed after resting for 0d, 5d, 10d, 20d, 40d, 80d, 120d, and 160d. Electron microscopy (SEM) was utilized to observe the soil structure and pore morphology at different scales, and nuclear magnetic resonance (NMR) was used to measure the aperture distribution ratio in the soil.



TABLE 1 Basic physical properties of loess in Xi'an.

Natural water content(%)	Natural density (g/cm <sup>3</sup> )	Relative density	Porosity	Plastic limit/ W <sub>p</sub> (%)	Liquid limit/ W <sub>L</sub> (%)	Plastic index <sub>IP</sub>
25.4	1.73	2.71	0.49	19.4	30.8	11.4

### 2.2.1 Preparation of the remolded samples at different resting ages

The loose soil sample is configured as the soil sample with the same water content as the undisturbed soil sample, and the dry density of the sample is the same as that of the undisturbed soil by using a triaxial standard compactor. After demoulding, it is sealed with plastic wrap and tin foil to prevent water evaporation. After resting different test ages, it is made into electron microscope observation sample or nuclear magnetic resonance test sample.

### 2.2.2 Observation of mesoscopic pore structure of soil

The configuration of scanning electron microscope equipment is illustrated in Figure 1. To conduct analyses, standard triaxial samples with a diameter of 3.91cm and a height of 8cm were prepared from the undisturbed and remolded soil samples of different resting ages. After drying the samples in an oven, the soil around the cylindrical side was removed to ensure that the structure of the selected samples is intact. The section size of the remaining central position is about a strip of soil with a side length of 1cm. The section was extracted as shown in Figure 2. After dust removal, the fresh section was put into the electron microscope lofting box for observation.

### 2.2.3 Calculation of soil pore proportion at different scales

The principle of nuclear magnetic resonance (NMR, MesoMR23-060H-1 Suzhou Niumai Analytical Instrument, China) technology is to obtain the distribution spectrum of longitudinal signal strength and transverse relaxation time  $T_2$  by measuring the relaxation characteristics of hydrogen ions in soil pore water. Then the distribution proportion of pores at different scales can be obtained through conversion. The conversion expression is as follows:

$$\frac{1}{T_2} \approx \rho_2 \left( \frac{2}{R} \right), \quad (1)$$

Where  $\rho_2$  represents the surface relaxation strength, which is dependent on the material properties;  $R$  is the pore radius; the area enclosed by the  $T_2$  spectral curve and the relaxation time of the abscissa is the total pore water content.

The configuration of the NMR device is shown in Figure 3. To conduct tests, standard triaxial samples with a diameter of 3.91 cm and a height of 8 cm were prepared. The prepared samples were wrapped with a hard plastic shell as shown in Figure 4 to prevent deformation of the saturated soil sample and change its structure during the test process. The outside of the hard plastic shell was sealed with tape, then packed with a saturator and vacuumed. When the saturation exceeded 95%, the saturator was removed, and the upper and lower ends of the sample were sealed with a plastic wrap to prevent test errors caused by the outflow of pore water inside the soil sample during the test process. The sample seal is illustrated in Figure 5.

During the resting process of the soil sample, thixotropy causes the accumulation of clay minerals inside the structure to produce flocs, thus increasing the strength. In this process, the water content of the soil remains unchanged, so the flocs belong to water-resistant collection. The soil samples observed by electron microscopy mainly produce dehydration consolidation after drying, and the saturated soil samples tested by nuclear magnetic resonance only affect the soluble and medium soluble substances in the soil, so the drying and water saturation effects are not easy to destroy the water-resistant insoluble substances produced by thixotropy.

## 3 Micropore changes during loess thixotropy

### 3.1 Observation of microstructure and pore changes in loess

In order to study the changes in the microstructure of loess during thixotropy and its correlation with the macroscopic thixotropy intensity, and explore the microstructure mechanism of the strength changes, the prepared samples were tested under various magnification rates. The results with a magnification of 300, 500, and 1000 times are shown in Figures 6, 7, 8, respectively. The development trend of overhead through macropores between large aggregates of soil samples at different resting ages can be obtained by 300 times observation. The change of cementation degree between small particles and the development trend of aperture in

TABLE 2 Composition and classification of loess particles.

Mass fraction of different particle sizes/%			Classify	
>0.075 mm	0.075–0.005 mm	<0.005 mm	Classified by plastic diagram	Classified by particle composition
12.5	63.2	24.3	CL	clay

TABLE 3 Concentration of different cements in loess (%).

Illite	Smectite	Kaolinite	Eutectic salt	Cation exchange capacity (mg/kg)	Free oxide	Organic matter
25.9	2.9	2.3	0.11	0.824	2.72	0.29

the soil macropore at different resting ages can be obtained by 500 times observation. The change of internal cementation degree and the development trend of aperture in the soil micropore at different resting ages can be obtained by 1000 times observation.

Figures 6A–I with a magnification of 300 times indicate that the remolded loess at different resting ages aggregates overhead and there is a small contact area between aggregates. Moreover, the overhead pores with an average size larger than 700  $\mu\text{m}$  are in a state of through-development. The aperture is longer in the three-dimensional space, and no significant change in pore structure is observed as the resting ages grows. The undisturbed loess has a closed macropore structure with the aperture of approximately 600  $\mu\text{m}$ . In this case, the overhead aggregation is relatively low, and the clay particles are closely consolidated with fine silt particles. It is observed that compared with the undisturbed loess, remolded loess with the same dry density and water content has the same porosity, but the macropore size of remolded loess is larger than that of undisturbed loess. Moreover, the consolidated area between the aggregates of the remolded loess is much smaller than that of the undisturbed loess, which decreases the strength of the remolded loess.

Figures 7A–I with a magnification of 500 times reveal the presence of 50–100  $\mu\text{m}$  contact cementation regions between the aggregates of 100–300  $\mu\text{m}$  in the remolded loess at different resting ages. It is also observed that as the resting ages grows, the cementation regions between the aggregates gradually increase and the regions

may even merge with each other. The length of the microcrack decreases or its width narrows, ultimately leading to the crack closure. This phenomenon may be attributed to the accumulation of newly generated clay cements in the crack due to thixotropy after soil resting. This phenomenon reduces the porosity connectivity at this size to a certain extent and increases the cohesion and friction between aggregates, which promotes the growth of the overall structural strength. In contrast, the undisturbed loess primarily contains closed pores, and there are almost no micro-cracks with loose cementation between aggregates.

Figures 8A–I show the results with a magnification of 1000 times, indicating that the remolded loess contains numerous small particles with sizes ranging from 20–50  $\mu\text{m}$ . It is observed that as the resting ages increases, the degree of cementation among these small particles progressively intensifies, forming larger particles. In this case, the soil particles on the broken surface can be hardly peeled off by shear loads. Consequently, the occlusion between soil particles strengthens, enhancing the overall friction within the structure. In contrast, the undisturbed loess exhibits complete cementation among soil particles, and no loose tiny particle is observed in the undisturbed loess.

The observations of loess microstructure at different magnifications indicate that as the resting ages increases, the degree of cementation among the dispersed small aggregates (20–50  $\mu\text{m}$ ) within large aggregates increases, and the reinforced large aggregates enhance the

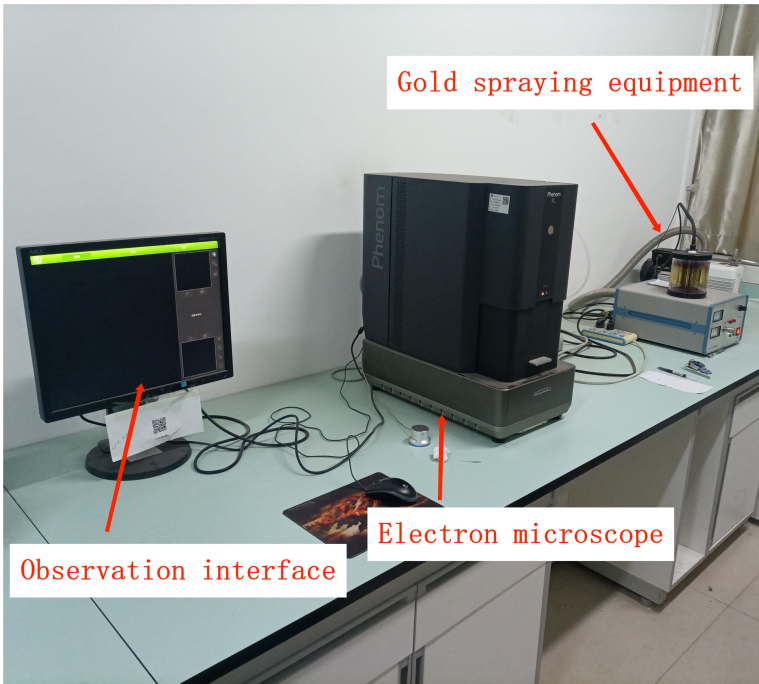


FIGURE 1  
Electron microscope equipment.



FIGURE 2  
Soil sample observation section.

friction force of the soil. Moreover, the newly formed cements accumulate between larger aggregates, resulting in the reduction of the microcrack lengths, narrowing the crack widths, or even the closure of microcracks. Cementing contact areas of 50–100  $\mu\text{m}$  gradually develop between the aggregates of 100–300  $\mu\text{m}$ , thereby increasing the cohesiveness and friction between the aggregates. These two effects increase the macroscopic structural strength of the soil.

## 3.2 Analysis of aperture distribution ratio at different scales in loess

### 3.2.1 $T_2$ spectrum and aperture distribution ratio curve conversion

The relationship between NMR relaxation time  $T_2$  and the signal strength is illustrated in Figure 9. It is observed that the relaxation time is directly proportional to aperture in soil. The smaller the relaxation time  $T_2$ , the smaller the aperture. Meanwhile, the lower the relaxation signal intensity, the smaller the proportion of the pore content in the total pore.

### 3.2.2 Pore division and thixotropic proportion calculation

In the aperture distribution ratio curve, a certain aperture is set as  $r_a$ , aperture 0 to  $r_a$  is the micropore, and the other aperture is set

as  $r_b$ ,  $r_b$  to 4000  $\mu\text{m}$  is the macropore,  $r_a$  to  $r_b$  is the mesopore. The division of different pore interval is depicted in Figure 10 and Figure 11. In Figure 9, it is easy to know that the ratio of aperture distribution of remodeled loess corresponding to  $r_b$  is about 0, so  $r_b$  is approximately 400  $\mu\text{m}$ . To determine  $r_a$ , it is defined that the pore segment with the increase of aperture distribution ratio with the increase of resting ages is the micropore segment, and the pore segment with the decrease of aperture distribution ratio is the mesopore segment. The peak value of aperture distribution ratio in the micropore segments at different resting ages is translated to the same peak value as that of soil samples at a resting age of 0d, so that the corresponding horizontal coordinate aperture is the same. It can be found in the figure that the aperture distribution ratio of the remolded soil samples under different resting ages overlaps around a small aperture interval. The aperture distribution ratio on the left side of the coincidence interval increases, while the aperture distribution ratio on the right side of the coincidence interval decreases. The minimum floating value of the coincidence interval is selected, and the corresponding aperture is about 7  $\mu\text{m}$ . Therefore, it is determined that the micropore is 0–7  $\mu\text{m}$ , the mesopore is 7–400  $\mu\text{m}$ , and the macropore is 400–4000  $\mu\text{m}$ .

It is known that the area enclosed by the aperture distribution ratio curve and the horizontal aperture represents the number of pores or microcracks. The number of pores within a certain aperture interval ( $r_x$ ,  $r_y$ ) in the soil is  $M$ , the aperture  $r_x$  corresponds to the



FIGURE 3  
Nuclear magnetic resonance instrument.



FIGURE 4  
Water retention and morphology of the sample were fixed.





FIGURE 5  
Soil sample saturation.

aperture distribution ratio  $\eta_x$ , and  $r_y$  corresponds to the aperture distribution ratio  $\eta_y$ , then  $M$  can be expressed as:

$$M = \frac{(\eta_x + \eta_y)(r_y - r_x)}{2} \quad (2)$$

Where  $M_0$  represents the total number of pores in the micropore segment at a resting age of 0d,  $M_t$  represents the total number of pores in the micropore segment of resting  $t$ , and  $M_u$  represents the total number of pores in the micropore segment of undisturbed soil. As the resting ages increases, the degree of change in the number of pore in micropore segments can be expressed by the thixotropic conversion ratio  $D$ :

$$D = \frac{M_t}{M_0} \quad (3)$$

As the resting ages increases, compared with the undisturbed soil, the degree of change in the number of pore of micropore segments can be expressed by the thixotropic conversion recovery ratio  $E$ :

$$E = \frac{M_u - M_0}{M_t - M_0} \quad (4)$$

Set the number of nuclear magnetic test points in the micropore segment to  $l$ , corresponding to the aperture distribution ratio  $\eta_1$ ,  $\eta_2$ ,  $\eta_3$  to  $\eta_b$ . The thixotropic conversion ratio  $D$  can be calculated as:

$$D = \frac{M_t}{M_0} = \frac{\sum_{i=1}^l \left( \frac{(\eta_{i,t} + \eta_{i+1,t})(r_{i+1} - r_i)}{2} \right)}{\sum_{i=1}^l \left( \frac{(\eta_{i,0} + \eta_{i+1,0})(r_{i+1} - r_i)}{2} \right)} = \sum_{i=0}^l \left( \frac{\eta_{i,t} + \eta_{i+1,t}}{\eta_{i,0} + \eta_{i+1,0}} \right) \quad (5)$$

The thixotropic conversion recovery ratio  $E$  is:

$$\begin{aligned} E &= \frac{M_u - M_0}{M_t - M_0} \\ &= \frac{\sum_{i=1}^l \left( \frac{(\eta_{i,u} + \eta_{i+1,u})(r_{i+1} - r_i) - (\eta_{i,0} + \eta_{i+1,0})(r_{i+1} - r_i)}{2} \right)}{\sum_{i=1}^l \left( \frac{(\eta_{i,t} + \eta_{i+1,t})(r_{i+1} - r_i) - (\eta_{i,0} + \eta_{i+1,0})(r_{i+1} - r_i)}{2} \right)} \\ &= \sum_{i=1}^l \left( \frac{(\eta_{i,u} + \eta_{i+1,u}) - (\eta_{i,0} + \eta_{i+1,0})}{(\eta_{i,t} + \eta_{i+1,t}) - (\eta_{i,0} + \eta_{i+1,0})} \right) \end{aligned} \quad (6)$$

In the mesopore and macropore, the  $D$  and  $E$  are calculated in the same way as in the micropores.

### 3.2.3 Analysis of aperture distribution ratio curve

Figure 12 depicts the relationship between aperture and aperture distribution ratio, obtained from Equation (1). The graph displays two peaks from left to right, representing micropores and macropores, respectively. The peak size of micropores in both undisturbed and remolded loess is around 1–2  $\mu\text{m}$ . When the particle size varies in the interval of 0–7  $\mu\text{m}$  and 200–4000  $\mu\text{m}$ , the proportion of undisturbed loess is larger than that of remolded loess. However, in the interval of 7–200  $\mu\text{m}$ , the distribution proportion of undisturbed loess is smaller than that of remolded loess.

The results demonstrate that as the resting ages increases, the proportion of peak micropores in the remolded loess continuously

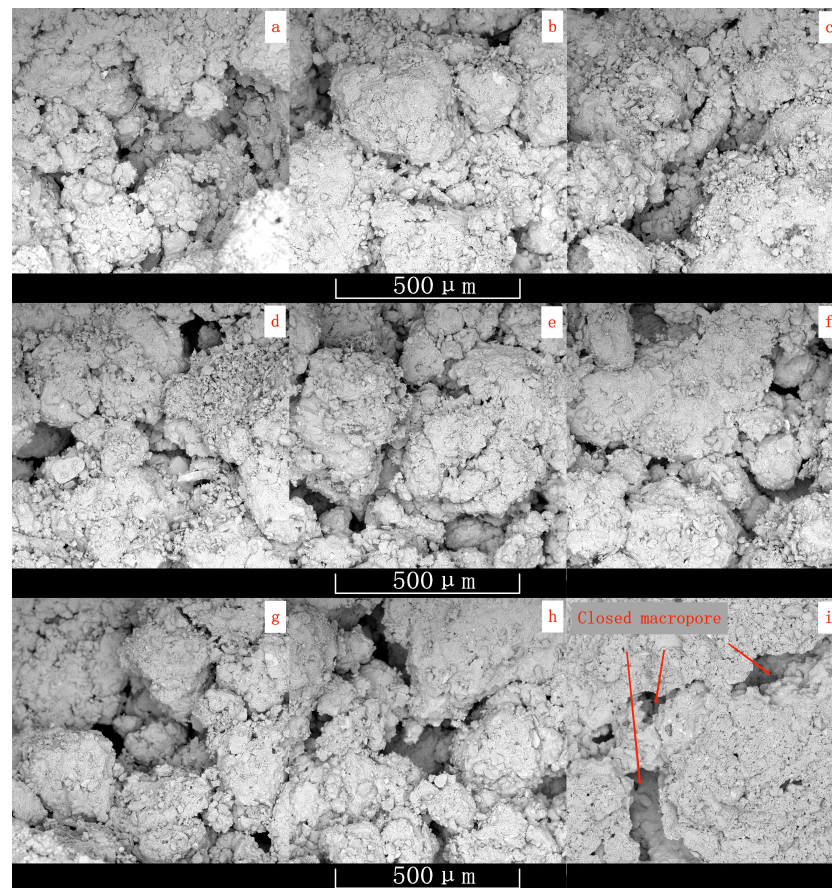


FIGURE 6  
Electron microscopic image of undisturbed soil and remodeled soil of different resting ages (A–I, x300).

increases. Compared with that in the remolded loess, the proportion of peak micropores in the remolded loess increased from 0.299% to 0.34%. The nuclear magnetic resonance test point data of 0–7  $\mu\text{m}$  micropore segment was brought into Equation (5) to calculate, and the thixotropic conversion ratio of the aperture representing a 13.9% increment. It is worth noting that the pores at this size are cemented pores, indicating that as the resting ages increases, disturbed clay particles in the soil gradually transit from the dispersed state to cemented state. Consequently, the proportion of cemented pores increases.

Figure 12 reveals that there are no new pore peaks within the undisturbed and remolded loess in the interval of 2–400  $\mu\text{m}$ . In this section, clay particles are filled in the inlay pores of coarse particles or the incohesive micro-cracks between small aggregates to varying degrees. As the aperture increases, the aperture distribution ratio ranging from 2–400  $\mu\text{m}$  indicates a unidirectional downward trend, and no pore peak appears at a certain scale.

Figure 12 reveals that as the resting ages increases, the aperture distribution ratio in the interval of 0–7  $\mu\text{m}$  in the remolded loess increases. This may be attributed to the accumulation of free cements in the coarse-grained mosaic pores so the number of mosaic pores above 7  $\mu\text{m}$  partially reduces. On the other hand, the number of pores smaller than 7  $\mu\text{m}$  increases. Figure 11 also indicates that the pore proportion of 7–400  $\mu\text{m}$  decreases

continuously, and the aperture distribution ratio of about 20  $\mu\text{m}$  changes significantly. The nuclear magnetic resonance test point data of 7–400  $\mu\text{m}$  mesopore segment was brought into Equation (5) to calculate, and the thixotropic conversion ratio of the aperture representing an decrement of 14.4%. This increment primarily originates from the accumulation of free cements or the internal adjustment of the soil structure in the pore section, which reduces the number of large micro-cracks between or within the aggregates. These results can also be observed in SEM images with different resting ages and magnifications of 500 and 1000 times.

The aperture interval of macropore in the undisturbed loess and remolded loess are concentrated between 400 and 3000  $\mu\text{m}$ . This interval is a through microcrack caused by the aeration of large aggregates in the soil. The peak of aperture distribution proportion of macropores in the remolded loess increased from 0.0179% to 0.0183% at a resting age of 160d compared with 0d. The nuclear magnetic resonance test point data of 400–4000  $\mu\text{m}$  macropore segment was brought into Equation (5) to calculate, and the thixotropic conversion ratio of the aperture representing an increment of 2.3%. Due to the difficulty of filling macropores with a limited content of cement, the proportion change may be caused by the shape change of large aggregates during thixotropic process.

An analysis was conducted on the aperture distribution in different size segments of undisturbed and remolded loess at



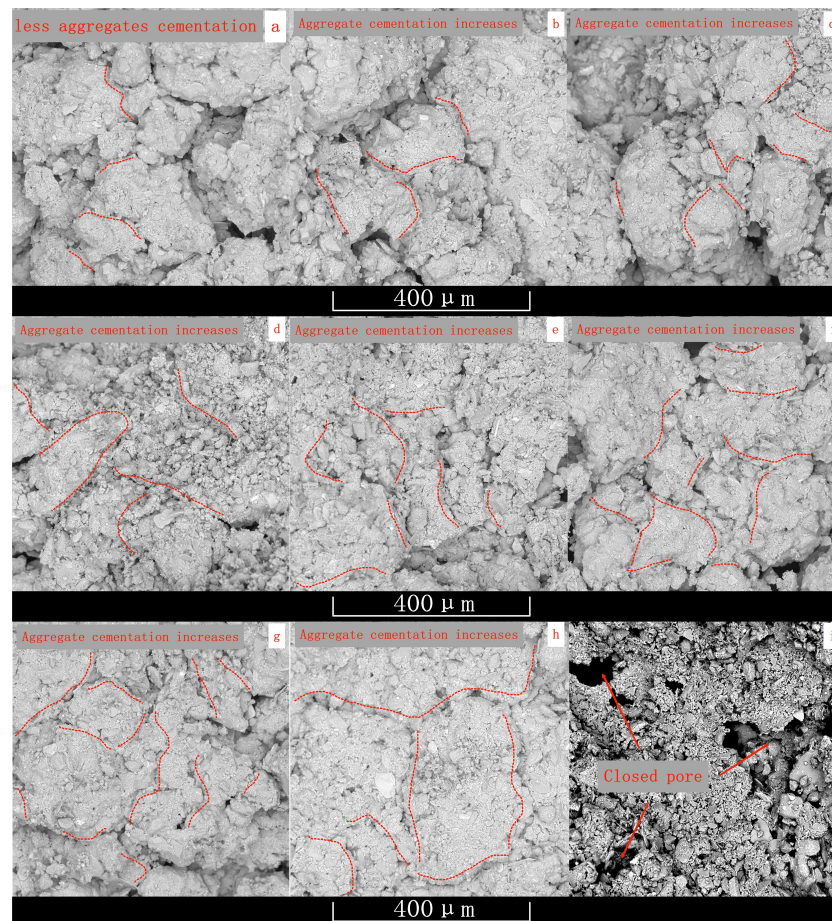


FIGURE 7  
Electron microscopic image of undisturbed soil and remodeled soil of different resting ages (A–I,  $\times 500$ ).

various resting ages. The results indicated that the proportion of micropores is 0.377% in the undisturbed loess, which is 0.078% higher than that in the remodeled loess at a resting age of 0d and is 0.037% higher than that in the remodeled loess at a resting age of 160d. According to Equation (6), the thixotropic conversion recovery ratio of micropores in the remodeled loess at a resting age of 160d is 53.2%.

Figure 12 reveals that the proportion of mesopores with an approximate size of 20  $\mu\text{m}$  changed significantly and the proportion of undisturbed loess was 0.141%, which is 0.074% lower than that of remodeled loess at a resting age of 0d. According to Equation (6), the thixotropic conversion recovery ratio of mesopores in the remodeled loess at a resting age of 160d is 76.0%.

Finally, Figure 12 demonstrates that the aperture distribution ratio of the peak value of macropores in the undisturbed loess is 0.065%, which is 0.0472% higher than that of the remodeled loess at a resting age of 0d and is 0.0468% higher than that of the remodeled loess at a resting age of 160d. According to Equation (6), the thixotropic conversion recovery ratio of macropores in the remodeled loess at a resting age of 160d is only 0.87%.

The performed analyses demonstrate that part of the evolution from remodeled to undisturbed loess is that the proportion of micropores (0–7  $\mu\text{m}$ ) and macropores (400–4000  $\mu\text{m}$ ) increases,

while the proportion of mesopores (7–400  $\mu\text{m}$ ) decreases. This may be attributed to the thixotropic process in which the number of cemented pores increases, while the number of aggregate micro-cracks decreases during the resting period of the remodeled loess. However, the number of macropores (400–4000  $\mu\text{m}$ ) in the remodeled loess does not increase significantly in a short time.

## 4 Analysis of the thixotropic micromechanical mechanism of loess

### 4.1 Relationship between soil particle interaction and mesostructural changes

The interactions between soil particles are complex, and the interaction between clay particles, water, and the charge system is one of the most common interactions. This interaction involves both attraction and repulsion forces, which contribute to cohesion observed in the attraction and repulsion between soil particles. The attraction between clay particles involves various forces, including electrostatic attraction, van der Waals force, interparticle cementation, and contact point bonding. Electrostatic attraction consists of Coulomb force and ion electrostatic force. Clay particles,

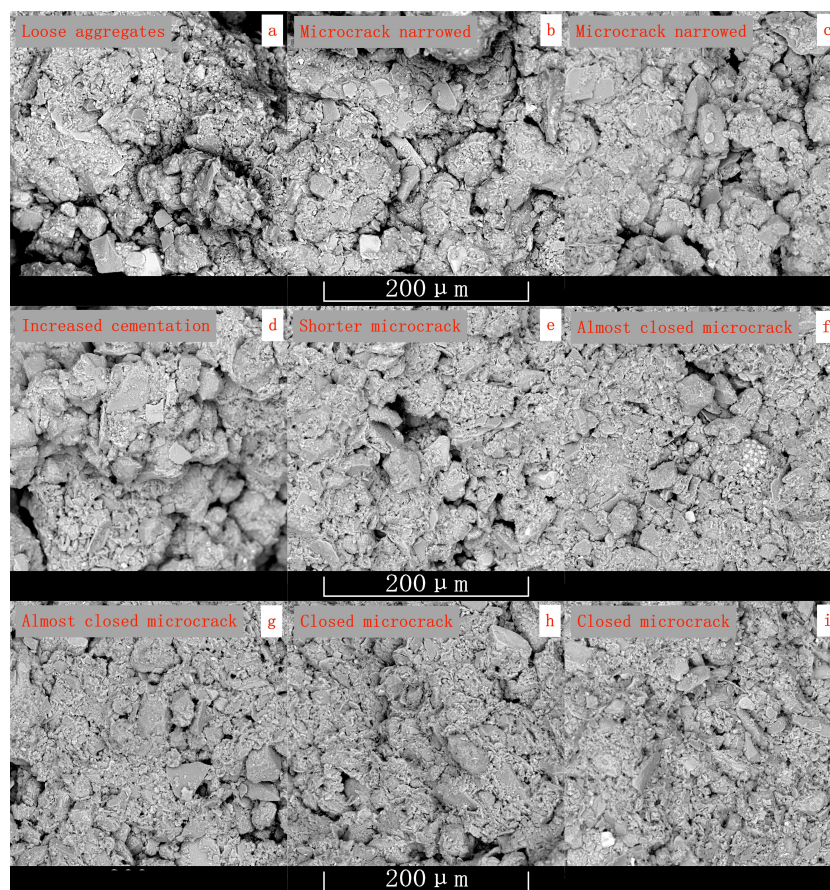


FIGURE 8  
Electron microscopic image of undisturbed soil and remodeled soil of different resting ages (A–I,  $\times 1000$ ).

which are typically in a sheet form, carry a negative charge on plane and edge regions. The Coulomb force induces positive and negative charges on clay particles to be attracted by face–edge contact. Moreover, the ionic electrostatic force results in the absorption of negatively-charged clay particles by cations in pore water. This

overlapping of double electric layers forms a common water film and attraction. When two polar molecules approach each other, one of the polar molecules will attract the opposite dipole. The cementation between clay particles comes from chemical reactions, including the interaction between clay particles (such as

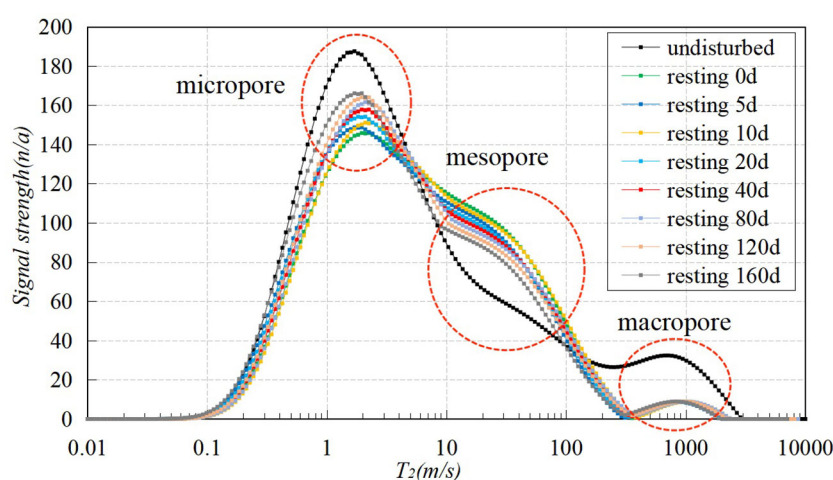


FIGURE 9  
Signal strength– $T_2$ .



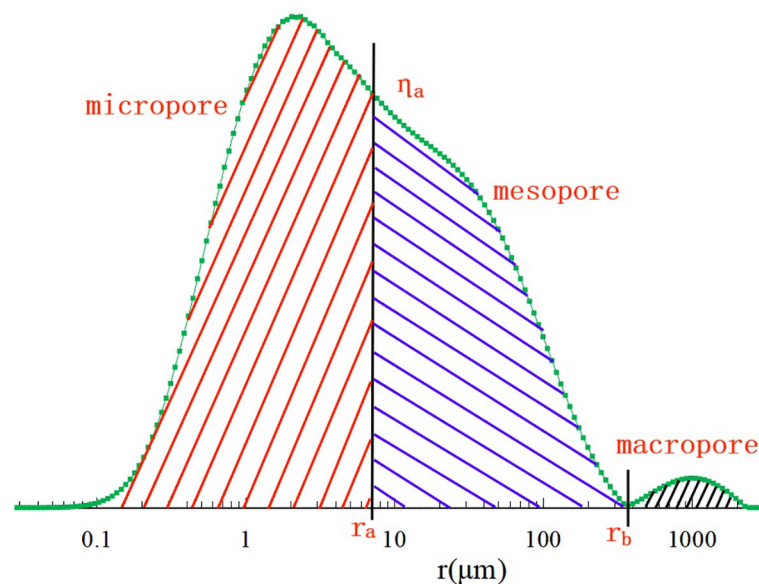


FIGURE 10  
Aperture partition diagram (a).

illite, montmorillonite, and kaolinite) and free oxides, organic matter, salt solution, and even coarse particles in the soil. Therefore, clay particles in the soil can be consolidated into clusters, or the coarse particles and detritus particles wrapped in minerals, forming large flocculation structures. Contact point bonding primarily originates from the deformation and compression of load, which reduces the contact distance of mineral particles and produces high-energy bonding.

The soil is compressed and deformed under the action of external loads. On the other hand, the shape and position of the soil particles change as the contact area between the soil particles increases. Consequently, the connection to the original structure breaks, the distribution of the pore water solution changes, and the removal of detrital particles, including detrital minerals and clay

particles, becomes more pronounced. Structural changes reflect the work done by external forces. When the soil is compressed and its volume remains constant, a portion of the compressive elastic deformation generated by soil particles is transformed into consolidation contact of soil particles, while the other portion cannot overcome the minimum gravitational distance of soil particles. In this case, the resultant force cannot overcome the repulsion between soil particles and transforms into elastic potential energy stored.

When the soil is compressed, clay particles and cationic water solution generated by the compression disturbance are redistributed in the newly formed pores. Furthermore, the clay–water–charge system re-establishes attraction, and more cements appear in the short term to form flocculated aggregates, which is consistent with

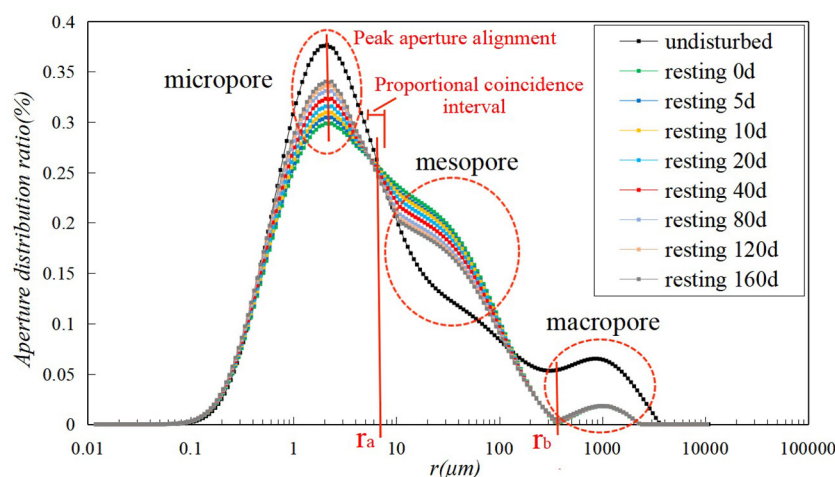


FIGURE 11  
Aperture partition diagram (b).

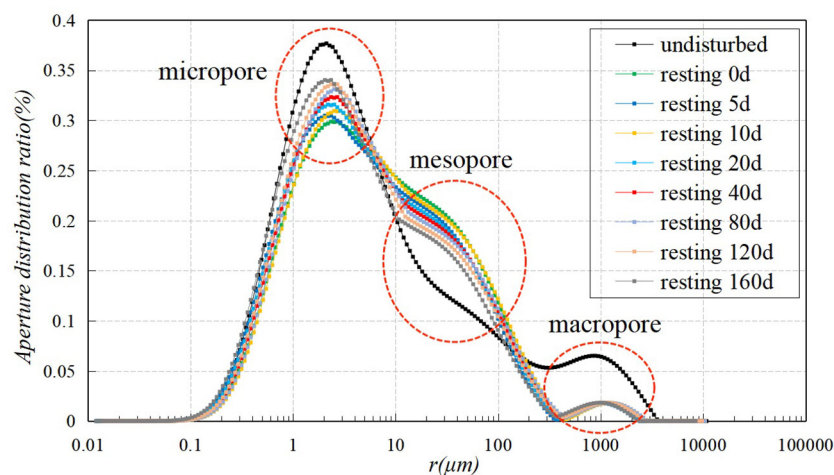


FIGURE 12  
Aperture distribution ratio.

the recently published report indicating that the proportion of clay thixotropic strength in many areas is only positively correlated with cation exchange capacity by Zhang et al. (2017). Meanwhile, the elastic potential energy stored in the soil is gradually released, which may change the shape of clay particles. This phenomenon may result in face–edge attraction under the action of Coulomb force, or change the position of particles. When the average distance between soil particles is relatively small, the cations establish a mutual attraction with the water film. The compression squeezes the saturated aqueous solution in some pores into the external pores, and the aqueous solution is evenly dispersed in the pores in the later resting ages. When the saturated solution contacts with soil particles nearby, they attract each other due to the ionic electrostatic force.

The longer the resting ages, the more energy dissipates in the system, the activity of soil particles weakens, the distribution of pore water becomes more uniform, fewer clay particles form cement, the cation exchange reaction weakens in the aqueous solution, and the strength growth range reduces. The thixotropic process lasts for a long time. This may be attributed to the attraction between clay particles to form cements and the gradual flocculation of aggregates to produce precipitation. This process is related to the number of clay particles involved per unit time and the concentration of cations in water. With the growth of resting ages, the number of clay particles and cation concentration involved in the cementation reaction becomes smaller, and the formation time of flocculation precipitation becomes longer. Therefore, the processing time of thixotropic strength growth is especially long.

## 4.2 Relationship between microstructural changes of loess and growth of thixotropic strength

During the experiment, external forces were applied to the soil to produce shear failure. The failure surface typically occurs in the area with weak cementation and small cementation areas, which are

often more extended. It may also occur through cracks. In order to improve the structural strength of soil, consolidation, and compaction techniques were initially applied to reduce initial pores. Consequently, the cementation area of soil particles increased and the shear strength of the failure surface enhanced. For a constant volume of soil under the action of the clay–water–charge system, newly generated thixotropic cements increase the cementation area between soil particles or increase the friction force. This process can be primarily categorized into four forms: wide crack uncontacted, crack convex occlusal contact, narrow crack contact, and slightly convex occlusal contact.

Figures 13A, B show the non-contact form of wide cracks. Due to the large width of the micro-crack, the content of newly generated cements attached to both sides of the aggregate decreases after the soil thixotropy. Consequently, a crack with a large width may not close completely and its ability to resist shear force becomes limited. As a result, the structural strength cannot be improved.

Figures 13C, D show the occlusal contact form with the fissure protuberance. The raised soil particles on both sides of the microcracks are in contact with each other, providing a certain resistance to shear forces. However, if the raised soil particles contain microcracks, they are prone to peel off and failure under stress. During the thixotropic process, the formation of cement enhances the closure of microcracks at the bulge, preventing the removal of raised soil particles, thereby increasing the friction force on the shear failure surface.

Figures 13E, F show the contact form of a narrow crack. Soil already has a consolidation cementing surface due to early compression so newly generated cements in the thixotropic process accumulate in the periphery of the original consolidated contact surface. As a result, the consolidated area of the aggregate contact point increases and the cohesion of the shear failure surface improves.

Figures 13G, H illustrate the occlusal contact form of slight raised. It is observed that the raised soil particles on both sides of the

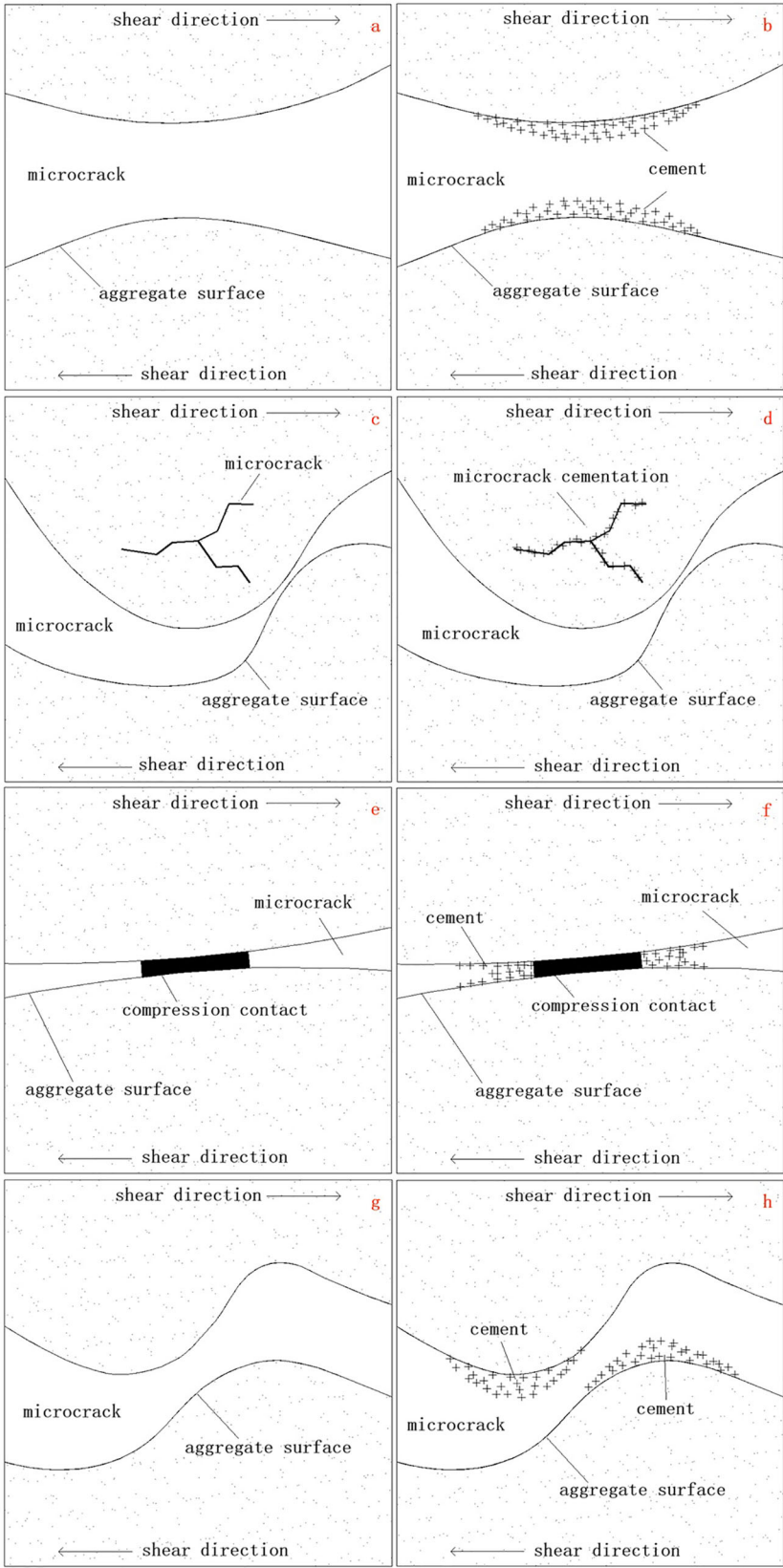


FIGURE 13  
Influence of soil structure change on micro-strength before and after thixotropy (A–H).

aggregate in the microcrack are relatively low, and the occlusal shear resistance is small. However, during the thixotropic process, the newly generated cements gather at the uplift, increasing their height and enhancing the shear resistance at the occlusal contact, thereby increasing the friction force of the shear failure surface.

## 5 Conclusion

In the present study, thixotropic mechanism of loess was investigated. The performed analyses revealed that Xi'an loess exhibits pronounced thixotropy. SEM photos of the remolded loess and undisturbed loess at different magnifications indicate that undisturbed loess contains closed macropores larger than 500  $\mu\text{m}$ , as well as inlaid pores between soil particles ranging from 10–40  $\mu\text{m}$ . In contrast, it is found that there is no microcrack with small aggregates. The remolded loess contained 700  $\mu\text{m}$  macropores in the aggregate frame, 100–300  $\mu\text{m}$  small aggregate microcracks, and 10–40  $\mu\text{m}$  inlay pores among soil particles. The results demonstrate that as the resting ages increases, the cementation and closure of 100–300  $\mu\text{m}$  microcracks shrink gradually, which improves the cohesion and friction between aggregates to a certain extent. This finding is of significant importance to improve the thixotropic strength of the remolded loess.

NMR results indicated that the proportions of micropores (0–7  $\mu\text{m}$ ) and macropores (200–4000  $\mu\text{m}$ ) in the undisturbed loess are higher than those in the remolded loess at different resting ages. Moreover, it is found that the proportion of mesopore (7–200  $\mu\text{m}$ ) is lower than those in the remolded loess at different resting ages. The proportion of micropores in the interval of 1–2  $\mu\text{m}$  in the reconstituted loess increased with the increase of the resting ages. At a resting age of 160d, the thixotropic conversion ratio  $D$  and thixotropic conversion recovery ratio  $E$  of remolded loess with micropores are 13.9% and 53.2%, respectively. The thixotropic conversion ratio  $D$  and thixotropic conversion recovery ratio  $E$  of remolded loess with mesopores are 14.4% and 76.0%, respectively. The thixotropic conversion ratio  $D$  and thixotropic conversion recovery ratio  $E$  of remolded loess with macropores are 2.3% and 0.8%, respectively. A portion of the evolution process from remolded to undisturbed loess is the thixotropic behavior of increasing the number of cemented pores and decreasing the number of aggregate microcracks.

The increase in the thixotropic strength in loess can be attributed to the micromechanical mechanism described as follows: when the soil is resting, the interaction between soil particles and aqueous solution re-establishes attractive forces within the disturbed clay particle–water–charge system. Consequently, more clay cements are absorbed in the microcracks of aggregates in a short time. Simultaneously, the elastic potential energy induced by compression weakens due to partial deformation and displacement of soil particles during resting storage. Moreover, the migration of pore water and some clay particles promotes the

mutual cementation of dispersed clay particles. The cementation area and the occlusal degree of soil particles at the meso level increased, which enhanced the structural strength at the macro level. However, the cation content of clay particles and water solution in the system is limited and is constantly consumed in the thixotropic process due to the formation of cements. The expansion of cements takes a longer time to form flocculant precipitation so the proportion of strength increasing with the resting ages decreases continuously.

## Data availability statement

The original contributions presented in the study are included in the article/Supplementary material. Further inquiries can be directed to the corresponding authors.

## Author contributions

All authors listed have made a substantial, direct, and intellectual contribution to the work and approved it for publication.

## Funding

The authors are grateful to the financial support from the National Natural Science Foundation of China (51979225, 52078421, 42007264, 51909204), the National Natural Science Foundation Youth Foundation (52009107), the China Postdoctoral Science Foundation (2019M663943XB), the Natural Science Basic Research Program of Shaanxi (2022JM-216), the Shaanxi Province key research and development plan project (2022ZDLSF07-02), and the Shaanxi Provincial Department of Education key laboratory project (20JS091).

## Conflict of interest

The authors declare that the research was conducted in the absence of any commercial or financial relationships that could be construed as a potential conflict of interest.

## Publisher's note

All claims expressed in this article are solely those of the authors and do not necessarily represent those of their affiliated organizations, or those of the publisher, the editors and the reviewers. Any product that may be evaluated in this article, or claim that may be made by its manufacturer, is not guaranteed or endorsed by the publisher.



## References

- Abdou, M. I., and Ahmed, H. E. S. (2013). A study on the thixotropy of Egyptian bentonite suspensions. *Pet. Sci. Technol.* 31 (19), 1980–1991. doi: 10.1080/10916466.2011.554060
- Abu-Farsakh, M., Rosti, F., and Souri, A. (2015). Evaluating pile installation and subsequent thixotropic and consolidation effects on setup by numerical simulation for full-scale pile load tests. *Can. Geotech. J.* 52 (11), 1734–1746. doi: 10.1139/cgj-2014-0470
- Aminpour, P. (2019). *Multiscale modeling of thixotropy in soft clays*. (Philadelphia, PA: Drexel University).
- Andersen, K. H., Lunne, T., Kvalstad, T. J., and Forsberg, C. F. (2008). “Deep water geotechnical engineering,” in *Proc. 24th Nat. Conf. of Mexican Soc. of Soil Mechanics*. 26–29. (Aguascalientes, Mexico).
- Barnes, H. A. (1997). Thixotropy—a review. *J. Non-Newtonian Fluid Mech.* 70 (1–2), 1–33. doi: 10.1016/S0377-0257(97)00004-9
- Blake, G. R., and Gilman, R. D. (1970). Thixotropic changes with aging of synthetic soil aggregates. *Soil Sci. Soc. Am. J.* 34 (4), 561–564. doi: 10.2136/sssaj1970.03615995003400040009x
- Boswell, P. G. H. (1948). A preliminary examination of the thixotropy of some sedimentary rocks. *Q. J. Geol. Soc.* 104 (1–4), 499–526. doi: 10.1144/GSL.JGS.1948.104.01-04.23
- Burgers, J. M., and Blair, G. W. S. (1949). *Report on the principles of rheological nomenclature* (Netherlands: North-Holland Publishing Company. International Council of Scientific Unions. Joint Committee on Rheology).
- Day, P. R., and Ripple, C. D. (1954). Effect of shear on suction in saturated clays. *Annual Reports I and II, Western Regional Research Project W-30*, 1955, 675–679. doi: 10.2136/sssaj1966.03615995003000060010x
- de Souza Mendes, P. R. (2009). Modeling the thixotropic behavior of structured fluids. *J. Non-Newtonian Fluid Mech.* 164 (1–3), 66–75. doi: 10.1016/j.jnnfm.2009.08.005
- Dexter, A. R., Horn, R., and Kemper, W. D. (1988). Two mechanisms for age-hardening of soil. *J. Soil Sci.* 39 (2), 163–175. doi: 10.1111/j.1365-2389.1988.tb01203.x
- Díaz-Rodríguez, J. A., and Santamarina, J. C. (1999). “Thixotropy: the case of Mexico city soils,” in *XI Panamerican Conf. on Soil Mech. and Geotech. Eng.* 441–448. (Brazil).
- Doglion, A., and Simeone, V. (2013). “Recovery of strength along shear surfaces in clay soils,” in *Landslide Science and Practice* (Berlin, Heidelberg: Springer), 183–188.
- Dullaert, K., and Mewis, J. (2006). A structural kinetics model for thixotropy. *J. NonNewtonian Fluid Mech.* 139 (1–2), 21–30. doi: 10.1016/j.jnnfm.2006.06.002
- Gagnoud, M., Lajeunesse, P., Desrosiers, G., Long, B., and Stora, G. (2008). Litho- and biofacies analysis of postglacial marine mud using CT-scanning. *Eng. Geol.* 103 (3), 106–111. doi: 10.1016/j.enggeo.2008.06.010
- Heymann, L., Noack, E., Kämpfe, L., and Beckmann, B. (1996). “Rheology of printing inks—some new experimental results,” in *Proceedings of the XIIth Congress on Rheology*. Ed. Ait-Kadi, JM James and MC Williams. (Quebec, Canada: Laval University), 451–452.
- Jacobsson, A., and Pusch, R. (1972). Thixotropic action in remoulded quick clay. *Bull. Int. Assoc. Eng. Geology-Bulletin l'Association Internationale G'éologie l'Ing'énieur* 5 (1), 105–110. doi: 10.1007/BF02634659
- Jeong, S. W., Locat, J., and Leroueil, S. (2012). The effects of salinity and shear history on the rheological characteristics of illite-rich and Na-montmorillonite-rich clays. *Clay Clay Miner.* 60 (2), 108–120. doi: 10.1346/CCMN.2012.0600202
- Jiang, H., Mu, J., Zhang, J., Jiang, Y., Liu, C., and Zhang, X. (2022). Dynamic evolution in mechanical characteristics of complex supporting structures during large section tunnel construction. *Deep Underground Sci. Eng.* 1 (2), 183–201. doi: 10.1002/dug2.12027
- Liu, J., Xue, Y., Fu, Y., Yao, K., and Liu, J. (2023). Numerical investigation on microwave-thermal recovery of shale gas based on a fully coupled electromagnetic, heat transfer, and multiphase flow model. *Energy* 263, 126090. doi: 10.1016/j.energy.2022.126090
- Lu, N. Z., Suhayda, J. N., Prior, D. B., Bornhold, B. D., Keller, G. H., Wiseman, W. J., et al. (1991). Sediment thixotropy and submarine mass movement, Huanghe Delta, China. *Geo-Mar. Lett.* 11 (1), 9–15. doi: 10.1007/BF02431049
- Mitchell, J. K. (1961). Fundamental aspects of thixotropy in soils. *Trans. Am. Soc. Civ. Eng.* 126 (1), 1586–1620. doi: 10.1061/TACEAT.0008103
- Olphen, H. V. (1977). An introduction to clay colloid chemistry. *Soil Science*, 97 (4), 290. (USA).
- Osipov, V. I., Nikolaeva, S. K., and Sokolov, V. N. (1984). Microstructural changes associated with thixotropic phenomena in clay soils. *Geotechnique* 34 (3), 293–303. doi: 10.1680/geot.1984.34.3.293
- Pardo, G. S., Sarmah, A. K., and Orense, R. P. (2019). Mechanism of improvement of biochar on shear strength and liquefaction resistance of sand. *Geotechnique* 69 (6), 471–480. doi: 10.1680/jgeot.17.P.040
- Perret, D., Locat, J., and Martignoni, P. (1996). Thixotropic behavior during shear of a finegrained mud from Eastern Canada. *Eng. Geol.* 43 (1), 31–44. doi: 10.1016/0013-7952(96)00031-2
- Peterfi, T. (1927). Die abhebung der befruchtungsmembran bei seeigeleiern: Eine kolloidchemische Analyse des Befruchtungsvorganges. *Wilhelm Roux'Archiv für Entwicklungsmechanik der Organismen* 112, 660–695. doi: 10.1007/BF02253780
- Rinaldi, V. A., and Clari'a, J. J. (2016). Time dependent stress-strain behavior of bentonite slurries; effect of thixotropy. *Powder Technol.* 291, 311–321. doi: 10.1016/j.powtec.2015.12.036
- Shahriar, A. R., Abedin, M. Z., and Jadid, R. (2018). Thixotropic aging and its effect on 1-D compression behavior of soft reconstituted clays. *Appl. Clay Sci.* 153, 217–227. doi: 10.1016/j.clay.2017.12.029
- Skempton, A. W., and Northey, R. D. (1952). The sensitivity of clays. *Geotechnique* 3 (1), 30–53. doi: 10.1680/geot.1952.3.1.30
- Sun, X., Li, X., Zheng, B., He, J., and Mao, T. (2020). Study on the progressive fracturing in soil and rock mixture under uniaxial compression conditions by CT scanning. *Eng. Geol.* 279, 105884. doi: 10.1016/j.enggeo.2020.105884
- Sun, H., Masin, D., Najsner, J., Nedela, V., and Navratilova, E. (2019). Bentonite microstructure and saturation evolution in wetting-drying cycles evaluated using ESEM, MIP and WRC measurements. *G'éotechnique* 69 (8), 713–726. doi: 10.1680/jgeot.17.P.253
- Xue, Y., Liu, S., Chai, J., Liu, J., Ranjith, P. G., Cai, C., et al. (2023b). Effect of water-cooling shock on fracture initiation and morphology of high-temperature granite: Application of hydraulic fracturing to enhanced geothermal systems. *Appl. Energy* 337, 120858. doi: 10.1016/j.apenergy.2023.120858
- Xue, Y., Liu, J., Liang, X., Li, X., Wang, S., Ma, Z., et al. (2023a). Influence mechanism of brine-gas two-phase flow on sealing property of anisotropic caprock for hydrogen and carbon energy underground storage. *Int. J. Hydrogen Energy* 48 (30), 11287–11302. doi: 10.1016/j.ijhydene.2022.05.173
- Xue, Y., Ranjith, P. G., Gao, F., Zhang, Z., and Wang, S. (2023c). Experimental investigations on effects of gas pressure on mechanical behaviors and failure characteristic of coals. *J. Rock Mechanics Geotechnical Eng.* 15 (2), 412–428. doi: 10.1016/j.jrmge.2022.05.013
- Yang, Z., Qi, W., Ding, Y., Jiang, Y., Yang, X., Yang, X., et al. (2023). Numerical investigation on the spewing mechanism of earth pressure balance shield in a high-pressure water-rich sand stratum. *Deep Underground Sci. Eng.* 2 (1), 74–87. doi: 10.1002/dug2.12032
- Zhang, X. W., Kong, L. W., Yang, A. W., and Sayem, H. M. (2017). Thixotropic mechanism of clay: a microstructural investigation. *Soils Found.* 57 (1), 23–35. doi: 10.1016/j.sandf.2017.01.002



## OPEN ACCESS

## EDITED BY

Liang Chen,  
China University of Mining and  
Technology, China

## REVIEWED BY

Xiao Tan,  
Sichuan University, China  
Ning Li,  
Luoyang Institute of Science and  
Technology, China

## \*CORRESPONDENCE

Zhengzheng Cao

✉ caozz2008@126.com

Yi Xue

✉ xueyi@xaut.edu.cn

RECEIVED 29 June 2023

ACCEPTED 08 September 2023

PUBLISHED 29 September 2023

## CITATION

Wang L, Zhang W, Cao Z,  
Xue Y, Liu J, Zhou Y, Duan C  
and Chen T (2023) Effect of weakening  
characteristics of mechanical properties of  
granite under the action of liquid nitrogen.  
*Front. Ecol. Evol.* 11:1249617.  
doi: 10.3389/fevo.2023.1249617

## COPYRIGHT

© 2023 Wang, Zhang, Cao, Xue, Liu, Zhou,  
Duan and Chen. This is an open-access  
article distributed under the terms of the  
[Creative Commons Attribution License](#)  
(CC BY). The use, distribution or  
reproduction in other forums is permitted,  
provided the original author(s) and the  
copyright owner(s) are credited and that  
the original publication in this journal is  
cited, in accordance with accepted  
academic practice. No use, distribution or  
reproduction is permitted which does not  
comply with these terms.

# Effect of weakening characteristics of mechanical properties of granite under the action of liquid nitrogen

Linchao Wang<sup>1</sup>, Wan Zhang<sup>1</sup>, Zhengzheng Cao<sup>2\*</sup>, Yi Xue<sup>1\*</sup>,  
Jianqiang Liu<sup>3</sup>, Yang Zhou<sup>3</sup>, Chenyang Duan<sup>3</sup> and Tong Chen<sup>4</sup>

<sup>1</sup>School of Civil Engineering and Architecture, Xi'an University of Technology, Xi'an, China,

<sup>2</sup>International Joint Research Laboratory of Henan Province for Underground Space Development and Disaster Prevention, Henan Polytechnic University, Jiaozuo, Henan, China, <sup>3</sup>Shaanxi Geological Survey Center of Hydrogeology, Engineering Geology and Environmental Geology, Shaanxi Institute of Geological Survey, Xi'an, China, <sup>4</sup>Zibo Aojing Garden Co., Ltd, Zibo, Shandong, China

Liquid nitrogen fracturing and hot dry rock geothermal development are both emerging technologies in the field of energy. However, during the extraction of geothermal energy, it can cause the evolution of geological fractures, leading to the diffusion of groundwater and pollutants, thereby causing environmental pollution issues. Currently, geothermal energy has become a focal point in the global development of renewable energy. However, traditional hydraulic fracturing methods used in harnessing geothermal resources suffer from limitations such as limited fracture creation, uncertain initiation points, and environmental pollution. In contrast, liquid nitrogen has emerged as a promising reservoir stimulation technique, exhibiting significant effects on rock fracturing. In this study, we conducted three-point bending tests on granite samples subjected to liquid nitrogen treatment at temperatures of 300°C, with varying numbers of cooling cycles. Changes in fundamental mechanical parameters were analyzed. Additionally, through acoustic emission monitoring, we studied the variations in characteristic parameters of acoustic emissions under different cooling cycle conditions. Furthermore, based on the theory of energy evolution, we analyzed the energy evolution process during sample failure under different cooling cycle conditions. Using a compact scanning electron microscope, we observed changes in the microstructure of granite and analyzed the influence of cooling treatment on its surface characteristics and failure modes, thereby revealing the thermal damage process of granite. Moreover, by employing a non-metallic ultrasonic testing analyzer, we scanned the fracture surface morphology of granite and investigated the variations in fracture surface morphology features and surface roughness parameters caused by cooling treatment. The results indicate that liquid nitrogen cooling treatment can more effectively reduce the mechanical properties of rocks, and this effect is further enhanced at high temperatures. Under the condition of 300°C, after undergoing different cycles of liquid nitrogen cooling, granite will exhibit a more diverse macroscopic and microscopic structural failure characteristics, consistent with the expected formation of fluid flow channels in high-temperature rock formations.

## KEYWORDS

liquid nitrogen, granite, mechanical properties, failure characteristics, acoustic emission, cracks

# 1 Introduction

Liquid nitrogen fracturing technology is an emerging technique for extracting geothermal hot dry rock resources, which can significantly improve the fracture structure of high-temperature formations and enhance the efficiency of geothermal energy extraction. However, Liquid nitrogen fracturing technology may have some significant impacts on the ecological environment. Firstly, the preparation of liquid nitrogen and the construction of geothermal reservoirs require a large amount of water resources, which could potentially damage water supply systems and ecosystems in certain areas. Secondly, the used wastewater and waste materials may contain certain chemicals or heavy metals, posing a certain threat to water sources and ecosystems. Thirdly, geothermal energy extraction through Liquid nitrogen fracturing technology can cause surface changes, which may have a significant impact on local topography, vegetation, animal habitats, and ecosystem stability. Therefore, it is important to be mindful of environmental protection and minimize potential impacts on local ecosystems during the process of energy extraction. Understanding the specific degradation effects of Liquid nitrogen fracturing technology on hot dry rock reservoirs is crucial prior to engaging in geothermal energy extraction and environmental protection.

Energy is a fundamental driver of sustainable development and societal progress, intricately intertwined with national security and the overall well-being of a society. Throughout history, energy revolutions have propelled industrial advancements and shaped the global landscape (Wang et al., 2020). Amidst the escalating challenges of environmental pollution, climate change, and the depletion of fossil fuel reserves, there is a growing sense of urgency to prioritize the development and utilization of clean, renewable energy sources (Batchelor, 1985; Li et al., 2019; Chen et al., 2022; Kang et al., 2023). Geothermal energy, a noteworthy non-fossil fuel source, offers diverse applications along with its inherent cleanliness and recyclability. Its vast reserves position geothermal energy as a vital alternative for future societal development. Geothermal resources encompass hydrothermal and enhanced geothermal systems (EGS), classified based on extraction conditions and origins (Climo et al., 2016). Hydrothermal resources currently dominate global geothermal utilization, accounting for approximately 10% of identified reserves. Conversely, EGS represents an emerging strategic energy source, with the potential to drive global energy growth. Acting as a reservoir for geothermal energy within the Earth's interior, EGS epitomizes a widely distributed, abundant, and environmentally friendly geothermal resource. Typically comprised of granite, granodiorite, and biotite granite, EGS reservoir rocks exemplify common compositions (Lu and Wang, 2015). EGS geothermal resources primarily refer to economically viable, shallow-depth, high-temperature rock bodies with low permeability. The energy contained within EGS reservoirs at depths of 3–10 kilometers is much greater than that of global fossil fuels (Xu et al., 2012). The effective development of EGS resources holds significant implications for global energy restructuring, combating climate change, and bolstering air quality control (Ma et al., 2020). However, the challenges lie in the low porosity, low permeability, compactness,

and substantial burial depth of high-temperature EGS resources, making extraction difficult. To establish effective hydraulic connections, enhance heat transfer efficiency, and surmount these obstacles, the U.S. proposed the concept of EGS. EGS entails the construction of geothermal reservoirs using artificial methods and comprises two subsystems. The first subsystem centers around developing and constructing underground heat reservoirs, achieved by enhancing reservoir permeability through various stimulation techniques. This allows for the creation of artificial reservoirs within low-porosity, low-permeability, high-temperature rock formations. The injection of cold water into the reservoirs via injection wells facilitates heat extraction, subsequently enabling the extraction of hot water or steam to the surface through production wells. The second subsystem involves utilizing the extracted geothermal water for on-surface power generation and heating systems. High-temperature water is a crucial resource for electricity generation, with the cooled water subsequently being recycled back into the underground reservoir (Wang and Li, 2008). This technology maximizes the utilization of deep geothermal resources distributed worldwide, offering substantial competitive advantages in terms of environmental impact, climate suitability, and economic viability.

Creating effective fluid pathways within EGS reservoirs poses a significant challenge. Reservoir stimulation techniques, such as hydraulic fracturing, thermal stimulation, and chemical stimulation, are commonly employed (Guo et al., 2020). Among these techniques, hydraulic fracturing currently stands as the most widely utilized and efficient method for reservoir modification (Xu et al., 2015; Xue et al., 2023a). Through hydraulic fracturing, fractures are generated, providing essential flow channels for fluid heat transfer. However, practical engineering often yields a single large fracture, which fails to meet the desired requirements of sufficient heat exchange area in EGS projects. Additionally, traditional hydraulic fracturing techniques entail uncertainties in fracture initiation, environmental pollution, and the risk of induced seismic events (Chen et al., 2019). At the same time, the chemical additives used in hydraulic fracturing techniques and chemical stimulation methods may contaminate groundwater and cause environmental pollution. In light of the drawbacks associated with traditional reservoir stimulation technologies, it is imperative to propose a new reservoir fracturing technique. Liquid nitrogen, as an innovative waterless fracturing technique, holds promise for EGS development (Huang and Meng, 2018). When dry rock contacts liquid nitrogen as the fracturing fluid, considerable thermal stress arises due to the substantial temperature difference between the two (Zhang S. et al., 2018). Consequently, numerous thermally induced cracks emerge in the reservoir, facilitating the establishment of a fracture network in EGS reservoirs. Liquid nitrogen undergoes a phase transition to gas under high temperatures, which further increases the extent of fracturing in reservoir rocks. Nitrogen gas itself is colorless and odorless, belonging to inert gases, and does not cause pollution to the environment. Against this engineering backdrop, exploring the cooling treatment of high-temperature rocks using liquid nitrogen serves as a vital foundation for the application of waterless fracturing in oil and gas extraction, geothermal resource development, and deep rock mechanics

studies (Wang et al., 2023; Xue et al., 2023b). Furthermore, this study's sequence of experiments and numerical calculations elucidates the potential application of nitrogen-induced fracturing in EGS development, offering guidance and technical parameters for nitrogen-induced fracturing in geothermal development.

The liquid nitrogen fracturing technology has not been applied in actual engineering of hot dry rock reservoirs yet. Scholars both domestically and internationally have conducted extensive research on the feasibility and mechanism of this technology. Cai et al. (2015) summarized the mechanism and key technologies of rock fracturing using liquid nitrogen. They pointed out that liquid nitrogen fracturing has advantages such as high efficiency and effective extraction of reservoir heat energy. Cai et al. (2016b) and Memon et al. (2020) conducted a series of mechanical experiments to research the mechanical characteristics and surface changes of rock under liquid nitrogen cooling. They analyzed the mechanism and influencing factors of rock fracturing induced by liquid nitrogen. Furthermore, the potential application of liquid nitrogen fracturing technology in petroleum engineering and shale gas development was explored, alongside the proposition of utilizing liquid nitrogen jet fracturing as a technique to enhance reservoir production. Through numerical simulation and experimental verification, the findings demonstrated that liquid nitrogen jet fracturing has obvious advantages compared to conventional liquid nitrogen fracturing techniques. Li et al. (2016) proposed a new liquid nitrogen gasification fracturing technology for low-permeability oil and gas reservoirs. Zhang et al. (2015) conducted laser microcosmic observation experiments and found that the cooling of coal by liquid nitrogen can cause thermal stress and stress concentration, resulting in the generation and expansion of microcracks within the original samples. Grundmann et al. (1998) conducted experiments on shale fracturing with liquid nitrogen, and their findings displayed that compared to traditional extraction methods, liquid nitrogen fracturing can increase gas production rate by up to 8%. Coetzee et al. (2014) discovered that fracturing with liquid nitrogen is capable of encouraging the development and expansion of rock fractures. According to McDaniel et al. (1997), when liquid nitrogen is introduced into coalbed gas reservoirs, it produces thermal shock, which causes physical changes in the fracture surfaces, impeding the closure of hydraulic fractures and thermally induced fractures.

Stephen (2013), in an article introducing waterless fracturing, demonstrated through experiments the influence of thermal impact on rocks during liquid nitrogen fracturing. Cha et al. (2014) found that when liquid nitrogen gets into interaction with rocks, a temperature gradient is formed on the surface, causing internal micro-damage to the rocks. When liquid nitrogen gets into interaction with the adjacent medium near the borehole, a cold impact is generated, causing severe contraction of the rock framework, resulting in fracture and the generation of numerous microcracks. Finnie et al. (1979) studied the fracture propagation pattern of rocks after liquid nitrogen treatment by injecting liquid nitrogen into the center of cubic rock samples and provided an analytical solution for the elastic body in a semi-infinite space under cooling conditions.

The process of developing enhanced geothermal reservoirs with the aid of liquid nitrogen fracturing technology differs from other reservoir modification methods. When exposed to high-temperature rock, liquid nitrogen generates significant thermal stress on the reservoir surface, resulting in the formation of numerous thermal-induced cracks and intricate fracture networks. These fractures facilitate the expansion of heat transfer surfaces, aligning with our development objectives.

Several studies have demonstrated that different cooling techniques exert notable influences on the mechanical characteristics of granite and shale. For instance, natural cooling and water cooling alter the mechanical performance of granite, with water cooling treatments being detrimental to its mechanical properties. Furthermore, liquid nitrogen cooling induces considerable damage to the mechanical characteristics of both granite and shale, leading to a reduction in peak stress, elastic modulus, longitudinal wave velocity, and other key mechanical characteristics (Wang et al., 2013; Cai et al., 2016a; Huang et al., 2016; Liang et al., 2018; Wu et al., 2018; Liu et al., 2023).

In addition, the thermal stresses caused by rapid temperature changes significantly affect rock integrity, resulting in diverse variations in the mechanical parameters of different rock types during thermal cycling processes. Coarse-grained heterogeneous rocks tend to exhibit crack propagation, whereas fine-grained homogeneous rocks tend to experience crack closure (Hall, 1999; Kim et al., 2014; Zhang F. et al., 2018).

Based on the aforementioned investigations, the impacts of various thermal cycling frequencies on rock mechanics, acoustic emission characteristics, and energy evolution patterns can be studied through three-point bending tests and acoustic emission monitoring systems. These research endeavors contribute to a comprehensive comprehension of how rock's physical and mechanical qualities change during liquid nitrogen-assisted enhanced geothermal reservoir development, providing scientific foundations for engineering practices.

## 2 Experimental materials and procedures

### 2.1 Experimental materials

Based on statistics from internationally representative Enhanced Geothermal Systems (EGS) projects, the predominant lithology of EGS reservoir rocks both domestically and internationally is usually granite (igneous rock) or metamorphic rock. Therefore, in this study, granite is chosen as the focus of research. The granite samples used in the experiment exhibit lithological consistency with the rocks found in underground storage reservoirs of liquefied natural gas (LNG), thus making them suitable as load-bearing rock layers for large-scale LNG storage facilities. Following the guidelines outlined by the International Society for Rock Mechanics (ISRM) (Hardy, 1981), the specimens are prepared as semi-circular disk-shaped samples with a diameter (D) of 76 mm, radius (R) of 38 mm, thickness (B) of



30 mm, and an initial crack length ( $a$ ) of 14 mm. To ensure uniformity, meticulous care is taken to polish the surfaces of the specimens, resulting in a smooth and even finish. Granite as shown in Figure 1.

## 2.2 Experimental equipment

As shown in Figure 2, a variety of instruments and equipment were used in the experiment, including a heating chamber, liquid nitrogen tank, vernier caliper, electronic scale, rock mechanics testing machine (capable of applying loads perpendicular to the sample surface), non-metallic ultrasonic testing and analysis instrument, and a three-point bending fixture. These devices were utilized for different experimental objectives to ensure the accuracy of the experiment.

## 2.3 The experimental scheme

To conduct the experiment, the selected rock samples were categorized into multiple groups and assigned numerical labels based on the number of cycles: 3, 5, 7, 9, 15, and 20. Initially, each sample was subjected to a controlled heating process inside a calibrated heating chamber, gradually reaching a target temperature of 300°C. After reaching the target temperature, the specimen is kept at a constant temperature in the heating chamber for 3 hours. This ensured uniform thermal conditions throughout the samples, guaranteeing consistent heating across both their internal and external regions. Following the completion of the thermal treatment, the samples were swiftly extracted from the heating chamber and rapidly immersed in a liquid nitrogen tank for an hour-long cooling period. Careful attention was paid to prevent overflowing of the liquid nitrogen, considering the vigorous boiling that ensues when immersing high-temperature rocks. Once the cooling process was finalized, the samples were placed back into

the same controlled environment for subsequent three-point bending experiments. The experiment utilizes the CSS-44100 Testing Machine. To ensure the accuracy and reliability of the experiment, we set up multiple parallel samples for each cycle.

The specimen was securely affixed to the three-point bending fixture, ensuring compatibility between its size, shape, and fracture behavior with the adjusted lower support rollers and upper loading head. During the three-point bending experiment, displacement control is employed, with a loading rate set at 0.1mm/min. Adjacent to this setup, a high-speed camera was strategically positioned to meticulously record the temporal evolution of the specimen's response to the loading conditions, diligently transmitting the acquired data to a dedicated computer system. Consequently, a comprehensive load-displacement curve was meticulously constructed, while purpose-built image analysis software enabled an intricate examination of the surface displacement and strain fields exhibited by the specimen. By meticulously analyzing the displacement of the loading head, the applied load, and the unique deformation characteristics observed near the crack tip area, we were able to accurately calculate the fracture toughness and crack propagation velocity inherent to the rock material.

## 3 Mechanical behavior of granite

The load-displacement curve serves as an invaluable tool to elucidate the intricate deformation and failure mechanisms intrinsic to the bending process of granite specimens. Figure 3 shows a classic load-displacement curve of samples. Typically, this curve manifests itself through three distinctive phases: the elastic stage, the elastic-plastic stage, and the failure stage. By referring to the initial dataset, which has not undergone any treatments, we can gain insightful observations.

During the elastic stage (AB), granite demonstrates a linear relationship between its deformation and the applied load,



FIGURE 1  
Granite sample.



FIGURE 2  
Experimental equipment: (A) Electronic scale; (B) Non-metallic ultrasonic monitoring analyzer; (C) Liquid nitrogen tank; (D) Heating box.

meticulously abiding by Hooke's Law. Within this stage, the deformation encountered by the granite sample proves to be entirely recoverable, restoring the specimen to its original configuration upon unloading.

As the applied load progressively intensifies, the elastic-plastic stage (BC) commences, whereby the deformation no longer mirrors the applied load in a linear fashion, prompting the characteristic curve to deviate from its linear trajectory. Intriguingly, this stage showcases a combination of both elastic and plastic deformation within the granite sample, thereby instigating the creation of intricate

networks of microcracks and voids. Importantly, it is crucial to note that the plastic deformation encountered by the granite specimen proves to be inherently irreversible, inescapably leaving a discernible degree of residual deformation upon unloading.

Ultimately, as the load surpasses a critical threshold, the failure stage (post C) ensues, heralding a profound deviation from the previously established linear relationship between load and deformation. Indeed, within this stage, the granite specimen experiences a rapid progression in microcrack propagation and void connectivity, invariably resulting in a precipitous decline in both strength and stiffness.

To investigate the impact of the number of cycles at a constant temperature on the load-displacement curve of granite, we conducted a comparative analysis of the curves presented in Figure 4. Herein, we derive the following observations. In the elastic stage, the load-displacement curve manifests a gentler slope with the number of treatments rises, signifying a decrease in the elastic modulus of granite. However, the resulting variations were found to be inconspicuous. During the elastic-plastic deformation stage, the length and slope of this phase exhibit a pattern of initial ascent followed by subsequent descent, reaching an extremal point after 20 cycles. This intriguing trend suggests that granite's yield strength and plastic deformation capability experience progressive augmentation before diminishing returns set in as the number of cycles escalates, attaining their zenith after 20 cycles. In the failure stage, the maximum load displays a comparable pattern of progression before reaching a turning point at 20 cycles. This phenomenon illuminates the fact that granite's compressive strength and failure capacity undergo an

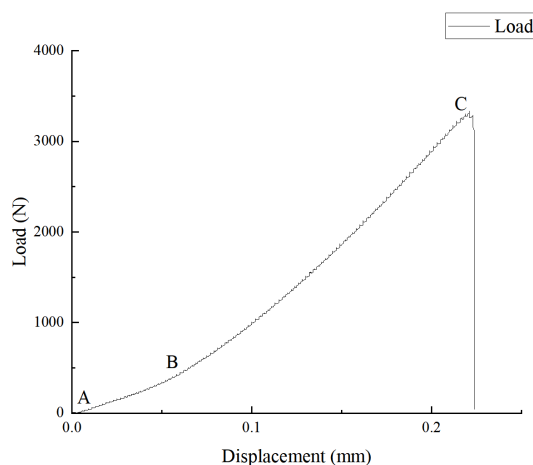
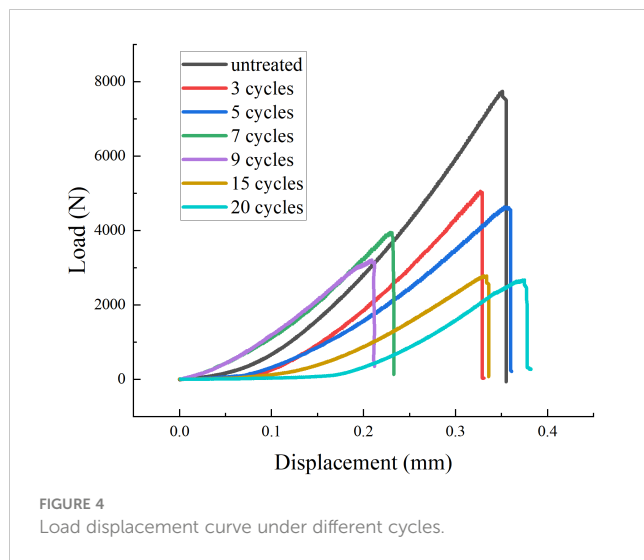


FIGURE 3  
Load-displacement curve.

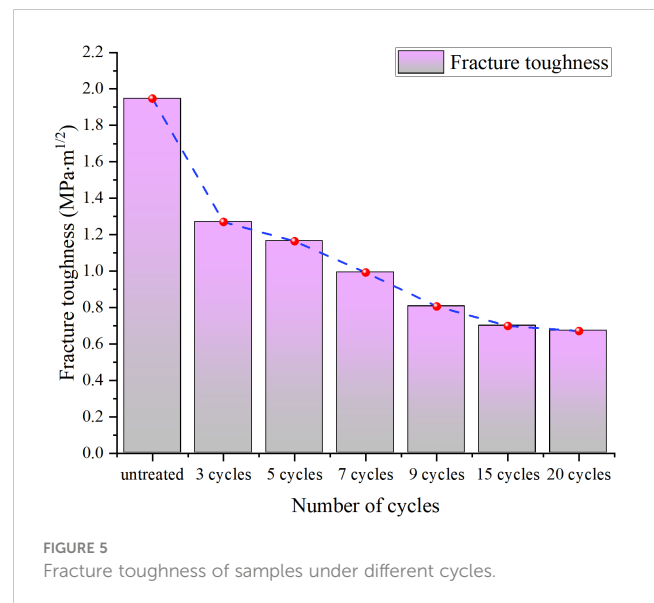


analogous progression, culminating in their peak performance after 20 cycles. Furthermore, computational analyses corroborate these findings by documenting an analogous evolution in fracture toughness. Collectively, these observations furnish indisputable evidence that varying the number of cycles under constant temperature conditions yields a weakening impact on the mechanical characteristics of rocks, concurrently reaching an optimal state approximately after 20 cycles.

Fracture toughness analysis is conducted next. Fracture toughness is a significant physical-mechanical parameter of rocks and an important indicator in rock fracture mechanics. Three-point bending experiments are frequently employed to ascertain the fracture toughness, which serves as a measure of a rock's resistance to both crack initiation and propagation. It is a crucial measure in rock fracturing processes and requires careful attention. Therefore, studying the variation pattern of fracture toughness in granite under the influence of liquid nitrogen can provide valuable insights.

Figure 5 shows the Fracture toughness of samples under different cycles. In this study, the fracture toughness of granite was initially calculated to be  $1.95 \text{ MPa}\cdot\text{m}^{1/2}$  without any treatment involving liquid nitrogen. After several liquid nitrogen treatments, the Fracture toughness of granite continuously decreased to  $0.70 \text{ MPa}\cdot\text{m}^{1/2}$ . It is obvious that the cracking resistance of granite tends to weaken after liquid nitrogen circulation. This could be attributed to changes in microstructures and stress distribution within the granite caused by the liquid nitrogen cycling, resulting in nonlinear variations in fracture toughness. Therefore, it is essential to consider the number of liquid nitrogen cycles during practical engineering construction to achieve optimal results.

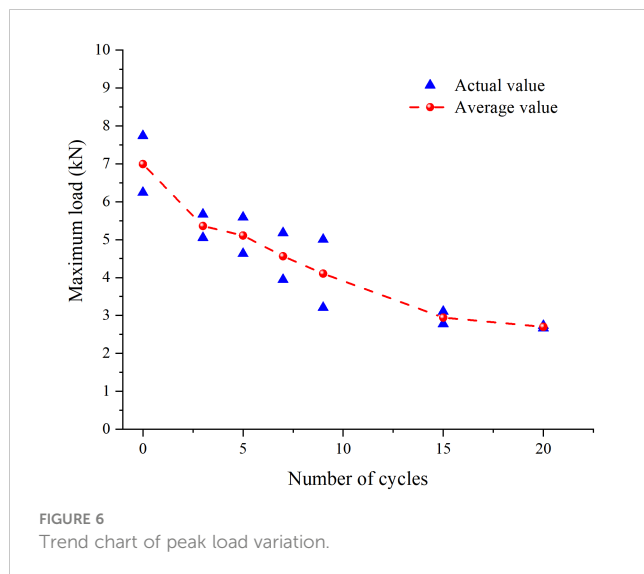
Through observation and analysis, it is evident that the untreated granite, serving as the control group, reached a peak load of 7742.1 N and a maximum displacement of 0.35 mm. The fracture toughness value determined at this specific point was  $K=1.95 \text{ MPa}\cdot\text{m}^{1/2}$ . After 3 cycles, the peak load increased to 5052.0 N, with a maximum displacement of 0.33 mm, resulting in a fracture toughness of  $K=1.27 \text{ MPa}\cdot\text{m}^{1/2}$ . In the case of 5 cycles, the peak load



reached 4630.2 N, with a maximum displacement of 0.35 mm, yielding a fracture toughness of  $K=1.16 \text{ MPa}\cdot\text{m}^{1/2}$ . For 7 cycles, the peak load reached 3946.2 N, with a maximum displacement of 0.23 mm, leading to a fracture toughness value of  $K=0.99 \text{ MPa}\cdot\text{m}^{1/2}$ . As for 9 cycles, the peak load reached 3206.4 N, with a maximum displacement of 0.21 mm, resulting in a fracture toughness of  $K=0.81 \text{ MPa}\cdot\text{m}^{1/2}$ . With 15 cycles, the peak load reached 2780.7 N, while the maximum displacement was 0.33 mm, leading to a fracture toughness value of  $K=0.70 \text{ MPa}\cdot\text{m}^{1/2}$ . Finally, after 20 cycles, the peak load reached 2670.0 N, with a maximum displacement of 0.38 mm, resulting in a fracture toughness of  $K=0.67 \text{ MPa}\cdot\text{m}^{1/2}$ .

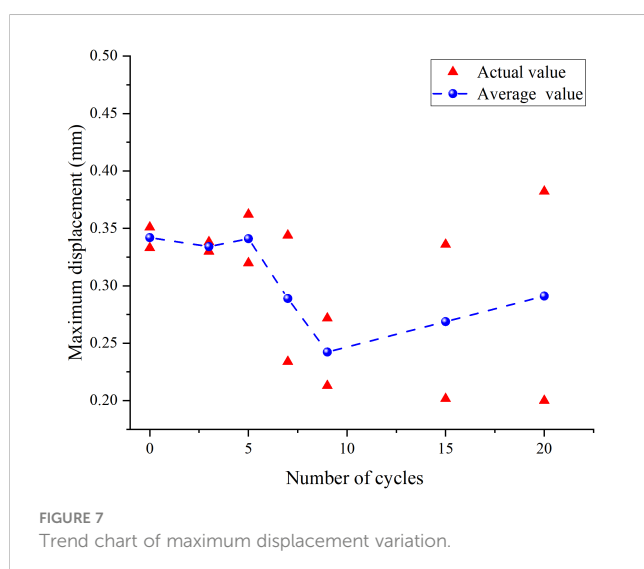
By comparing Figures 4, 5, a distinct correlation can be observed between the variations in peak load and fracture toughness. First, regardless of the number of cycles, the load-displacement curve exhibits initial steady and gradual growth, followed by rapid ascent to the peak before sharply declining upon granite failure. This is a characteristic failure behavior of granite under three-point bending experimental conditions. From the comparison chart, it can be observed that, under the condition of  $300^\circ\text{C}$ , as the number of treatments rises, the maximum peak load shows a decreasing trend. This suggests that the mechanical properties of rocks weaken with an increase in the number of cycles. This could be attributed to the complex physical and chemical processes, such as the generation of microcracks and stress relaxation within the granite, resulting from thermal cycling, leading to nonlinear changes in its mechanical properties.

Figure 6 is the variation trend of load at the peak point of granite under different cycles. Based on Figure 6, it can be seen that, it can be seen that the mechanical properties of granite gradually exhibit a weakening trend with an increasing number of cycles. Firstly, analyzing the relationship between maximum load and cycle number, the average curve of maximum load for both sets of samples shows a downward trend. This suggests that granite undergoes an weaken in its mechanical properties after liquid nitrogen treatment. Excessive cycles of liquid nitrogen treatment



noticeably weaken the mechanical properties of granite, and the more cycles performed, the more pronounced the weakening characteristics. This may be attributed to factors such as thermal stress and thermal shock generated within the granite after liquid nitrogen treatment, affecting its compressive strength and fracture toughness.

Additionally, an examination of the relationship between maximum displacement and cycle number reveals a same pattern. Figure 7 is the variation trend of displacement at the peak point of granite under different cycles. With an increasing number of cycles, the maximum displacement resulting from three-point bending displays an initial decrease followed by an increase. Moreover, as the number of cycles increases, the weakening characteristics become more pronounced. This phenomenon may be attributed to factors such as thermal expansion and contraction within the granite after liquid nitrogen treatment, resulting in changes in internal strain and displacement and thus affecting the plastic deformation capacity and fracture toughness of the granite. The variation pattern of load displacement at the peak point may be caused by the combined



effect of liquid nitrogen effect and the mechanical properties of granite itself.

## 4 Analysis of acoustic emission characteristics of granite

### 4.1 Introduction of acoustic emission experiment

Materials, when subjected to external forces and temperature fluctuations, undergo deformation or fracture due to stress variations at structural defects. During this process, the material rapidly releases energy, generating a transient elastic wave and emitting sound. This phenomenon is known as acoustic emission (Grosse et al., 2021).

By analyzing the collected acoustic emission signals in experiments, the damage status of rocks during the loading process can be understood. The acoustic wave signals are precisely processed, and then damage assessment is conducted based on the variation patterns of characteristic parameters (Grosse et al., 2021). Parameter analysis is the most commonly used signal processing method. In this experiment, ring count and energy count are adopted as indicators for single-parameter analysis.

### 4.2 Acoustic emission characteristics of granite deformation and failure

To acquire acoustic emission data from high-temperature granite during the three-point bending process, a real-time acoustic emission acquisition system was employed. This system facilitated the collection of signals emitted by the granite as it underwent failure under different cycle numbers at a constant temperature. Figure 8 shows the acoustic emission ringing counts of granite under different cyclic conditions.

Upon analyzing the initial dataset, a clear correlation between the three stages of failure in the three-point bending process and the fluctuation in acoustic emission ring count was observed, as depicted in the Figure 8. During the initial elastic stage of granite loading, the damage is minimal, resulting in a low ring count rate and stable signals. The cumulative ring count curve exhibits slow and nearly horizontal growth. In this stage, the acoustic emission signals mainly arise from the closure of pre-existing cracks within the rock specimen and the sliding friction between rock particles. In the elasto-plastic deformation stage, the ring count signals remain inactive. However, compared to the elastic stage, events in this stage exhibit larger amplitudes, and the cumulative ring count gradually increases with an increasing slope in the curve. This is because granite, during this stage, achieves its optimal load-bearing state through the dislocation slip of microcracks and subtle adjustments in structure. Consequently, new microcracks and pores are generated within the granite, leading to an increase in acoustic emission signals.

During the stage of unstable crack propagation, which is close to the failure stage, as the loading continues, there is a sudden increase



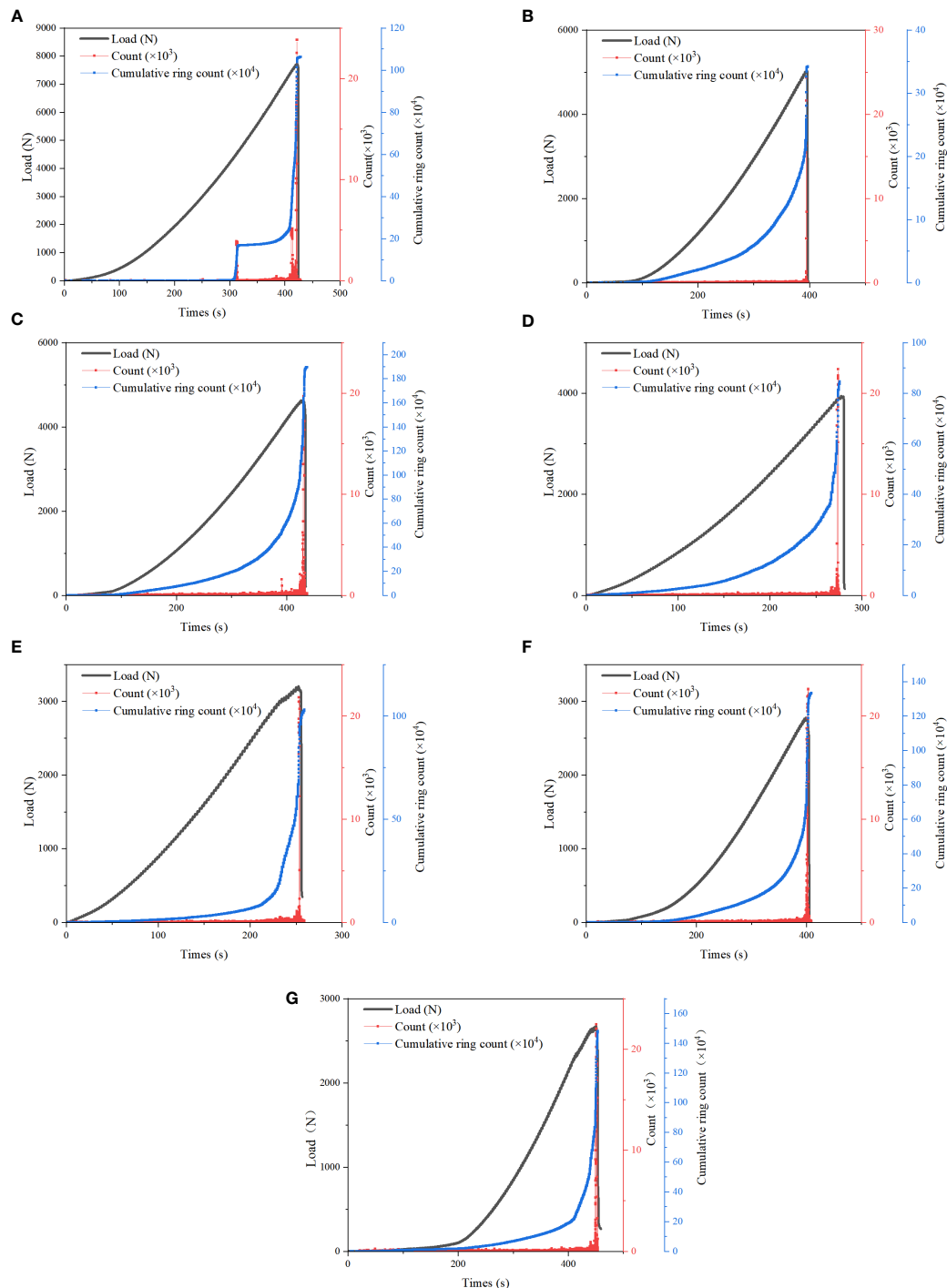


FIGURE 8

Ringing counts of granite under different cycle conditions: (A) untreated; (B) 3 cycles; (C) 5 cycles; (D) 7 cycles; (E) 9 cycles; (F) 15 cycles; (G) 20 cycles.

in the ring count, and the signals become active with the appearance of multiple sharp peaks. The cumulative ring count exhibits a rapid and concave-shaped growth, with both the magnitude of change and the slope of the curve increasing quickly. In this stage, the rock begins to fracture, leading to the generation, propagation, and connection of a large number of microcracks, forming macroscopic fractures. In this stage, the acoustic emission signals' distinctive parameters exhibit

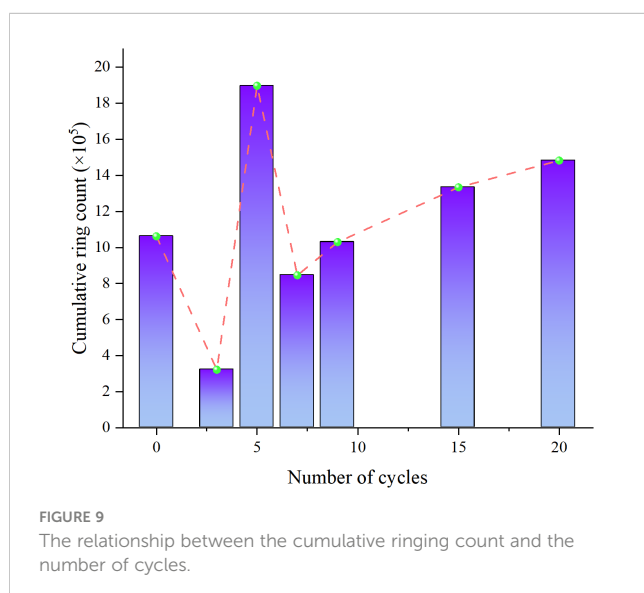
a significant association with the level of rock failure, thereby offering valuable insights into the mechanisms and progression of rock failure.

During the stage of failure, the ring count signal exhibits a rapid increase, showing distinct bursts and pulsations. The cumulative ring count curve displays a steep increasing trend, corresponding to the peaks on the load-displacement curve. This phenomenon can be attributed to the extensive fracturing and fragmentation experienced

by granite during this particular stage, leading to the substantial release of acoustic energy. Furthermore, during the failure stage, the ring count increases rapidly, reaching its peak at the moment when the curve descends, and the magnitude of the increase in the cumulative ring count is the greatest at this point. This indicates that the rock experiences large-scale fracturing and fragmentation, releasing tremendous acoustic energy. After the rock sample completely loses its load-bearing capacity and fails, the ring count rapidly decreases to zero as the stress within the rock mass is released. This finding suggests that no additional cracks or damages are generated within the rock during this stage, leading to the absence of further acoustic emission signals.

The analysis of the cumulative ring count and cycle number in Figure 9 reveals significant effects of liquid nitrogen on the granite. The trend displays a discernable pattern of initial decrease followed by subsequent increase, reaching its peak between 5 to 7 cycles. This indicates that the development of cracks and damages within the granite initially intensifies and then diminishes as the cycle number increases, with a peak occurrence between 5 and 7 cycles. The cumulative ring count of the liquid nitrogen-cooled granite exhibits a consistent trend that aligns closely with the load-displacement curve. Additionally, these signals can reflect the process and mechanisms of granite failure.

Figure 10 shows the acoustic emission energy counts of granite under different cyclic conditions. As depicted in the Figure 10, the variations in energy counting follow a similar pattern to that of ring counting, allowing for analysis across three distinct stages. During the stage of compression and densification of granite fissures, internal microcracks and pores gradually undergo closure due to pressure, resulting in low energy counting signals. The magnitudes of these signals are typically in the single digits, and the cumulative energy counting curve remains relatively unchanged with an almost horizontal slope. This suggests that, during this stage, the acoustic emission signals in granite mainly arise from the closure of pre-existing cracks and friction between particles, with minimal energy release. During the elastic-plastic stage, it is observed that the energy counting amplitude experiences a marginal increase while maintaining a relatively low level.



Towards the end of this stage, the cumulative energy counting curve begins a gradual ascent. This indicates that new microcracks and pores are being generated in the granite, leading to an increase in energy release, albeit still at a relatively low level.

During the stage of crack propagation, which is close to the point of failure, there is an increase in energy counting. The cumulative energy counting curve exhibits distinct abrupt points of rapid increase, with the cumulative values rising swiftly. At this stage, the rock begins to fracture, and a lot of microcracks generate, propagate, and connect to form macroscopic fissures. The magnitude of acoustic emission energy counting is mostly affected by two elements: the frequency of instantaneous acoustic emission events and the amount of strain energy released by the rock during the formation of microcracks. Therefore, it may be concluded that the granite has strong mineral particle connection before the cooling process. The bonds between some mineral particles, however, are broken after undergoing cryogenic cooling treatment due to thermal stress. As a result, there is an increased propensity for relatively stable microcracks to merge, which eventually results in unstable crack propagation and failure. This process is characterized by the release of a substantial amount of acoustic energy within the rock, resulting in a pronounced escalation in both energy counting and cumulative energy counting.

During the stage of failure, when the load-displacement curve undergoes a sudden decrease, the energy counting reaches a peak of magnitudes in the tens of thousands, and the cumulative energy counting exhibits the greatest variation at this point. This indicates that the rock undergoes extensive fracture and fragmentation during this stage, releasing tremendous acoustic energy. The rock specimen completely loses its bearing capacity, resulting in a macroscopic failure surface. It suggests that the rock no longer generates new cracks and damage during this stage, and the acoustic emission signals cease to occur. In this stage, the characteristic parameters of the acoustic emission signals exhibit a strong correlation with the rock's failure strength, offering valuable insights into the magnitude and pattern of rock failure.

Analyzing the connection between the cumulative energy counting and the number of cycles in Figure 11, it is evident that the liquid nitrogen cooling treatment has an important impact on the cumulative energy counting of granite, exhibiting a trend of initial decrease followed by increase, with the maximum value reached between the 5th and 7th cycles. The cumulative energy counting exhibits an initial decrease followed by a subsequent increase as the number of cycles rises. This observation suggests that the release of internally generated acoustic energy in the granite follows a similar pattern, with the peak occurring between the 5th and 7th cycles. The cumulative energy counting of the granite, as influenced by the liquid nitrogen cooling treatment, exhibits a coherent trend that aligns closely with the load-displacement curve.

### 4.3 Classification of AE cracks

Firstly, the RA and AF values were calculated using data collected by sensors in acoustic emission experiments. Subsequently, a density plot was generated to analyze the differences in AF-RA distribution

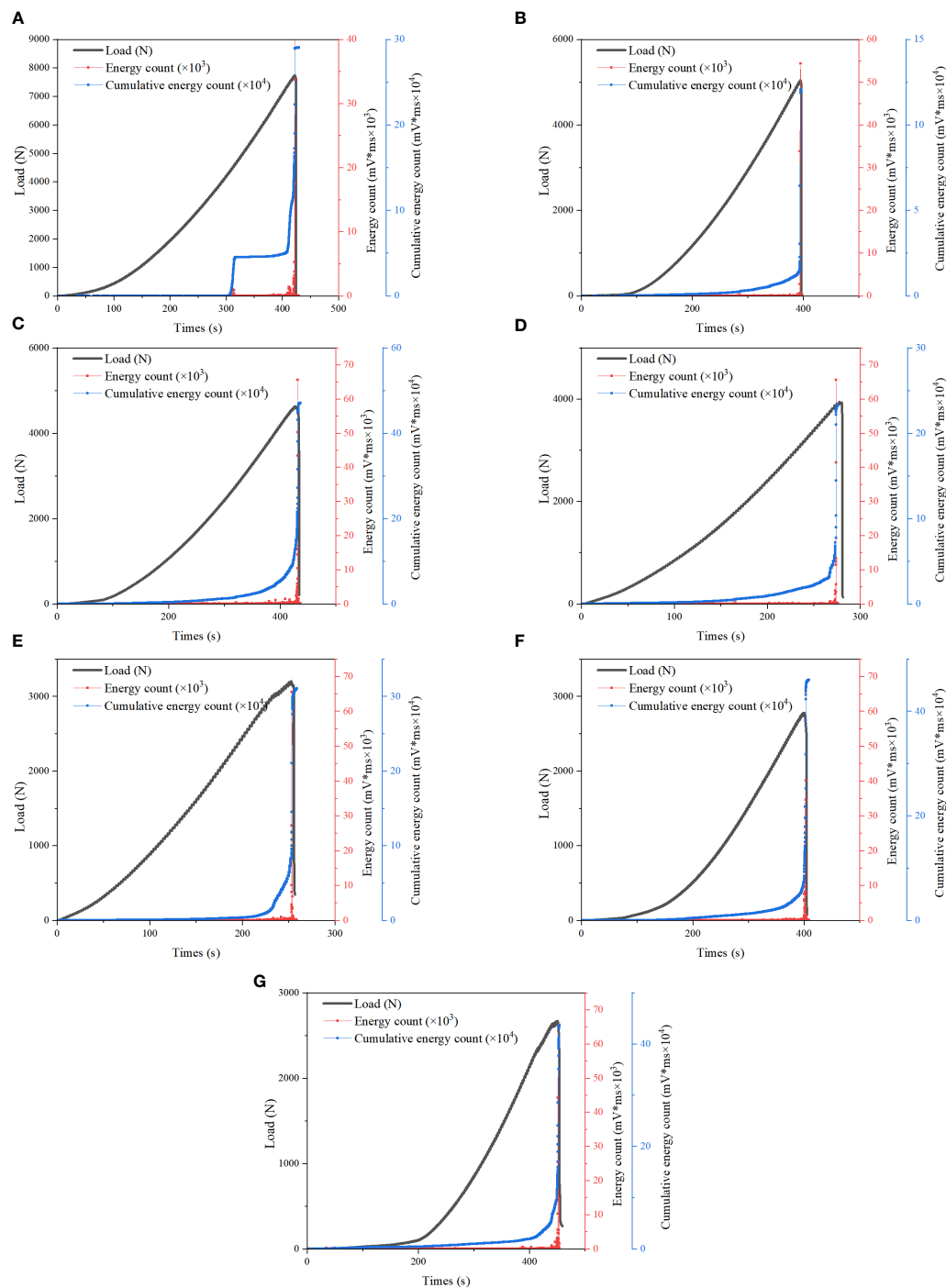


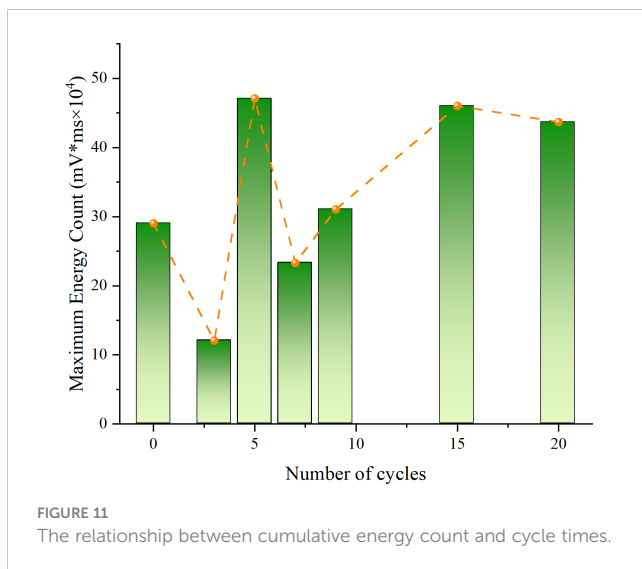
FIGURE 10

Energy counts of granite under different cycle conditions: (A) untreated; (B) 3 cycles; (C) 5 cycles; (D) 7 cycles; (E) 9 cycles; (F) 15 cycles; (G) 20 cycles.

for different experimental conditions. We selected two sets of experimental results. To begin with, the analysis of the first dataset reveals the density plot of AF-RA data for granite obtained from the acoustic emission experiment, as illustrated in Figure 12. The analysis demonstrates that granite exhibits a wide range of AF values, predominantly falling between 0–400 kHz. This indicates that the acoustic emission signals of granite encompass various frequency components, reflecting the complexity of its internal structure and composition. Moreover, the majority of AE signals in granite possess

low RA values, primarily below 40  $\mu\text{s}/\text{V}$ . Furthermore, it is noteworthy that most of the high-density data points lie above the diagonal line, which signifies tensile failure in the rock, while data points below the diagonal line indicate shear failure. This observation implies that the main failure mechanism observed in the acoustic emission experiment for granite is predominantly tensile failure rather than shear failure.

Lajtai (1969) proposed that in direct shear tests, jointed rock masses exhibit three primary modes of failure: shear failure, tensile



failure, and compressive failure. Additionally, other relevant research has suggested that shear cracks constitute a significant proportion of microcracks formed during compressive tests (compressive failure) and dominate the fracture process. Drawing upon these prior findings and the acoustic emission characteristics observed in our study, it becomes apparent that during three-point bending tests, the rock experiences the formation of tensile cracks, shear cracks, and mixed-mode cracks, with tensile cracks being the predominant type of microcrack. Consequently, failure or flexural failure in such tests occurs primarily under a tensile-dominated state. These results highlight the distinct stress conditions and failure modes exhibited by rocks in three-point bending tests compared to direct shear tests and compressive tests.

Subsequently, the analysis of the second set of data yielded results that were largely consistent with those of the first set. Here, we provide a brief analysis: The density plot of AF-RA data for the granite obtained from the acoustic emission tests is presented in Figure 13. The analysis reveals that the AF values of the granite exhibit a wide distribution range, primarily between 0 and 400 kHz. Most of the AE signals recorded from the granite correspond to low RA values, predominantly below 40  $\mu\text{s}/\text{V}$ . Furthermore, data points with medium to high density are predominantly located above the diagonal line, which indicates tensile failure, while those below the line reflect shear failure in the rock. These findings corroborate the outcomes derived from the initial dataset, suggesting that the three-point bending tests induce the development of various types of cracks in the granite, including tensile cracks, shear cracks, and mixed-mode cracks. Among them, tensile cracks emerge as the predominant form of microcrack. Consequently, the failure or flexural failure observed is primarily driven by tensile forces.

A three-point bending test on granite was conducted in this work to explore its fracture process using acoustic emission (AE) technology. A density plot of AE signals, specifically the Amplitude/Risetime ratio (RA) and average frequency (AF), was generated to analyze the variations in these parameters. The average frequency AF is the ringing count/duration. The experimental findings are as follows:

The average frequency (AF) of the granite exhibits a wide distribution range, primarily between 0 and 400 kHz, indicating that the AE signals of the granite consist of multiple frequency components. On the other hand, the amplitude/risetime ratio (RA) of the granite shows a narrow distribution range, mainly between 0 and 10. This implies that the AE signals in the granite are predominantly generated and propagated by the formation and extension of microcracks, rather than by the formation and propagation of macroscopic fissures.

The AF-RA density plot of the granite can be divided into three distinct regions, corresponding to different failure modes: tensile failure, shear failure, and mixed mode failure. The region associated with tensile failure is located in the lower left corner of the density plot, characterized by low RA and low AF signals. This indicates that tensile failure generates low-frequency and low-amplitude AE signals. On the other hand, the density plot reveals that the region linked to shear failure is situated in the upper right corner, distinguished by elevated RA and AF signals. This suggests that shear failure produces high-frequency and high-amplitude AE signals. The mixed mode failure region is situated in the middle part of the density plot, displaying moderate RA and moderate AF signals. This implies that mixed mode failure generates AE signals with intermediate frequencies and amplitudes.

And the AF-RA density plot of the granite is directly connected to its mechanical properties and can reflect the failure strength and mode of the granite. Generally, when tensile failure dominates in the granite, it exhibits lower strength, and the AE signals are concentrated in the lower left corner of the density plot. Conversely, when shear failure predominates in the granite, it demonstrates higher strength, and the AE signals concentrate in the upper right corner of the density plot. When the granite experiences mixed mode failure, its strength falls between the two aforementioned modes, and the AE signals are distributed in the middle part of the density plot.

## 5 Ultrasonic testing of granite

Porosity and longitudinal wave velocity are important physical parameters for evaluating the degree of internal structural damage in rocks. Ultrasonic detection experiments were carried out to test and analyze the pore structure of high-temperature granite under different cooling conditions. The experimental procedure employed a non-metallic ultrasonic testing and analysis instrument to transmit and receive ultrasonic signals through high-temperature granite samples. The non-metallic ultrasonic testing and analysis instrument was equipped with two sensor probes, capable of measuring parameters such as amplitude (dB), frequency (kHz), Ultrasonic Time ( $\mu\text{s}$ ), and velocity (km/s). During testing, the two sensor probes were handheld, aligned with the specimen surface, and positioned in an inverted manner. Each specimen was subjected to three repetitions, and the average longitudinal wave velocity was calculated after excluding any outliers. The experimental results indicated a significant decrease in the longitudinal wave velocity of the cooled high-temperature granite, indicating changes in the internal pore structure of the rock.



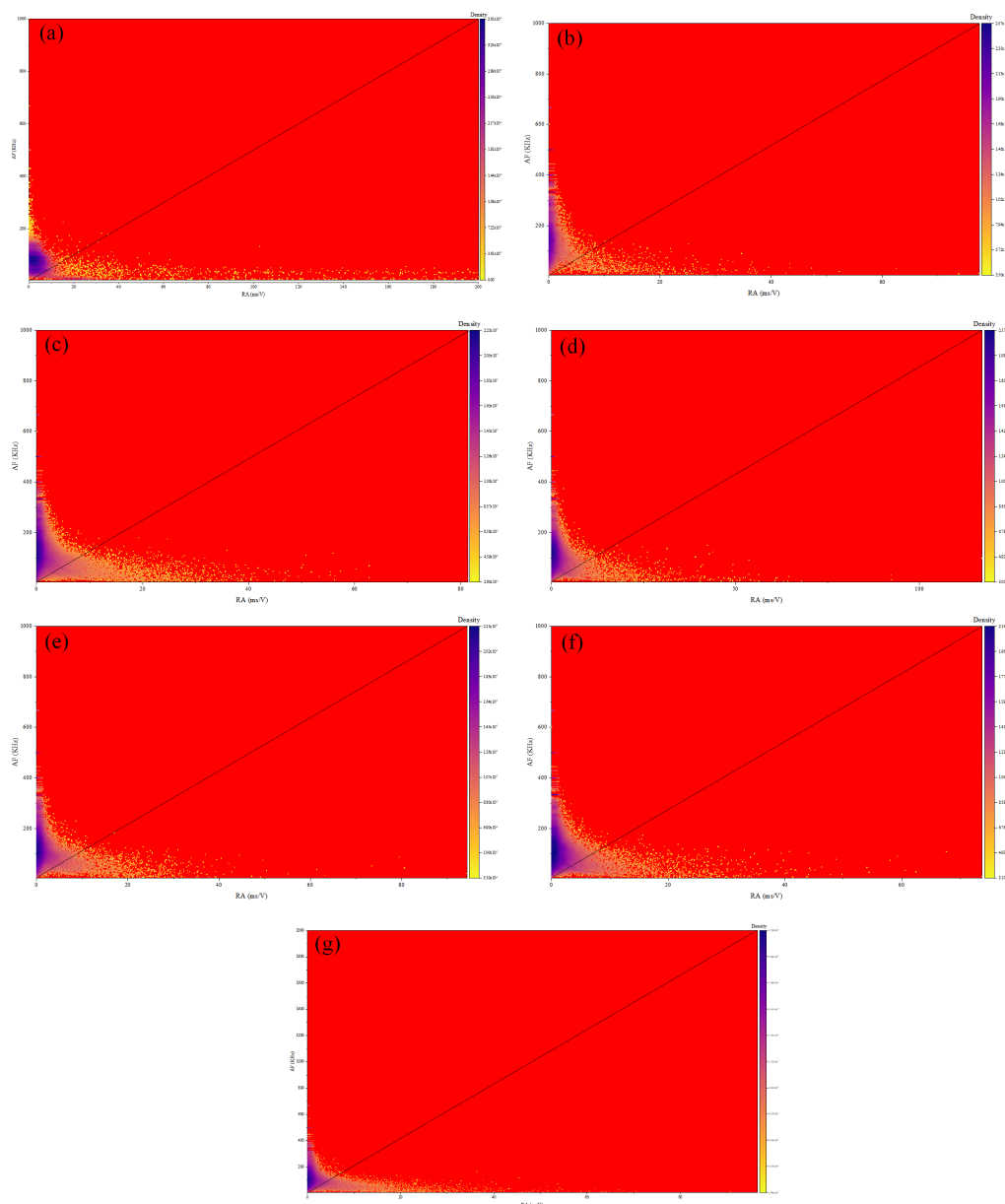


**FIGURE 12** Distribution density map after treatment of different cycles in group 1: (A) untreated; (B) 3 cycles; (C) 5 cycles; (D) 7 cycles; (E) 9 cycles; (F) 15 cycles; (G) 20 cycles.

After being subjected to liquid nitrogen cooling, high-temperature granite experiences significant changes in its internal pore structure and thermodynamic parameters. The application of thermal stress during the cooling process surpasses the tensile strength of the rock, leading to the initiation of new cracks and the propagation of existing ones. Consequently, damaged regions are formed within the rock. In order to investigate the patterns of pore structure changes in cooled high-temperature granite and the varying effects of different cooling methods on rock damage, ultrasonic longitudinal wave velocities were measured using a non-metallic ultrasonic testing and analysis instrument at various stages before and after heating.

A comparison of the fluctuations in longitudinal wave velocity of granite specimens before and after different cycles of high-temperature treatment and liquid nitrogen cooling is given in Figure 14. Prior to the high-temperature cycles and liquid nitrogen cooling, there was little difference in the longitudinal wave velocity among the granite specimens. This was because we initially selected samples with similar wave velocities for the study using ultrasonic straight-through method, aiming to minimize the dispersion and heterogeneity among the specimens. The wave velocity of each specimen was immediately measured using ultrasonic straight-through method after being heated to 300°C in each cycle, and then compared with the results before the high-

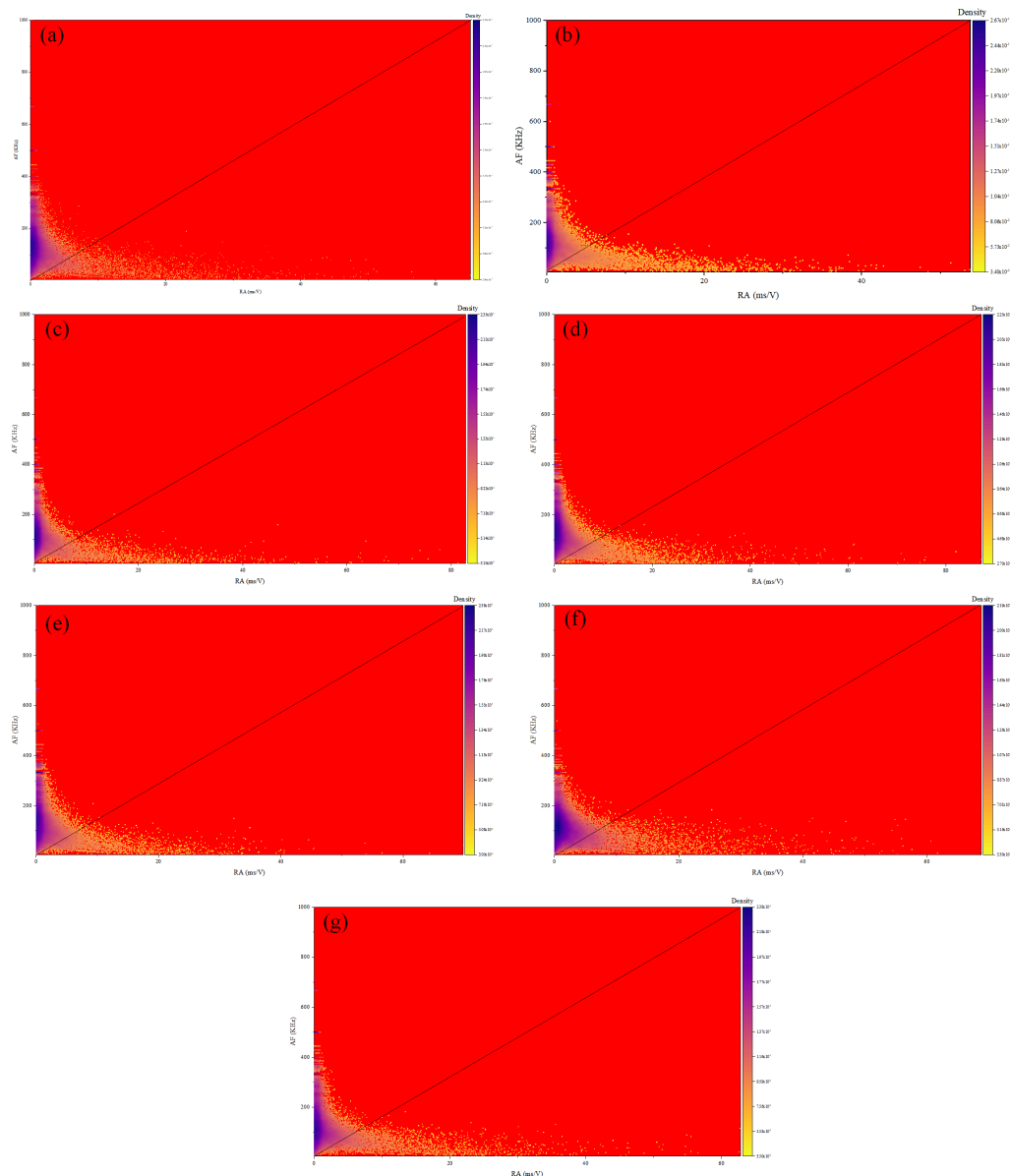


FIGURE 13

Distribution density map after treatment of different cycles in group 2: (A) untreated; (B) 3 cycles; (C) 5 cycles; (D) 7 cycles; (E) 9 cycles; (F) 15 cycles; (G) 20 cycles.

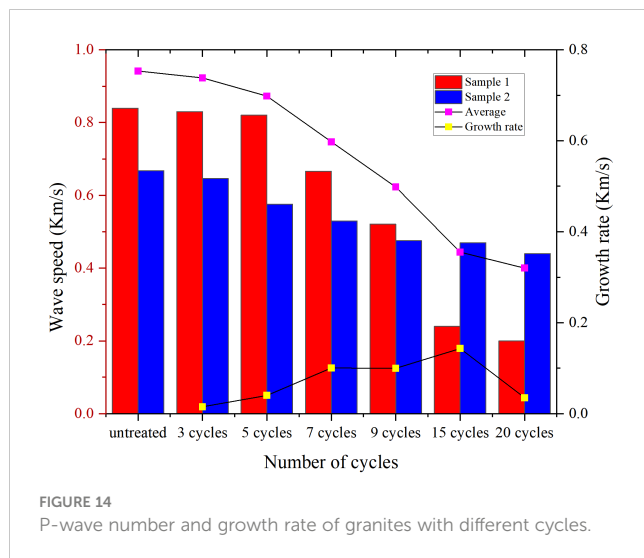
temperature cycles. After the cycles, a slight decrease in the longitudinal wave velocity was observed for each granite specimen. This is primarily attributed to the evaporation of free water in the internal pores of granite when it is heated, leading to an increase in porosity and a decrease in density.

The variation trend of longitudinal wave velocity for each granite specimen under different cycle numbers can be observed from Figure 14. Prior to the 7th cycle, the decay rate of longitudinal wave velocity for each granite specimen in both groups was relatively slow and slightly increased with increasing heating temperature and cooling rate. However, after the 7th cycle, a sharp decline in longitudinal wave velocity was evident for each granite specimen in both groups, with a significant increase observed as the heating temperature and cooling rate increased.

This indicates that high-temperature granite undergoes significant physical changes and structural damage after being treated with liquid nitrogen cooling, transitioning from its original dense and brittle state to a loose and fragile state with increased ductility. Additionally, the thermal stress and strain induced by high-temperature and rapid cooling lead the generation of numerous defects within the granite and the enlargement of existing cracks and pore sizes.

## 6 Conclusion

The main purpose of this study is to investigate the mechanical behavior and damage effects of granite under the influence of liquid



nitrogen. Firstly, the mechanical properties of the rock are explored through three-point bending tests with varying numbers of cycles. Secondly, the acoustic emission characteristics and energy evolution of the granite samples are studied using an acoustic emission monitoring system. The fracture mode of the granite is analyzed using AF-RA acoustic emission cloud mapping. Finally, the changes in internal fractures and pores of the granite are quantitatively analyzed using a non-metallic ultrasonic detector. The main conclusions are as follows:

- (1) The load-displacement curve of granite can generally be separated into three sections. In the elastic stage, under the same temperature conditions, the more cycles there are, the slower the upward trend of the curve and the less significant the variations. In the elastoplastic deformation stage, the length and slope of the stage show different results influenced by the number of cycles. In the failure stage, the trend of the maximum load-bearing capacity of granite exhibits a similar pattern to the aforementioned stages. From the analysis of mechanical data, it can be observed that the peak strength of granite tends to decrease with an increasing number of liquid nitrogen cooling cycles. This indicates that different cycle numbers have a certain impact on weakening the mechanical performance of the rock at the same temperature.
- (2) By analyzing the evolution pattern of acoustic emission (AE) signals in granite, we can identify several characteristics. In the initial compaction stage, the damage effect is weak, and the signal amplitude is low. In the elastic stage, the cumulative ring-down counts show a slow increasing trend, with significant increments and growth rates. In the elastoplastic stage, frequent AE events occur and multiple peak points appear, resulting in a rapid rise of the cumulative count curve that takes on a concave shape. In the failure stage, both types of signals experience sharp growth, with the maximum increment of the cumulative count curve reached. In tension or tension-dominant fractures, the AF-RA data

distribution primarily falls within a rectangle along the long side of AF and the short side of RA. Conversely, in shear or shear-dominant fractures, the AF-RA data distribution mainly falls within a rectangle along the long side of RA and the short side of AF.

- (3) Through ultrasonic testing experiments conducted on granite, it has been discovered that the longitudinal wave velocity of granite changes during the process of rock fracture, reflecting the microstructure and crack propagation inside the rock. As the number of cycles grows, the longitudinal wave velocity and splitting tensile strength of granite specimens gradually decrease, showing a decreasing trend. This indicates a reduction in the elastic modulus of granite and an intensification of damage. These observations imply significant alterations to the internal pore structure of the rock, potentially culminating in the generation or extension of cracks. Consequently, porosity increases while density decreases.

## Data availability statement

The original contributions presented in the study are included in the article/supplementary material. Further inquiries can be directed to the corresponding authors.

## Author contributions

LW: Methodology, Software, Writing – Original Draft. WZ: Conceptualization, Data curation. ZC: Writing – Reviewing and Editing. YX: Conceptualization, Data curation. JL: Writing – Reviewing and Editing. YZ: Visualization. CD: Software, Validation. TC: Software, Validation. All authors contributed to the article and approved the submitted version.

## Funding

The authors are grateful to the financial support from the National Natural Science Foundation of China (52004082, 12002270, 52274096, 42007264, and 52174073), the Key Research and Development Program of Shaanxi Province, China (2022ZDLSF07-06, 2023-YBSF-369), and the Natural Science Basic Research Program of Shaanxi (2022JC-LHJJ-08).

## Conflict of interest

Author TC is employed by the company Zibo Aojing Garden Co., Ltd.

The remaining authors declare that the research was conducted in the absence of any commercial or financial relationships that could be construed as a potential conflict of interest.

## Publisher's note

All claims expressed in this article are solely those of the authors and do not necessarily represent those of their affiliated

organizations, or those of the publisher, the editors and the reviewers. Any product that may be evaluated in this article, or claim that may be made by its manufacturer, is not guaranteed or endorsed by the publisher.

## References

- Batchelor, A. S. (1985). Progress in hot dry rock exploitation. *Int. J. Energy Res.* 9 (3), 377–390. doi: 10.1002/er.4440090312
- Cai, C. L., Gensheng, I., Huang, Z., and Feng, G. (2016a). Thermal cracking effect of liquid nitrogen on shale and its application analysis in hydraulic fracturing. *J. China Univ. Petrol.* 40, 79–85. doi: 10.3969/j.issn.1673-5005.2016.01.0
- Cai, C., Huang, Z., Li, G., Gao, F., Wei, J., and Li, R. (2016b). Feasibility of reservoir fracturing stimulation with liquid nitrogen jet. *J. Petrol. Sci. Eng.* 144, 59–65. doi: 10.1016/j.petrol.2016.02.033
- Cai, C., Li, G., Huang, Z., and Chi, H. (2015). A waterless fracturing treatment: liquid nitrogen fracturing and its application prospect. *Научные труды НИПИ Нефтегаз ГНКАР* 3, 35–40. doi: 10.5510/OGP20150300250
- Cha, M., Yin, X., Kneafsey, T., Johanson, B., Alqahtani, N., Miskimins, J., et al. (2014). Cryogenic fracturing for reservoir stimulation—Laboratory studies. *J. petrol. Sci. Eng.* 124, 436–450. doi: 10.1016/j.petrol.2014.09.003
- Chen, G., Sun, Y., Xu, Z., and Li, X. (2022). Hydrogeological feasibility of mine water deep geological storage in Baotashan coarse sandstone: A case study in Ordos Basin. *Deep Underground Sci. Eng.* 1 (2), 148–164. doi: 10.1002/dug2.12022
- Chen, Z., Xu, G., and Jiang, M. (2019). The current status and development recommendations for dry hot rock fracturing technologies at home and abroad. *Petrol. Drilling Tech.* 47 (6), 1–8. doi: 10.1191/syzts.2019110
- Climo, M., Carey, B., Seward, A., and Bendall, S. (2016). Strategies for increasing geothermal direct use in New Zealand. *Proceed.: Geother. Resour. Council Trans* 40, 689–694.
- Coetzee, S., Neomagus, H. W., Bunt, J. R., Strydom, C. A., and Schobert, H. H. (2014). The transient swelling behaviour of large (–20+ 16 mm) South African coal particles during low-temperature devolatilisation. *Fuel* 136, 79–88. doi: 10.1016/j.fuel.2014.07.021
- Finnie, I., Cooper, G. A., and Berlie, J. (1979). Fracture propagation in rock by transient cooling. *Int. J. Rock Mech. Min. Sci. Geomech. Abst.* 16 (1), 11–21. Pergamon. doi: 10.1016/0148-9062(79)90771-X
- Grosse, C. U., Ohtsu, M., Aggelis, D. G., and Shiotani, T. (2021). *Acoustic emission testing: Basics for research—applications in engineering* (Springer Nature). Berlin, Springer-Verlag Berlin Heidelberg
- Grundmann, S. R., Rodvelt, G. D., Dials, G. A., and Allen, R. E. (1998). “Cryogenic nitrogen as a hydraulic fracturing fluid in the devonian shale,” in *SPE Eastern regional meeting*. SPE–51067.
- Guo, Q. H., He, T., Zhuang, Y. Q., Luo, J. L., and Zhang, C. H. (2020). Expansion of fracture network in granites via chemical stimulation: a laboratory study. *Earth Sci. Front.* 27 (1), 159. doi: 10.13745/j.esf.sf.2019.12.2
- Hall, K. (1999). The role of thermal stress fatigue in the breakdown of rock in cold regions. *Geomorphology* 31 (1–4), 47–63. doi: 10.1016/S0169-555X(99)00072-0
- Hardy, H. R. (1981). Applications of acoustic emission techniques to rock and rock structures: a state-of-the-art review. *Acoustic emissions geotech. Eng. practice STP* 750, 4–92.
- Huang, X. Q., and Meng, Q. K. (2018). Feasibility study on application of liquid nitrogen in hot dry rock drilling. *Explor. Eng. (Rock Soil Drill Tunn)* 45 (2), 22–25.
- Huang, Z. P., Zhang, Y., Sun, Y. K., Liu, C. Y., and Wu, W. D. (2016). Mechanical and acoustic characteristics of high temperature limestone with water cooling treatment. *J. Cent. South Univ. (Science Technology)* 12, 4181–4189. doi: 10.11817/j.issn.1672-7207.2016.12.0
- Kang, H., Li, W., Gao, F., and Yang, J. (2023). Grouting theories and technologies for the reinforcement of fractured rocks surrounding deep roadways. *Deep Underground Sci. Eng.* 2 (1), 2–19. doi: 10.1002/dug2.12026
- Kim, K., Kemeny, J., and Nickerson, M. (2014). Effect of rapid thermal cooling on mechanical rock properties. *Rock mech. rock Eng.* 47, 2005–2019. doi: 10.1007/s00603-013-0523-3
- Lajtai, E. Z. (1969). Shear strength of weakness planes in rock. *Int. J. Rock Mech. Min. Sci. Geomech. Abst.* 6 (5), 499–515. doi: 10.1016/0148-9062(69)90016-3
- Li, T. L., Cao, W. J., Wang, Y. W., Guo, J., and Jiang, F. M. (2019). Laboratory study on hydraulic fracturing and acoustic emission monitoring of enhanced geothermal system. *Adv. New Renewable Energy* 7 (3), 241–248. doi: 10.3969/j.issn.2095-560X.2019.03.00
- Li, Z., Xu, H., and Zhang, C. (2016). Liquid nitrogen gasification fracturing technology for shale gas development. *J. Petrol. Sci. Eng.* 138, 253–256. doi: 10.1016/j.petrol.2015.10.033
- Liang, M., Zhang, S. H., and Shu, B. (2018). Effect of different cooling ways on Brazilian tension characteristics of heat-treated granite. *J. Water Resour. Water Eng.* 29 (2), 186–193. doi: 10.11705/j.issn.1672-643X.2018.02.3
- Liu, J., Xue, Y., Fu, Y., Yao, K., and Liu, J. (2023). Numerical investigation on microwave-thermal recovery of shale gas based on a fully coupled electromagnetic, heat transfer, and multiphase flow model. *Energy* 263, 126090. doi: 10.1016/j.energy.2022.126090
- Lu, C., and Wang, G. (2015). Current status and prospect of hot dry rock research. *Sci. Technol. Rev.* 33 (19), 13–21. doi: 10.3981/j.issn.1000-7857.2015.19.00
- Ma, W., Wang, Y., Wu, X., and Liu, G. (2020). Hot dry rock (HDR) hydraulic fracturing propagation and impact factors assessment via sensitivity indicator. *Renewable Energy* 146, 2716–2723. doi: 10.1016/j.renene.2019.08.097
- McDaniel, B. W., Grundmann, S. R., Kendrick, W. D., Wilson, D. R., and Jordan, S. W. (1997). “Field applications of cryogenic nitrogen as a hydraulic fracturing fluid,” in *SPE Annual Technical Conference and Exhibition*. SPE–38623.
- Memon, K. R., Mahesar, A. A., Ali, M., Tunio, A. H., Mohanty, U. S., Akhondzadeh, H., et al. (2020). Influence of cryogenic liquid nitrogen on petro-physical characteristics of mancos shale: an experimental investigation. *Energy Fuels* 34 (2), 2160–2168. doi: 10.1021/acs.energyfuels.9b03700
- Stephen, R. (2013). In search of the waterless fracture. *J. petrol. Technol.* 65 (06), 46–54. doi: 10.2118/0613-0046-JPT
- Wang, P., Chen, Y. L., Zhou, X. L., Gao, S. S., and Zhao, H. Z. (2013). Impact of rapid cooling in water on residual mechanical properties of granite under high temperature. *J. Water Resour. Water Eng.* 24 (3), 54–63.
- Wang, S. L., and Li, C. (2008). Reservoir technology in enhanced geothermal systems. *Machinery Design Manufacture* 9, 141–143.
- Wang, G. L., Liu, Y. G., Zhu, X., and Zhang, W. (2020). The status and development trend of geothermal resources in China. *Earth Sci. Front.* 27 (1), 1. doi: 10.13745/j.esf.2020.1.1
- Wang, L., Xue, Y., Cao, Z., Wu, X. J., Dang, F. N., and Liu, R. (2023). Mechanical properties of high-temperature granite under liquid nitrogen cooling. *Geofluids* 2023, 3819799. doi: 10.1155/2023/3819799
- Wu, X., Huang, Z., Li, R., Zhang, S., Wen, H., Huang, P., et al. (2018). Investigation on the damage of high-temperature shale subjected to liquid nitrogen cooling. *J. Natural Gas Sci. Eng.* 57, 284–294. doi: 10.1016/j.jngse.2018.07.005
- Xu, T., Zhang, Y., Yu, Z., Hu, Z., and Guo, L. (2015). Laboratory study of hydraulic fracturing on hot dry rock. *Sci. Technol. Rev.* 33 (19), 35–39. doi: 10.3981/j.issn.1000-7857.2015.19.00
- Xu, T., Zhang, Y., Zeng, Z., and Bao, X. (2012). Technology progress in an enhanced geothermal system (Hot dry rock). *Keji Daobao/ Sci. Technol. Rev.* 30 (32), 42–45. doi: 10.3981/j.issn.1000-7857.2012.32.00
- Xue, Y., Liu, S., Chai, J., Liu, J., Ranjith, P. G., Cai, C., et al. (2023a). Effect of water-cooling shock on fracture initiation and morphology of high-temperature granite: Application of hydraulic fracturing to enhanced geothermal systems. *Appl. Energy* 337, 120858. doi: 10.1016/j.apenergy.2023.120858
- Xue, Y., Ranjith, P. G., Gao, F., Zhang, Z., and Wang, S. (2023b). Experimental investigations on effects of gas pressure on mechanical behaviors and failure characteristic of coals. *J. Rock Mech. Geotech. Eng.* 15 (2), 412–428. doi: 10.1016/j.jrmge.2022.05.013
- Zhang, S., Huang, Z., Zhang, H., Guo, Z., Wu, X., Wang, T., et al. (2018). Experimental study of thermal-crack characteristics on hot dry rock impacted by liquid nitrogen jet. *Geothermics* 76, 253–260. doi: 10.1016/j.geothermics.2018.08.002
- Zhang, C. H., Wang, L. G., Zhao, Q. S., and Li, W. L. (2015). Permeability evolution model and numerical analysis of coupled coal deformation, failure and liquid nitrogen cooling. *J. Hebei Univ. Sci. Technol.* 36 (1), 90–99. doi: 10.7535/hbkd.2015yx01016
- Zhang, F., Zhao, J., Hu, D., Skoczylas, F., and Shao, J. (2018). Laboratory investigation on physical and mechanical properties of granite after heating and water-cooling treatment. *Rock Mech. Rock Eng.* 51, 677–694. doi: 10.1007/s00603-017-1350-8



# Frontiers in Earth Science

Investigates the processes operating within the major spheres of our planet

Advances our understanding across the earth sciences, providing a theoretical background for better use of our planet's resources and equipping us to face major environmental challenges.

## Discover the latest Research Topics

[See more →](#)

### Frontiers

Avenue du Tribunal-Fédéral 34  
1005 Lausanne, Switzerland  
[frontiersin.org](https://frontiersin.org)

### Contact us

+41 (0)21 510 17 00  
[frontiersin.org/about/contact](https://frontiersin.org/about/contact)

